



**Photocatalytic conversion of methane to C₂ Products
in a flow reactor**

Xiyi Li

2022

A thesis submitted for the partial fulfilment of the requirements for the degree of
Doctor of Philosophy at University College London

Department of Chemical Engineering,

University College London,

London, United Kingdom

Declaration

I, Xiyi Li, confirm that the work presented in this thesis is my own. Where information has been derived from other sources, I confirm that this has been indicated in the thesis.

.....

Signature

.....

Date

I. Acknowledgements

Firstly, I would like to express sincere gratitude to my supervisor Prof. Junwang Tang for his tremendous guidance and support of my PhD research journey. When I was confused with the experimental results, research directions and even career developments, he always kindly and patiently helped me to focus and to move forward. I am also thankful to my secondary supervisor Prof Gopinathan Sankar for the guidance and encouragement. In particular, he helped to shape my research attitude and research methods during the Mphil to PhD transfer viva.

I wish to thank all the members including the Alumni of the Solar Energy and Advanced Materials research group at UCL. Great thanks to Chao Wang and Youxun Xu, for their kind suggestions and discussion, providing the best atmosphere for me to learn and to live. I also want to express my gratitude to Jijia Xie, for his help for all the reaction set-ups and analysis instruments. I am very thankful for the team-work and support from Hui Wang, Qingning Yang, Haimiao Jiao, Zhe Yuan, Ayoola Shoneye, Madasamy Thangamuthu, Fernando Jose Torres, Elan Mistry and other group members.

A huge appreciation must go to all technicians at the Department of Chemistry, including Mr Martin Vickers, Mr Steven Firth, and Professor Robert G. Palgrave, for their kind guidance in the operation of XRD, PL/Raman and XPS, respectively.

I would also like to thank Fangjia Zhao, Liquan Zhang, Yiyun Liu, Junrun Feng and Yue Wen from other research groups at UCL, who have always been helpful regarding my needs for research equipment. I am grateful for the great support from Jianlong

Yang at Northwest University to address my urgent needs on material characterisation, even during his holiday. Meanwhile, other collaborators, Dr Juan J. Delgado at Universidad de Cádiz, Dr Natalia Martsinovich at the University of Sheffield, Yi Yang and Prof Jiaguo Yu at the Wuhan University of Technology, Chao Li and Prof Alexander Cowan at the University of Liverpool, Dr Qiong Liu at Guangdong Academy of Sciences are also involved in my project aiding advanced techniques and DFT simulations.

Dr Feng Wu, Dr Qian Guo and Dr Yunhong Pi, with expertise in organic chemistry and/or photochemistry, always kindly help me to gain an insightful understanding of the mechanism analysis at any moment.

Finally, I would like to acknowledge my support funding, GRS and ORS at UCL. I am also deeply grateful to my parents in China for their financial support and more importantly for their love.

UCL Research Paper Declaration Form: referencing the doctoral candidate's own published work(s)

Please use this form to declare if parts of your thesis are already available in another format, e.g. if data, text, or figures:

- have been uploaded to a preprint server;
- are in submission to a peer-reviewed publication;
- have been published in a peer-reviewed publication, e.g. journal, textbook.

This form should be completed as many times as necessary. For instance, if you have seven thesis chapters, two of which containing material that has already been published, you would complete this form twice.

1. For a research manuscript that has already been published (if not yet published, please skip to section 2):	
a) Where was the work published? (e.g. journal name)	Nature Reviews Materials
b) Who published the work? (e.g. Elsevier/Oxford University Press):	Springer Nature
c) When was the work published?	28/06/2022
d) Was the work subject to academic peer review?	Yes
e) Have you retained the copyright for the work?	Yes
<p>[If no, please seek permission from the relevant publisher and check the box next to the below statement]:</p> <p><input type="checkbox"/> <i>I acknowledge permission of the publisher named under 1b to include in this thesis portions of the publication named as included in 1a.</i></p>	

2. For a research manuscript prepared for publication but that has not yet been published (if already published, please skip to section 3):			
a) Has the manuscript been uploaded to a preprint server? (e.g. medRxiv):	Please select.	If yes, which server? Click or tap here to enter text.	
b) Where is the work intended to be published? (e.g. names of journals that you are planning to submit to)	Click or tap here to enter text.		
c) List the manuscript's authors in the intended authorship order:	Click or tap here to enter text.		
d) Stage of publication	Please select.		
3. For multi-authored work, please give a statement of contribution covering all authors (if single-author, please skip to section 4):			
J.T. conceived and supervised the progress of the entire project. X.L. drafted and revised the majority of the paper. C.W. participated in drafting and revising the article.			
4. In which chapter(s) of your thesis can this material be found?			
Chapter 2, 7, and 8			
5. e-Signatures confirming that the information above is accurate (this form should be co-signed by the supervisor/ senior author unless this is not appropriate, e.g. if the paper was a single-author work):			
Candidate:	Click or tap here to enter text.	Date:	11/07/2022

Supervisor/ Senior Author (where appropriate):	Click or tap here to enter text.	Date:	24/08/2022
---	----------------------------------	--------------	------------

UCL Research Paper Declaration Form: referencing the doctoral candidate's own published work(s)

Please use this form to declare if parts of your thesis are already available in another format, e.g. if data, text, or figures:

- have been uploaded to a preprint server;
- are in submission to a peer-reviewed publication;
- have been published in a peer-reviewed publication, e.g. journal, textbook.

This form should be completed as many times as necessary. For instance, if you have seven thesis chapters, two of which containing material that has already been published, you would complete this form twice.

1. For a research manuscript that has already been published (if not yet published, please skip to section 2):	
f) Where was the work published? (e.g. journal name)	Angewandte Chemie International Edition
g) Who published the work? (e.g. Elsevier/Oxford University Press):	Wiley
h) When was the work published?	25/06/2020
i) Was the work subject to academic peer review?	Yes
j) Have you retained the copyright for the work?	Yes
<p>[If no, please seek permission from the relevant publisher and check the box next to the below statement]:</p> <p><input type="checkbox"/> <i>I acknowledge permission of the publisher named under 1b to include in this thesis portions of the publication named as included in 1a.</i></p>	

2. For a research manuscript prepared for publication but that has not yet been published (if already published, please skip to section 3):		
e) Has the manuscript been uploaded to a preprint server? (e.g. medRxiv):	Please select.	If yes, which server? Click or tap here to enter text.
f) Where is the work intended to be published? (e.g. names of journals that you are planning to submit to)	Click or tap here to enter text.	
g) List the manuscript's authors in the intended authorship order:	Click or tap here to enter text.	
h) Stage of publication	Please select.	
3. For multi-authored work, please give a statement of contribution covering all authors (if single-author, please skip to section 4):		
<p>X.L. proposed the idea, designed and conducted experiments, analysed data and drafted the article. J.X. assisted with the design of reaction system and conduction of activity test. H.R. helped with the data analysis. C.W. assisted with the synthesis of materials. J.T. designed the project and supervised the progress of the whole project.</p>		
4. In which chapter(s) of your thesis can this material be found?		
Chapter 4		
5. e-Signatures confirming that the information above is accurate (this form should be co-signed by the supervisor/ senior author unless this is not appropriate, e.g. if the paper was a single-author work):		

Candidate:	Click or tap here to enter text.	Date:	11/07/2022
Supervisor/ Senior Author (where appropriate):	Click or tap here to enter text.	Date:	24/08/2022

UCL Research Paper Declaration Form: referencing the doctoral candidate's own published work(s)

Please use this form to declare if parts of your thesis are already available in another format, e.g. if data, text, or figures:

- have been uploaded to a preprint server;
- are in submission to a peer-reviewed publication;
- have been published in a peer-reviewed publication, e.g. journal, textbook.

This form should be completed as many times as necessary. For instance, if you have seven thesis chapters, two of which containing material that has already been published, you would complete this form twice.

1. For a research manuscript that has already been published (if not yet published, please skip to section 2):	
k) Where was the work published? (e.g. journal name)	Click or tap here to enter text.
l) Who published the work? (e.g. Elsevier/Oxford University Press):	Click or tap here to enter text.
m) When was the work published?	Click or tap to enter a date.
n) Was the work subject to academic peer review?	Please select.
o) Have you retained the copyright for the work?	Please select.
<p>[If no, please seek permission from the relevant publisher and check the box next to the below statement]:</p> <p><input type="checkbox"/> <i>I acknowledge permission of the publisher named under 1b to include in this thesis portions of the publication named as included in 1a.</i></p>	

2. For a research manuscript prepared for publication but that has not yet been published (if already published, please skip to section 3):		
i) Has the manuscript been uploaded to a preprint server? (e.g. medRxiv):	No	If yes, which server? Click or tap here to enter text.
j) Where is the work intended to be published? (e.g. names of journals that you are planning to submit to)	Nature Communications	
k) List the manuscript's authors in the intended authorship order:	Xiyi Li, Chao Wang, Jianlong Yang, Youxun Xu, Yi Yang, Jiaguo Yu, Juan J. Delgado, Natalia Martsinovich, Junwang Tang	
l) Stage of publication	Submitted	
3. For multi-authored work, please give a statement of contribution covering all authors (if single-author, please skip to section 4):		
<p>J.T. designed the project and supervised the progress of the whole project. X.L. proposed the idea, designed and conducted experiments, analysed data and drafted the article. C.W. assisted with the conduction of activity test and characterization. J.Y. Performed the in-situ EPR experiments as well as contributed to the discussion of the EPR results and TPR results. Y.X. contributed to the discussion of the photocatalytic mechanism. Y.Y. and J.Y. carried out in-situ XPS measurements. J.J.D. carried out the STEM. N.M. conducted the DFT calculations.</p>		
4. In which chapter(s) of your thesis can this material be found?		
Chapter 5		

5. e-Signatures confirming that the information above is accurate (this form should be co-signed by the supervisor/ senior author unless this is not appropriate, e.g. if the paper was a single-author work):

Candidate:	Click or tap here to enter text.	Date:	11/07/2022
Supervisor/ Senior Author (where appropriate):	Click or tap here to enter text.	Date:	24/08/2022

UCL Research Paper Declaration Form: referencing the doctoral candidate's own published work(s)

Please use this form to declare if parts of your thesis are already available in another format, e.g. if data, text, or figures:

- have been uploaded to a preprint server;
- are in submission to a peer-reviewed publication;
- have been published in a peer-reviewed publication, e.g. journal, textbook.

This form should be completed as many times as necessary. For instance, if you have seven thesis chapters, two of which containing material that has already been published, you would complete this form twice.

1. For a research manuscript that has already been published (if not yet published, please skip to section 2):	
p) Where was the work published? (e.g. journal name)	Click or tap here to enter text.
q) Who published the work? (e.g. Elsevier/Oxford University Press):	Click or tap here to enter text.
r) When was the work published?	Click or tap to enter a date.
s) Was the work subject to academic peer review?	Please select.
t) Have you retained the copyright for the work?	Please select.
<p>[If no, please seek permission from the relevant publisher and check the box next to the below statement]:</p> <p><input type="checkbox"/> <i>I acknowledge permission of the publisher named under 1b to include in this thesis portions of the publication named as included in 1a.</i></p>	

2. For a research manuscript prepared for publication but that has not yet been published (if already published, please skip to section 3):		
m) Has the manuscript been uploaded to a preprint server? (e.g. medRxiv):	No	If yes, which server? Click or tap here to enter text.
n) Where is the work intended to be published? (e.g. names of journals that you are planning to submit to)	Nature Chemistry	
o) List the manuscript's authors in the intended authorship order:	Xiyi Li, Chao Li, Youxun Xu, Qiong Liu, Mounib Bahri, Liquan Zhang, Nigel D. Browning, Alexander J. Cowan, Junwang Tang	
p) Stage of publication	Not yet submitted	
3. For multi-authored work, please give a statement of contribution covering all authors (if single-author, please skip to section 4):		
<p>J.T. designed the project and supervised the progress of the whole project. X.L. proposed the idea, designed and conducted experiments, analysed data and drafted the article. C.L. and A.J.C. assisted with the TAS measurement. Y.X. contributed to the discussion of the photocatalytic mechanism. Q.L. carried out in-situ DRIFTS measurements. M. B. and N.D.B. carried out the STEM. L. Z. assisted with Au sputter process.</p>		
4. In which chapter(s) of your thesis can this material be found?		
Chapter 6		
5. e-Signatures confirming that the information above is accurate (this form should be co-signed by the supervisor/ senior author unless this is not appropriate, e.g. if the paper was a single-author work):		

Candidate:	Click or tap here to enter text.	Date:	11/07/2022
Supervisor/ Senior Author (where appropriate):	Click or tap here to enter text.	Date:	24/08/2022

II. Abstract

The predicted substantial reserve of methane hydrate and shale gas, far beyond the sum of other fossil fuels, indicates an extremely attractive while challenging chemical synthesis process in which methane, instead of crude oil can be used as a building block for diverse chemical synthesis in a potentially low-carbon process. Among various direct methane conversion to value-added chemicals processes, photocatalytic oxidative coupling of two methane molecules to produce C₂ products (C₂H₆/C₂H₄) is one of the most general and highly profitable but challenge processes for long chain chemical synthesis. However, due to the highly stable methane molecules and the more reactive C₂ products, there is an obvious dilemma: an extreme condition (e.g., high energy or strong oxidants) required to activate the highly stable C-H bonds in methane, while a mild condition needed to avoid the overoxidation of C₂ products.

In the project, a flow system for photocatalytic oxidative coupling of methane was designed for the first time, which allows the manipulation of residence time and the CH₄/O₂ ratio for precise evaluation of the potential photocatalysts. The robust and classic anatase TiO₂ was selected as a basic semiconductor for the investigation of methane activation. The most general electron acceptor in photocatalysis, Pt nanoparticles, and the widely used species for methane activation in thermocatalysis, CuO_x clusters were introduced on TiO₂ to work synergistically. The optimised sample Cu_{0.1}Pt_{0.5}/TiO₂ shows the highest yield of C₂ product of 6.8 μmol h⁻¹ at a space velocity of 24000 ml g⁻¹ h⁻¹, more than twice the sum of the activity of Pt/TiO₂ (1.07 μmol h⁻¹) and Cu/TiO₂ (1.9 μmol h⁻¹), it was also the highest among photocatalytic methane conversion under atmospheric pressure when it was published. High C₂ selectivity of

60% is also comparable to that attained by conventional high-temperature (>943 K) thermal catalysis. Characterisation data confirms that Pt acts as an electron acceptor to promote the charge separation, while holes are recommended to be accepted by CuO_x to avoid overoxidation of as-formed C_2 products.

However, the yield rate and apparent quantum efficiency (AQE) are still low and the short stability test period is another concern. Therefore, a series of noble metals were loaded on TiO_2 to form new photocatalysts, which usually act as charge sink to promote charge transfer in photocatalysis and show unique catalytic performance for C-H bond activation in traditional catalysis. Among them, Pd loading shows the exceptional activity and then a series of non-noble transition metals as the second component was introduced to form nanoalloy to assemble multi-function to enhance the activity and stability. The optimised sample PdCu/ TiO_2 shows an unprecedented activity, e.g., 116 h^{-1} of TOF and 12642 of TON even under a high space velocity of $342000 \text{ mL gcat}^{-1} \text{ h}^{-1}$ and >110 hours stability with the high C_2 selectivity (75%) in a flow reactor operated at room temperature. In particular, the highest methane conversion rate of $2480 \mu\text{mol g}^{-1} \text{ h}^{-1}$ to C_2 products operated at room temperature has been achieved, 20 times higher than the results reported before. The highest AQE of 8.4% is also obtained among all ambient photocatalytic methane conversion to C_2 processes, indicating it is an energy-efficient process. In-situ EPR, XPS and DFT calculations indicated that the unprecedented activity and stability are due to synergetic effect between Pd and Cu in the nanoalloy. The photoholes from TiO_2 can be transferred to Pd, which lowers the oxidative potential to selectively abstract the pre-soften C-H bond in methane to form C_2 products. While the introduction of

metallic Cu can weaken the adsorption of C₂ products, avoiding the further consecutive reaction for coke formation.

Despite of the great improvement of activity and stability, the C₂ yield rate and C₂ selectivity is relatively moderate. The limitations of this flow reactor have also not been carefully considered, such as the relationship between activity and catalyst mass, the light utilisation efficiency and the thickness of membrane. In addition, the fabrication procedure of the photocatalysts is time-consuming and difficult to produce at large scale, impeding its further practical application. Therefore, a Au/TiO₂ photocatalyst produced via a facile and rapid (60 seconds) sputter method was developed. After optimisation of both photocatalyst and reaction system, a very high C₂ yield rate of 468 $\mu\text{mol h}^{-1}$ (23.4 $\text{mmol g}^{-1} \text{h}^{-1}$) with a decent C₂ selectivity of ca. 90% can be obtained. The highest AQE of ca. 10% has also been achieved among all the reported methane conversion at ambient conditions. The charge transfer pathway is proposed based on the in situ XPS and transient absorption spectroscopy (TAS) measurements. The surface chemistry reaction between substrates and catalysts is investigated by in situ EPR and in situ DRIFTS. It has been found that the metallic Au nanoparticles work as a hole acceptor to efficiently extract the photoholes on TiO₂ and drive the selective oxidation of methane to methyl radicals for further C-C coupling.

III. Impact statements

Direct conversion of methane to high-value chemicals and fuels is widely accepted as a valuable route to alleviate the pressure of decreasing reserves of crude oil and reduce carbon emission during chemical synthesis. Oxidative coupling of methane (OCM) to C_2 (C_2H_6 and C_2H_4) products is considered as one of the most promising catalytic technologies to upgrade methane, but very harsh reaction conditions (e.g., >953 K) are needed to activate the inert methane molecule, which often results in overoxidation and carbon accumulation impeding its commercialisation. Photocatalysis, employing photo energy instead of thermal energy to generate energetic carriers that pre-activate methane molecules and reduce the activation energy, has been regarded as a promising alternative to drive this “holy grail” catalytic reaction under mild conditions. However, the photocatalytic methane conversion to C_2 process is at the infant stage and studies so far were mainly on the trail test of photocatalytic potential with a simple batch reactor, far away from real industrial application. In this thesis, the photocatalytic OCM flow fix-bed reactor has been developed for the first time, providing a scientific evaluation system in this filed, which already stimulates follow-up investigations since firstly published. Based on this flow reactor, unprecedented photocatalytic activities have been achieved, such as the highest C_2 yield rate of $468 \mu\text{mol h}^{-1}$, highest C_2 selectivity of ca. 90%, highest AQE of ca. 10%, longest stability of >110 hours etc., among all the reported photocatalytic methane conversion to C_2 processes. This is the first example in which the space time rate ($23.4 \text{ mol kg}_{\text{cat}}^{-1} \text{ h}^{-1}$ for C_2 or $24.5 \text{ mol kg}_{\text{cat}}^{-1} \text{ h}^{-1}$ for C_{2+}) in photocatalytic methane conversion under mild condition can be comparable to the benchmark thermal catalysts in OCM processes at the high temperature (>953 K). In the meantime, the superiority of selectivity control in

photocatalysis has also been demonstrated, in which the selectivity to C_2/C_{2+} is also at least 20% higher than that in conventional OCM processes. This thesis shows the great potential to develop photocatalytic methane conversion to replace traditional thermocatalysis for real industrial application. This thesis also finds an effective approach to improve the C_2 selectivity in photocatalysis via the control of the oxidative potential by design of co-catalysts (e.g., nanoclusters, nanoparticles, nanoalloys). Furthermore, a systematic method of the mechanism investigation is also demonstrated in this work for the researcher in this field, including the photophysics to resolve charge transfer and the surface chemistry to reveal the reaction pathways, which involves the combination of in situ techniques (e.g., EPR, XPS, DRIFTS), spectroscopies techniques (e.g., TAS, TRPL) and DFT simulation. This work is of great interest to a wide audience in the fields of nanotechnology (nanoalloy), energy, selective catalysis, photochemistry, environmental purification, and even chemical engineering. Overall, this thesis has successfully provided an effective and green method to directly convert methane to valuable chemicals, consistent with the goals of transition to the clean technology with net zero carbon emissions as underlined by UN Climate Change Conference UK 2021 (COP 26).

IV. Publication & conferences

Publications

- 1) **Xiyi Li**, J. J. Xie, H. Rao, C. Wang, J. W. Tang*. Platinum- and CuO_x-Decorated TiO₂ Photocatalyst for Oxidative Coupling of Methane to C₂ Hydrocarbons in a Flow Reactor. *Angew. Chem. Int. Ed.*, **2020**, 132, 19870-19875.
- 2) **Xiyi Li**, C. Wang, J. W. Tang*. Methane transformation by photocatalysis. *Nat. Rev. Mater.* DOI: 10.1038/s41578-022-00422-3.
- 3) **Xiyi Li**, C. Wang, J. L. Yang, Y. X. Xu, Y. Yang, J. G. Yu, J. J. Delgado, N. Martinsovich, J. W. Tang*. Efficient and stable oxidative coupling of methane to C₂ hydrocarbons over PdCu alloy loaded TiO₂ photocatalyst in a flow reactor. Submitted to *Nat. Commun.*
- 4) Q. N. Yang, **Xiyi Li**, J. W. Tang*. Tuning selectivity among acetalization, pinacol coupling, and hydrogenation reactions of benzaldehyde by catalytic and photochemical pathways at room temperature. *Mater. Today. Energy*, **2022**, 23, 100890.
- 5) H. Wang, **Xiyi Li**, Q. S. Ruan, J. W. Tang*. Ru and RuO_x decorated carbon nitride for efficient ammonia photosynthesis. *Nanoscale*, **2020**, 12, 12329-12335.
- 6) Y. Yang*, **Xiyi Li**, H.Q. Zhu, X.H. Xu, L.L. Bao. Chemical removal of m-cresol: a critical review. *Rev. in Chem. Eng.*, **2021**, DOI: 10.1515/revce-2021-0001.

- 7) T.J. Miao, C. Wang, L. Xiong, **Xiyi Li**, J.J. Xie, J.W. Tang*. In Situ Investigation of Charge Performance in Anatase TiO₂ Powder for Methane Conversion by Vis–NIR Spectroscopy. ACS. Catal., **2021**, 11, 13, 8226-8238.
- 8) H. Wang, H. Wang, Z. W. Wang, L. Tang, G. M. Zeng*, P. Xu*, M. Chen, T. Xiong, C. Y. Zhou, **Xiyi Li**, D. L. Huang, Y. Zhu, Z. X. Wang, J. W. Tang*. Covalent organic framework photocatalysts: structures and applications. Chem. Soc. Rev., **2020**, 49, 4135-4165.
- 9) Q. Q. Hou, **Xiyi Li**, Y. H. Pi, J. Xiao*. Construction of In₂S₃@NH₂-MIL-68(In)@In₂S₃ Sandwich Homologous Heterojunction for Efficient CO₂ Photoreduction. Ind. Eng. Chem. Res., **2020**, 59, 20711–20718.
- 10) Y. H. Pi, S. Jin, **Xiyi Li**, S. Tu, Z. Li, J. Xiao*. Encapsulated MWCNT@MOF-derived In₂S₃ tubular heterostructures for boosted visible-light-driven degradation of tetracycline. Appl. Catal. B Environ., **2019**, 256, 117882.
- 11) J. J. Xie, **Xiyi Li**, J. Guo, L. Luo, J. J. Delgado, N. Martsinovich, J. W. Tang*. Highly Selective Oxidation of Benzene to Phenol with Air at Room Temperature Promoted by Water. Nat. Commun., **2022**, in revision.

Conference presentations

- 1) Xiyi Li, J. W. Tang*, Poster presentation, Photocatalytic oxidative coupling of methane over TiO₂-based catalysts, **6th EPSRC Centre for Nature Inspired Engineering (CNIE) Advisory Board, Conference and Workshop**, London, January 2020
- 2) Xiyi Li, J. W. Tang*, Poster presentation, Photocatalytic oxidative coupling of methane over TiO₂-based catalysts, **2nd Joint UK Solar Fuels Network Super Solar workshop on Solar Energy Conversion and Storage**, Imperial College London, London, December 2019

V. Table of contents

Declaration.....	1
I. Acknowledgements.....	2
II. Abstract.....	16
III. Impact statements	19
IV. Publication & conferences	21
<i>Publications.....</i>	<i>21</i>
<i>Conference presentations</i>	<i>23</i>
V. Table of contents	24
VI. List of tables.....	29
VII. List of figures	30
1 Introduction.....	41
1.1 <i>Background.....</i>	<i>41</i>
1.2 <i>Motivation, aim and objectives.....</i>	<i>43</i>
1.3 <i>Report outline</i>	<i>47</i>
2 Literature Review.....	48
2.1 <i>Principles of photocatalytic methane conversion.....</i>	<i>48</i>
2.2 <i>Development of photocatalytic materials</i>	<i>53</i>
2.2.1 <i>Semiconductor materials</i>	<i>54</i>

2.2.2	Non-semiconductor materials.....	65
2.2.3	Co-catalysts	66
2.3	<i>Reaction system design</i>	70
2.3.1	Batch systems.....	71
2.3.2	Flow systems	73
2.3.3	Other reaction systems	74
2.4	<i>Mechanistic understanding</i>	76
2.4.1	Photophysics.....	77
2.4.2	Reaction steps and surface chemistry	80
2.5	<i>Conclusion</i>	86
3	Methodology	89
3.1	<i>Powder X-ray diffraction (PXRD)</i>	89
3.2	<i>Raman spectroscopy</i>	90
3.3	<i>Photoluminescence spectroscopy (PL)</i>	91
3.4	<i>Time-resolved photoluminescence (TRPL)</i>	91
3.5	<i>Ultraviolet-Visible (UV-Vis) spectroscopy</i>	92
3.6	<i>Microscopes (SEM, TEM)</i>	93
3.7	<i>X-ray photoelectron spectroscopy (XPS)</i>	94
3.8	<i>Electron paramagnetic resonance (EPR)</i>	94
3.9	<i>Transient absorption spectroscopy (TAS)</i>	95
3.10	<i>Diffuse reflectance infrared Fourier transform spectroscopy (DRIFTS)</i>	96
3.11	<i>Photo-electrochemical test</i>	97
3.12	<i>Photocatalytic activity tests</i>	98

4 Modification of TiO₂ with Pt nanoparticles and CuO_x clusters for efficient photocatalytic conversion of methane 100

<i>4.1</i>	<i>Introduction</i>	<i>100</i>
<i>4.2</i>	<i>Experimental section</i>	<i>101</i>
4.2.1	Fabrication of photocatalysts.....	101
4.2.2	Characterisation.....	104
4.2.3	Photocatalytic activity test.....	105
4.2.4	Calculation of selectivity	105
4.2.5	Calculation of apparent quantum efficiency (AQE) based on the conversion of methane 105	
<i>4.3</i>	<i>Results and discussion</i>	<i>106</i>
4.3.1	Preliminary investigations	106
4.3.2	Photocatalytic OCM over Pt _x Cu _y /PC-50	107
4.3.3	Characterisation of the optimised sample Cu _{0.1} Pt _{0.5} /PC-50	113
4.3.4	Photocatalytic mechanism of the optimised sample Cu _{0.1} Pt _{0.5} /PC-50	118
<i>4.4</i>	<i>Conclusion</i>	<i>123</i>

5 Efficient and highly selectively oxidative coupling of methane to C₂ hydrocarbons over PdCu nanoalloy loaded TiO₂ 125

<i>5.1</i>	<i>Experimental section</i>	<i>127</i>
5.1.1	Photocatalysts fabrication.....	127
5.1.2	Characterisations	129
5.1.3	Photocatalytic reaction for methane conversion.....	130
5.1.4	Calculation of the C ₂ selectivity	130
5.1.5	Calculation of apparent quantum efficiency (AQE).....	131
5.1.6	Calculation of turnover number (TON) and turnover frequency (TOF).....	131
5.1.7	Computational details.....	132

5.2	<i>Results and discussion</i>	132
5.2.1	Photocatalytic activities.....	132
5.2.2	Characterisations of the photocatalysts	144
5.2.3	Investigation of photo-induced charge transfer	154
5.2.4	Investigation of the photocatalytic mechanism	160
5.3	<i>Conclusion</i>	166
6	Au/TiO₂ catalyst for photocatalytic oxidative coupling of methane with high selectivity and efficiency	170
6.1	<i>Experimental section</i>	171
6.1.1	Materials preparation.....	171
6.1.2	Materials characterisations	173
6.1.3	Photocatalytic activity for methane conversion.....	174
6.1.4	The calculation of CH ₄ conversion rate and C ₂ /C ₂₊ selectivity	175
6.1.5	Apparent quantum efficiency (AQE)	175
6.2	<i>Results and discussion</i>	176
6.2.1	Preliminary investigation	176
6.2.2	Rapid preparation of Au/TiO ₂ on glass fibre membranes.....	177
6.2.3	Photocatalytic OCM activity over Au/TiO ₂ /membrane.....	179
6.2.4	Characterisation of the optimised sample.....	190
6.2.5	Investigation of the photocatalytic mechanism	193
6.3	<i>Conclusion</i>	208
7	Overall conclusions	210
8	Future works	215
9	References	219

VI. List of tables

Table 2-1 Change of ΔG^0 (298 K) for various methane conversion reactions	52
Table 4-1 Representative works on photocatalytic methane conversion to ethane/ethene at room temperature and atmospheric pressure.....	109
Table 4-2 Control experimental results of the photocatalytic OCM over $\text{Cu}_{0.1}\text{Pt}_{0.5}/\text{PC}-50$	112
Table 5-1 The weight percentage of Pd and Cu in $\text{Pd}_{0.1}\text{Cu}_{0.1}/\text{TiO}_2$ detected by ICP-OES and AAS	136
Table 5-2 Representative works on photocatalytic methane conversion to ethane/ethylene operated at room temperature.....	138
Table 5-3 DFT calculations results of methane adsorption on TiO_2 , Pd and PdCu.	161
Table 5-4 DFT calculations results of ethane adsorption on Pd and PdCu.....	164
Table 6-1 Comparison of methane conversion to ethane/ethylene over different photocatalysts	182
Table 6-2 Comparison of this work with representative OCM thermal catalysts (Note that some publications may use C_{2+} rather than C_2 taking higher hydrocarbons into account. Thus, the values for C_2 are in blue while the values for C_{2+} are in orange).	187
Table 10-1 Representative photocatalysts used for methane conversion to various products	254

VII. List of figures

- Figure 2-1 The principle of photocatalysis involves excitation of electrons from the valence band to the conduction band (step 1), charge separation and transportation to the reaction sites (step 2), charge recombination (step 3), surface reduction reaction (step 4) and surface oxidation reaction (step 5). Adapted with permission from ref.¹, Springer Nature Limited.....49
- Figure 2-2 Methane can be activated by different mechanisms photocatalytically. The C-H bond can be directly activated by photoholes, photoelectrons or energy from localised surface plasmon resonance or indirectly activated by RO· radicals such as ·OH or CH₃O· or chemical loop processes through mediates, such as metal cationic species or lattice oxygen. Reprinted with permission from ref.¹, Springer Nature Limited.50
- Figure 2-3 Schematic illustration of the methane conversion process over Ga-Doped and Pt-Loaded porous TiO₂-SiO₂. Reprinted with permission from ref.¹⁸, American Chemical Society.....55
- Figure 2-4 Demonstration of C-H and C=C bond polarization over polar crystal planes of ZnO nanostructures. Reprinted with permission from ref. ⁸⁸, American Chemical Society.57
- Figure 2-5 Schematic demonstration of methane conversion to methanol over FeOOH/m-WO₃. Reprinted with permission from ref. ⁹⁵, Elsevier.59
- Figure 2-6 Schematic demonstration of methane activation process over BiVO₄/V₂O₅. Reprinted with permission from ref. ⁷⁴, American Chemical Society.....61

Figure 2-7 Schematic demonstration of C-H bond activation on the surface of GaN m-plane. Reprinted with permission from ref. ¹⁰ , American Chemical Society.	63
Figure 2-8 Cu-single-atom Ru alloy catalyst for DRM reaction. Reprinted with the permission from ref. ²¹ , Springer Nature Limited.	65
Figure 2-9 Schematic demonstration of plasma-assisted conversion of CH ₄ and CO ₂ into CO and C ₂ H ₄ over Ag/TiO ₂ . Reprinted with permission from ref. ⁴⁵ , American Chemical Society.....	68
Figure 2-10 Schematic demonstration of methane partial oxidation to methanol over FeO _x /TiO ₂ . Reprinted with the permission from ref. ¹² , Springer Nature Limited.	69
Figure 2-11 A batch reactor is equipped with a circulation pump to improve the mass transfer of methane. Reprinted with permission from ref. ⁴⁰ , Elsevier.....	71
Figure 2-12 The influence of reactants' pressure on the direct oxidation of methane to oxygenates was investigated over Au-loaded ZnO photocatalyst. Reprinted with permission from ref. ⁸⁶ , ACS	72
Figure 2-13 A flow reactor was first reported for the photocatalytic oxidative coupling of methane reaction. Reprinted with permission from ref. ⁴⁸ , CC BY 4.0 (https://creativecommons.org/licenses/by/4.0/).	73
Figure 2-14 A two-phase reaction system was used for photo-oxidation of CH ₄ by NaClO ₂ . Reprinted with permission from ref. ¹²⁵ , Wiley.....	75
Figure 2-15 A chemical loop was used for stoichiometric methane conversion to ethane over Ag-H ₃ OW ₁₂ O ₄₀ /TiO ₂ . Reprinted with permission form ref. ³⁶ , Springer Nature Limited.	76

Figure 2-16 Transient absorption spectra (TAS) of charge dynamics in Rh/TiO ₂ (red), Rh/ZrO ₂ (green), and Rh/SiO ₂ (blue) after photoexcitation. Reprinted with permission from ref. ³¹ , ACS.	78
Figure 2-17 In-situ Iron 2p XPS spectra of FeO _x /TiO ₂ in the dark and under light irradiation. Reprinted with permission from ref. ¹² , Springer Nature.	83
Figure 2-18 The schematic presentation of operando TOF-MS for the characterization of liquid products in methane conversion. Reprinted with permission from ref. ¹⁴³ , Cellpress.	85
Figure 3-1 X-ray scattering on a crystal surface (Bragg's Law).....	90
Figure 3-2 The schematic illustration of the photocatalytic OCM flow system	99
Figure 4-1 Photocatalytic OCM process over different photocatalysts (Reaction conditions: O ₂ :CH ₄ = 1: 180, 5% of CH ₄ , GHSV = 12000 mL g ⁻¹ h ⁻¹ , 365 nm LED, r.t.)	106
Figure 4-2 C ₂ production of photocatalytic OCM over Cu _x /PC-50 (x = 0.05, 0.1, 0.2, 0.3, 0.4). (Reaction condition: O ₂ : CH ₄ = 1 : 240, GHSV = 12000 mL g ⁻¹ h ⁻¹ , 10% of CH ₄ , 365 nm LED 20 W,40°C).....	107
Figure 4-3 Methane conversion and C ₂ selectivity of photocatalytic OCM over Cu _{0.1} Pt _y /PC-50 (y = 0.1, 0.5, 1.0, 1.5, 2.0 wt%), Cu _{0.1} /PC-50, PC-50, Pt _{0.5} /PC-50 and Pt _{0.5} Cu _{0.1} /PC-50 (Reaction condition: O ₂ : CH ₄ = 1 : 400, GHSV = 24000 mL g ⁻¹ h ⁻¹ , 10% of CH ₄ , 365 nm LED 40 W,40°C. The error bar for the production rate of C ₂ products were obtained by three activity tests.)	108
Figure 4-4 Stability test of photocatalytic OCM over Cu _{0.1} Pt _{0.5} /PC-50 (Reaction condition: Reaction condition: O ₂ : CH ₄ = 1 : 400, GHSV = 24000 mL g ⁻¹ h ⁻¹ , 10% of CH ₄ , 365 nm LED 40 W,40 °C).....	113

Figure 4-5 PXRD patterns of Cu _{0.1} Pt _{0.5} /PC-50, Pt _{0.5} /PC-50, Cu _{0.1} /PC-50 and PC-50	114
Figure 4-6 Raman spectra of Cu _{0.1} Pt _{0.5} /PC-50, Pt _{0.5} /PC-50, Cu _{0.1} /PC-50 and PC-50	114
Figure 4-7 EDX element mappings (Ti, Cu and Pt) of Cu _{0.1} Pt _{0.5} /PC-50.....	115
Figure 4-8 TEM (a) and HR-TEM(b) images of Cu _{0.1} Pt _{0.5} /PC-50.....	115
Figure 4-9 Cu 2p (a) and Pt 4f (b) XPS spectra of Cu _{0.1} Pt _{0.5} /PC-50.....	116
Figure 4-10 Ti 2p XPS spectra of Cu _{0.1} Pt _{0.5} /PC-50, Pt _{0.5} /PC-50, Cu _{0.1} /PC-50 and PC- 50.....	117
Figure 4-11 Cu 2p XPS spectra of Cu _{2.0} /PC-50.....	117
Figure 4-12 (a) XRD and (b-d) XPS spectra of Cu _{0.1} Pt _{0.5} /PC-50 before and after reaction.....	118
Figure 4-13 UV-DRS spectra of Cu _{0.1} Pt _{0.5} /PC-50, Pt _{0.5} /PC-50, Cu _{0.1} /PC-50 and PC- 50.....	119
Figure 4-14 EPR spectra of Cu _{0.1} Pt _{0.5} /PC-50 (light on and light off) and Pt _{0.5} /PC-50 (light off).....	120
Figure 4-15 PL spectra of Cu _{0.1} Pt _{0.5} /PC-50, Pt _{0.5} /PC-50, Cu _{0.1} /PC-50 and PC-50 ..	121
Figure 4-16 Photocurrent of Cu _{0.1} Pt _{0.5} /PC-50, Pt _{0.5} /PC-50, Cu _{0.1} /PC-50 and PC-50	121
Figure 4-17 Possible photocatalytic OCM process over Cu _{0.1} Pt _{0.5} /PC-50.....	122
Figure 5-1 C ₂ yield rate over different noble co-catalysts decorated TiO ₂ with the equal mole amount to Pd. (Reaction condition: gas hourly space velocity (GHSV = 342 000 mL g _{cat} ⁻¹ hour ⁻¹), CH ₄ : O ₂ = 114: 1, 10% of CH ₄ , Ar as balance gas, 365 nm LED 40 W, 30 °C).....	133

Figure 5-2 C₂ yield rate of photocatalytic OCM over Pd/TiO₂ with different Pd wt%. (Reaction condition: GHSV = 342 000 mL g_{cat}⁻¹ hour⁻¹, CH₄: O₂ = 114: 1, 10% of CH₄, Ar as balance gas, 365 nm LED 40 W, 30 °C)134

Figure 5-3 The trend of C₂ yield rate over TiO₂, Pd/ TiO₂, PdCu/ TiO₂, PdNi/ TiO₂, PdCo/ TiO₂, and PdFe/ TiO₂ within the first 1.5 hours with the second component of 0.1 wt%. (Reaction condition: GHSV = 342 000 mL g_{cat}⁻¹ hour⁻¹, CH₄: O₂ = 114: 1, 10% of CH₄, Ar as balance gas, 365 nm LED 40 W, 30 °C)135

Figure 5-4 The stability and temporal profile of C₂ yield of Pd/TiO₂, Cu/TiO₂, and PdCu/TiO₂. (Reaction condition: GHSV = 342 000 mL g_{cat}⁻¹ hour⁻¹, CH₄: O₂ = 114: 1, 10% of CH₄, Ar as balance gas, 365 nm LED 40 W, 30 °C) 136

Figure 5-5 CH₄ conversion to various products over TiO₂, Pd/TiO₂, PdCu/TiO₂, and Cu/TiO₂ at 1.5 hour. (Reaction condition: GHSV = 342000 mL g_{cat}⁻¹ hour⁻¹, CH₄: O₂ = 114: 1, 10% of CH₄, Ar as balance gas, 365 nm LED 40 W, 30 °C)137

Figure 5-6 CH₄ total conversion rate and C₂ selectivity over PdCu/TiO₂ with different CH₄: O₂ ratios (the ratio was 53: 1, 114: 1, 174: 1, and 373: 1, respectively). Error bars in the figure were the standard error values from three runs.138

Figure 5-7 Photocatalytic OCM process under various controlling conditions. (Reaction condition: GHSV = 342 000 mL g_{cat}⁻¹ hour⁻¹, CH₄: O₂ = 114: 1, 10% of CH₄, Ar as balance gas, 365 nm LED 40 W, 30 °C)141

Figure 5-8 C₂ generation over PdCu/TiO₂ during a 112 hours reaction with the CH₄: O₂ ratio at 373: 1, these data were collected every 30 minutes.

(Reaction condition: GHSV = 342 000 mL g_{cat}⁻¹ hour⁻¹, CH₄: O₂ = 373: 1, 10% of CH₄, Ar as balance gas, 365 nm LED 40 W, 30 °C) 142

Figure 5-9 Summary of TON and TOF achieved on PdCu/TiO₂ and other reported representative photocatalysts ($\lambda > 300$ nm) under room temperature (1: AuPd/ZnO³⁷; 2: Au/ZnO¹⁷; 3: Ga₂O₃-K⁶¹; 4: MgO-SiO₂⁷⁰; 5: Ce-Al₂O₃⁶⁵; 6: Au/WO₃¹⁷⁸; 7: Ag-H₃PW₁₂O₄₀/TiO₂³⁶; 8: Pt-CuO_x/TiO₂⁴⁸; 9: Pt/Ga-TiO₂-SiO₂¹⁸; 10: Au/TiO₂³⁰; 11: TiO₂/SiO₂⁶⁰; 12: SiO₂-Al₂O₃-TiO₂⁵⁷; 13: H-MOR⁵⁵; 14: FSM-16²⁹; 15: GaN: ZnO¹⁹⁵; 16: Zn₅(OH)₈Cl₂·H₂O¹⁹⁶, 17: this work.). The insert figure is the zoomed rectangle region indicated with the dash line in the figure showing the range of TON between 0-10 and TOF between 0-0.9. Among them, the values of photocatalyst 3, 4, 13 and 14 are still too small to see in the enlarged insert. The calculation method is shown in section 5.1.6. 143

Figure 5-10 XRD spectra of TiO₂, Pd/TiO₂, Cu/TiO₂ and PdCu/TiO₂..... 144

Figure 5-11 Raman spectra of TiO₂, Pd/TiO₂, Cu/TiO₂ and PdCu/TiO₂..... 145

Figure 5-12 UV-Vis absorption spectra of TiO₂, Pd/TiO₂, Cu/TiO₂ and PdCu/TiO₂..... 146

Figure 5-13 Representative STEM image and particle size distributions of PdCu alloy over PdCu/TiO₂ 146

Figure 5-14 HR-TEM image of PdCu/TiO₂..... 147

Figure 5-15 HAADF-STEM image and EDX elements mapping of PdCu/TiO₂ 147

Figure 5-16 HAADF-STEM image and EDX element mapping of the selected area (element mapping of the PdCu nanoparticles and the support). 148

Figure 5-17 Representative STEM image and particle size distributions of PdCu alloy over PdCu/TiO ₂ after reactions.....	149
Figure 5-18 Top view of HAADF-STEM image and EDX element mapping of PdCu/TiO ₂ after reactions.....	149
Figure 5-19 The trend of C ₂ yield rate of Pd _{1.0} /TiO ₂ (a) and Pd ₁ Cu ₁ /TiO ₂ (b) over time.....	150
Figure 5-20 XPS spectra of Pd ₁ /TiO ₂ and Pd ₁ Cu ₁ /TiO ₂ (Pd 3d) before reaction.....	151
Figure 5-21 XPS spectra of Pd ₁ Cu ₁ /TiO ₂ (Cu 2p) before reaction.....	151
Figure 5-22 Auger Cu LMM spectrum of Pd ₁ Cu ₁ /TiO ₂ before reaction.....	152
Figure 5-23 XPS spectra of Pd ₁ Cu ₁ /TiO ₂ (Pd 3d) before and after the reaction.....	152
Figure 5-24 XPS spectra of Pd ₁ Cu ₁ /TiO ₂ (Cu 2p) before and after the reaction.....	153
Figure 5-25 Auger Cu LMM spectrum of Pd ₁ Cu ₁ /TiO ₂ before and after reactions.....	153
Figure 5-26 In situ EPR spectra of TiO ₂ under dark conditions and light irradiation in an argon atmosphere.....	154
Figure 5-27 In situ EPR spectra of TiO ₂ and Pd/TiO ₂ in an argon atmosphere and CH ₄ atmosphere upon light irradiation.....	155
Figure 5-28 Valence-band XPS spectra of TiO ₂ , Pd ₁ /TiO ₂ , and Pd ₁ Cu ₁ /TiO ₂	156
Figure 5-29 In situ Pd 3d XPS spectra of PdCu/TiO ₂ under the dark condition and under light irradiation.....	156
Figure 5-30 In situ EPR spectra of PdCu/TiO ₂ under argon atmosphere and CH ₄ atmosphere upon light irradiation.....	157

Figure 5-31 Photoluminescence spectra of TiO ₂ , Pd/TiO ₂ , Cu/TiO ₂ and PdCu/TiO ₂	158
Figure 5-32 Electrochemical oxygen reduction spectra over TiO ₂ , Pd/TiO ₂ , Cu/TiO ₂ and PdCu/TiO ₂ in 0.1 M KOH electrolyte.	159
Figure 5-33 Photocurrent densities of TiO ₂ , Pd/TiO ₂ , Cu/TiO ₂ and PdCu/TiO ₂	159
Figure 5-34 DFT calculated structures of methane adsorption on anatase, Pd and PdCu surfaces.	160
Figure 5-35 Raman spectra of Pd/TiO ₂ before and after 5 hours of reaction in the range of 1000-3000 cm ⁻¹	162
Figure 5-36 Raman spectra of PdCu/TiO ₂ before and after 110 hours of reaction in the range of 1000-3000 cm ⁻¹	162
Figure 5-37 DFT calculated structures of ethane adsorption on Pd and PdCu surfaces. (For colours in Fig. 4a and b: red – O, pink – Ti, tan – Pd, orange – Cu, teal – C, white – H. Brighter colours of metal atoms denote atoms in the top (surface) layer)	163
Figure 5-38 Possible reaction scheme for photocatalytic OCM over PdCu/TiO ₂ . ..	166
Figure 6-1 Schematic illustration of Au _{60s} /TiO ₂ on glass fibre membrane preparation procedure.....	172
Figure 6-2 C ₂ selectivity over different noble metal co-catalysts decorated TiO ₂ with equal molar amount at 1.5 hour reaction time. (Reaction condition: gas hourly space velocity (GHSV = 342 000 mL g _{cat} ⁻¹ hour ⁻¹), CH ₄ : O ₂ = 114: 1, 10% of CH ₄ , Ar as balance gas, 365 nm LED 40 W, 30 °C)	176
Figure 6-3 The relationship between Au loading amount and the sputtering time..	177
Figure 6-4 UV-Vis absorption spectra of membranes with different Au sputter time on 5 mg TiO ₂ and pure Au without TiO ₂ with 120s sputtering time. The insert is	

the photo of Au/TiO ₂ on the glass fibre membranes (from left to right is Au0s, Au20s, Au40s, Au60s, Au90s, Au120s, Au240s).....	178
Figure 6-5 Photocatalytic OCM activity over Au/TiO ₂ with different Au sputtering times (Au 0 s, Au 20 s, Au 40 s, Au 60 s, Au 90 s, Au 120 s, Au 240 s) on 5 mg TiO ₂ . (Reaction condition: 320 mL/min CH ₄ and 4 mL/min Air, 365 nm LED 100 W, 338 K).....	179
Figure 6-6 Photocatalytic OCM activity over Au60s/TiO ₂ with different amounts of TiO ₂ (5 mg, 10 mg, 15 mg, 20 mg, 30 mg and 40 mg). (Reaction condition: 320 mL/min CH ₄ and 4 mL/min Air, 365 nm LED 100 W, 338 K)	180
Figure 6-7 Photocatalytic OCM activity over Au60s/TiO ₂ operated at different temperatures (338 K, 353 K, 373 K and 393 K). (Reaction condition: 20 mg TiO ₂ , 320 mL/min CH ₄ , 4 mL/min Air, 365 nm LED 100 W)	181
Figure 6-8 Photocatalytic OCM activity over Au60s/TiO ₂ at 393 K with different Air flow rates. (Reaction condition: 20 mg TiO ₂ , 320 mL/min CH ₄ , 365 nm LED 100 W).....	185
Figure 6-9 AQE of four Au60s/TiO ₂ (20 mg TiO ₂) membranes prepared at similar procedures but different times.....	185
Figure 6-10 Stability test of Au60s/TiO ₂ under the optimised reaction condition (Reaction condition: 20 mg TiO ₂ , 320 mL/min CH ₄ , 12 mL/min Air, 393 K, 365 nm LED 100 W).....	188
Figure 6-11 Controlling experiments over Au60s/TiO ₂ under at optimised reaction condition (The normal reaction condition: 20 mg TiO ₂ , 320 mL/min CH ₄ , 12 mL/min Air, 393 K, 365 nm LED 100 W.).....	189
Figure 6-12 XRD patterns of TiO ₂ with different Au sputter times (0 s, 5s, 10 s, 20 s, 60 s and 90 s).	190

Figure 6-13 Top view SEM image (a) and EDX image of Au60s/TiO ₂ membrane (b for Ti element, c for Au element); Side view SEM image (d) and EDX image of Au60s/TiO ₂ membrane (e for Ti element, f for Au element).....	191
Figure 6-14 STEM-HAADF image of Au60s/TiO ₂ (a), STEM-BF image of Au60s/TiO ₂ (b), particle sizes distribution of Au on TiO ₂ (c), high resolution STEM-HAADF image of Au nanoparticle (d) and high-resolution STEM-BF image of Au nanoparticle (e).....	192
Figure 6-15 The XPS spectra of Au 4f in Au60s/TiO ₂	193
Figure 6-16 The UV-Vis reflectance spectrum of BiVO ₄ /TiO ₂ mixed membranes (BiVO ₄ , 10 mg TiO ₂ (top)-BiVO ₄ (bottom), 15 mg TiO ₂ (top)-BiVO ₄ (bottom), 20 mg TiO ₂ (top)-BiVO ₄ (bottom)).....	194
Figure 6-17 Photocatalytic OCM activity over Au120s/TiO ₂ , Au120s/SnO ₂ , Au120s/Ta ₂ O ₅ , and Au120s/GaN. (Reaction condition: CH ₄ : O ₂ = 114: 1, 40 W 365 nm LED, 285 mL/min total flow rate, 10% of CH ₄ , 303 K).....	195
Figure 6-18 In situ XPS spectra of Au60s/TiO ₂ (Au 4f) under dark and light irradiation conditions.	195
Figure 6-19 a. TAS spectra of TiO ₂ excited by pulsed 355 nm excitation (0.40 mJ cm ⁻²) at the time scale of 10 μs under argon atmosphere, oxygen atmosphere and methanol vapor, respectively; b. TAS decay kinetics of TiO ₂ probed at 500 nm and excited by pump 355 nm excitation under argon and oxygen atmosphere, respectively; c. TAS decay kinetics of TiO ₂ probed at 950 nm and excited by pump 355 nm excitation under argon and oxygen atmosphere, respectively; d. TAS decay kinetics of TiO ₂ probed at 950 nm and excited by pump 355 nm excitation under argon atmosphere with or without methanol vapor, respectively.	196

Figure 6-20 a. TAS spectra of TiO ₂ and Au/TiO ₂ excited by pulsed 355 nm excitation (0.40 mJ cm ⁻²) observed at 10 μs under argon atmosphere, respectively; b. TAS decay kinetics of TiO ₂ and Au/TiO ₂ probed at 550 nm excited by pump 355 nm under argon atmosphere; c. TAS decay kinetics of TiO ₂ and Au/TiO ₂ probed at 950 nm excited by pump 355 nm under argon atmosphere; d. Normalisation of TAS decay kinetics of TiO ₂ and Au/TiO ₂ probed at 950 nm and excited by pump 355 nm under argon atmosphere.	198
Figure 6-21 Photoluminescence spectra of TiO ₂ and Au ₆₀ s/TiO ₂	199
Figure 6-22 TRPL spectra of TiO ₂ and Au ₆₀ s/TiO ₂	201
Figure 6-23 In situ EPR spectra of superoxide radicals using DMPO as a spin trap over TiO ₂ and Au ₆₀ s/TiO ₂ in CH ₃ OH aqueous solution under 5 minutes light irradiation.	202
Figure 6-24 In situ EPR spectra of hydroxyl radicals using DMPO as a spin trap over TiO ₂ and Au ₆₀ s/TiO ₂ in aqueous solution under 5 minutes light irradiation. .	203
Figure 6-25 In situ CH ₄ adsorption DRIFTS spectrum for TiO ₂ (a) and Au ₆₀ s/TiO ₂ (b) under dark condition.	204
Figure 6-26 In situ DRIFTS spectra of photocatalytic methane conversion over TiO ₂ (a) and Au ₆₀ s/TiO ₂ (b).	206
Figure 6-27 (a) Photocatalytic OCM activity over TiO ₂ operated at different temperatures (329 K, 338 K and 358 K). (Reaction condition: 20 mg TiO ₂ , 320 mL/min CH ₄ , 4 mL/min Air, 365 nm LED 100 W); (b) Kinetics of methane conversion over Au ₆₀ s/TiO ₂ and TiO ₂ catalysts.	207
Figure 6-28 Possible photocatalytic OCM process over Au ₆₀ s/TiO ₂	208

1 Introduction

1.1 Background

With the decreasing reserves of crude oil and the predicted substantial reserve of methane hydrate and shale gas, there is an emerging demand to utilize methane as a fundamental feedstock for chemical synthesis instead of oil for the next decades.^{1,2} Furthermore, a remarkable increase will occur in the natural gas production in the whole world, from 133.1 to 191.6 quadrillion British thermal units by 2050 (International Energy Outlook 2019), suggesting the importance of efficient methane conversion and utilisation.³ Currently, except using for cooking, only indirect conversion of CH₄ via syngas (a certain ratio of H₂ to CO) process reaches a commercial scale, dominating near-term industrial practices for the conversion of natural gas.^{4,5} Unfortunately, this multi-stage process is not only energy-intensive (e.g., temperature >773 K) and large capital cost, but also is accompanied by enormous CO₂ emission.⁶ Therefore, there are manifest financial and environmental incentives to stimulate the academic communities and industry to develop effective and green approaches to directly transform methane into value-added chemicals.

However, owing to the inert nature of methane, such as the highly symmetrical molecule with a tetrahedral geometry, the lack of dipole moment and low polarizability ($2.84 \times 10^{-40} \text{ C}^2 \cdot \text{m}^2 \cdot \text{J}^{-1}$) and the high C-H bond energy of 439 kJ mol⁻¹ under the standard condition,^{7,8} the direct conversion of methane always requires harsh

reaction condition (high temperature and high pressure), often accompanied by low conversion, small selectivity, bad catalysts stability and excess by product CO₂.^{1,8,9} After decades of research, the industrial application of direct conversion of methane is still a grand challenge for chemistry.

Photocatalysis, employing photons mostly operated under mild conditions instead of thermal energy to drive chemical processes, has been regarded as a promising alternative to traditional thermocatalysis. Unlike methane conversion by thermocatalysis, which requires large activation energy due to methane's inertness, photocatalysis generates very energetic carriers that preactivate methane and substantially reduce the activation energy. This preactivation process even allows uphill (thermodynamically unfavourable) reactions to proceed at room temperature, overcoming the conventional thermodynamical barrier. Furthermore, of those reactions often carried out at very high temperatures (such as non-oxidative coupling of methane (NOCM) or non-oxidative methane dehydroaromatization at >673 K, sometimes even >1,273 K), the product yield by the thermocatalysis at room temperature is estimated to be about 0.0002% and 0.000007%, respectively, due to thermodynamic equilibrium;^{10,11} the special function of photons can break the limitation of the thermodynamic equilibrium, leading to a 100 to 10,000 times improvement in yield. In addition, photocatalytic reactions are theoretically expected to avoid harsh reaction conditions, overoxidation and catalyst deactivation. The heat generated by the reaction can also be readily dissipated. At the same time, the spatial separation of redox reaction sites within one photocatalyst can, to some extent, further prevent the unnecessary collision of radicals. All these factors contribute to the

advantage of photocatalytic methane conversion in the control of high selectivity. Thus, almost all the products of interest can find a photocatalytic system with a selectivity of >90% and even 100%. In particular, the past five years have witnessed an explosion of various products photocatalytically synthesised from methane, such as methanol¹²⁻¹⁴, formaldehyde¹⁵, ethanol¹⁶, ethane and ethylene¹⁷⁻¹⁹, acetone²⁰, benzene¹⁰ and syngas²¹, but they are still at the infant stage due to low yield.

1.2 Motivation, aim and objectives

Although substantial progress has been made in the development of photocatalytic methane conversion to different products, there are at least five factors needed to be comprehensively investigated in this field, such as the development of efficient photocatalysts, design of highly selective co-catalysts, selection of appropriate reactions systems, understanding reaction mechanisms and excellent stability.

The reported photocatalytic methane conversion often exhibits low apparent quantum efficiency (AQE). Apart from a AQE as high as 60% achieved by Pt/black TiO₂ at very high temperature 773 K²² the rest examples under ambient conditions are often less than 10% and some even less than 1%.¹ By contrast, a higher AQE is commonly reported in other photocatalytic processes, in particular, for water splitting (up to 96%).²³ The low light utilisation efficiency of photocatalytic methane conversion is generally limited by the high recombination of photo-induced e⁻/h⁺ and the lack of active sites for methane activation. Most examples in photocatalytic methane conversion consist of the main semiconductor photocatalyst with a very positive

valence band, e.g., TiO₂, WO₃, ZnO, BiVO₄ and a co-catalyst e.g., noble metals and transition metals. The main purpose of the introduction of a co-catalyst reported in this filed is mainly for the promotion of charge separation, less considering other factors of a methane conversion system, such as conversion, selectivity, and stability. A single-function species may not meet the requirements and combination of multiple components with complementary functions or assembly of multiple functions into one species has to be developed.

The development of reaction systems is equally important than the photocatalysts. Most photocatalytic reactors are batch reactors, in which products could not be removed in time after generation, indicating the inevitable possibility of overoxidation. Nearly all the products are easier to be activated and converted compared with methane, thus obtaining the desired products with a high yield and high selectivity is very difficult from the thermodynamic view in a batch reactor. This system is however readily used to test the photocatalytic potential and there are limited parameters that could be optimized to improve the yield (selectivity). In addition, adsorption of methane and desorption of products mainly rely on spontaneous gas diffusion in a batch reactor, implying that mass transfer, rather than photocatalytic efficiency itself, could be a key limiting factor for the low efficiency. In contrast to batch reactors, flow reactors can control the detention time of methane and products on the catalyst surface, thus an effective way to overcome the above-mentioned disadvantages. As the development of photocatalytic conversion of methane is targeted to replace traditional thermocatalysis for real industrial application, it is undoubted and necessary to carry out the reaction in a flow system.

Compared with the fast development of the catalyst materials, little is still known about the mechanism behind every methane conversion reaction, including photophysics and photochemistry. Currently, the mechanisms are always given as basic concepts as those in other photocatalytic reactions, like “electrons reduce oxidant and holes oxidize reductant, respectively.” However, the identification of charge carrier pathways and the understanding of the basic steps, in particular, their influences on the final activity, selectivity and stability are often neglected. Using complementary time-resolved spectroscopies, in-situ technologies, and even DFT simulation, rather than one technique alone, is highly recommended to monitor the generation and transportation of photo-induced carriers and more importantly, their interaction with the absorbed reactant and product molecules.

Particular attention should also be paid to the reliability and stability of a photocatalyst. Although many of the methane conversion photocatalysts reported are stable during their corresponding cyclic tests or continuous runs, most of the durability tests are too short (<50 h or <10 cycles) to give a comprehensive view of their stability. For example, although coke formation is a universal issue in thermocatalysis at high temperatures, it has seldom been observed in photocatalysis, owing to the merits of mild, low-temperature reaction conditions. However, it may be also because of the low conversion rate in photocatalysis and it could become a problem in long-term runs. In addition, the carbon source of products should also be scrutinized as the simulated methane gas used in a laboratory always contains impurities, such as ethane. Thus, a proper control experiment or isotope-label experiment is needed to identify the carbon source of the products.

Among various reactions, the coupling of methane molecules to produce C₂₊ products (C₂H₆/C₂H₄) is one of the most general and highly profitable processes. The aim of this project is thus to develop robust and stable TiO₂-based photocatalysts to convert methane into value-added C₂₊ products with the highest conversion rate, selectivity, stability, and AQY under ambient conditions in a flow reactor, together with critical fundamental understanding. Thus, the objectives of this project include

1. Design and optimize the co-catalysts to modify the anatase TiO₂. The function of the co-catalyst is not only limited to retard the recombination of photo-induced e⁻/h⁺ but also accelerate the interface interaction (e.g., C-H bond activation, methane adsorption). The design of co-catalysts would consider both structures (e.g., composition, particles sizes, chemical states) and properties (e.g., band position, redox potential). More importantly, the synergy effects between multi-components assembled in one component are crucial.
2. Design and construct a flow reaction system to rigidly evaluate the photocatalysts under different conditions, such as temperatures (room temperature to 200 °C), CH₄/O₂ ratio (500: 1 to 1: 50 and even anaerobic condition), and flow rate (3 mL min⁻¹ to 350 mL min⁻¹).
3. The activity, stability and reproducibility should be next target, such as stability of >100 hours, high AQY of > 10% and high selectivity of 90% to C₂.
4. Fundamental understanding of the photophysics and photochemistry, including the charge transfer behaviour (by e.g., TAS, in situ XPS), the capture

of active intermediates (by e.g., in situ EPR), reaction pathways by DFT simulation.

1.3 Report outline

This project focuses on the efficient coupling of methane to value-added C₂ products with high selectivity and stability. In the first chapter, the background of methane conversion and the motivation for photocatalytic methane conversion was illustrated. The development of photocatalysts, photocatalytic reactors and mechanism understanding in photocatalytic methane conversion will be thoroughly reviewed in the second chapter. The methodology for the photocatalysts synthesis, characterisation techniques and photocatalytic activity tests are shown in Chapter 3. In Chapter 4, the decoration of anatase TiO₂ nanoparticles with Pt nanoparticle and CuO_x cluster for photocatalytic OCM is presented. Next, the synergic effects of Pd and Cu is discussed in Chapter 5, leading to an unprecedented high TON/TOF and stability. A facile and rapid sputter method to deposit Au on TiO₂ is investigated in chapter 6, which produces highest C₂ selectivity and C₂ yield rate. The conclusions are summarised in chapter 7 And the future works are illustrated in the Chapter 8.

2 Literature Review

This Chapter covers the three key elements in photocatalytic methane conversion, including materials, reactor, and mechanism. The Chapter starts with the principles of photocatalytic methane conversion. Then, the development of photocatalysts and co-catalysts is given, to comprehensively examine the strategies to improve selectivity and yield for desired products and catalyst stability. The comparison of batch and flow reaction systems and the discussion of the efforts to understand the photophysical and surface chemical reaction mechanisms are then presented.

2.1 Principles of photocatalytic methane conversion

The basic mechanism of photocatalysis is illustrated in Figure 2-1.^{1,24,25} When irradiated by a light source with proper wavelength, a photocatalyst harvests photons and the electrons populate the conduction band, leaving holes in the valence band. The recombination of many electrons and holes produces thermal energy, while the other photo-generated carriers migrate to the surface to initiate chemical reactions with reactants.

Footnote: Part of the content in this chapter has been published in Nat. Mater. Rev.,2022, DOI: 10.1038/s41578-022-00422-3.

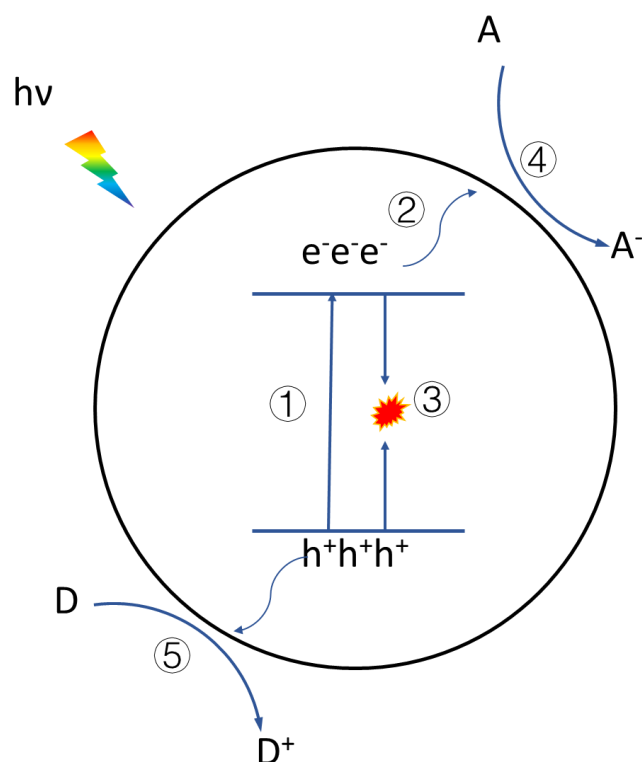


Figure 2-1 The principle of photocatalysis involves excitation of electrons from the valence band to the conduction band (step 1), charge separation and transportation to the reaction sites (step 2), charge recombination (step 3), surface reduction reaction (step 4) and surface oxidation reaction (step 5). Adapted with permission from ref.¹, Springer Nature Limited.

The reaction between charges and methane can take several different pathways, as shown in Figure 2-2.¹ The C-H bond can be directly activated by photoholes, photoelectrons or energetic carriers from plasmonic metals. In the direct activation by photoholes, a metal oxide semiconductor such as TiO_2 ¹² or ZnO ²⁶ generates photoholes (or lattice O^- species) with high oxidative power (approximately +3 V versus standard hydrogen electrode)^{27,28} to abstract hydrogen from the C-H bond. Photoholes are not only from the classic semiconductors but some pure silica with active nonbridging oxygen hole centres ($\equiv\text{Si}-\text{O}\cdot$), for instance, can also react with methane to generate methyl radical under high-energy ultraviolet (UV) light.²⁹

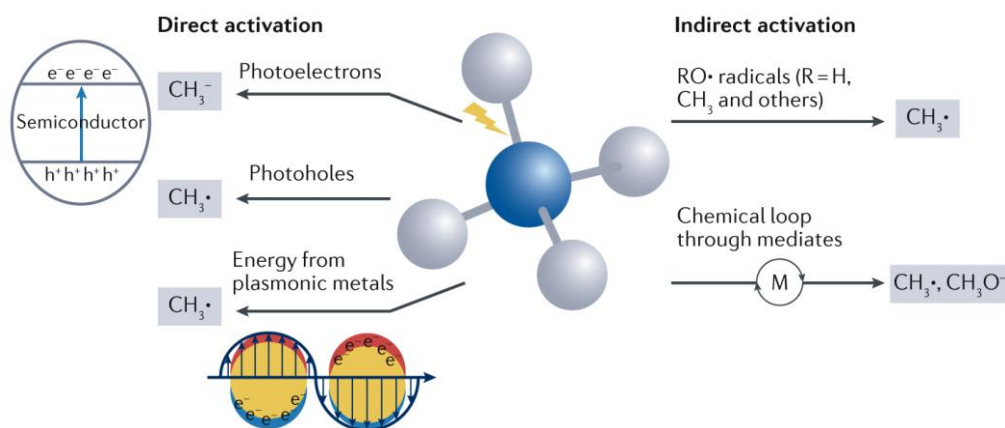


Figure 2-2 Methane can be activated by different mechanisms photocatalytically. The C-H bond can be directly activated by photoholes, photoelectrons or energy from localised surface plasmon resonance or indirectly activated by RO• radicals such as •OH or CH₃O• or chemical loop processes through mediates, such as metal cationic species or lattice oxygen. Reprinted with permission from ref.¹, Springer Nature Limited.

The activation by photoelectrons was only recently reported, in which the C-H bond was reduced and cleaved by the photoelectrons to form methyl anion for further generation of ethane.³⁰ However, this pathway was mainly proposed by density functional theory calculations. As the electron affinity of methane (EA) was very high (-1.9 eV),² thus the activation of C-H by electron input needs more direct experimental evidence in future research. A plasmonic metal such as Cu, Ag, or Rh can also activate the C-H bond. When the metal is under irradiation, the localised surface plasmon resonance induces enhanced light absorption and, thus, the efficient generation of energetic hot carriers.²¹ The injection of either energetic carriers or energy into the molecular orbital of the methane molecule can weaken and activate the strong C-H bond.^{31,32}

The C-H bond can also be indirectly activated by OR radicals or through a chemical loop process by mediates. In the first case, the most frequently observed intermediate

is the hydroxyl radical (OH), which is easily generated in the presence of surface hydroxyl ions, adsorbed water or added hydrogen peroxide (H₂O₂). Hydroxyl radicals can abstract a hydrogen atom from methane to generate methyl radicals,³³ owing to their high oxidative potential ($E^\ominus=2.73$ V).³⁴ The high-energy electrophilic alkoxy radical (\cdot OR) functions similarly.³⁵ In the chemical loop process,^{36,37} a mediate such as a metal cationic species or lattice oxygen is used to carry out photocatalytic methane oxidation by two interconnected steps: first, the interaction between methane and the photocatalyst at the expense of the mediate to generate the products with high selectivity, followed by the regeneration of reduced mediate species with oxidants (O₂, H₂O) to complete the catalytic cycle.

Methane can be used to synthesize diverse products through different reaction pathways by photocatalysis or thermocatalysis, and the major processes are listed in Table 2-1. These products include methanol (CH₃OH) and ethanol (CH₃CH₂OH) through partial oxidation of methane (POM), ethane (CH₃CH₂OH) through partial oxidation of methane (POM), ethane (C₂H₆) and ethylene (C₂H₄) through the oxidative coupling of methane (OCM) and NOCM benzene (C₆H₆) through non-oxidative methane dehydroaromatization, syngas (CO and H₂) through steam reforming of methane (SRM) and dry reforming of methane (DRM) and carbon dioxide (CO₂) through total oxidation. It should be noted that some reactions are thermodynamically feasible only with the assistance of oxygen (Table 2-1, entries 3-4, 7, 9-10, 13-14), while the others do not require oxygen. Furthermore, these reactions are always accompanied by thermodynamically more favourable but unexpected side reactions, no matter whether under aerobic conditions (for example, CO₂, Table 2-1, entry 14)

or under anaerobic conditions (for example, cokes, Table 2-1, entry 15), making the development of a catalyst with high yield and high selectivity very challenging.

Table 2-1 Change of ΔG^0 (298 K) for various methane conversion reactions

Entry	Main product	Reaction name	Chemical equation	ΔG^0 (298 K) kJ mol ⁻¹
1	Syngas	Steam reforming of methane (SRM)	$\text{CH}_4 + \text{H}_2\text{O} \rightarrow \text{CO} + 3\text{H}_2$	142.1
2		Dry reforming of methane (DRM)	$\text{CH}_4 + \text{CO}_2 \rightarrow 2\text{CO} + 2\text{H}_2$	170.7
3		Partial oxidation of methane (POM)	$2\text{CH}_4 + \text{O}_2 \rightarrow 2\text{CO} + 4\text{H}_2$	-173
4	CH ₃ OH	POM	$2\text{CH}_4 + \text{O}_2 \rightarrow 2\text{CH}_3\text{OH}$	-222.6
5		Methane to methanol with water	$\text{CH}_4 + \text{H}_2\text{O} \rightarrow \text{CH}_3\text{OH} + \text{H}_2$	117.3
6	C ₂ H ₅ OH	Methane to ethanol with water	$2\text{CH}_4 + \text{H}_2\text{O} \rightarrow \text{C}_2\text{H}_5\text{OH} + 2\text{H}_2$	161.7
7	HCHO	POM	$2\text{CH}_4 + \text{O}_2 \rightarrow 2\text{HCHO} + 2\text{H}_2$	-103.6
8	CH ₃ COCH ₃	Methane to acetone with CO ₂	$2\text{CH}_4 + \text{CO}_2 \rightarrow \text{CH}_3\text{COCH}_3 + \text{H}_2\text{O}$	114.1
9		Oxidative coupling of methane (OCM)	$2\text{CH}_4 + \text{O}_2 \rightarrow \text{C}_2\text{H}_4 + 2\text{H}_2\text{O}$	-287.6

10	C ₂ H ₄ /C ₂ H ₆	OCM	$4\text{CH}_4 + \text{O}_2 \rightarrow 2\text{C}_2\text{H}_6 + 2\text{H}_2\text{O}$	-320
11		Non-oxidation coupling of methane (NOCM)	$2\text{CH}_4 \rightarrow \text{C}_2\text{H}_6 + \text{H}_2$	68.6
12	C ₆ H ₆	Non-oxidative methane dehydroaromatization (MDA)	$6\text{CH}_4 \rightarrow \text{C}_6\text{H}_6 + 9\text{H}_2$	433.9
13		Oxidative aromatization of methane	$12\text{CH}_4 + 9\text{O}_2 \rightarrow 2\text{C}_6\text{H}_6 + 18\text{H}_2\text{O}$	-3247
14	CO ₂	Total oxidation	$\text{CH}_4 + 2\text{O}_2 \rightarrow \text{CO}_2 + 2\text{H}_2\text{O}$	-800.9
15	Carbon	Pyrolysis	$\text{CH}_4 \rightarrow \text{C} + 2\text{H}_2$	50.7

2.2 Development of photocatalytic materials

Photocatalytic materials are at the core of achieving decent yield and selectivity for methane conversion. Many materials have been reported over the past few decades (Table 10-1 in Appendix section). The photocatalytic materials consist of a substrate semiconductor that absorbs light and generates redox pairs (e^-/h^+) and a co-catalyst on which the thermodynamic barrier of methane activation is lowered and the selectivity to target products is manipulated. Representative photocatalysts and co-catalysts, especially those developed over the past 5 years will be reviewed.

2.2.1 Semiconductor materials

The semiconductor photocatalyst is the most basic component of a photocatalytic system. Theoretically, a photohole in the valence band or the highest occupied molecular orbital of a photocatalyst with an oxidation potential ($>+1.75$ V versus standard hydrogen electrode) is required to activate the inert C-H bond in a methane molecule.³⁶ Other activation pathways have also been reported, as mentioned earlier. In principle, a semiconductor that exhibits high activity in equivalent photocatalytic processes (for instance, water splitting, CO₂ conversion and nitrogen reduction) could be theoretically applicable in methane conversion, including oxides and nitrides.

Binary metal oxides. TiO₂ is the most studied semiconductor photocatalyst and has been used for NOCM, OCM, POM, DRM and SRM.^{31,38-41} The first attempt of TiO₂ in photocatalytic methane activation can be dated back to 1978, while the products obtained were mainly CO₂.⁴² Later, methane activation and water splitting were combined, which simultaneously produce H₂, CO, CO₂, C₂H₄ and C₂H₆. Such various products resulted in a relatively low selectivity toward the desired product, and the yield rate (at the level of 2 μmol h⁻¹) was still far from satisfactory.^{43,44} Proper design of TiO₂ with a specific structure can enhance the interactions between catalyst surface and reactants. An ordered hierarchical porous microarray of TiO₂ was synthesised by

using polystyrenes as a soft template and used for photocatalytic NOCM, as shown in Figure 2-3.¹⁸

In contrast to the inactive commercial TiO₂ (P25) for NOCM, this hierarchical

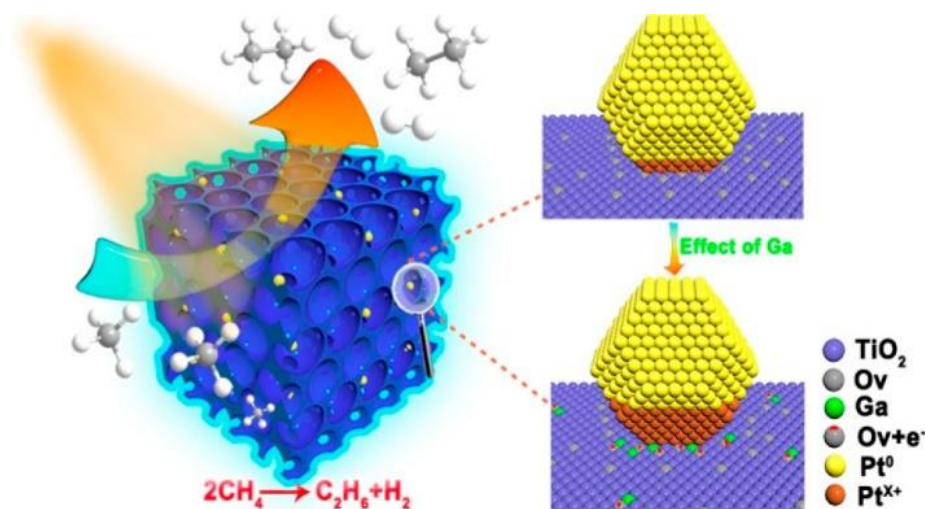


Figure 2-3 Schematic illustration of the methane conversion process over Ga-Doped and Pt-Loaded porous TiO₂-SiO₂. Reprinted with permission from ref.¹⁸, American Chemical Society.

structure exhibits a conversion rate of 0.41%. This significant change is attributed to the formation of ordered porous in TiO₂, which can largely increase the possibility and time of interaction between the active sites and methane molecules. With the doping of Ga and deposition of Pt, a methane conversion rate of 6% can be achieved after 4 h of irradiation, and the value can be further increased to as high as 28% with prolonged irradiation to 32 h. This activity is also higher than that of the mesoporous structure with a similar amount of Ga and Pt, further verifying the important role of interconnected hierarchical pores. Although this anatase framework exhibits a relatively high (90%) selectivity toward C₂H₆, its yield rate is still as low as 0.316 μmol h⁻¹. Apart from hydrocarbons, various products have also been achieved over TiO₂ with the precise design of an appropriate reaction process. Methane can be

utilized to photosynthesize amino acids with ammonia water over Pt/TiO₂.⁴⁵ While acetic acid can be produced by the conversion of CH₄ and CO₂ using phthalocyanine modified TiO₂.⁴⁶ In addition, TiO₂ also displayed an excellent synergistic effect as photo-redox support for noble metals in the photocatalytic SRM reaction recently.^{31,43,44}

Compared with TiO₂, ZnO has a similar band structure and has drawn attention in recent years with its unusual asymmetrical polar crystal structure.^{17,26,47,48} Owing to the intrinsic inner electric field formed by non-uniform charge distribution, it has a large spontaneous polarization of 0.047 C/m² along [0001] direction.^{49,50} This unique structure can not only facilitate charge separation during photocatalysis but also provide the polar facets (0001) to activate the highly symmetrical methane molecules. The impact of polar facets was investigated by conducting a photocatalytic methane oxidation reaction over two single-crystalline ZnO, (0001) dominated nanosheets and (01 $\bar{1}$ 0) dominated nanorods, as shown in Figure 2-4.⁵¹ The rate constant for ZnO nanosheets is more than ten times larger than that of ZnO nanorods, verifying the positive effect of polar facets in methane conversion.

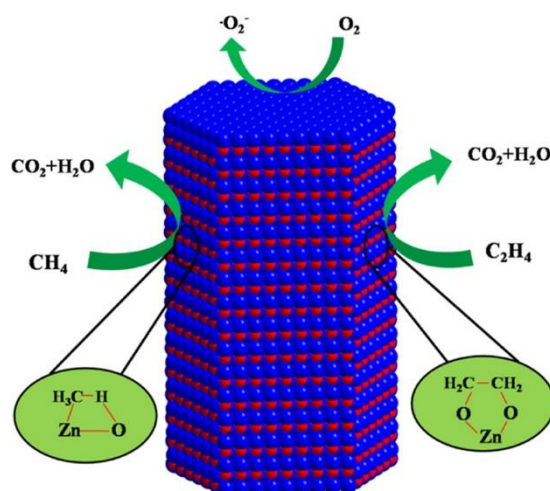


Figure 2-4 Demonstration of C-H and C=C bond polarization over polar crystal planes of ZnO nanostructures. Reprinted with permission from ref. ⁵¹, American Chemical Society.

Using this material as a polar base, a series of heterojunctions, such as Ag/ZnO,²⁶ CuO/ZnO,⁴⁷ and ZnO/La_{0.8}Sr_{0.2}CoO₃,⁵² have been constructed for photocatalytic total oxidation of greenhouse gas CH₄. The highest operation capacity can be achieved by Ag/ZnO, reaching 100% removal of 100 ppm CH₄ with a 25 mL min⁻¹ flow rate. Moreover, ZnO/La_{0.8}Sr_{0.2}CoO₃ exhibits ~2 times higher CH₄ conversion under light irradiation than that with thermal heating. Photoexcitation of ZnO can facilitate the reversible charge transfer, resulting in a higher lattice oxygen activity for methane oxidation. The decoration of proper co-catalysts on ZnO can further expand the product scope toward value-added chemicals during photocatalytic methane conversion. A facet tailored ZnO nanosheets with exposed {001} planes was prepared for NOCM with the aid of a gold co-catalyst.¹⁷ Benefiting from the synergistic effect between the internal electric field of polar ZnO and plasmonic Au nanoparticles, the dehydrogenative process proceeded smoothly with a linear correlation between the C₂H₆ and H₂ yield rate (ca. 0.0113 μmol h⁻¹). Changing the reaction system, the same component (Au/ZnO) also exhibits excellent performance (125 μmol h⁻¹ yield rate

and >95% selectivity) in selective photocatalytic oxidation of methane to oxygenates with O₂ in water.

WO₃ with a deep valence band is also a widely used photocatalyst for methane activation. The first example of photocatalytic partial oxidation of methane over WO₃ was presented in 1997, in which the driving force for methane to methanol was changed from photolysis of water by ultraviolet to photocatalysis by visible light.⁵³ Then, the study focused on the influence of experimental parameters, such as light source, scavengers, radical generator, and amount of catalysts.^{54,55} In 2004, the performance of photocatalytic conversion of methane to methanol was compared over WO₃, TiO₂ and NiO.³⁸ Although WO₃ has the maximum methane conversion (29%) than that of TiO₂ (21%) and NiO (20%), the formed methanol is degraded soon due to overoxidation. The same group then impregnated Ag⁺ on WO₃ to increase the yield of methanol, but the degradation of methanol still cannot be avoided.⁵⁶ Similar strategy was applied through the addition of cation as the electron scavengers.⁵⁷ The production of methanol is increased by two and a half times with the additive of Fe³⁺, but the selectivity to methanol is only 58%.⁵⁷ As methanol is more active than methane, it is reasonable to see the low selectivity of these reaction systems. Moreover, the driving force for methane activation in these reactions is hydroxyl radical (OH), which is a highly oxidative but non-selective radical. A fluorinated WO₃ was used to gain an insight into the reaction mechanism.⁵⁸ It was found that WO₃/F exhibited a decreased yield of methanol and 94% of the generated methanol is related to the hydroxyl radicals on the surface of WO₃. Thus, the addition of H₂O₂ lowers the selectivity (from 22% to 13.7%) of methanol as it only increases the concentration of free OH radicals in the solution. Afterwards, lanthanum was introduced to a mesoporous WO₃ to

promote the generation of OH groups on the surface of WO₃. These OH groups act as hole traps to produce hydroxyl radicals on the catalyst surface rather than solution, and a large improvement of selectivity to methanol was observed, from 22% to 47%.⁵⁹ Recently, a breakthrough was achieved by amorphous FeOOH loaded mesoporous WO₃ (FeOOH/m-WO₃), which presents a methane conversion rate of 4.77 μmol h⁻¹ with high selectivity of 91.0% to methanol, as shown in Figure 2-5.⁶⁰ Interestingly, H₂O₂ is indispensable for the generation of methanol in this system, and FeOOH plays an important role to react with H₂O₂ to generate more hydroxyl radicals. This inconsistent phenomenon with former literature indicated that the mechanism of methane conversion to methanol over WO₃ is still unclear.

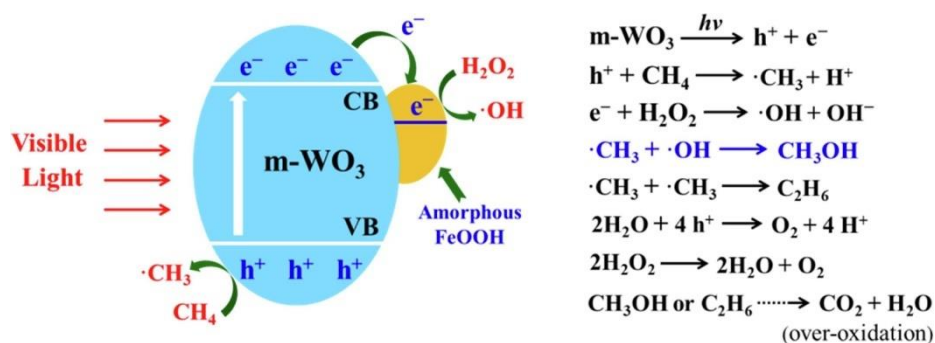


Figure 2-5 Schematic demonstration of methane conversion to methanol over FeOOH/m-WO₃. Reprinted with permission from ref. ⁶⁰, Elsevier.

Inorganic porous material, such as silica, alumina, and zeolite with highly dispersed metal oxide species on their surfaces, is another important group of photocatalysts studied for methane conversion. The attempt of using silica-related materials for non-oxidative coupling of methane started in 1978, such as V/SiO₂,⁴² Ag/zeolite Y,⁶¹ Mo/SiO₂,⁶² and the first example of pure silica-alumina material without the deposition of transition metals was reported in 1998.⁶³ A total yield of ~5% coupling products (e.g. C₂H₆, C₂H₄, C₃H₈) was obtained using SiO₂-Al₂O₃ under UV irradiation for 18 h. Afterwards, some other pure silica materials (e.g. MCM-41, FSM-

16) were also found active in photocatalytic NOCM in 2006.²⁹ The main product is ethane and FSM-16 exhibits the highest yield rate ($0.019 \mu\text{mol h}^{-1}$) of ethane among them. However, this rate is extremely low, one magnitude order lower than that of modified TiO_2 ($0.316 \mu\text{mol h}^{-1}$) with the same amount of catalyst mentioned above.¹⁸ Silica was also loaded with dispersive cation species of Ce, Mg, Ga, Ti, Zr, and Zn for photocatalytic NOCM.⁶⁴⁻⁷³ Among them, Ga-ETS-10 and $(\text{Zn}^+, \text{Zn}^{2+})$ -ZSM-5 reported by the same group exhibit the highest methane conversion rate, $5.96 \mu\text{mol h}^{-1}$ with 200 mg catalyst and $6 \mu\text{mol h}^{-1}$ with 1 g catalyst, respectively.^{66,72} These activities are even better than that of traditional semiconductors, and in particular, $(\text{Zn}^+, \text{Zn}^{2+})$ -ZSM-5 exhibits extremely high selectivity (99.6%) to ethane. The key to this high activity is the presence of univalent zinc ion, which can accept the electrons from the zeolite framework and exhibit a long lifetime to activate the C-H bond of methane. The reaction can shift from thermodynamically unfavourable to thermodynamically favourable in the presence of oxygen, thus involvement of oxygen is another strategy to promote methane conversion. A commercial beta zeolite ($\text{Si}/\text{Al}=12.5$) with a relatively large population of silanol groups was used as a photocatalyst for methane conversion in the presence of 20 vol% oxygen at 0.5 bar.⁷⁴ A extremely high methane conversion rate ($481 \mu\text{mol h}^{-1}$) was achieved with a decent selectivity (99%) to liquid C_1 oxygenated products (CH_3OH , CH_2O and HCOOH). It should be noted that an energy-intensive deep UV (185 nm) light source is needed to activate the silanol groups. And a further desorption process is required to obtain the products. Actually, these two issues commonly existed at almost all the silica, alumina and zeolite systems, despite of the great development of these materials in the past decade. The application of deep UV irradiation may involve the contribution from photochemistry/photolysis reaction rather than photocatalysis. Furthermore, the desorption processes were usually

carried out under relatively high temperature (normally >523 K). Rigorously, it should be careful when treating these systems as pure photocatalysis. Apart from being the photo-redox centre, the important function of these porous should not be neglected, that is the excellent support for photo-active centre. For example, V and Bi were co-loaded on a zeolite framework, in which the formation of V_2O_5 manipulated the acid-base properties to decrease undesired production of CO_2 and the additional low amounts of Bi formed the heterostructure $BiVO_4/V_2O_5$, as shown in Figure 2-6.⁷³

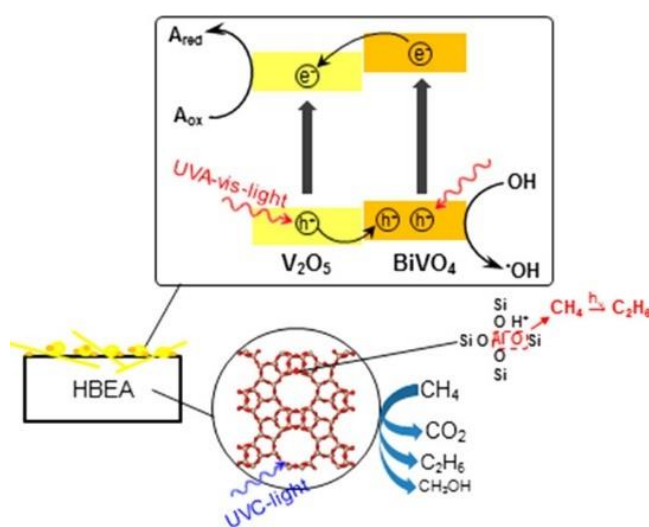


Figure 2-6 Schematic demonstration of methane activation process over $BiVO_4/V_2O_5$. Reprinted with permission from ref. ⁷³, American Chemical Society.

A 100% of methanol selectivity was obtained by this sample when the radiation from deep UV was filtered. It is reasonable that the much formation of highly oxidative radicals (e.g., $\cdot OH$) via photolysis by shorter wavelengths (UVC) is detrimental to the controlled oxidation process. Recently, a new utilization of silica was presented in the photocatalytic DRM.⁷⁵ Apart from being a support for the deposition of active species, silica clusters were prepared to modify the surface of Ni nanocrystal. Such modification almost completely prevents the cokes accumulation and the catalyst shows excellent durability for up to 700 h. Based on the development of these inorganic porous materials, it is easy to find that their roles gradually shifted from

active photo-redox centre to others, e.g., supports, promoters. This is more adaptive to these materials and it also consistent with their roles widely reported in thermocatalytic methane conversion.^{5,76,77}

Besides, some large-bandgap oxides, such as Ga₂O₃, MgO and ZrO₂, have also been tested in DRM or NOCM.^{69,78–83} However, these oxides photocatalysts had limited light absorption (<300 nm) and thus, low activity.

Ternary metal oxides. A variety of ternary metal oxides with a chemical formula of A_xB_yO_z (where A and B = metal) also exhibit activity in photocatalytic methane conversion. A classic group of them is bismuth-based materials, such as BiVO₄ and Bi₂WO₆,⁸⁴ because their valence bands are deep enough to oxidize water to hydroxyl radicals for methane activation. Too many free radicals may lead to hard control of the oxidation process, leading to the dilemma of poor selectivity (<50%) to methanol. Using nitrite ions as a hydroxyl radical scavenger can significantly increase the selectivity (>90%).⁸⁵ In addition, a recent result reported that the selectivity to methanol over BiVO₄ could be manipulated by the exposed facets.⁸⁶ The {102} and {012} surface facets can efficiently extract holes but possess intermediate surface reactivity, thus leading to a high selectivity (>80% in the first 2 h) to methanol. A study in 1969 reported that CuMoO₄ could drive the aerobic oxidation of methane to methanol at a selectivity of nearly 100% under 373 K¹⁴, no further study on this catalyst is found. SrTiO₃ is another efficient photocatalyst that can activate methane molecules to produce different products with various co-catalysts.^{87,88} When decorated with Rh-based co-catalyst, the catalyst can promote the dry reforming of methane under UV light irradiation without heat supply, which breaks the limitation of thermal catalyst for syngas production.⁸⁸ The surface temperature of the catalyst can increase

to 573 K under irradiation without external heating. A linear generation of H₂ and CO at 270 μmol h⁻¹ can be obtained and the high apparent quantum efficiency is achieved at 5.9% (λ = 365 nm). This generation rate is around 15 times higher than the theoretical value in thermal catalysis under this temperature. Unlike thermocatalysis, no accumulation of cokes and aggregation of nanoparticles was observed during the long-term experiment. Apart from DRM reaction, K₂Ti₆O₁₃, a catalyst with a similar band structure as TiO₂, exhibits a hydrogen production rate of 90 μmol h⁻¹ via steam reforming of methane when decorated with Rh-based co-catalysts.⁸⁹

Nitrides. Nitrides are emerging as materials for photocatalytic methane conversion, boasting an expanded scope of products. For instance, a GaN nanowire with 97% of m-planes was active in methane dehydrogenation to benzene under UV irradiation at room temperature, as shown in Figure 2-7.¹⁰

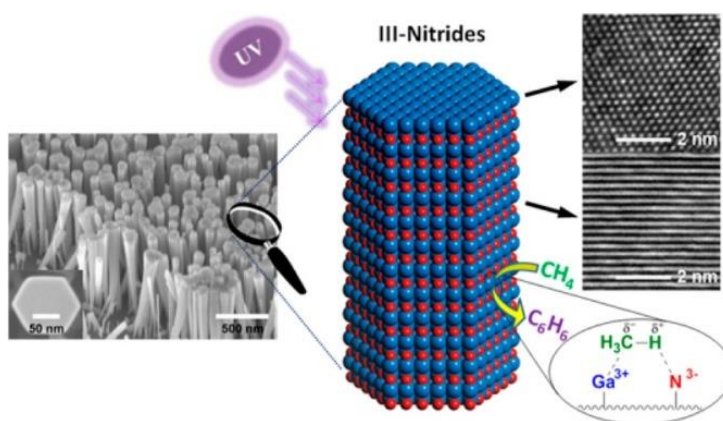


Figure 2-7 Schematic demonstration of C-H bond activation on the surface of GaN m-plane. Reprinted with permission from ref. ¹⁰, American Chemical Society.

A yield rate of 0.019 μmol h⁻¹ with a decent selectivity (96.8%) to benzene can be obtained over the optimum sample Si-doped n-type GaN. This is the first and only example of photocatalytic methane conversion to benzene. The C-H bond in CH₄ could be activated through the polarization on the exposed m-plane, leading to the

generation of methyl radicals. However, the reason for the ordered coupling of these methyl radicals, especially the following cyclization and dehydrogenation process is still unclear. This research shows that the boundary of products could be continuously broken through the careful selection and subtle design of the photocatalyst, although the mechanisms behind these breakthroughs need further investigation. Graphitic carbon nitride, the most popular polymeric photocatalyst has been gradually reported in photocatalytic methane conversion recently. Different modifications of this polymeric resulted in different products and/or processes, such as Ru/Zn-g-C₃N₄ for methane coupling with CO₂,⁹⁰ Cu/g-C₃N₄ for methane coupling and CO₂ reduction,⁹¹ Cu-0.5/PCN for methane oxidation to ethanol,¹⁶ La/g-CNT for DRM,⁹² and g-CN for partial oxidation of methane to methanol with H₂O₂.⁹³ The example of methane to ethanol was seldom reported using inorganic photocatalysts.¹⁶ Benefiting from the synergy of Cu species and the adjacent C atom in the framework of polymeric carbon nitride (PCN), the as-formed hydroxymethyl or methyl groups on Cu can combine with methoxy groups on the C atom to generate ethanol at a yield rate of 2.12 μmol h⁻¹. This example demonstrates the unique structural advantage of polymeric photocatalyst in methane conversion. The carbon cycle in this reaction is still unclear without the ¹³C isotope experiment because carbon to couple with the intermediate CH₃OH can come from either the framework of carbon nitride or methane. Therefore, the ¹³C isotope label experiment is indispensable for the photocatalyst containing carbon atoms.

2.2.2 Non-semiconductor materials

Other materials have been proved to be active in methane conversion. Recently, metal nanoparticles with a plasmonic effect have demonstrated great promise in photocatalytic DRM, such as Ni,^{75,94–96} Au,⁹⁷ CuRu.²¹ Among them, the decoration of single-Ru atomic sites on the Cu nanoparticles leads to an efficient photocatalytic DRM process under low temperatures, as shown in Figure 2-8.

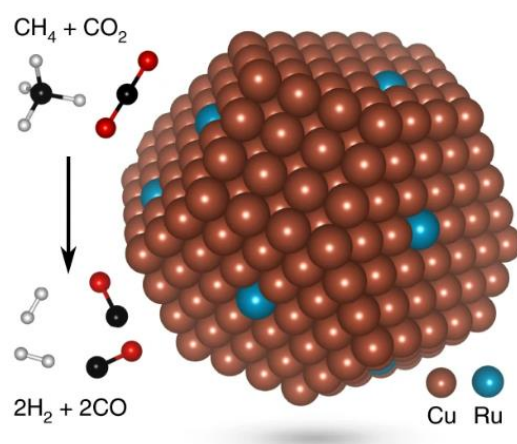


Figure 2-8 Cu-single-atom Ru alloy catalyst for DRM reaction. Reprinted with the permission from ref. ²¹, Springer Nature Limited.

Under white light irradiation, the surface temperature (T_s) of photocatalyst increases due to the photothermal effect. The conversion of methane is always higher than that of thermocatalysis under the same temperature for all space velocities used. The largest difference can reach nearly three times, indicating the great potential of photocatalytic methane conversion in gradual complement and replacement of thermocatalysis. Moreover, a high selectivity (>99%) to H₂/CO was observed for the long term (50 h) without the notable formation of cokes. Through quantum mechanical studies, the author revealed a different activation process that suppresses the reverse-water-gas-shift often happened in thermocatalysis, leading to higher selectivity.

Homogenous photocatalytic organic synthesis via ligand-to-metal transfer (LMCT) is booming in modern photoredox catalysis, which is an emerging area in CH₄ conversion.^{98,99} An inexpensive cerium salt was used as an efficient photocatalyst, which realises the photocatalytic amination, alkylation, and arylation of methane with the cooperation of simple alcohol catalysts. This is the first systematic research on photocatalytic methane functionalization. In order to validate the possibility of scaled-up application, benefit the ease of handling gaseous CH₄ and enhance the mass transfer between gas and liquid phases, a continuous-flow microreactor was set up. A yield rate of 25 μmol h⁻¹ for *tert*-butyloxycarbonyl (BOC)-protected monomethylhydrazine as the amination product. This study indicates that more intriguing opportunities rely on the discovery of new photocatalysts to realize more transformation of methane.

2.2.3 Co-catalysts

The co-catalyst is another key component in an efficient methane conversion photocatalyst system. There are generally two functions or pathways for co-catalysts to promote performance. The separation of photo-generated electrons or/and holes is an important and general role of co-catalysts in most photocatalytic systems. On the other hand, a co-catalyst can be the active site to lower the thermodynamic barriers in methane activation or/and act as the formation sites of certain intermediates or products. As such, both noble metals and non-precious transition-metal-based species have been extensively used.

Noble metals. Owing to appropriate work functions, noble metals are considered ideal electron sinks in photocatalysis, and photoinduced electrons and holes can be separated to suppress charge recombination. an be separated to suppress charge

recombination.^{26,43,44,89,100} Moreover, some other functions can be observed by these noble metals, as discussed below. Modification of commercial ZnO nanoparticles with various noble metals (Pt, Pd, Au and Ag) significantly enhances its activity in partial methane oxidation with oxygen.⁴⁸ Interestingly, the selectivity toward liquid products (CH₃OH and CH₃OOH) can vary with the type of co-catalysts. Pt and Pd co-catalysts can shift the selectivity to CH₃OH compared with the samples decorated with Au and Ag. Such difference can be attributed to another perspective, in which oxygen reduction reaction (ORR) was another important half-reaction, apart from methane oxidation, within this catalytic cycle. The Au and Ag are efficient in the two-electron ORR process to produce H₂O₂ or CH₃OOH, while Pd and Pt are more selective in the four-electron ORR process to form H₂O or CH₃OH. Rh is another noble metal co-catalyst that is usually used in reforming methane. And its function can change according to the wavelength of the light source. In a photocatalytic SRM example, the surface plasma resonance (SPR) effect of Rh nanoparticle was excited by visible light, donating hot electrons to the coupling TiO₂.³¹ Then, it became positively charged to accept σ electrons of methane and facilitated C–H bond cleavage. While in a photocatalytic DRM reaction under ultraviolet light irradiation, Rh acted as an electron acceptor to promote the CO₂ reduction half-reaction.⁸⁸ Similar light source depending effect was also observed over an Ag/TiO₂ ensemble for photocatalysis of CH₄ and CO₂ into ethylene, as shown in Figure 2-9.¹⁰¹ A full spectrum was required to induce the SPR effect on Ag nanoparticles and the photoelectric effect on TiO₂. Thus, an electron transfer balance was constructed between these two active components under certain condition. The hot electrons induced by SPR effect were consumed by the photoholes on TiO₂ eventually, leading to the accumulation of positive charged Ag species and photoelectrons on TiO₂, respectively. As the CH₄ and

CO₂ can be adsorbed separately on Ag and TiO₂, respectively, the CO and C₂H₄ could be generated on each site with a yield rate of 114 μmol h⁻¹ and 68.6 μmol h⁻¹.

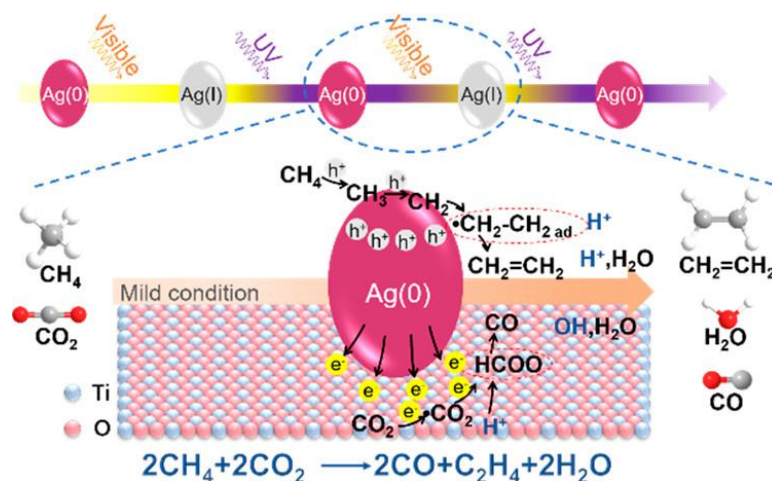


Figure 2-9 Schematic demonstration of plasma-assisted conversion of CH₄ and CO₂ into CO and C₂H₄ over Ag/TiO₂. Reprinted with permission from ref. ¹⁰¹, American Chemical Society.

Non-previous metals. Non-precious metal-based species are another important part of the methane conversion co-catalyst. The functions can be separated as promotion of charge separation, methane activation and oxidant activation, which is similar to that of noble metals. Although the mechanisms of different co-catalysts could be easily attributed to these three types, the selection of appropriate co-catalysts varies according to different reaction systems. For example, highly dispersed iron species can act as high-performance co-catalyst to promote the photocatalytic methane conversion to methanol over TiO₂, as shown in Figure 2-10.¹² After the decoration of Fe species, a four-times enhancement of methanol production was observed, leading to extremely high selectivity to methanol (>90%). Iron species can not only accept electrons to promote charge separation, but also lower the activation barrier for H₂O₂ reduction. Thus, more H₂O₂ can be reduced by photoelectrons transferred from TiO₂ to Fe species to generate ·OH radicals, while more photoholes on TiO₂ can oxidize

methane to give $\text{CH}_3\cdot$ radicals. The combination of these two radicals produces more methanol.

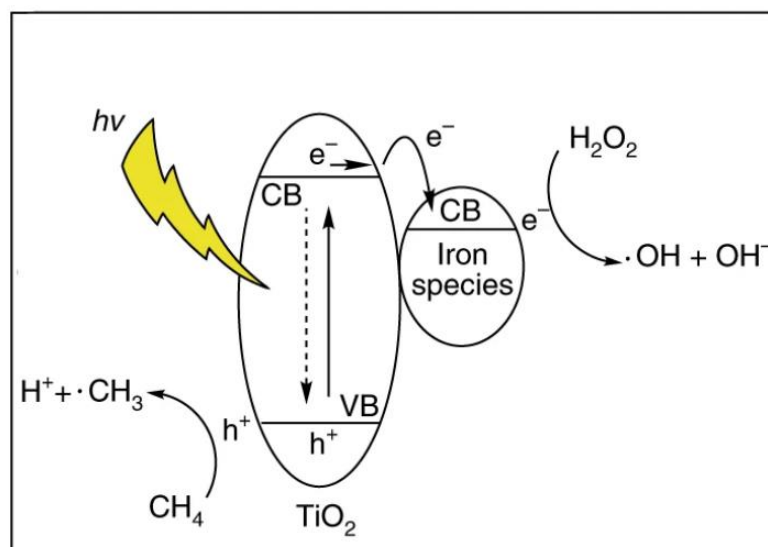


Figure 2-10 Schematic demonstration of methane partial oxidation to methanol over $\text{FeO}_x/\text{TiO}_2$. Reprinted with the permission from ref. ¹², Springer Nature Limited.

The universality of the iron species in this reaction system was further confirmed by a FeOOH/WO_3 photocatalyst.⁶⁰ Similar activation mechanism of H_2O_2 was also reported by a copper species on graphitic carbon nitride,¹⁶ but the copper species also provided an active site for methane adsorption and activation in this case. The introduction of cations to adsorb and activate methane is an effective strategy to promote the conversion. This strategy has been widely used in thermocatalysis, in which Al^{3+} , Zn^{2+} , Ga^{3+} etc. were reported to form metal-methyl intermediates via dissociated adsorption of methane under elevated temperatures.¹⁰² Inspired by this phenomenon, Ga^{3+} was deposited on titanosilicate zeolite material (ETS-10), which significantly increased the conversion of methane (from nearly 0 to 15%). Surprisingly, the polarization of the C-H bond can even happen under room temperature over Ga^{3+} , thus the C-H bond was weakened and the abstraction became easier by the

photogenerated radicals. Methane activation can also be improved by enhancing methane's adsorption on the non-precious co-catalyst. For example, SrCO₃ improved the methane adsorption capacity of SrTiO₃ by an acid-base interaction (SrCO₃:basic oxide, CH₄: Lewis acid).⁸⁷ This explanation was further supported by a study in which the photocatalytic methane combustion performance of TiO₂ was enhanced by SrCO₃.⁴⁰

Unlike conventional methane conversion, photocatalytic methane conversion must take into account the photophysical process as well as the catalytic process. Therefore, if one co-catalyst is not sufficient to achieve an ideal result, it may be effective to introduce another co-catalyst with complementary functions to work synergistically. When Pt nanoparticles and CuO_x clusters were decorated together on anatase TiO₂ for photocatalytic OCM,¹⁰⁰ the metallic Pt species acted as electron acceptors to efficiently separate charge carriers, while copper species accepted photoholes and lowered their oxidation potential to avoid overoxidation of target C₂ products. In SRM over K₂Ti₆O₁₄-based photocatalysts,⁸⁹ metallic Rh and Rh₂O₃ nanoparticles were used as electron and hole acceptors, respectively, to promote reduction (hydrogen production) and oxidation (methane oxidation) reactions.

2.3 Reaction system design

The reaction system, especially the type of reactor, is another effective way to manipulate the reaction rate and selectivity. Compared with the development of the catalysts themselves, far less attention has been paid to this aspect in photocatalysis.

2.3.1 Batch systems

The majority of the reactors used for photocatalytic methane conversion are slurry batch reactors, in which gas is purged through a reactor containing a catalyst before the reaction or during the reaction.^{10,12,16,18} In these reactors, products cannot be removed as they are generated, and products cannot be removed as they are generated, increasing the possibility of overreaction, especially overoxidation. Nearly all the products of methane conversion reactions are easier to be activated than methane itself. Thus, thermodynamically obtaining the desired products with a high yield and selectivity is very challenging in a batch reactor. This type of simple system can only be employed to initially screen photocatalysts, and there are limited parameters that can be optimized to improve the yield and selectivity. In addition, adsorption of methane and desorption of products mainly rely on spontaneous gas diffusion in these batch reactors, especially in a gas-solid two-phase reaction such as NOCM, owing to the lack of strong forces to facilitate the mass transfer. This phenomenon implies that mass transfer, rather than photocatalytic efficiency itself, is likely one limiting factor for the low yield rate.

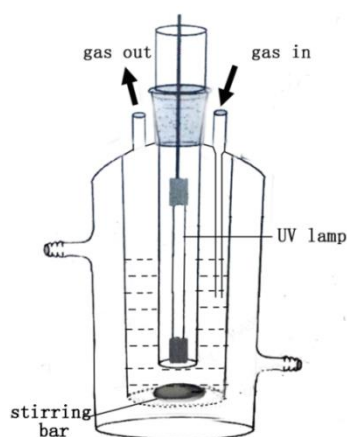


Figure 2-11 A batch reactor is equipped with a circulation pump to improve the mass transfer of methane. Reprinted with permission from ref.⁴⁰, Elsevier.

Some strategies have been introduced to improve the conversion and/or yield in batch systems. A circulating pump was installed at the external circuit to promote the mass transfer, as shown in Figure 2-11.^{43,44} With the assistance of a pump, the reactant gas could circulate with a flow rate of 10 mL/min in the system. The methane molecules could have a good interaction with the suspension, leading to an efficient catalytic process. Thus, it achieved a top level of the yield of the C₂ product (2.08 μmol h⁻¹ over Pt/TiO₂ and 2.13 μmol h⁻¹ over Pd/TiO₂, respectively) among all TiO₂-based photocatalysts in atmospheric batch reactors. Increasing the pressure of the reaction system is another way to enhance the interaction between reactants and catalysts. For example, the influence of pressure on the direct oxidation of methane to oxygenates was investigated over a Au-loaded ZnO photocatalyst, as shown in Figure 2-12.⁴⁸ With increasing CH₄ pressure, the solubility of methane in water also increased, leading to a higher yield of desired products. It is interesting to note that the yield of CO₂ increased only slightly with the increasing pressure, and, thus, the selectivity of oxygenate liquid products was very high (>95%). This, in part, indicates the influence of mass transfer on the performance of the photocatalysts.

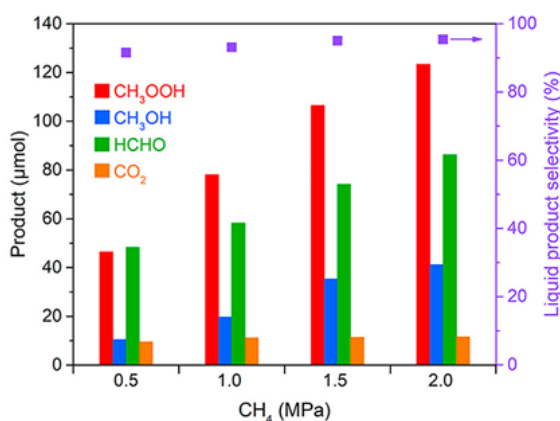


Figure 2-12 The influence of reactants' pressure on the direct oxidation of methane to oxygenates was investigated over Au-loaded ZnO photocatalyst. Reprinted with permission from ref.⁴⁸, ACS

2.3.2 Flow systems

Developing the knowledge learnt from the batch reactor, a flow system can be an effective way to improve mass transfer. A flow reactor can adjust the residence time of methane and products and control the interaction between molecules and catalysts. The single-run conversion rate can be evaluated, which is a very valuable reference for subsequent applications. Moreover, unlike the uneven distribution of reactants in batch reactors, the reactant molecules are dispersed evenly in a flow system. Given these advantages, it is important to assess photocatalytic activity in a flow system and, so far, flow reactors have been used mainly in photocatalytic methane reforming and methane degradation,^{21,26,41,47,88} which were hard to show its superiority in the control of selectivity due to the relatively simple distribution of products.

In an example of a continuous flow photocatalytic process, OCM was performed over modified TiO₂ at room temperature and atmospheric pressure in a flow reactor, as shown in Figure 2-13.¹⁰⁰

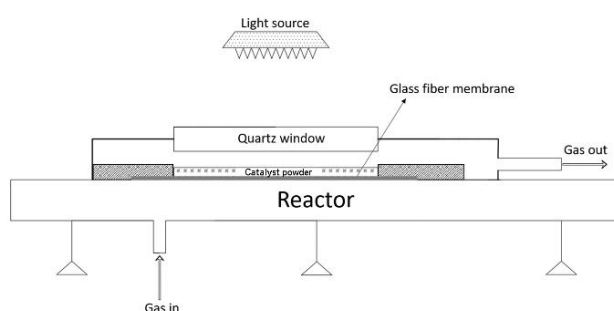


Figure 2-13 A flow reactor was first reported for the photocatalytic oxidative coupling of methane reaction. Reprinted with permission from ref.¹⁰⁰, CC BY 4.0 (<https://creativecommons.org/licenses/by/4.0/>).

The reactor enables a readily tuned ratio of CH₄ to O₂ with a relatively evenly distributed gas stream through the catalyst bed and accurate online product analysis.

Benefiting from the promoted mass transfer and controlled reaction time in a flow system, the optimized CuPt/TiO₂ photocatalyst represented the highest yield of C₂ products (6.8 μmol h⁻¹) among all TiO₂-based photocatalytic methane conversions. Moreover, the C₂ selectivity was as high as 60%, comparable with that of a traditional thermal catalyst (such as Li/MgO) at a high temperature (>943 K). In a similar flow reactor strategy, photocatalytic NOCM has been carried out over Pd/Ga₂O₃.⁷⁸ The selectivity to ethane could be improved by increasing the flow rate. The fast flow promoted the migration of methyl radicals for coupling, rather than further oxidation by holes to unexpected products (for example, cokes). In addition, the shorter contact time decreased the possibility of successive coupling reactions to other products, such as propane. All these results indicate the superiority of a flow system over a batch system.

2.3.3 Other reaction systems

To further improve the selectivity of the desired products, some clever designs have also been employed. For example, a two-phase system of perfluorohexane and water was used for the photo-oxidation of CH₄ with chlorine dioxide radical (ClO₂·) and molecular oxygen, as shown in Figure 2-14.¹⁰³ Although this reaction is photochemical rather than photocatalytic, the two-phase strategy may be useful for the latter. Owing to the more inert nature of perfluorohexane than CH₄, the generated CH₃ and Cl radicals prefer to attack CH₄. Moreover, the gas reactants, CH₄ and O₂, have high solubility in perfluorohexane, whereas the oxygenated products, CH₃OH and HCOOH, are more soluble in water. The oxygenation of CH₄ proceeded in perfluorohexane and the products transferred to water, avoiding further oxidation, and resulting in a 99% conversion of methane without CO or CO₂ production. A similar

concept was tested in other photocatalytic reactions, such as the photocatalytic synthesis of H_2O_2 .¹⁰⁴

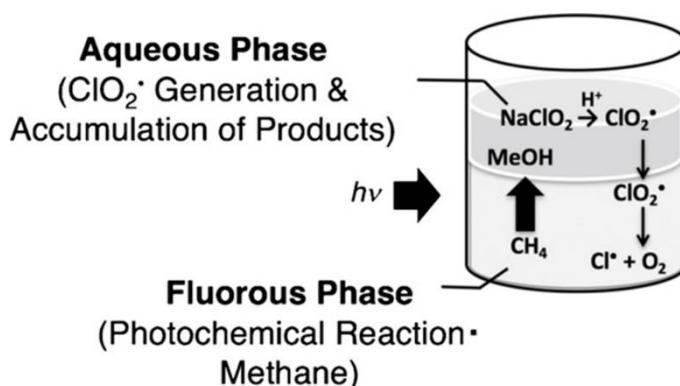


Figure 2-14 A two-phase reaction system was used for photo-oxidation of CH_4 by NaClO_2 . Reprinted with permission from ref.¹⁰³, Wiley.

Another strategy is to use a chemical loop in which methane conversion and regeneration of catalysts are two separate steps. This type of loop was used for stoichiometric methane conversion to ethane on $\text{Ag-H}_3\text{OW}_{12}\text{O}_{40}/\text{TiO}_2$, as shown in Figure 2-15.³⁶ The photoelectrons were consumed by Ag^+ species to form metallic Ag, while CH_4 was activated by the photoholes to generate CH_3^\bullet , which coupled into C_2H_6 . The production of C_2H_6 stopped after the Ag^+ species were completely reduced. The metallic Ag species were then recovered into their original oxidation state through UV irradiation in the presence of air. The Ag^+/Ag^0 redox couple served as an important mediator to separate O_2 reduction from the methane oxidation step and over oxidation was effectively avoided. This strategy alleviates the uncontrollable radical oxidative process.

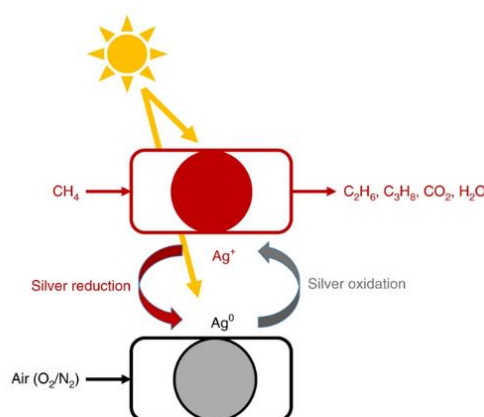


Figure 2-15 A chemical loop was used for stoichiometric methane conversion to ethane over $\text{Ag-H}_3\text{OW}_{12}\text{O}_{40}/\text{TiO}_2$. Reprinted with permission from ref. ³⁶, Springer Nature Limited.

Similarly, in a photocatalytic methane conversion to ethane and ethylene over AuPd/ZnO , methane reacted with the lattice oxygen of ZnO , producing C_2H_4 and H_2O .³⁷ Of the total lattice oxygen, 3.68% was consumed after photocatalytic reaction for 8 h. The oxygen vacancies formed could be easily compensated by subsequent water rinsing. So far, the chemical loop strategy has only been applied in a batch reactor. Combining a flow reactor with a chemical loop is an attractive approach for future studies.

2.4 Mechanistic understanding

Mechanistic study of photocatalytic methane conversion has significantly lagged behind catalyst development. Photocatalytic methane conversion can typically be understood by two interlinked processes, photophysics and chemistry.

2.4.1 Photophysics

In photocatalysis, the lifetime of the charge carriers should be longer than the timescale of relevant surface reactions. The time-resolved spectroscopies provide a powerful way to monitor the generation and lifetime of photoinduced carriers. Three complementary technologies can be useful in this regard: time-resolved resonance Raman spectroscopy (TRRS), transient absorption spectroscopy (TAS) and time-resolved infrared (TRIR) spectroscopy.^{105–108} Using these techniques together may allow observation of charge carriers and reaction intermediates and elucidate fundamentals of the photophysical processes. However, few studies have applied these spectroscopies to photocatalytic methane conversion. Thus, in addition to describing those few examples, the use of these techniques in related photocatalytic processes is also described to show their potential in the methane conversion field.

TAS is widely used to observe the photoinduced electrons and holes, determine their lifetimes and compare the charge dynamics with a wide timescale, ranging from picoseconds to milliseconds in many photocatalytic processes.^{109–112} In a typical example, TAS revealed the mechanism of photocatalytic SRM over Rh/TiO₂ under visible light illumination, as shown in Figure 2-16.³¹ After excitation, the Rh/TiO₂ exhibited a significantly faster rise of transient absorption than those of Rh/ZrO₂ and Rh/SiO₂, indicating the promotion of ultrafast charge separation. Then, the comparison of rising time and multiexponential decay was obtained by fitting the transient absorption of Rh/TiO₂. The longer lifetime of hot electrons guarantees the longer lifetime of the electron-deficient state at Rh nanoparticles, leading to the more efficient activation of methane under illumination.

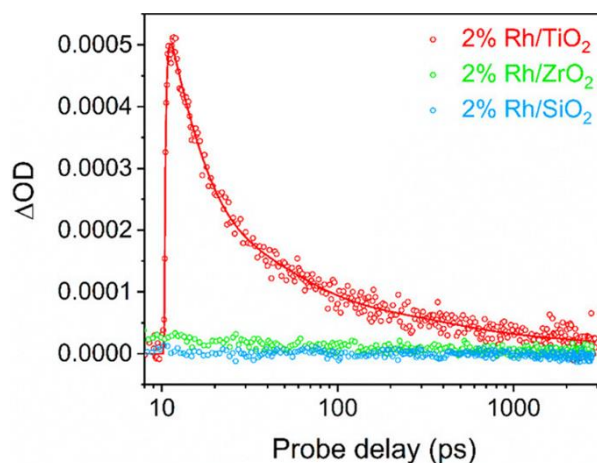


Figure 2-16 Transient absorption spectra (TAS) of charge dynamics in Rh/TiO₂ (red), Rh/ZrO₂ (green), and Rh/SiO₂ (blue) after photoexcitation. Reprinted with permission from ref. ³¹, ACS.

TAS, together with the manipulation of experimental conditions, can also help identify the timescale of interfacial reactions, such as measuring the lifetime of holes and the kinetics of the reactions between photoholes and water.¹¹⁰ The lifetime of holes could be directly observed and more importantly, they could be changed by the addition of different scavengers, such as Ag⁺ or Pt. O₂ evolution was then found to be at a timescale of seconds over oxide photocatalysts. These results provide solid evidence that extending the lifetime of holes can promote photocatalysis, thus guiding the material design. However, there is a lack of in-depth understanding of the reaction kinetics for photocatalytic methane conversion.

The probes of TAS are usually located in the visible-to-near-infrared region, making it difficult to monitor species with featureless absorption spectra in this region, such as the vibrations of reactants and intermediates.^{105,113} TRIR spectroscopy is, thus, a powerful complementary tool to cover the mid-infrared range. It has also been used to trace the kinetics of photoinduced carriers in homogenous and heterogeneous systems.^{105,114–116} For example, since the photoelectrons are trapped in shallow states

to absorb infrared light, TRIR spectroscopy can monitor the electron decay in TiO₂ and Pt/TiO₂ under O₂/H₂O atmosphere.¹¹⁶ The introduction of water vapour significantly slowed the decay of transient infrared absorbance at 2,000 cm⁻¹ and the lifetime of photoelectrons was extended up to 0.9 s, which was attributed to the abstraction of holes by hydroxyl anions, thus mitigating charge carrier recombination. Moreover, the timescale (10-100 μs) of superoxide radical generation was also monitored by this technique. Taking into account the important role of the superoxide radicals in photocatalytic methane conversion, TRIR shows a strong potential to observe the reaction mechanism involved with oxygen, although it has seldom been used so far for this process.

For short-lived intermediates and electronically excited states that have a complex or negligible infrared response, TRRS provides a complementary means to visualise the molecular fingerprint, where the Raman operational window spreads from the deep UV to the visible region and can be monitored in the middle to far-infrared region. The UV region, which is important for conjugated catalysts, is particularly attractive, given the surge in polymeric photocatalysts and potential conjugated products. A combination of TAS and TRRS was used to investigate the homogeneous photoredox reaction of an anthraquinone derivative.¹³⁸ In the TAS spectra, the transient species exhibited absorbance at 383 and 430 nm with a first-order kinetic decay. However, the absorption spectra were broad and little structural information could be acquired. TRRS was able to extract structural information, revealing that the transient species overlapped with the Raman bands of the triplet excited state of the anthraquinone derivative at 1,570 cm⁻¹. The transient ketyl radical species of this anthraquinone

derivative could be analysed after a comparison of the spectra at 200 ns with the modelled spectra, demonstrating the effectiveness of TRRS.

2.4.2 Reaction steps and surface chemistry

From a chemical perspective, to reveal the reaction pathway, both the catalytic surface and the interaction between the surface and the reactants have to be paid particular attention. In most cases, significant effort was devoted to the activation of the first C-H bond in the CH₄ molecule to form methyl radicals, but it is not always the most important rate-determining step in the full catalytic cycle.¹¹⁷ So far, only those photocatalytic reactions with a limited number of elementary steps are fully understood. For example, in NOCM and OCM, the coupling of as-formed methyl radicals after C-H activation produces the final products.^{30,100,118} In contrast to these simple processes, it is hard to rationalize a consistent reaction pathway. Using one photocatalytic methane conversion reaction to methanol as an example, the intermediate hydroxyl radicals may react with methyl groups to form methanol^{12,60,119} or may act as the active species to abstract H from methane.^{57,120} Even the generation of hydroxyl radicals involves different pathways according to different catalytic processes: they could be directly generated by photoholes with water;¹²¹ by the reaction between photoelectrons and H₂O₂, which could either be from external addition or formed in situ;^{16,60} or by the reaction between singlet oxygen and water.¹¹⁹ Thus, it is difficult to establish a unified pathway for each route, although the intermediates might be similar. For the reactions that involve multiple elementary steps and/or multi-carbon products, such as the generation of C₂₊, the mechanisms have mostly been based on speculation without solid experimental evidence. Therefore, to draw the full picture of each photocatalytic methane conversion process,

operando or at least in situ characterisation must be used to monitor the active catalytic sites at the molecular level, investigate their interactions with molecules and possible transformations, and observe the different intermediates.

In situ IR spectroscopy has been widely used in photocatalytic methane conversion to observe species on the catalysts' surface.^{16,17,26,41,47,57,87,90,101} Owing to the organic nature of this reaction, many vibrational modes are sensitive to IR, such as C-H, O-H, C-O, CH₃-O, and C=O, which helps reveal the mechanism behind the surface chemistry. The intensity of typical $\nu(\text{C-H})$ vibration modes of methane at around 3015 cm^{-1} can be readily monitored during methane conversion, whereas the other bands can vary from one process to another. For example, the decreasing intensities of $\nu(\text{C-H})$ accompanied by the gradual growth of CO₂ under irradiation could be observed, along with the increasing bands attributed to chemisorbed H₂O.²⁶ More telling was a newly formed band corresponding to the $\delta(\text{CHO})$ of chemisorbed aldehyde, which slowly increased during the reaction, unlike other products. Based on this, CH₄ was proposed to react with O₂ at first to form HCHO and H₂O, then the intermediate HCHO further reacted with O₂ to form CO₂. The advance of coupling in situ FTIR spectroscopy with isotopic labelling is emphasized to study the role of lattice oxygen in metal oxides during photocatalytic methane conversion. These lattice oxygen species were found to activate methane and be regenerated through a mechanism like the Mars-van Krevelen mechanism (a chemical loop) when the reactants contain oxygen atoms (O₂ or CO₂, for instance).^{41,88} However, this reaction pathway cannot be applied to the continuous selective generation of hydrogen and hydrocarbons in NOCM over metal oxide photocatalysts.^{17,18}

In situ EPR is another widely used technique to monitor active species that contain unpaired electrons in photocatalytic methane conversion.^{18,22,26,44,47,48,52,82,87,88} Compared with in situ FTIR, in situ EPR can capture those relatively more active species, such as transition metal ions in paramagnetic valence states, radicals and free electrons.¹²² The most common species that have been observed by in-situ EPR in photocatalytic methane conversions, such as superoxide radicals ($O_2^{\bullet-}$), hydroxyl radicals (OH^{\bullet}) and methyl radicals (CH_3^{\bullet}). For instance, this technique was carried out to investigate the mechanism of photocatalytic POM.⁴⁸ The CH_3^{\bullet} only existed under the introduction of CH_4 gas while OH^{\bullet} could be always produced in such a system. Moreover, the amount of both species could significantly increase after depositing cocatalysts (e.g. Pt, Pd, Au) on ZnO, indicating the promotion of hydrogen abstraction by cocatalysts. In addition, this technique was also used to capture another active radical, HOO^{\bullet} , which was proposed as a mild oxidative intermediate to form CH_3OOH with CH_3^{\bullet} rather than overoxidation. Apart from the monitoring of radicals, the in situ EPR could also provide information on photocatalysts during the reaction, e.g., oxygen vacancy, photoholes ($O^{\bullet-}$). For example, charge transfer process over Rh/SrTiO₃ during DRM reaction condition was elucidated by in-situ EPR under different atmosphere.⁸⁸ Under inert N₂ atmosphere, the signal attributed to trapped holes could be observed over both Rh/SrTiO₃ and bare SrTiO₃, while the signal assigned to photoelectrons could only be detected over bare SrTiO₃. This suggests that Rh nanoparticles was an electron acceptor in their system. Interestingly, the intensity of photoholes remained similar under CO₂ atmosphere, but it clearly decreased under CH₄ or CH₄/CO₂ atmosphere. Thus, they concluded that the photoholes only reacted with CH₄. So far, the condition during the use of in situ EPR was more or less different from the real experimental condition, such as the addition of spin trapper (e.g. DMPO),

extremely low temperature, thus it is highly expected to measure with closer adaption of real experimental condition in future work.

As a complementary technique, in situ X-ray photoelectron spectroscopy (XPS) provides information about the composition and chemical environment of the catalytic sites, acquiring rich information and understanding of the dynamic process. Only a few studies of photocatalytic methane conversion have used in situ XPS so far.^{12,60} In an investigation of highly dispersed iron species (FeOOH and Fe₂O₃) on TiO₂ support during photocatalytic selective oxidation of methane to methanol (Figure 2-17),¹² both Fe 2p_{3/2} and 2p_{1/2} peaks shifted to lower binding energy upon light irradiation, indicating the role as electron acceptor of iron species during the photocatalytic reaction. Similarly, an in-situ XPS was used to investigate active sites

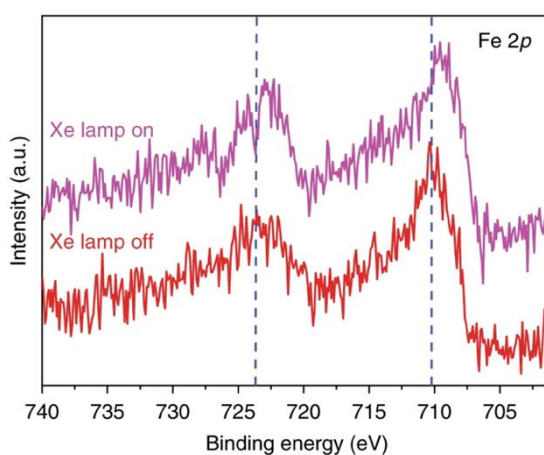


Figure 2-17 In-situ Iron 2p XPS spectra of FeO_x/TiO₂ in the dark and under light irradiation. Reprinted with permission from ref. ¹², Springer Nature.

and charge transfer over FeOOH/m-WO₃ under visible light illumination.⁶⁰ The Fe 2p binding energy also shifted about 0.4 eV toward lower binding energy compared with that in dark conditions, suggesting the electron transfer from m-WO₃ to FeOOH under irradiation. Furthermore, after the introduction of H₂O₂, the Fe 2p binding

energy positively shifted back. It indicates that the photoelectrons transferred to FeOOH would further react with H₂O₂. Therefore, the use of in-situ XPS can help to gain an in-depth understanding of the function of surface species during the photocatalytic reaction.

In situ X-ray absorption spectroscopy (XAS) can extract quantitative chemical and structural information about a photocatalyst, to reveal the correlations between catalyst activity and its structure. Although it has not yet been reported for photocatalytic methane conversion, an example of its application to thermal methane conversion is discussed here to illustrate its potential for photocatalysis. With selective methane conversion to methanol over a copper-exchanged zeolite as the reaction of interest, in situ XAS was used to observe the reaction mechanism at Cu^{II} oxide centres.⁷⁶ The intensity of the peak assigned to Cu^I increased after the introduction of CH₄ at 473 K, indicating the interaction between Cu^{II} and methane. As water vapour was introduced to regenerate Cu^{II}, the intensity of the Cu^I peak decreased. Moreover, a new peak attributed to the hydrated Cu^{II} species appeared. In this way, the in situ XAS data helped to unravel the methane oxidation and regeneration processes over Cu^{II} active sites.

The above techniques mostly examine surface species, surface structure and composition under in situ conditions. Compared with these in situ technologies, *Operando* measurement is a technique that emphasises the real-time characterisation of catalysts under actual reaction processes (the same reaction conditions, in the same reactor system). *Operando* tests can provide rich and accurate information on the catalytic process in real-time for mechanistic studies, such as active intermediates, reaction pathways and full catalytic cycle, which helps to correlate the activity and

selectivity with the catalyst structure. An *operando* TOF-MS was used to track the evolution of liquid products for methane direct conversion during the high-pressure reaction (Figure 2-18).¹²³ Briefly, a capillary reactor coupling with TOF-MS was used to extract and analyse the products in time, thus the reaction mechanism could be elucidated. The signal assigned to CH₃OH and CH₃OOH increased with time, while those of HOCH₂OOH and HCOOH remained almost unchanged. In the last 300 minutes, the intensity of the signal for HOCH₂OOH and HCOOH remarkably increased and the rate of CH₃OH generation slowed down. Thus, CH₄ was considered to be oxidised to CH₃OH and CH₃OOH first and then further oxidised to HOCH₂OOH and HCOOH, indicating TOF-MS is a powerful tool to understand the reaction pathway.

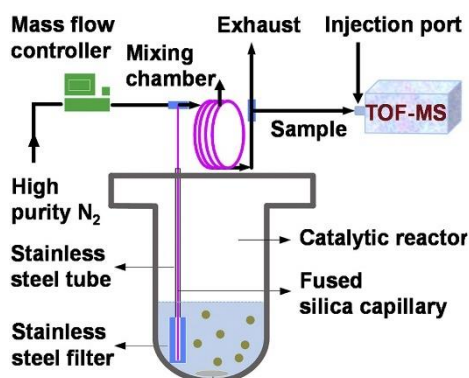


Figure 2-18 The schematic presentation of *operando* TOF-MS for the characterization of liquid products in methane conversion. Reprinted with permission from ref.¹²³, Cellpress.

Apart from the TOF-MS, diffuse reflectance FT-IR spectroscopy (DRIFTS) is one of the most accessible techniques to elucidate heterogeneous catalytic reactions under *operando* conditions.¹²⁴ For example, it was used to investigate the active sites and the enhanced carbon resistant ability over Ni-Ru catalysts in thermocatalytic DRM reaction.¹²⁵ Under the consistent catalytic kinetic conditions, this spectroscopy technique allows the direct observation and analysis of the important intermediates

(e.g., carbonyls, carbonates species) online, revealing that the presence of Ru promoted the carbon gasification and alleviated the dissociation of CO. The *operando* technologies can not only observe the transformation and intermediates of substances (e.g., TOF-MS, DRIFTS, as mentioned above), but also be widely used to gain an in-depth understanding of the catalysts' structural transformation (e.g., XANES, near atmospheric pressure (NAP)-XPS). An *operando* XAS experiment was carried out to abstract the nature of active Pd species under the genuine condition of methane combustion.¹²⁶ Through the observation of the Pd K edge spectra and the monitoring of methane conversion at the same time, the temperature-dependent active species (Pd oxide species at <950 K and reduced Pd at >950 K) could be resolved. Similarly, an *operando* NAP-XPS technique was used to determine the surface composition of a bimetallic CuNi catalyst during methane decomposition.¹²⁷ From the Ni 2p_{3/2} and Cu 2p_{3/2} spectra, a conclusion was drawn that Ni would propagate to the surface during the reaction even if the surface was rich in Cu at the beginning. For more information about the use of *operando* techniques in heterogeneous catalysis, one related review article is recommended.¹²⁸ Overall, the reaction mechanism of photocatalytic methane conversion can be accurately elucidated by these state-of-the-art technologies.

2.5 Conclusion

This chapter summarised the current progress on the photocatalytic conversion of methane into high-value chemicals, covering the development of photocatalysts and co-catalysts, the utilisation of different reaction systems, and the fundamental understanding of the underlying reaction mechanism with respect to photophysics and chemistry. Despite the substantial progress that has been made in the development of

photocatalytic methane conversion to various products, there is still a long way for the translation of lab experiments to an industrial scale.

Firstly, the efficiency of photocatalysts in methane conversion is quite low. The highest AQY reported in photocatalytic methane conversion was 60% over Pt/black TiO₂,²² and most of the other catalysts exhibited a lower AQY, even less than 10%. In contrast, higher AQY is commonly reported in other photocatalytic processes, in particular for water splitting (up to 96%, $350 < \lambda < 360$ nm)²³, indicating the big challenges facing and a significant improvement needed for the photocatalytic methane conversion. The second challenge lies in the development of co-catalysts as they play a pivotal role in manipulating products' yield and selectivity. Although the reported co-catalysts covered a wide field, including nanoparticles, clusters and single atoms, the in-depth understanding of the real active sites, and in particular, the synergy between them at the atomic scale is still unclear. The third challenge is the design of an appropriate reaction system. Most of the reactors reported are batch reactors. A flow system will be undoubtedly more applicable. However, the use of flow reactors is rather challenging, considering the complex methane conversion process, and the cost and safety issues related. The fourth challenge is the in-depth understanding of the mechanism behind every photocatalytic methane conversion process, including both photophysics and photochemistry. Compared with the fast development of materials domain, the research on the photophysics of these materials is significantly lacking. Moreover, the mechanism investigation of chemical processes mainly focuses on the activation of the first C-H bond, while the investigation of the full catalytic cycle, especially the elementary reactions in the gas phase is equally important. The

last challenge is the reliable and reproducible results achieved by photocatalysis, which requires further improvement.

3 Methodology

This Chapter describes all material characterisation technologies used in this thesis and the photocatalytic OCM reaction system for activity measurements.

3.1 Powder X-ray diffraction (PXRD)

Powder X-ray Diffraction (PXRD) was carried out to analyze and identify the crystalline structure of the as-synthesized materials. When an X-ray beam as an electromagnetic wave irradiates a crystal, it should be scattered by the atoms in the crystalline structure. In the crystal, atoms arrange periodically thus a fixed phase difference between these scattering waves is expected. These scattering waves will strengthen each other in some specific directions and eliminate in other directions, leading to diffraction patterns. As atoms arrange uniquely in every crystal, the corresponding diffraction pattern is different from each other. The patterns are affected by the size, shape, and orientation of the unit cell, while the intensity of the signal is determined by the types of atoms and their specific location within the unit cell. Therefore, phase analysis and identification can be performed with PXRD. The principle of diffraction can be explained by Bragg's law $n\lambda=2d\sin\theta$ (Figure 3-1), where d corresponds to the spacing between crystal layers; λ corresponds to the wavelength of incident X-ray; θ corresponds to incident angle; n corresponds to an integer. When all the parameters satisfy this law, the diffraction will enhance.

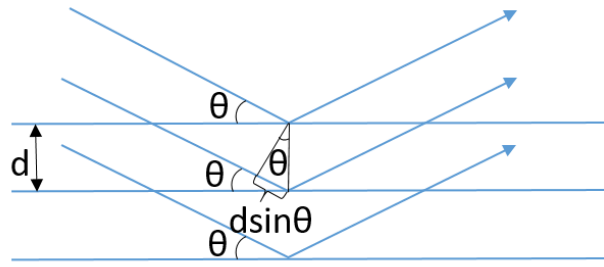


Figure 3-1 X-ray scattering on a crystal surface (Bragg's Law)

In the thesis, the measurements were conducted in a Stoe STADI-P instrument (2° to 40°, step 0.5 ° at 5.0 s/step) using Mo K α 1 (wavelength 0.70930, 50 kV and 30 mA) and a Rigaku SmartLab SE (10° to 80°, step 0.5 ° at 5.0 s/step) using a Cu K α 1 source (wavelength 1.5406, 60 kV, 60 mA).

3.2 Raman spectroscopy

Raman spectroscopy can be used to investigate vibrational modes and rotation modes within lattices and molecules, as well as other low-frequency modes. Raman signal is an inelastic scattering resulting from the interaction between incident laser with molecular vibration or other excitations. Thus, the energy of the scattering light will shift up or down, corresponding to anti-stokes shift or stokes shift, while stokes shift happen in most cases. This energy decay can be expressed by the formula below:

$$\Delta w = \left(\frac{1}{\lambda_0} - \frac{1}{\lambda_1} \right) \quad \text{Eq. 3-1}$$

Where Δw is the Raman shift, λ_0 is the wavelength of the incident laser and λ_1 is the Raman spectrum wavelength, respectively.

In this thesis, the experiments were conducted at Renishaw InVia Raman with 325 nm, 442 nm, and 514 nm excitation lasers and the wavenumber range was from 100-3500 cm^{-1} .

3.3 Photoluminescence spectroscopy (PL)

Photoluminescence (PL) can be illustrated as a process in which a sample absorbs a photon to an excited state and then emit a photon back to a ground energy state. Regarding photocatalysis, the intensity of PL after excitation corresponds to the extent of radiative recombination of photo-induced e^-/h^+ .

In this thesis, the experiment was carried out by Renishaw InVia Raman with a 325 nm excitation laser ranging from 200 – 800 nm.

3.4 Time-resolved photoluminescence (TRPL)

Time-resolved photoluminescence (TRPL) can be used as a complement tool to steady state PL, which can investigate the dynamics of excited species with photoluminescence emission. In photocatalysis, the lifetime of an excited state can correspond to the dynamics of photo-induced charge carriers, reflecting the charge separation and migration processes.

In this thesis, the experiment was carried out by an FLS 920 fluorescence lifetime spectrophotometer (Edinburgh instrument, UK) with a 340 nm excitation laser and 455 nm detection wavelength. The TRPL decay curves were fitted by equation as below:

$$I(t) = A_1 e^{-\frac{t}{\tau_1}} + A_2 e^{-\frac{t}{\tau_2}} \quad \text{Eq. 3-2}$$

where I_0 is the baseline correction value, A_1 and A_2 are the pre-exponential factors, τ_1 and τ_2 are the respective lifetime in the radiative and nonradiative process. The intensity average lifetime (τ_{av}) can be obtained using Eq. 3-3

$$\langle \tau_{av} \rangle = \frac{\sum_{i=1}^{i=n} A_i \tau_i^2}{\sum_{i=1}^{i=n} A_i \tau_i} \quad \text{Eq. 3-3}$$

3.5 Ultraviolet-Visible (UV-Vis) spectroscopy

Ultraviolet-visible (UV-Vis) diffuse reflectance spectroscopy is a tool to measure the light absorption of catalysts in solid-state. Barium sulphate powder is used as a standard reference in the range of 200 – 800 nm. The relative reflectance can be converted to the Kubelka-Munk function $F(R)$, as shown by the equation below:

$$F(R) = \frac{(1-R)^2}{2R} \quad \text{Eq. 3-4}$$

The bandgap of the materials can be estimated from equations 3-5, also known as the Tauc plot.¹²⁹

$$(\alpha h\nu)^{1/n} = A(h\nu - E_g) \quad \text{Eq. 3-5}$$

Where α corresponds to the optical absorption coefficient, h corresponds to the Plank's constant, ν corresponds to light frequency, A is a constant, and E_g is the bandgap of the tested sample. The value of n is corresponding to the nature of the semiconductor (direct band semiconductor, $n=1/2$; indirect band semiconductor, $n=2$). Through a plot

of $(\alpha h\nu)^{1/n}$ versus photon energy $h\nu$, an extrapolation from the linear region towards the x-axis could obtain the value of E_g (bandgap of semiconductor).

All the data in this thesis were collected by an Agilent Carry 3500 UV-Vis-NIR spectrophotometer with a diffuse reflectance unit and a SHIMADZU UV-2550 in reflectance mode.

3.6 Microscopes (SEM, TEM)

Scanning Electron Microscope (abbreviated as SEM) is an electron microscope that studies morphology, particle sizes and structure of materials. Generally, SEM is to detect secondary electrons emitted by atoms after interaction with the high energy electron beam. It produces high-resolution three-dimensional images.

A transmission electron microscope (abbreviated as TEM) is a technology that generates two-dimensional images with resolutions as high as 0.5 angstroms. It projects an accelerated and focused electron beam onto a thin sample, which will collide with the atoms to change directions. The interaction is related to the density and thickness of the samples, thus leading to different magnification images.

In this thesis, a JEOL JSM-7401F SEM equipped with Energy Dispersive-X-Ray (EDX) was applied to analyze the micro-morphology and composition information of the materials on carbon tips. TEM images were obtained with a JEOL2010 while samples were diluted in ethanol and dispersed on a conductive copper/gold grid. STEM imaging was conducted using a double Cs aberration-corrected FEI Titan3

Themis 60-300 equipped with an X-FEG gun, a monochromator and an XEDS ChemiSTEM.

3.7 X-ray photoelectron spectroscopy (XPS)

X-ray photoelectron spectroscopy (known as XPS) is a quantitative tool to determine the composition, valence states and electronic interaction in the materials. X-ray is used to excite the electrons from 1 nm to 10 nm below the surface of materials and simultaneously measure the kinetic energy and number of the escaping electrons. The relationship between binding energy and kinetic energy is presented by the following formula:

$$E_b = E_x - (E_k + \Phi) \quad \text{Eq. 3-6}$$

Where E_b is the binding energy of electrons, E_x is the photo energy of X-ray and Φ is the work function of the analyzer, respectively.

In this thesis, XPS Analysis was carried out in two instruments, Kratos Axis SUPRA XPS and ThermoScientific XPS K-alpha. In situ XPS experiment was conducted using a Thermo Fisher ESCALAB 250Xi equipped with a 365 LED light source. All the XPS analysis was performed with CasaXPS software and the spectra were calibrated with C 1s peak at 284.8 eV.

3.8 Electron paramagnetic resonance (EPR)

Electron paramagnetic resonance (EPR) is a technology widely applied to study materials with unpaired electrons, such as metal complexes, metal ions and organic

radicals. In solid catalysis, it can provide valuable information about the structure, chemical states, active sites, and dispersion.

In this thesis, EPR spectra were measured by a MS-5000 spectrometer and a NUKER E500-9.5/1.2 spectrometer. For powder samples, the ex/in situ EPR was performed either at ambient temperature or 100 K. Different gas atmospheres such as argon, air, and methane were provided with a 365 nm LED as the light source. For liquid samples, different DMPO solutions were used as a radical capture reagent to identify hydroxyl radicals and superoxide radicals during light irradiation (300 W Xenon lamp).

3.9 Transient absorption spectroscopy (TAS)

Transient absorption spectroscopy (in short TAS) is a useful tool to determine the behavior and dynamics of photo-induced carriers in photocatalysis. TA signals can be obtained through two operation modes, transmittance and reflectance, and the TA signals are generally displayed as the change of absorbance/optical density ($\Delta O.D.$). The observed TA spectrum is contributed by three components, such as absorption of photo-induced states (positive signal), stimulated emission (negative signal), and ground state bleaching (negative signal).

In this thesis, μ s-s timescale TAS measurements were carried out using the third harmonic output of a Nd:YAG laser (Continuum, Surelite I-10, 355 nm, 6 ns pulse width). The laser output was transmitted to the sample via a liquid light guide. Sample was excited at 355 nm with an intensity of 0.40 mJ cm^{-2} at 0.66 Hz. A 104 W tungsten lamp coupled with a monochromator (OBB Corp., typically set to 4 nm resolution) was used as the probe light. The $\Delta O.D.$ of the sample was calculated by measuring the

transmitted light using a Si Photodiode and a homemade amplification system coupled to both an oscilloscope (Textronix TDS 220) and data acquisition card (National Instruments NI-6221). The oscilloscope data were for the study at the microseconds time scale while the DAQ card covered milliseconds to seconds. The data was averaged over 200 laser shots per wavelength to improve the ratio of the signal to noise.

3.10 Diffuse reflectance infrared Fourier transform spectroscopy (DRIFTS)

Diffuse reflectance infrared fourier transform spectroscopy (DRIFTS) is a useful tool to analyse the adsorbates on the surface of catalysts, such as the interaction of reactant molecules, formation of reaction intermediates and products. It can provide rich information of powder and solid samples under near or even real reaction conditions through collection of the diffuse scattering light after IR irradiation.

In this thesis, in situ DRIFTS was carried out using a Thermo Fisher Nicolet IS50 II FTIR spectrometer at the range of 4000 to 650 cm^{-1} . 1 mg powder catalyst sample was spread at the bottom of the Harrick IR cell and the chamber was sealed with two ZnSe windows. The system was degassed for 0.5 hour under Ar atmosphere to remove the adsorbates. Each spectrum was recorded by averaging 64 scans at a resolution of 2 cm^{-1} and the final spectrum was obtained by subtraction of background. Before CH_4 introduction, the samples were measured again to obtain the 0 min spectrum. Subsequently, 50 mL/min CH_4 gas (99.999%) was introduced to the chamber and the spectrum was collected under the CH_4 atmosphere at 5, 10, 15, 20, 25, and 30 min. After 30 min of CH_4 adsorption process, the sample was irradiated by a 300 W Xenon

lamp (PLS-SXE300, Perfect light) with a 380 nm filter. The spectrum was collected at 5, 10, 15, 20, 25, and 30 min.

3.11 Photo-electrochemical test

The electrochemical oxygen reduction reactions were conducted on a Metrohm Autolab potentiostat with a three-electrode system. A photocatalyst loaded glassy carbon rotating disk (RDE, 3 mm diameter) was used as a working electrode, a glassy carbon rod worked as a counter electrode and Hg/HgO (1 M NaOH) was used as a reference electrode in O₂ saturated 0.1 M of KOH electrolyte, respectively. For the preparation of the working electrode, 4 mg of photocatalysts powder was added into 1 mL of suspension containing 700 μ L of deionised water, 264 μ L of ethanol, and 36 μ L of nafion solution (Sigma-Aldrich, Nafion® 117 solution, 5 w/w). After sonication for 30 minutes, a homogenous ink was obtained and 5 μ L of the ink was deposited onto the glassy carbon RDE, followed by rotating drying for 1 hour under room temperature. Linear sweep voltammograms (LSV) were carried out at a rotation rate of 1600 rpm and a scan rate of 10 mV s⁻¹ in the voltage range of 0.2 – 1.1 V vs. RHE.

The photocurrent investigation was carried out on Gamry Instrument Interface 5000E potentiostat under chopped illumination. The electrode was prepared by dispersion of viscous pastes of pristine TiO₂ or modified TiO₂ onto fluorine-doped tin oxide (FTO). Two methods have been developed for the preparation of the working electrode. The first method was using 10 μ L of the ink prepared with the same recipe as that used in the oxygen reduction reaction was spin-coated on a 0.5 x 1 cm FTO glass with an exposure area of 0.5 x 0.5 cm at 500 rpm for 0.5 minutes followed by 1000 rpm for 4 minutes. The process was repeated 3 times and dried at 80°C for 120 minutes. The

second method was to mix 30 mg TiO₂ or modified TiO₂, 60 mg of ethylcellulose, 6 drops of terpineol and 1 ml ethanol together and grounded them for 10 minutes to prepare pastes. The coating process was kept at 70 °C to improve their adhesion. The total exposed area of the film was 1.0 cm². Then, the photocatalyst coated FTO electrode was installed as a working electrode, the Pt plate worked as the counter electrode and Ag/AgCl was used as the reference electrode in the 0.1 M Na₂SO₄ electrolyte. The applied potential was set as 0.2 V vs. Ag/AgCl and a 450 W Xe lamp or 150 W Xenon lamp equipped with an AM 1.5 G filter was used as the light source. The light illumination was chopped at a regular time interval (e.g., 20 s) during the whole measuring period.

3.12 Photocatalytic activity tests

The photocatalytic activity of the as-synthesized samples toward methane conversion was investigated in a flow reactor connected with a gas chromatography (GC), as shown in Figure 3-2. Typically, a certain amount of photocatalyst was weighed and dispersed in de-ionised water. The suspension was allowed to be sonicated for at least 15 minutes to make sure the good dispersion of the powders. Then, the suspension was filtered with a glass fibre membrane (diameter 37 mm, pore size 0.22 µm) to produce a uniform film, which was dried at 60 °C for 12 hours. After drying the film, it was fixed in the reactor using a stainless ring and sealed with a rubber O-ring. A temperature probe was inserted from the bottom of the reactor to monitor the temperature of the reaction. The flow rate and ratio of different gases (air, methane, argon, BOC 99.999%) were adjusted by three mass flow controllers (MFC, Bronkhorst). The film was then irradiated by a 100 W 365 nm LED (Beijing Perfect

Light, PLS-LED 100). For each experiment, the system was allowed to purge with gases at an expected ratio for at least one hour to reach the equilibrium of adsorption-desorption before testing. The outlet gases were detected by an Agilent 7820 GC equipped with an online injection valve at regular time intervals (30 minutes). In this GC, two columns (CarbonPlot and Molecular 5A) are connected with thermal conductivity detectors (TCD) to analyze H₂, O₂, N₂, and CH₄, respectively. Another column (HP-PLOT Q) is linked with flame ionization detectors (FID) to analyze organic products, such as C₂H₄, C₂H₆, CH₃OH, and C₂H₅OH. To quantify the low concentration of CO₂ or CO, the reactor outlet was also linked to another GC (Varian 450) equipped with the flame ionization detector coupled with a methaniser.

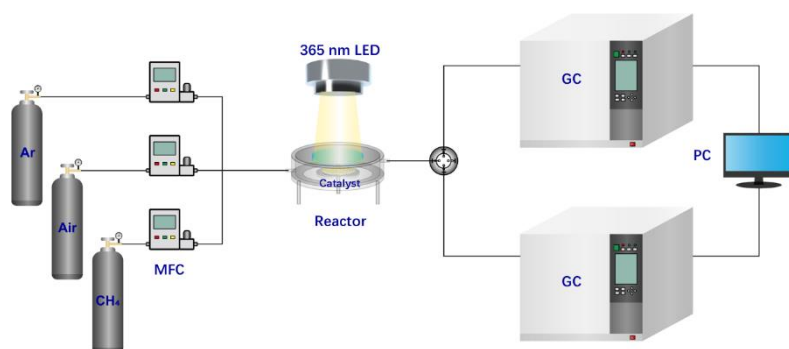


Figure 3-2 The schematic illustration of the photocatalytic OCM flow system

4 Modification of TiO₂ with Pt nanoparticles and CuO_x clusters for efficient photocatalytic conversion of methane

4.1 Introduction

With the increasing discovery of shale gas and methane hydrate, research on the direct utilization of its major component (methane) for valuable chemicals and fuels is vigorous and thriving, while very challenging.^{2,12} Oxidative coupling of methane (OCM) has been considered to be one of the most vital processes to convert methane to C₂ (C₂H₆ and C₂H₄) products. The yield of C₂ products is still far away from the techno-economic target for commercialization due to the over-oxidation and harsh reaction conditions.¹³⁰ Photocatalysis with its adjustable redox potential, spatial separation of redox reaction sites and operation under very mild conditions provides a very promising pathway to achieve high selectivity to C₂ products with very moderate energy input.¹³¹ However, the efficiency in photocatalysis has been limited by several factors: (1) the high recombination rate of photoinduced carriers in the intrinsic semiconductor greatly limits their quantum efficiency, thus resulting in low conversion; (2) the pristine photocatalysts with an unmodified interface lead to poor selectivity because of overoxidation by the extremely oxidative photoholes in the valence band (VB) of the photocatalyst and the lack of active centers; (3) the majority of photocatalytic methane conversion reactions were carried out in batch reactors and it is theoretically hard to avoid overoxidation as the long residence time in the batch reactor favours the thermodynamically stable product CO₂.

Footnote: Part of the content in this chapter has been published, *Angew. Chem. Int. Ed.*, 2020, 59, 1-7

Herein, after screening a series of semiconductors, TiO₂ as one of the most robust and classic semiconductors was selected as the main photocatalyst base. Then, considering the relatively more negative valence band of either CuO/Cu₂O than TiO₂ and also the role of Cu clusters in specific supportors (e.g., zeolites) as an active centre for C-H bond activation in methane,^{76,132–134} CuO_x clusters were introduced on TiO₂ to work as the active site for methane activation and manipulation of products selectivity. Moreover, Pt nanoparticles, as the most efficient electrons acceptors in photocatalysis to facilitate the separation of photo-induced e⁻/h⁺, were further incorporated to enhance the conversion rate.^{27,135} The optimised sample Cu_{0.1}Pt_{0.5}/TiO₂ shows the highest yield of C₂ product of 6.8 μmol h⁻¹ at a space velocity of 24000 ml g⁻¹ h⁻¹, more than twice the sum of the activity of Pt/TiO₂ (1.07 μmol h⁻¹) and Cu/TiO₂ (1.9 μmol h⁻¹), it was also the highest among photocatalytic methane conversion under atmospheric pressure when it was published. High C₂ selectivity of 60% is also comparable to that attained by conventional high-temperature (>943 K) thermal catalysis.

4.2 Experimental section

4.2.1 Fabrication of photocatalysts

Synthesis of Cu_x/PC-50: Cu was introduced by a wet impregnation method. In a typical experiment, different concentration of different concentrations of Cu(NO₃)₂·2.5H₂O (98%, Alfa Aesar) dissolved in 150 μL deionized (DI) water was added to 200 mg of TiO₂ (Millennium PC-50) under vigorous stirring in an alumina crucible. After drying at 70 °C for 3 h, the crucible was equipped with a lid and transferred to a muffle furnace (Carbolite, CWF 1300). The mixture was calcined at 400 °C for 4 h with a heating rate of 5 °C/min. The samples synthesized by this

impregnation method were denoted as $\text{Cu}_x/\text{PC-50}$ ($x = 0.05, 0.1, 0.2, 0.3, 0.4$ wt.%, corresponding to the loading weight percentage of Cu at TiO_2).

Synthesis of $\text{Pt}_{0.5}/\text{PC-50}$: Pt was introduced by a photodeposition method. Typically, 250 mg TiO_2 was dispersed into a solution of 27 mL DI water and 3 mL methanol. Then, 0.5 wt.% (the weight percentage of Pt to TiO_2) of H_2PtCl_6 (99.995%, Sigma-Aldrich) was added to the above solution and allowed to be bubbled with argon (99.999%, BOC) for 20 minutes. Afterwards, the suspension was stirred under irradiation with a Multichannel 365 nm LED (Perfect Light, Beijing) at 25 °C for 3h. The samples were collected by centrifugation, washed with DI water three times and dried at 70 °C for 6 h.

Synthesis of $\text{Cu}_{0.1}\text{Pt}_y/\text{PC-50}$: Pt was introduced by photodeposition method and then Cu was incorporated by wet impregnation method. Typically, 250 mg TiO_2 was dispersed into a solution of 27 mL DI water and 3 mL methanol. Then, a different amount (0.1~2.0 wt. %, the weight percentage of Pt to TiO_2) of H_2PtCl_6 was added to the above solution and allowed to be bubbled with argon for 20 minutes. Afterwards, the suspension was stirred under irradiation with a Multichannel 365 nm LED at 25 °C for 3h. The samples were collected by centrifugation, washed with DI water three times and dried at 70 °C for 6 h. The samples obtained here were denoted as $\text{Pt}_y/\text{PC-50-unheating}$ ($y = 0.1, 0.5, 1.0, 1.5, 2.0$). The following deposition of Cu was similar to the procedure mentioned in the preparation of $\text{Cu}_x/\text{PC-50}$, except for the change of precursor from PC-50 to $\text{Pt}_y/\text{PC-50}$ ($y = 0.1, 0.5, 1.0, 1.5, 2.0$).

Synthesis of Pt_{0.5}Cu_{0.1}/PC-50: The synthesis of Pt_{0.5}Cu_{0.1}/PC-50 was similar to the synthesis of Cu_{0.1}Pt_{0.5}/PC-50 but the adding order of Pt and Cu was reversed.

Heating treatment: In order to maintain the consistent experimental condition, Pt_{0.5}/PC-50-unheating and TiO₂ were also heated at a muffle furnace with the program used in the preparation of Cu_x/PC-50. They were denoted as Pt_{0.5}/PC-50 and PC-50, respectively in the following section without special note.

Synthesis of g-C₃N₄: 5 g of Urea was added to a 25 mL crucible and Aluminum foil was used to cover the crucible with the cap. Then the crucible was transferred to a muffle furnace (Carbolite, CWF 1300). The mixture was calcinated at 570 °C for 4 h with a heating rate of 5 °C/min.

Synthesis of BiVO₄: BiVO₄ was synthesized by a method similar to previous report.¹³⁶ Equal mole amount of Bi₂O₃ and V₂O₅ were added in 0.5 M HNO₃ aqueous solution. The mixture was stirred at room temperature for 96 hours. Then, the precipitate was collected by centrifugation, washed with DI water for three times and dried at 60°C. Afterwards, the sample was calcinated at 500 °C for 3 hours with a heating rate of 10 °C/min in a muffle furnace.

Synthesis of ZnCdS: ZnCdS was synthesized by a reported method with a few modifications.¹³⁷ Typically, 0.5 mmol of Cd(CH₃COO)₂ and 0.5 mmol of Zn(CH₃COO)₂ were dissolved in 150 mL DI water under stirring. Then, 4 mmol of thiourea was added to the above mixture. The solution was maintained at 95 °C under stirring for 12 hours. Afterwards, the sample was collected by centrifugation, washed with DI water for three times and dried at 60 °C.

Commercial In₂O₃ (99.99%, Sigma-Aldrich), MoS₂ (98%, Alfa Aesar), WO₃ (99%, Sigma-Aldrich), CdS (98%, Alfa Aesar) and GaN (99.99%, Alfa Aesar) were used in the preliminary investigations without further treatments.

4.2.2 Characterisation

The powder X-ray diffraction (XRD) patterns were measured in a Stoe STADI-P instrument (2° to 40°, step 0.5 ° at 5.0 s/step) using Mo K α 1 (wavelength 0.70930 Å, 50 kV and 30 mA). Ultraviolet-visible diffuse reflectance spectroscopy (UV-Vis DRS) measurements were conducted by an Agilent Carry 3500 UV-Vis-NIR spectrophotometer with a diffuse reflectance unit. Raman spectroscopy was conducted at Renishaw InVia Raman with a 514 nm excitation laser, ranging from 100 – 1200 cm⁻¹. X-ray photoelectron spectroscopy (XPS) measurements were performed using a ThermoScientific XPS K-alpha and the obtained results were analyzed by Casa XPS software. A JEOL JSM-7401F SEM equipped with Energy Dispersive-X-Ray (EDX) was applied to analyze the micro-morphology and composition information of the materials on carbon tips. The transmission electron microscopy (TEM) images and high-resolution transmission electron microscopy (HRTEM) images were obtained using a JEOL 2010 instrument. Photoluminescence (PL) spectra were collected by Renishaw InVia Raman with a 325 nm excitation laser ranging from 200 – 800 nm. Electron paramagnetic resonance (EPR) was measured by a MS-5000 spectrometer at ambient temperature (288 K). Powder samples (~30 mg) were weighed in quartz tubes and sealed with septa. Microwave power was set at 100 microwatts, while the frequency was 9.485 GHz. A 365 nm LED (80 mW cm⁻²) was applied for the experiment under irradiation.

4.2.3 Photocatalytic activity test

The photocatalytic activity measurement of methane oxidation was carried out using the set-up described in **Section 3.9**.

4.2.4 Calculation of selectivity

The main products were C₂H₆, C₂H₄, CO₂ and a trace amount of other products. Thus, the selectivity of C₂ products were calculated as below:

$$C_2 \text{ selectivity} = \frac{2 \times (n_{C_2H_6} + n_{C_2H_4})}{2 \times n_{C_2H_6} + 2 \times n_{C_2H_4} + n_{CO_2}} \times 100\%$$

in which n is the molar rate of different products.

4.2.5 Calculation of apparent quantum efficiency (AQE) based on the conversion of methane

$$AQE = \frac{(2 \times n_{C_2H_6} + 4 \times n_{C_2H_4} + 8 \times n_{CO_2}) \times N_A}{\text{Number of incident photons}} \times 100\%,$$

in which n is the molar generation rate of different products, N_A is the Avogadro constant, and the irradiation area was approximately 10 cm². The light intensity was 160 mw/cm².

4.3 Results and discussion

4.3.1 Preliminary investigations

A series of semiconductors was first investigated to explore their potential for photocatalytic OCM reaction, as shown in Figure 4-1. Among them, only PC-50 (TiO_2) exhibits a yield rate ($0.6 \mu\text{mol h}^{-1}$) of C_2 products ($\text{C}_2\text{H}_6/\text{C}_2\text{H}_4$). Although some semiconductors e.g., BiVO_4 , and WO_3 , also have a deep valence band with enough oxidative potential to abstract the C-H bond in methane molecule, this result indicates that the half-reaction reduction to activate oxygen to remove the as-formed protons is equally important. Therefore, PC-50 as a commercial anatase TiO_2 was selected as the main photocatalyst for subsequent investigation.

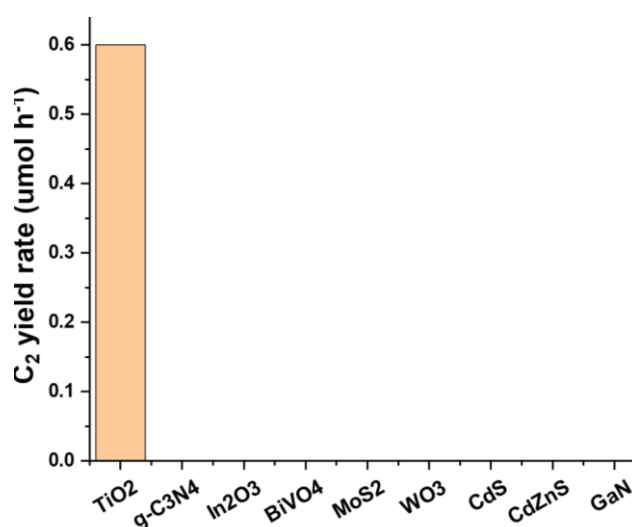


Figure 4-1 Photocatalytic OCM process over different photocatalysts (Reaction conditions: $\text{O}_2:\text{CH}_4 = 1: 180$, 5% of CH_4 , GHSV = $12000 \text{ mL g}^{-1} \text{ h}^{-1}$, 365 nm LED, r.t.)

4.3.2 Photocatalytic OCM over $\text{Pt}_x\text{Cu}_y/\text{PC-50}$

The photocatalytic activities of the as-prepared samples for OCM were evaluated in a flow system at room temperature and under atmospheric pressure. It has been widely reported that the photo-induced holes at the VB of TiO_2 tended to promote the mineralization of CH_4 into CO_2 through deep dehydrogenation.⁴⁴ The VB of CuO and Cu_2O were around 0.75 eV and 0.99 eV more negative (vs. NHE) compared with TiO_2 , respectively.¹³⁴ It indicates a selectivity to C_2 products rather than CO_2 after the introduction of copper species because copper species were expected to accept the photo-induced holes from TiO_2 and dramatically lower their oxidation potential. Furthermore, Cu^{II} clusters as active sites have been observed to selectively oxidise methane in thermocatalysis,^{76,138} as mentioned in the previous section. The optimisation of copper amount was first undertaken, as shown in Figure 4-2.

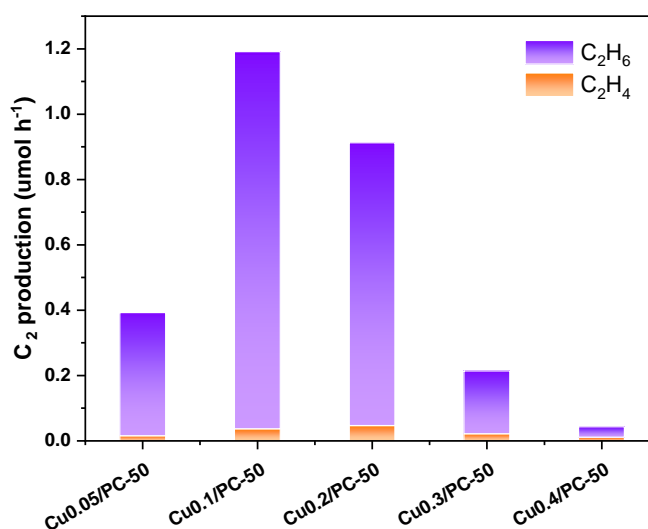


Figure 4-2 C_2 production of photocatalytic OCM over $\text{Cu}_x/\text{PC-50}$ ($x = 0.05, 0.1, 0.2, 0.3, 0.4$). (Reaction condition: $\text{O}_2 : \text{CH}_4 = 1 : 240$, $\text{GHSV} = 12000 \text{ mL g}^{-1} \text{ h}^{-1}$, 10% of CH_4 , 365 nm LED 20 W, 40°C)

It shows a volcanic trend with an increasing weight percentage of Cu and the highest C_2 production rate is achieved over $Cu_{0.1}/PC-50$ ($1.2 \mu\text{mol h}^{-1}$). An excessive amount of Cu species may act as a recombination centre of photo-induced electrons and holes,¹³⁹ leading to the decrease in C_2 yield rate. After optimisation of the Cu amount, Pt was added as a widely known electron acceptor to facilitate the charge separation and conversion rate.²⁷ In order to test the photocatalytic efficiency under a relatively harsh condition, the space velocity was increased from $12000 \text{ mL g}^{-1} \text{ h}^{-1}$ to $24000 \text{ mL g}^{-1} \text{ h}^{-1}$. Then, the samples with bimetallic co-catalysts were investigated, as shown in Figure 4-3. The conversion of methane increases compared with the pristine PC-50 while the yield of both C_2 products and CO_2 increases after the co-deposition of Pt and Cu species.

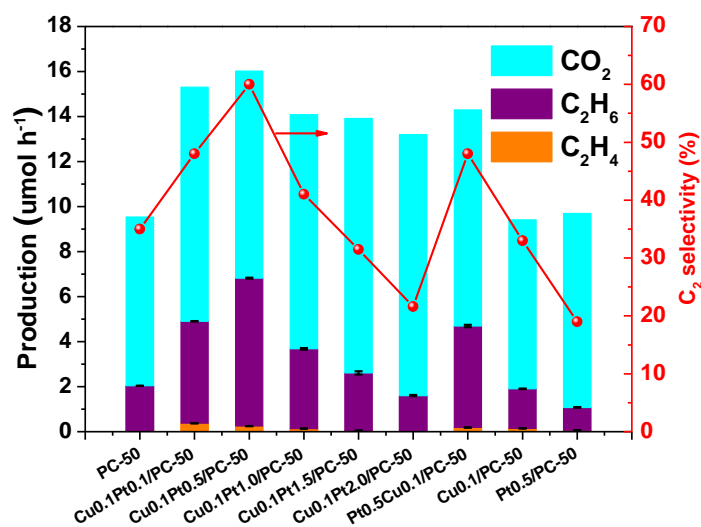


Figure 4-3 Methane conversion and C_2 selectivity of photocatalytic OCM over $Cu_{0.1}Pt_y/PC-50$ ($y = 0.1, 0.5, 1.0, 1.5, 2.0$ wt%), $Cu_{0.1}/PC-50$, PC-50, $Pt_{0.5}/PC-50$ and $Pt_{0.5}Cu_{0.1}/PC-50$ (Reaction condition: $O_2 : CH_4 = 1 : 400$, GHSV = $24000 \text{ mL g}^{-1} \text{ h}^{-1}$, 10% of CH_4 , 365 nm LED 40 W, 40°C . The error bar for the production rate of C_2 products were obtained by three activity tests.)

This is probably attributed to more separated photo-induced carriers available through the efficient transfer of electrons and holes to Pt and Cu species, respectively. It should be noted that the selectivity to C_2 products firstly increases compared with selectivity

to CO₂ with the increasing amount of Pt in the Pt and Cu co-loaded samples. However, over-increasing Pt causes a reduction of both yield and selectivity to C₂ products. The yield of C₂ products on the optimised sample Cu_{0.1}Pt_{0.5}/PC-50 is 6.8 μmol h⁻¹, more than 2 times higher than the sum of Pt_{0.5}/PC-50 (1.07 μmol h⁻¹) and Cu_{0.1}/PC-50 (1.9 μmol h⁻¹), indicating the synergistic effect between Pt and Cu species. More importantly, the yield of CO₂ only increases by around 20% compared with pristine PC-50, suggesting the indispensable role of Cu species in the manipulation of C₂ selectivity. Remarkably, this yield is about four times higher than the reported production rate of C₂H₆ and C₂H₄ by photocatalytic methane conversion with irradiation of > 300 nm over different catalysts under atmospheric pressure and room temperature, as shown in Table 4-1. Given that some reactions in Table 4-1 were NOCM reactions, their yields were relatively low due to the high thermodynamic barriers.¹⁴⁰ Furthermore, the optimised sample shows a C₂ selectivity as high as 60%, nearly two

Table 4-1 Representative works on photocatalytic methane conversion to ethane/ethene at room temperature and atmospheric pressure

Samples	Reaction type	Reactor type	Conditions	The yield rate of C ₂ H ₄ and C ₂ H ₆
Cu _{0.1} Pt _{0.5} /PC-50 (This work)	OCM	Flow reactor	Room temperature; 40 W 365 nm LED; 0.1 g catalyst; O ₂ : CH ₄ = 1 : 400, GHSV = 24000 g ⁻¹ h ⁻¹ , 10% of CH ₄ ;	6.8 μmol h ⁻¹
ZrO ₂ /SiO ₂ (0.1) ⁷¹	NOCM	Batch reactor	310 K; Reaction time 3 h; 0.5 g catalyst; 200 μmol CH ₄	0.0365 μmol h ⁻¹

MgO ¹⁴¹	Methane oxidation	Batch reactor	293 K; High-pressure mercury lamp; Reaction time 3 h; 399.9 Pa N ₂ O; 4.2 μmol CH ₄	0.00268 μmol h ⁻¹
MgO/SiO ₂ (2.0) ¹⁴²	NOCM	Batch reactor	310 K; 300 W Xe lamp; Reaction time 3 h; 0.2 g catalyst; 200 μmol CH ₄	0.0092 μmol h ⁻¹
Au/ZnO nanosheets ¹⁷	NOCM	Batch reactor	Ambient temperature; 300 W Xe lamp; Reaction time 4 h; 0.001 g catalyst; 22.3 μmol CH ₄	0.0113 μmol h ⁻¹
0.5%Pt/TiO ₂ ⁴⁴	Methane oxidation	Batch reactor	298 K; Philips UV lamps (TUV 4W/G4 T5); Reaction time 6 h; 0.075 g catalyst; 80 mL CH ₄	2.08 μmol h ⁻¹
Ga ₂ O ₃ -K ⁶⁹	NOCM	Batch reactor	Room temperature; 300 W Xe lamp; Reaction time 3 h; 0.2 g catalyst; 200 μmol CH ₄	0.054 μmol h ⁻¹
SiO ₂ -Al ₂ O ₃ -TiO ₂ ¹⁴³	NOCM	Batch reactor	Room temperature; 250 W Xe lamp; Reaction time 3 h; 1.0 g catalyst; 200 μmol CH ₄	0.74 μmol h ⁻¹
(Zn ⁺ , Zn ²⁺)-ZSM-5 ⁷²	NOCM	Batch reactor	303 K; 150 W high-pressure Hg lamp; Reaction time 8 h; 1.0 g catalyst; 200 μmol CH ₄	2.988 μmol h ⁻¹
Pt/Ga-TiO ₂ -SiO ₂ ¹⁸	NOCM	Batch reactor	333 K; 300 W Xe lamp; Reaction time 4 h; 0.2 g catalyst; 44.6 μmol CH ₄	0.314 μmol h ⁻¹
Ce(0.5)/Al ₂ O ₃ ⁷⁰	NOCM	Batch reactor	310 K; 300 W Xe lamp; Reaction time 3 h; 0.2 g catalyst; 200 μmol CH ₄	0.1178 μmol h ⁻¹
FSM-16 ²⁹	NOCM	Batch reactor	310 K; 300 W Xe lamp; Reaction time 3 h; 0.2 g catalyst; 200 μmol CH ₄	0.018 μmol h ⁻¹

Ga-ETS-10-0.2 ¹⁴⁴	NOCM	Batch reactor	303 K; 150 W high-pressure Hg lamp; Reaction time 5 h; 0.2 g catalyst; 200 $\mu\text{mol CH}_4$	2.3 $\mu\text{mol h}^{-1}$
1.5%Pd/TiO ₂ ⁴³	Methane oxidation	Batch reactor	298 K; Philips UV lamps (254 nm, TUV 4W/G4 T5); Reaction time 6 h; 0.075 g catalyst; 80 mL CH ₄	2.13 $\mu\text{mol h}^{-1}$

times than the pristine PC-50, which is also comparable to the traditional catalysts (e.g., Li/MgO) operated at $>943\text{ K}$.^{130,145} The apparent quantum efficiency (AQE) based on the methane conversion of Cu_{0.1}Pt_{0.5}/PC-50 and PC-50 was calculated. The AQE of Cu_{0.1}Pt_{0.5}/PC-50 (0.5% at 365 nm) is nearly two times higher than that of PC-50 (0.25% at 365 nm), indicating the higher utilisation of light energy. The further addition of Pt led to decreased C₂ selectivity and increased CO₂ yield with the highest CO₂ yield reaching 11.6 $\mu\text{mol h}^{-1}$. Too many Pt nanoparticles might lead to the excessive formation of O₂⁻, which is the major component of overoxidation.¹⁴⁶ Accordingly, Pt_{0.5}/PC-50 only exhibits an increased yield of CO₂ while the lowest yield of C₂ products compared with PC-50. This results in the highest selectivity to CO₂ (ca. 80%) again due to the increasing photo-induced electrons available for O₂⁻ generation and strong oxidative holes at the VB of TiO₂. The preparation order of two co-catalysts was changed to observe its effect. Another photocatalyst Pt_{0.5}Cu_{0.1}/PC-50 was thus prepared. Interestingly, it exhibits a decreased C₂ yield (4.7 $\mu\text{mol h}^{-1}$) compared with Cu_{0.1}Pt_{0.5}/PC-50, indicating that the deposition sequence of co-catalysts also has an important influence on the performance. The function of Pt is considered to accept photo-induced electrons and help charge separation. If the Cu species were firstly deposited, some of them would block the contact between Pt particles and TiO₂, leading to reduced charge separation efficiency, thus lowering the

conversion and yield. It is noted that the yield of C₂ products over Cu_{0.1}/PC-50 is lower than that of PC-50, while the yield of CO₂ is similar. This is because of some recombination of photo-induced electrons and holes in Cu species, which will be discussed in detail in section 4.3.4. This could lead to the decreased generation of methyl radicals, which would have a more negative effect on the coupling to C₂ species than deep oxidation to CO₂ because of the second-order nature of the coupling reaction to C₂ products.¹⁴⁷ While some remaining highly oxidative holes with the O₂⁻ formed by the remaining electrons continue to proceed with the overoxidation of methane to CO₂. Thus, the yield of CO₂ exhibits nearly no change while the yield of C₂ products decreases after the single introduction of Cu species, emphasising the important role of Pt nanoparticles in the synergistic effect. Please note in the current system, only ethane, ethylene and CO₂ as products could be detected by the GC. Thus, the C₂ selectivity mentioned above was calculated based on the measured products. No products could be detected when the reaction was carried out in the absence of methane or without light irradiation, as shown in Table 4-2. This confirm that it is a photocatalytic process with CH₄ as the only carbon source.

Table 4-2 Control experimental results of the photocatalytic OCM over Cu_{0.1}Pt_{0.5}/PC-50

Order	CH ₄	LED	Products
1	×	√	×
2	√	×	×

The stability of the optimised sample $\text{Cu}_{0.1}\text{Pt}_{0.5}/\text{PC-50}$ was then tested. No decay of C_2 yield except slight fluctuation can be observed during 8 h reaction, as shown in Figure 4-4.

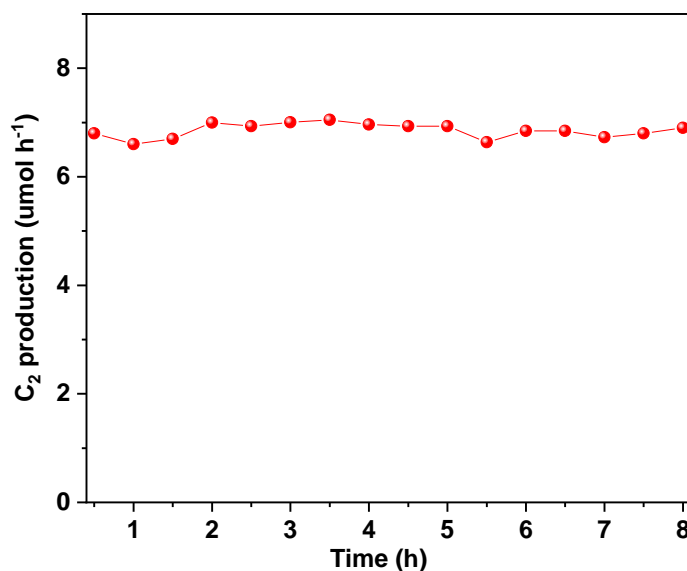


Figure 4-4 Stability test of photocatalytic OCM over $\text{Cu}_{0.1}\text{Pt}_{0.5}/\text{PC-50}$ (Reaction condition: Reaction condition: $\text{O}_2 : \text{CH}_4 = 1 : 400$, $\text{GHSV} = 24000 \text{ mL g}^{-1} \text{ h}^{-1}$, 10% of CH_4 , 365 nm LED 40 W, 40 °C)

4.3.3 Characterisation of the optimised sample $\text{Cu}_{0.1}\text{Pt}_{0.5}/\text{PC-50}$

To gain an insight into the structure and photocatalytic properties of $\text{Cu}_y\text{Pt}_x/\text{PC-50}$, a series of characterisations was conducted. The crystal structures of as-prepared samples were firstly investigated by PXRD, as shown in Figure 4-5. All peaks can be indexed to the standard card of anatase TiO_2 (JCPDS no. 84-1286). After the introduction of copper and platinum, the XRD spectra remained unchanged indicating a stable framework of PC-50. Additionally, the spectra displayed no extra peaks for

copper or platinum species, most likely because of their low amount and/or high dispersion.¹⁴⁸

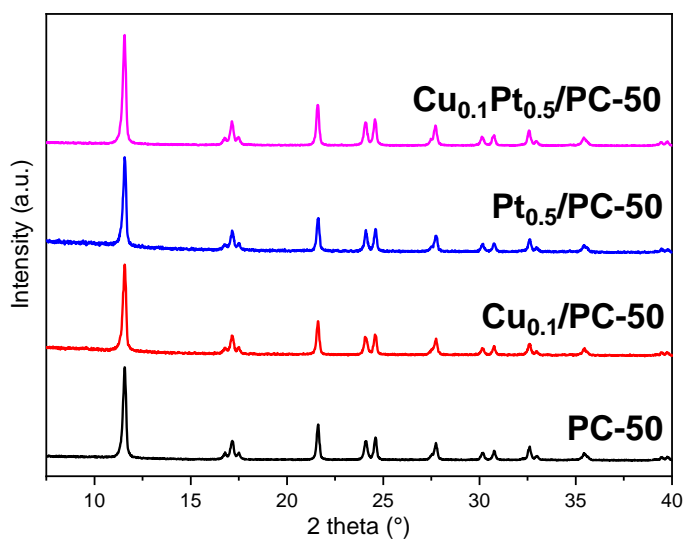


Figure 4-5 PXRD patterns of $\text{Cu}_{0.1}\text{Pt}_{0.5}/\text{PC-50}$, $\text{Pt}_{0.5}/\text{PC-50}$, $\text{Cu}_{0.1}/\text{PC-50}$ and PC-50

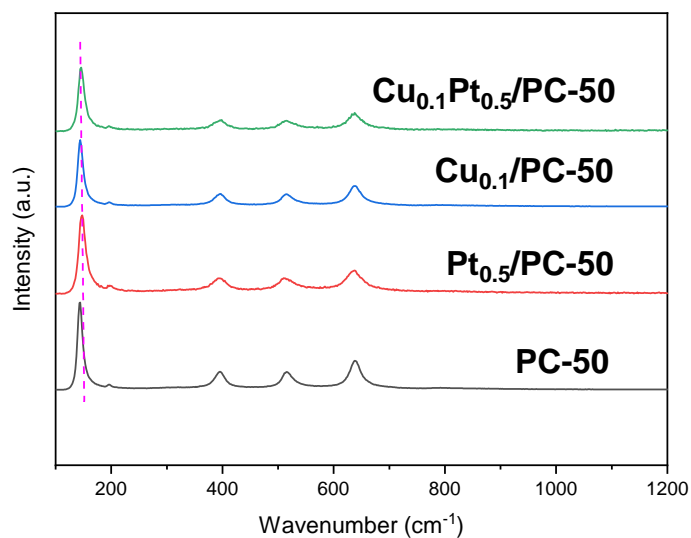


Figure 4-6 Raman spectra of $\text{Cu}_{0.1}\text{Pt}_{0.5}/\text{PC-50}$, $\text{Pt}_{0.5}/\text{PC-50}$, $\text{Cu}_{0.1}/\text{PC-50}$ and PC-50 . The anatase structure was further supported by Raman spectroscopy, as shown in Figure 4-6. The typical Raman peaks for anatase TiO_2 could be clearly observed at 144 cm^{-1} (E_g), 198 cm^{-1} (E_g), 399 cm^{-1} (B_{1g}), 512 cm^{-1} (A_{1g}) and 639 cm^{-1} (E_g), respectively.¹⁴⁹ Notably, a slight blue shift and broadening of the 144 cm^{-1} Raman peak could be observed after the introduction of co-catalysts, in particular

$\text{Cu}_{0.1}\text{Pt}_{0.5}/\text{PC-50}$ and $\text{Cu}_{0.1}/\text{PC-50}$. This could be explained as the surface strain after surface modification.¹⁵⁰ To further investigate the distribution, particle size and composition of $\text{Cu}_{0.1}\text{Pt}_{0.5}/\text{PC-50}$, EDS mapping and HRTEM were provided in Figure 4-7 and Figure 4-8.

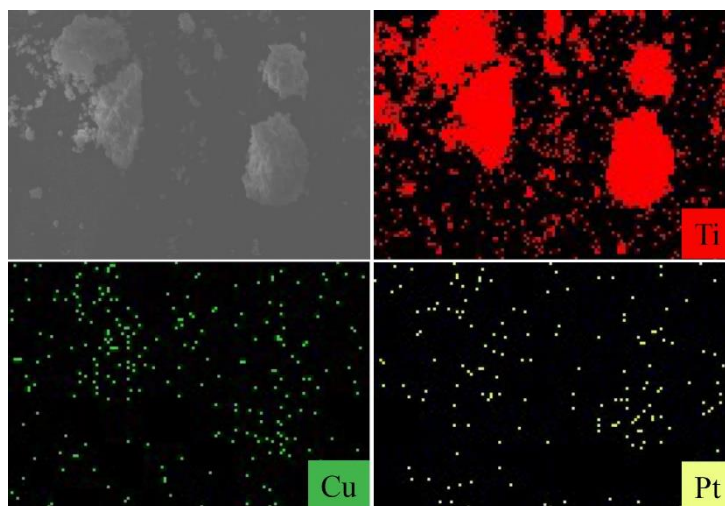


Figure 4-7 EDS element mappings (Ti, Cu and Pt) of $\text{Cu}_{0.1}\text{Pt}_{0.5}/\text{PC-50}$

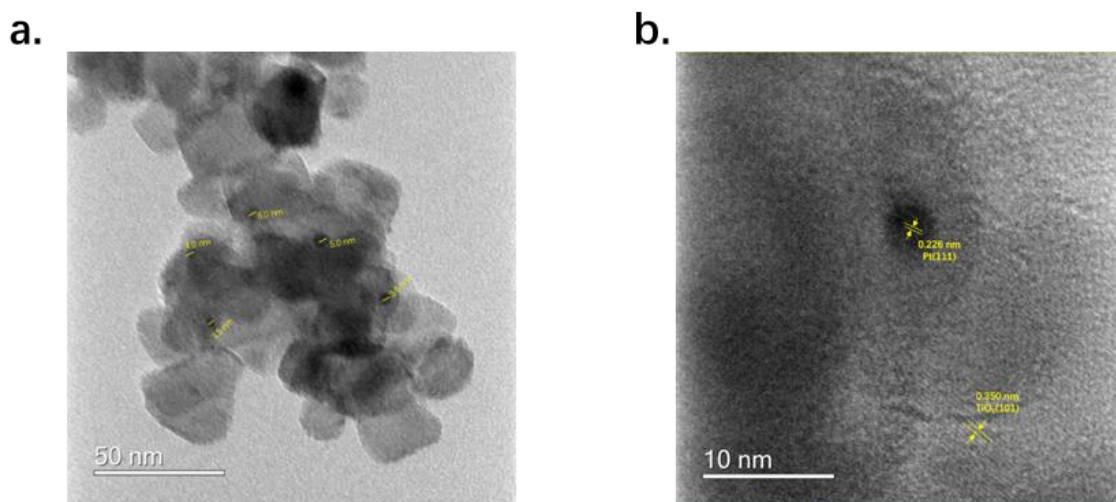


Figure 4-8 TEM (a) and HR-TEM(b) images of $\text{Cu}_{0.1}\text{Pt}_{0.5}/\text{PC-50}$

The EDS mapping shows that Cu and Pt dispersed homogeneously on the support of TiO_2 , in good agreement with the XRD results. As shown in Figure 4-8a, some nanoparticles were dispersed on PC-50 with diameters from 3.5 to 6 nm. These nanoparticles were further identified by HRTEM (Figure 4-8b), in which the d spacing

of lattice fringes could be attributed to Pt (111, 0.226 nm) and anatase TiO₂ (101, 0.350 nm).¹⁵¹ The particles of copper species have not been observed at this resolution, suggesting the existence of smaller clusters.

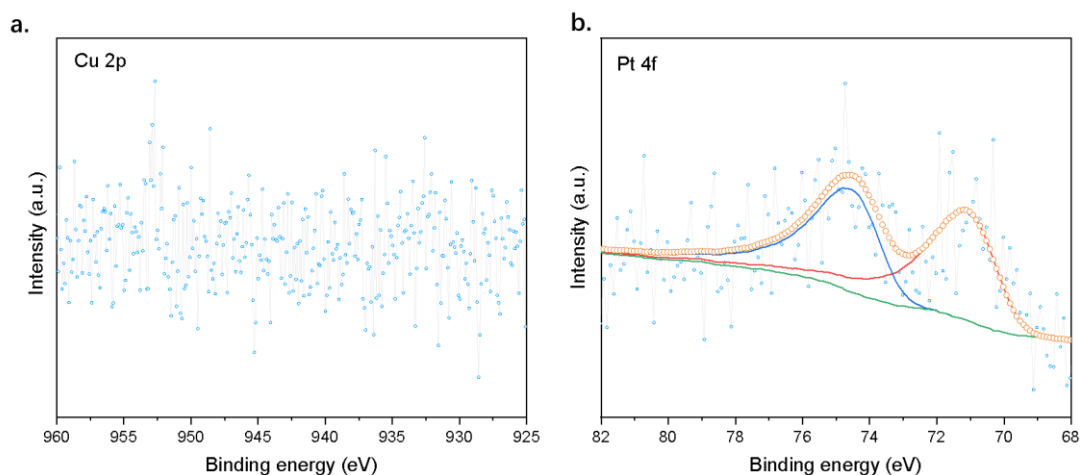


Figure 4-9 Cu 2p (a) and Pt 4f (b) XPS spectra of Cu_{0.1}Pt_{0.5}/PC-50.

The chemical states of co-catalysts on the optimum catalyst (Cu_{0.1}Pt_{0.5}/PC-50) were then analysed by XPS, as shown in Figure 4-9. Due to the low loading amount of copper species, no clear Cu 2p peak was observed on Cu_{0.1}Pt_{0.5}/PC-50. While two peaks at 71.2 and 74.6 eV could be assigned to the metallic states of Pt were identified.¹⁵² Although a clear Cu 2p peak could not be seen with 0.1 wt% loadings, the influence of Cu species in the composites could be noted from Ti 2p spectra, as shown in Figure 4-10. Compared with PC-50 and Pt_{0.5}/PC-50, the binding energy of Ti 2p_{3/2} transition shifted to lower binding energy over Cu_{0.1}/PC-50 and Cu_{0.1}Pt_{0.5}/PC-50. The lower binding energy suggested the electrons probably transferred from Cu to Ti, thus indicating the interaction between the co-catalysts and PC-50.¹⁵³ In order to identify the chemical states of Cu on PC-50, a sample (Cu_{2.0}/PC-50) prepared by the same procedure but with a large loading amount of copper species was used, as shown

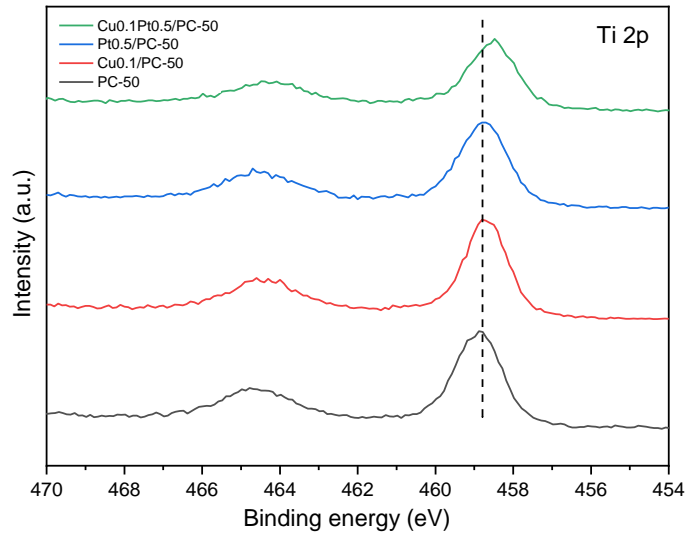


Figure 4-10 Ti 2p XPS spectra of $\text{Cu}_{0.1}\text{Pt}_{0.5}/\text{PC-50}$, $\text{Pt}_{0.5}/\text{PC-50}$, $\text{Cu}_{0.1}/\text{PC-50}$ and PC-50

in Figure 4-11. The peaks attributed to $\text{Cu } 2p_{3/2}$ and $\text{Cu } 2p_{1/2}$ at around 933.4 and 953.9 eV, coupling with the shake-up satellite peak at around 942.6 eV, indicated the main existence of fully oxidized Cu^{II} species.¹⁵⁴ In addition, a small amount of Cu^{I} ($\text{Cu}^{\text{II}}/\text{Cu}^{\text{I}}=5:1$) could be found with peaks at 932.2 and 952 eV, respectively. It is believed that similar species were formed on the best sample, $\text{Cu}_{0.1}\text{Pt}_{0.5}/\text{PC-50}$.

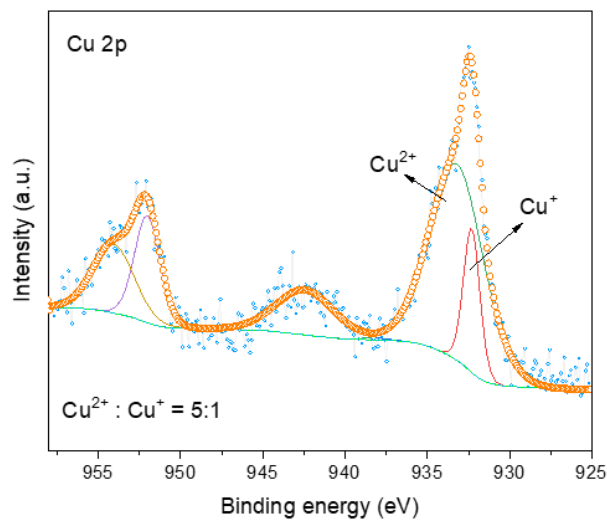


Figure 4-11 Cu 2p XPS spectra of $\text{Cu}_{2.0}/\text{PC-50}$.

The stability of the photocatalyst was also evaluated by the comparison of XRD and XPS spectra before and after reaction, as shown in Figure 4-12. The structure of catalysts and the chemical states of active species remained unchanged during the reaction. This result agrees with the 8 hours stability test, indicating the excellent stability of Cu_{0.1}Pt_{0.5}/PC-50.

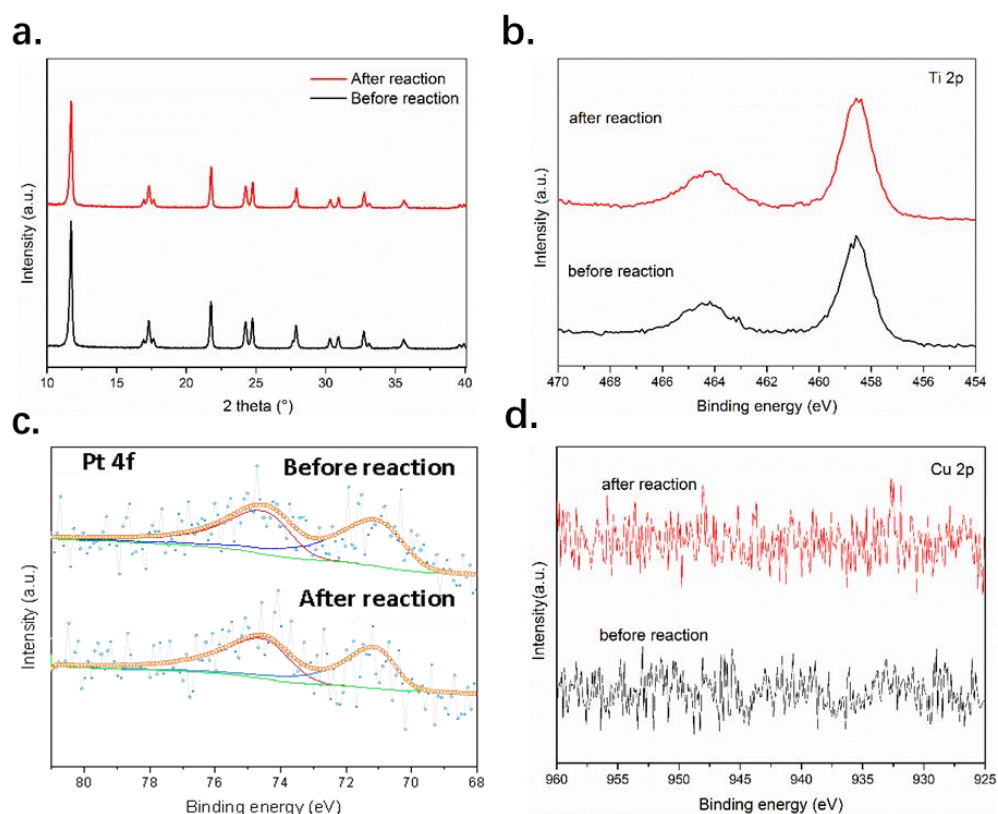


Figure 4-12 (a) XRD and (b-d) XPS spectra of Cu_{0.1}Pt_{0.5}/PC-50 before and after reaction

4.3.4 Photocatalytic mechanism of the optimised sample Cu_{0.1}Pt_{0.5}/PC-50

The photoabsorption properties of the as-prepared samples were investigated by ultraviolet-visible diffuse reflectance spectroscopy (UV/Vis DRS). After the introduction of CuO_x clusters, the photoabsorption was enhanced in the range from 200 to 320 nm, as shown in Figure 4-13, most likely because of charge transfer

between oxygen and isolated copper (II) species and the charge transfer in clusters.¹⁵⁵

The absorption edge remained almost unchanged for all the samples, thus indicating the intact band structure of PC-50 and the little contribution from CuO_x absorption.

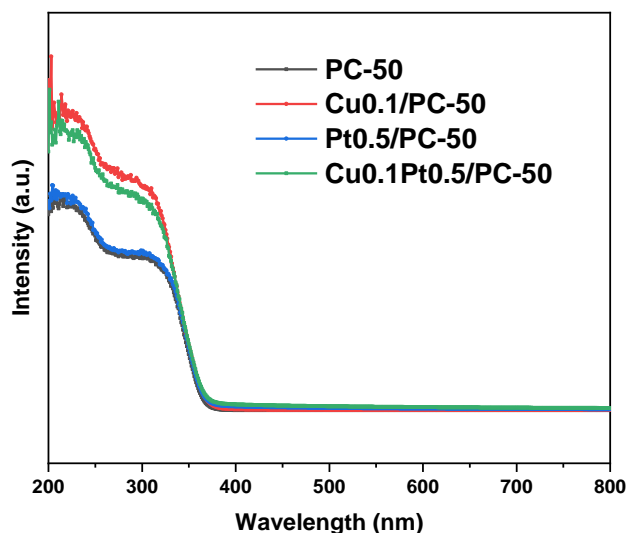


Figure 4-13 UV-DRS spectra of $\text{Cu}_{0.1}\text{Pt}_{0.5}/\text{PC-50}$, $\text{Pt}_{0.5}/\text{PC-50}$, $\text{Cu}_{0.1}/\text{PC-50}$ and PC-50

To further unravel the chemical state of copper species and the charge transfer, in situ EPR was carried out, as shown in Figure 4-14. Compared with $\text{Pt}_{0.5}/\text{PC-50}$, $\text{Cu}_{0.1}\text{Pt}_{0.5}/\text{PC-50}$ exhibits new spectra corresponding to CuO hyperfine structure owing to $I = 3/2$ of Cu^{II} , indicating the existence of long-range dipolar interactions between different CuII sites resulted in the broadening of spectral lines, the anisotropic hyperfine structure could be found after careful analysis: $g_{\parallel} = 2.395$ with $A_{\parallel} \approx 100$ G was obtained, whereas the value for $g_{\perp} = 2.05$ could not be resolved. These resonance parameters were in agreement with the distorted octahedral coordination of Cu^{II} ions in CuO clusters.¹⁵⁶ This result suggested the existence of a high distribution of CuO clusters, which explained the invisible copper species in HRTEM. This result was also consistent with the Cu 2p XPS analysis. Upon 365 nm LED illumination, the intensity of the Cu^{II} signal was expected to decrease if the CuII ions could accept electrons to

form EPR-silent Cu^{I} sites.¹⁵⁶ However, the spectra under chopped light almost overlapped, indicating the photoinduced electrons were trapped by Pt rather than the CuO sites. Thus, the introduction of Pt was important to impede charge recombination on CuO_x clusters, resulting in improved performance of $\text{Cu}_{0.1}\text{Pt}_{0.5}/\text{PC-50}$.

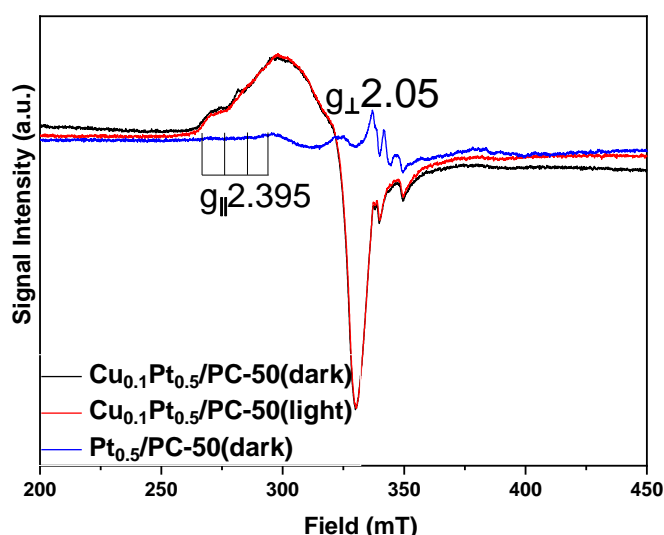


Figure 4-14 EPR spectra of $\text{Cu}_{0.1}\text{Pt}_{0.5}/\text{PC-50}$ (light on and light off) and $\text{Pt}_{0.5}/\text{PC-50}$ (light off)

The facilitation of charge transfer was further investigated by PL spectroscopy, as shown in Figure 4-15. An obvious band could be observed for the pristine PC-50, while the PL intensity decreased notably after the incorporation of Pt nanoparticles. This result suggested the efficient separation of photoinduced electrons and holes by Pt nanoparticles. In the case of $\text{Cu}_{0.1}/\text{PC-50}$, a photoluminescence spectrum with a fine structure was shown, which could be attributed to the highly dispersed copper species.⁷¹ According to the UV-Vis result, it was suggested that the photoexcitation occurred by charge transfer from oxygen to copper in the clusters. Considering the enhanced absorption in the UV region observed in UV/Vis DRS spectra and the larger enhanced emission in the PL spectra, the photoinduced carriers in PC-50 probably recombined in the CuO_x clusters over $\text{Cu}_{0.1}/\text{PC-50}$. This hypothesis was also

consistent with the analysis of the band structure mentioned above. More importantly, the PL intensity of $\text{Cu}_{0.1}\text{Pt}_{0.5}/\text{PC-50}$ was significantly lower than that of $\text{Cu}_{0.1}/\text{PC-50}$, thus indicating that the photoinduced electrons in PC-50 were transferred to Pt rather than to the CB of CuO_x clusters.

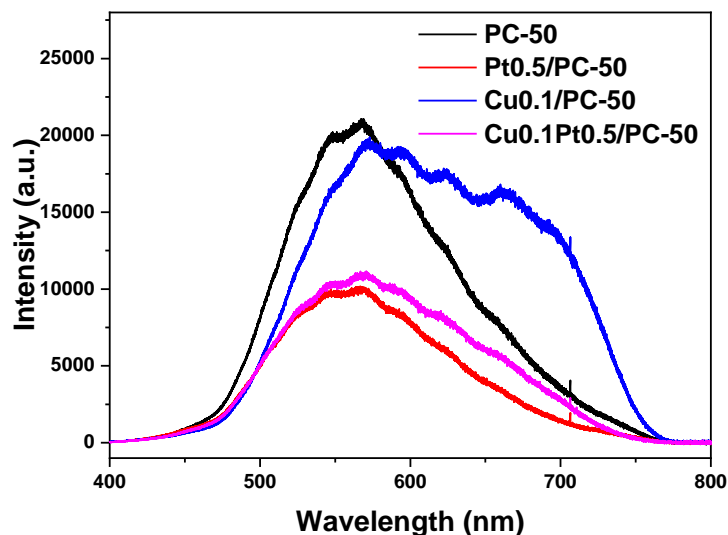


Figure 4-15 PL spectra of $\text{Cu}_{0.1}\text{Pt}_{0.5}/\text{PC-50}$, $\text{Pt}_{0.5}/\text{PC-50}$, $\text{Cu}_{0.1}/\text{PC-50}$ and PC-50

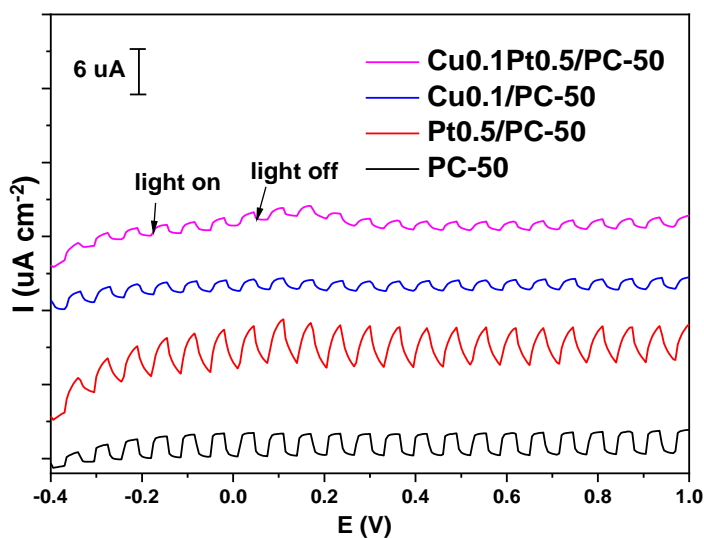


Figure 4-16 Photocurrent of $\text{Cu}_{0.1}\text{Pt}_{0.5}/\text{PC-50}$, $\text{Pt}_{0.5}/\text{PC-50}$, $\text{Cu}_{0.1}/\text{PC-50}$ and PC-50

The function of Pt as an electron sink was further consolidated by the transient photocurrent response, as shown in Figure 4-16. Compared with pristine PC-50, $\text{Pt}_{0.5}/\text{PC-50}$ exhibits higher photocurrent density because of the efficient transfer of

electrons to Pt nanoparticles, whereas the introduction of copper species resulted in a lower photocurrent response for both $\text{Cu}_{0.1}/\text{PC-50}$ and $\text{Cu}_{0.1}\text{Pt}_{0.5}/\text{PC-50}$. As mentioned above, the valence bands of CuO and Cu_2O were less positive than that of TiO_2 . This decay of photocurrent density could be explained by the weak oxidative capacity of photoinduced holes on CuO_x clusters.¹³⁴

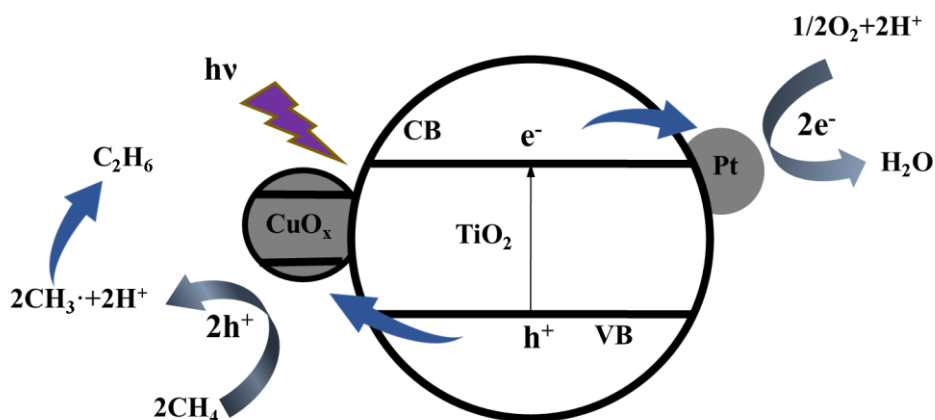


Figure 4-17 Possible photocatalytic OCM process over $\text{Cu}_{0.1}\text{Pt}_{0.5}/\text{PC-50}$

Based on the above characterisations and investigations, a probable mechanism of photocatalytic OCM over $\text{Cu}_{0.1}\text{Pt}_{0.5}/\text{PC-50}$ was proposed, as shown in Figure 4-17. Upon light irradiation, electrons could be excited from the VB of PC-50 to its CB and then migrate to Pt, while holes could be transferred to the VB of CuO_x clusters. This process not only retarded the recombination of photoinduced electrons and holes but also lowered the oxidation potential of photoinduced holes to avoid deep dehydrogenation and overoxidation. A C-H bond in CH_4 molecules was cleaved by the holes in the VB of CuO_x clusters to form methyl radicals and protons. The combination of methyl radicals formed ethane molecules, and deep dehydrogenation could lead to the formation of ethylene. O_2 could be reduced by electrons from Pt nanoparticles to form O_2^- , and the protons could be removed by O_2^- to form water.

The synergy effects between Pt and CuO_x clusters at reduction sites and oxidation sites, respectively, were highlighted to complete the catalytic cycle.

4.4 Conclusion

In summary, the first example of a continuous photocatalytic OCM process at room temperature and atmospheric pressure in a flow system was reported. The Pt nanoparticles and CuO_x clusters were introduced onto PC-50 by photodeposition and wet impregnation methods, respectively. The separation of photoinduced e⁻/h⁺ was facilitated and the oxidation potential of holes was lowered to avoid overoxidation, leading to high yield and selectivity towards C₂ hydrocarbons. The synergy of Pt nanoparticles and CuO_x clusters resulted in the increased C₂ yield (6.8 μmol h⁻¹), which was approximately 3.5 times as high as that observed with PC-50 and more than twice as high as the sum of the activity of Pt/PC-50 (1.07 μmol h⁻¹) and Cu/PC-50 (1.9 μmol h⁻¹), resulting in an AQE of 0.5% at 365 nm. The selectivity of 60% was also comparable to that of traditional OCM thermocatalysis, and the high photocatalytic activity remained stable after a long experimental period. Overall, this study provides an effective green route for methane upgrades. Although the results achieved in this chapter are attractive, it still needs further improvement due to several factors: 1. The yield rate is still very low, only at the level of several μmol h⁻¹; 2. The light utilisation efficiency is moderated as well compared with other photocatalytic processes, reflected by the small AQE value (<1%); 3. The stability test was only carried out for 8 hours, which is not convincing considering the general hundreds of hours test in thermocatalysis; 4. The charge transfer process was only observed using ex-situ

technologies, thus no direct evidence could be used to support the proposed pathway.

5. The interaction between the methane molecule and the co-catalyst has not been clearly clarified.

5 Efficient and highly selectively oxidative coupling of methane to C₂ hydrocarbons over PdCu nanoalloy loaded TiO₂

As mentioned in previous chapter, coupling of two methane molecules to produce C₂ products (C₂H₆/C₂H₄) is one of the most general and highly profitable processes^{2,130}, while it is much more challenging than C₁ production. The first example of photocatalytic oxidative coupling of methane (OCM) over CuO_x-Pt/TiO₂ in a flow reactor has been demonstrated in Chapter 4. However, similar to other photocatalytic couplings of methane processes, the yield of C₂ was very moderate (6.8 μmol h⁻¹) and the stability test was not convincing (about 8 h). Photocatalytic processes often exhibited high selectivity, however, the reported conversion rate and more importantly the stability are rather moderate, which are two equally important indexes, especially for future application.¹ Turnover number (TON) and Turnover frequency are widely regarded as the two most important factors to evaluate a catalyst, which can reflect both catalytic activity and catalyst's stability. The majority of the reported photocatalytic methane coupling flow systems represent a rather moderate TOF < 5 h⁻¹ or TON of < 10 due to either the low conversion rate and/or short stability period. Very recently a few benchmark studies such as oxidative coupling with water over Pd/Ga₂O₃¹⁵⁷, non-oxidative coupling over Au/TiO₂³⁰ and oxidative coupling with oxygen over Au-ZnO/TiO₂¹⁵⁸, improved TON to a few hundred, with the assistance of deep UV light (254 nm)¹⁵⁷ or the thermal effect (140 °C)¹⁵⁸. It is still a great challenge to achieve an efficient photocatalyst with both high TOF and TON for photocatalytic coupling of methane under ambient conditions (e.g., room temperature).

It is unambiguous that these three factors including conversion rates, selectivity, and stability have to be considered as a whole to demonstrate the potential of the photocatalytic technology. This requires a novel design strategy of photocatalysts, in particular, the active sites to achieve high conversion and selectivity with prolonged stability against coking and bleaching of active species. The formation of bimetallic catalysts via alloying one metal with another is an effective and universal strategy to improve catalyst performance and achieve high resistance to deactivation in thermocatalysis, such as steam reforming of methane over AuNi¹⁵⁹ and dry reforming of methane over Ni-Cu/Mg(Al)O.¹⁶⁰ The rapidly developing strategy offers a clue to manipulate the physicochemical properties of the surface of a catalyst to meet the versatile requirements for photocatalytic OCM.¹⁶¹ The photophysics and photochemistry required by these three factors can be translated into: i) high availability of photo-induced charge carriers; ii) efficient and selective activation of the first C-H bond in CH₄; iii) the appropriate binding of adsorbates to the catalyst to speed up the methane activation and to avoid subsequent reactions to coking.

Herein, a screening process was started from the investigation of a series of noble metals on the TiO₂ photocatalyst, which usually acts as charge sinks to promote charge transfer in photocatalysis²⁷ and show unique catalytic performance for activation of the C-H bond in traditional catalysis¹¹⁷. After Pd showed the exceptional activity as the most efficient co-catalyst, a series of non-noble transition metals as the second component was introduced to form bimetallic alloy co-catalysts to consolidate the activity and enhance the stability. The incorporation of Cu was found to dramatically enhance both activity and resistance to coking of the photocatalyst. PdCu/TiO₂ exhibits the highest methane conversion rate of 2480 μmol g⁻¹ h⁻¹ to C₂ products with

the highest quantum efficiency (AQE) of 8.4% among all the so-far reported photocatalytic methane conversion to C₂ products processes under ambient conditions. More importantly PdCu/TiO₂ represents the unprecedented TOF of 116 h⁻¹ and TON of 12,642 for the conversion to C₂ products, which is 20 times higher than the recent benchmark results^{30,162}. In addition, such high activity can remain during the 112 hours test, together with an excellent selectivity of 75% to C₂ (ethane and ethylene). The reason behind the holistically remarkable performance was then explored by comprehensive characterisations and DFT calculations.

5.1 Experimental section

5.1.1 Photocatalysts fabrication

A modified reduction method by NaBH₄ according to the previous report was used to prepare noble metals (Pd, Ru, Pt, Ag) decorated TiO₂¹⁶³. In a typical experiment, different amounts of PdCl₂ (Aldrich, 99.999%) aqueous solution (2.7 mg Pd/mL) were added to 100 mL of deionised water under stirring. Then, a polymer stabilizer, Poly (vinyl alcohol) (PVA, Aldrich, Mw 9000-10000, 80% hydrolyzed) aqueous solution (1%wt) was added with a weight ratio (polymer/metal) of 0.65. Afterwards, a certain amount of fresh NaBH₄ (Aldrich, ≥96%) aqueous solution (0.1 M) was added with a mole ratio (NaBH₄/Pd) of 5 and the solution was stirred for another 30 minutes. Next, the concentrated H₂SO₄ (0.25 mL) was introduced to the above solution under stirring along with 250 mg of TiO₂ (Millennium PC-50). After stirring for another 1 hour, the photocatalyst was obtained by centrifugation, washed with deionised water three times and dried in an oven for 12 hours at 60°C. The photocatalyst

synthesized by this method was denoted Pd_x/TiO₂ (x = 0.05, 0.1, 0.5, 1.0, wt%, corresponding to the added amount of Pd weight percentage with respect to TiO₂). The other noble metals decorated TiO₂, denoted M/TiO₂ (M = Pt, Ag, Ru, Au), were synthesized using a similar method with an equal mole amount to Pd in Pd_{0.1}/TiO₂.

For the synthesis of bimetallic alloy decorated TiO₂ photocatalyst, denoted PdM/TiO₂ (M= Cu, Ni, Co, Fe), a modified method was used referring to the previous report.¹⁶⁴ Typically, 0.25 mg Pd in the form of PdCl₂ aqueous solution (2.7 mg Pd/mL) was added to 45 mL of deionised water, followed by the addition of the equal molar amount of Cu(NO₃)₂•2.5H₂O (Alfa Aesar, 98%) aqueous solution. Subsequently, PVA aqueous solution (1% wt) was added with a weight ratio (polymer/Pd) of 1.3, which is two times the amount added in the synthesis of Pd_{0.1}/TiO₂. In addition, a certain amount of sodium citrate (Sodium citrate tribasic dihydrate, Sigma-Aldrich, ≥99.0%) aqueous solution (1.4 mg/mL) was mixed at a molar ratio of sodium citrate to metal at 2: 3. Then, the above mixture was purged with argon for more than 20 minutes under stirring. After the removal of air, a certain amount of fresh NaBH₄ aqueous solution (0.1 M) was injected into the above solution with a mole ratio of NaBH₄/Pd to 10 and the solution was stirred for another 1 hour at room temperature with continuous argon flow. Afterwards, 250 mg of TiO₂ was added to the above solution and the mixture was allowed to stir for another 0.5 h. The photocatalysts were collected by centrifugation, washed three times with deionised water and dried in a vacuum oven overnight. For the other metals (Ni, Co, Fe), a similar procedure was conducted except for the change of the metal nitrate precursors.

For the synthesis of controlling samples Cu/TiO₂, a similar procedure was conducted apart from the addition of Pd precursor. For the synthesis of the sample (Pd₁Cu₁/TiO₂) with a large loading amount (1wt% of Pd and equal mole amount of Cu), a similar procedure was carried out except for the ten times higher amount of related chemicals.

5.1.2 Characterisations

The powder X-ray (XRD) spectra were measured with a Rigaku SmartLab SE using a Cu K α 1 source (60 kV, 60 mA). Raman spectroscopy was performed at Renishaw InVia Raman Microscope with a 442 nm laser. Ultraviolet-visible diffuse reflectance spectroscopy (UV-Vis DRS) was recorded by a SHIMADZU UV-2550 in reflectance mode using standard BaSO₄ powder as a reference. UV-Probe software was used to convert the reflectance to absorbance via Kubelka-Munk transformation. XPS Analysis was carried out with two instruments. Most samples were measured using Kratos Axis SUPRA XPS while the Cu 2p and Cu LMM spectra of Pd₁Cu₁/TiO₂ were measured with a Thermo scientific XPS K-alpha with more scans to obtain a high signal to noise spectra. In situ XPS experiment was conducted using a Thermo Fisher ESCALAB 250Xi equipped with a 365 LED light source. All the XPS analysis was performed with CasaXPS software and the spectra were calibrated with C 1s peak at 284.8 eV. PL spectroscopy was collected by Renishaw InVia Raman with a 325 nm excitation laser. STEM imaging was conducted using a double Cs aberration-corrected FEI Titan³ Themis 60-300 equipped with an X-FEG gun, a monochromator and an XEDS ChemiSTEM. The element content was measured by a USA Perkin Elmer 8300 ICP-OES and a Z-2000 HITACHI Atomic Absorption

Spectrophotometers (AAS). In situ EPR was measured using a NRUKER E500-9.5/1.2 spectrometer with a 365 nm LED light source (71 W) under argon, air and CH₄ atmosphere, respectively at 100 K. During the EPR experiments, powder samples (~13 mg) were added in quartz tubes and sealed with septa, then purging by the different atmosphere.

5.1.3 Photocatalytic reaction for methane conversion

The photocatalytic activity measurement of methane oxidation was carried out using the set-up described in **Section 3.9** with a few modifications. To investigate the influences of different ratios of CH₄ to O₂, the real ratio was tuned to 53:1, 114:1, 176:1, 373:1 and 2018:1, respectively after a few calibrations (excluding the influence of temperature and gas line pressure). For the long-term experiment running, the ratio of CH₄ to O₂ was set as 373: 1, and the experiment was started after reaching equilibrium each morning and stopped in the evening. (*Note: Due to the safety requirement, the experiment was not allowed to run overnight with such high CH₄/O₂ flow rates. The film was left in the reaction chamber overnight and the total reaction time was calculated by accumulation*).

5.1.4 Calculation of the C₂ selectivity

The selectivity was calculated based on the observable products, including C₂H₆, C₂H₄, C₃H₈ and CO₂. The C₂ selectivity was calculated using the formula below:

$$C_2 \text{ selectivity} = \frac{2 \times (n_{C_2H_6} + n_{C_2H_4})}{2 \times n_{C_2H_6} + 2 \times n_{C_2H_4} + 3 \times n_{C_3H_8} + n_{CO_2}} \times 100\% \dots \dots \dots \text{eq. 5-1}$$

in which n is the molar rate of different products.

5.1.5 Calculation of apparent quantum efficiency (AQE)

The calculation of apparent quantum efficiency was based on the conversion of methane using the formula shown below:

$$\text{AQE} = \frac{(2 \times n_{\text{C}_2\text{H}_6} + 4 \times n_{\text{C}_2\text{H}_4} + 3 \times n_{\text{C}_3\text{H}_8} + 8 \times n_{\text{CO}_2}) \times N_A}{\text{Number of incident photons}} \times 100\% \dots \text{eq. 5-2}$$

in which n is the molar generation rate of different products, N_A is the Avogadro constant, and the irradiation area was approximately 7 cm². The light intensity was 160 mw/cm².

5.1.6 Calculation of turnover number (TON) and turnover frequency (TOF)

The calculation of TON and TOF was based on the C₂ product yields over the active sites PdCu alloy nanoparticle,

$$\text{PdCu molar amount} = \frac{\text{Catalyst amount} \times \text{Pd concentration}}{\text{The atomic weight of Pd}} + \frac{\text{Catalyst amount} \times \text{Cu concentration}}{\text{The atomic weight of Cu}} \dots \text{eq. 5-3}$$

$$\text{TON} = \frac{\text{Moles of C}_2 \text{ yield} \times 2}{\text{PdCu molar amount}} \dots \text{eq. 5-4}$$

$$\text{TOF} = \frac{\text{C}_2 \text{ yield rate} \times 2}{\text{PdCu molar amount}} \dots \text{eq. 5-5}$$

Noted: For the TON and TOF of other works presented in Figure 5-9, the calculation was based on the active site, such as noble metal co-catalyst in their stability test periods. For those with more than one co-catalyst, the calculation was based on the sum of the co-catalysts used for CH₄ activation.

5.1.7 Computational details

Computational simulations were conducted by my collaborator Dr N. Martsinovich from the Department of Chemistry, University of Sheffield. Density-functional theory (DFT) calculations were performed using CRYSTAL17 software,¹⁶⁵ with the PBE functional¹⁶⁶ and the D3 dispersion correction,¹⁶⁷ with a localised basis set and pseudopotential for Pd,¹⁶⁸ and localised all-electron basis sets for Cu,¹⁶⁹ Ti, O,¹⁷⁰ C and H¹⁷¹ obtained from the CRYSTAL web site.¹⁷² Pd and PdCu alloy were modelled using 2D-periodic (111)-oriented slabs with three atomic layers and a 3x3 extended surface unit cell, separated by a 500 Å vacuum gap in the vertical direction. In the PdCu alloy, one out of nine Pd atoms in each layer was replaced by a Cu atom. TiO₂ was modelled as a periodic slab of anatase with the (101) surface orientation and a 2x2 extended surface unit cell, with the thickness of 8 atomic layers, with slabs separated by a 500 Å vacuum gap. Lattice parameters were optimised for bulk Pd and anatase. Single methane or ethane molecules were adsorbed on one side of each slab, in a range of positions. All atom positions were fully optimised. Binding energies were calculated including the basis set superposition error correction.¹⁷³ Images of the calculated structures were produced using VMD software.

5.2 Results and discussion

5.2.1 Photocatalytic activities

Since noble metals are often regarded as charge sinks to promote charge separation to facilitate photocatalytic activity,²⁷ following the results founded in previous chapter, which indicate that TiO₂ is the best base photocatalyst, photocatalytic OCM reactions were then investigated over different noble

metals decorated TiO₂ (anatase) in a flow reactor using a 365 nm LED under room temperature and atmospheric pressure, as shown in Figure 5-1.

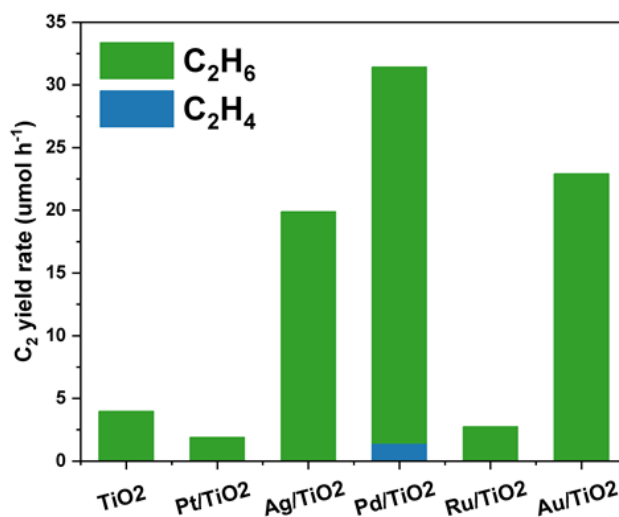


Figure 5-1 C₂ yield rate over different noble co-catalysts decorated TiO₂ with the equal mole amount to Pd. (Reaction condition: gas hourly space velocity (GHSV = 342 000 mL g_{cat}⁻¹ hour⁻¹), CH₄: O₂ = 114: 1, 10% of CH₄, Ar as balance gas, 365 nm LED 40 W, 30 °C)

Different effects on the C₂ yield rates are observed, following the trend: Pd/TiO₂ > Au/TiO₂ > Ag/TiO₂ > TiO₂ > Ru/TiO₂ > Pt/TiO₂. Compared with the low yield rate (ca. 4 μmol h⁻¹) of pristine TiO₂, an improvement of nearly 8 times is achieved after the loading of Pd. In addition to the enhancement of charge carrier transfer, such a promotion effect can also be attributed to the strong interaction between Pd nanoparticles and the C-H bond in CH₄.^{174,175} Pd was then selected as the best co-catalyst and its loading amount was optimized, as shown in Figure 5-2. The C₂ yield rate exhibits a volcano trend with the increasing loading wt% of Pd. After reaching 32 μmol h⁻¹ over Pd_{0.1}/TiO₂, less than a 20% increase can be observed with a five-fold increase in Pd loading amount, and further increase of loading amount to 1 wt% resulted in decreased

activity, which might be due to the fact that excessive Pd nanoparticles may obstruct the light penetration to TiO₂ due to scattering and/or absorption^{12,176}.

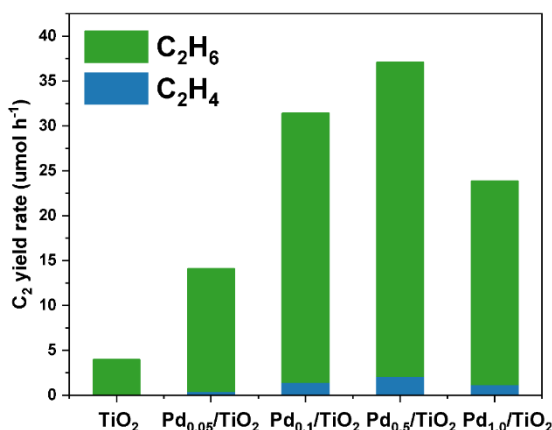


Figure 5-2 C₂ yield rate of photocatalytic OCM over Pd/TiO₂ with different Pd wt%. (Reaction condition: GHSV = 342 000 mL g_{cat}⁻¹ hour⁻¹, CH₄: O₂ = 114: 1, 10% of CH₄, Ar as balance gas, 365 nm LED 40 W, 30 °C)

Balancing the cost and performance of Pd cocatalyst, 0.1 wt% was selected as the optimum amount for the following study (denoted Pd/TiO₂ without specific notification). Unexpectedly, the performance of Pd/TiO₂ exhibits a declined trend when the reaction time was extended, as shown in Figure 5-3. In thermocatalytic methane conversion, the strong interaction of the catalyst with CH₄ (e.g., strong binding force to adsorbates or low activation energy barrier) often leads to consecutive reactions for coke accumulation.^{117,177} A recent example in the photocatalytic non-oxidative coupling of methane over Pd/Ga₂O₃ also reported the deposition of coke by a side reaction.⁷⁸ Thus, the deactivation of Pd/TiO₂ is likely due to the accumulation of cokes, which was proved in section 5.2.4. Transition metals can be used to form alloys with another active metal to enhance the coke resilience^{127,178}. Thus, a group of

transition metals were investigated to form an alloy with Pd and their mole amount was equal to that of Pd.

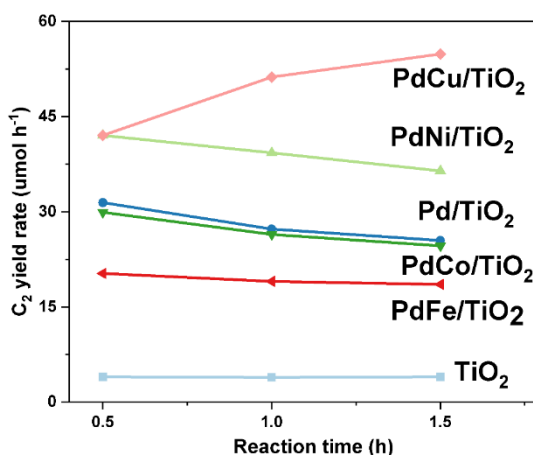


Figure 5-3 The trend of C₂ yield rate over TiO₂, Pd/ TiO₂, PdCu/ TiO₂, PdNi/ TiO₂, PdCo/ TiO₂, and PdFe/ TiO₂ within the first 1.5 hours with the second component of 0.1 wt%. (Reaction condition: GHSV = 342 000 mL g_{cat}⁻¹ hour⁻¹, CH₄: O₂ = 114: 1, 10% of CH₄, Ar as balance gas, 365 nm LED 40 W, 30 °C)

Taking the activity at 1.5 hours for comparison, Cu and Ni both improve the Pd/TiO₂ activity with respect to C₂ yield among Ni, Co, Cu, and Fe cocatalysts loaded photocatalysts, nearly 2.2 and 1.4 times higher than single Pd/TiO₂, respectively. More interestingly, all the other alloy decorated TiO₂ photocatalysts, including PdNi/TiO₂, PdCo/TiO₂ and PdFe/TiO₂, exhibit a declined trend similar to Pd/TiO₂ for C₂ yield rates, while the incorporation of Cu reverses the trend of C₂ yield rate, thus the best photocatalyst is the PdCu/TiO₂. The real concentration of the cocatalyst was then analysed by ICP-OES to be Pd 0.089% and Cu 0.051% listed in Table 5-1 (denoted as PdCu/TiO₂ unless otherwise specified).

Table 5-1 The weight percentage of Pd and Cu in Pd_{0.1}Cu_{0.1}/TiO₂ detected by ICP-OES and AAS

Element	Pd	Cu
Percentage (wt. %)	0.089	0.051

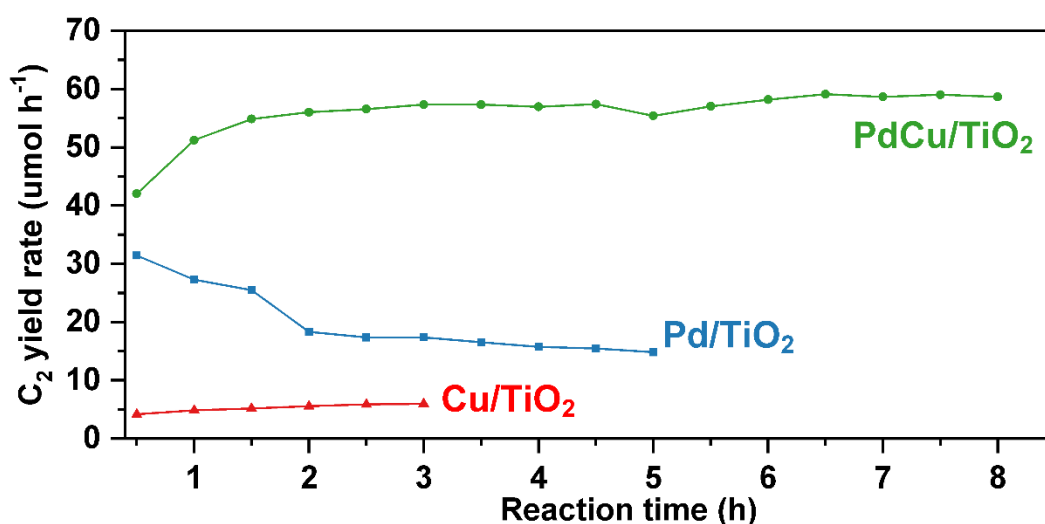


Figure 5-4 The stability and temporal profile of C₂ yield of Pd/TiO₂, Cu/TiO₂, and PdCu/TiO₂. (Reaction condition: GHSV = 342 000 mL gcat⁻¹ hour⁻¹, CH₄: O₂ = 114: 1, 10% of CH₄, Ar as balance gas, 365 nm LED 40 W, 30 °C)

Figure 5-4 further shows temporal C₂ yield on different photocatalysts and both Cu/TiO₂ and PdCu/TiO₂ show an almost stable activity while Pd/TiO₂ activity keeps a fast decay and then a slow decay with time. The yield rate of C₂ on Pd/TiO₂ decreases by 50% when the reaction time is prolonged to 5 hours. PdCu/TiO₂ represents the stable yield rate of ca. 57 μmol h⁻¹ for 8 hours.

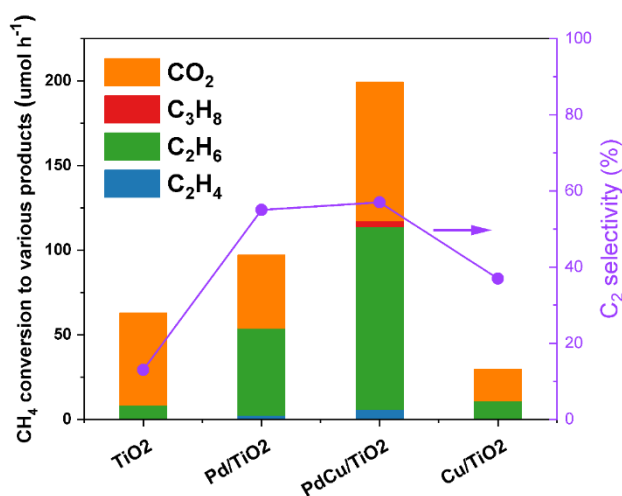


Figure 5-5 CH₄ conversion to various products over TiO₂, Pd/TiO₂, PdCu/TiO₂, and Cu/TiO₂ at 1.5 hour. (Reaction condition: GHSV = 342000 mL g_{cat}⁻¹ hour⁻¹, CH₄: O₂ = 114: 1, 10% of CH₄, Ar as balance gas, 365 nm LED 40 W, 30 °C)

The selectivity of C₂ products, CO₂ and C₃H₈ at 1.5 hour run was then investigated in detail, as shown in Figure 5-5. The introduction of Cu, Pd, and PdCu increases C₂ selectivity to 37%, 55% and 57% compared with the pristine TiO₂ (13%), respectively, and the total methane conversion rate on PdCu/TiO₂ is more than 3 times higher than that of pristine TiO₂. Afterwards, the ratio of CH₄ to O₂ was varied to investigate the optimum reaction conditions, as shown in Figure 5-6. When the ratio of CH₄ to O₂ is 53: 1, the C₂ yield rate reaches as high as 62 μmol h⁻¹ (1240 μmol g⁻¹ h⁻¹), corresponding to the methane conversion to C₂ rate of 124 μmol h⁻¹ (2480 μmol g⁻¹ h⁻¹), being the highest among all the reported photocatalytic methane conversion to C₂ products processes under ambient conditions (Table 5-2).

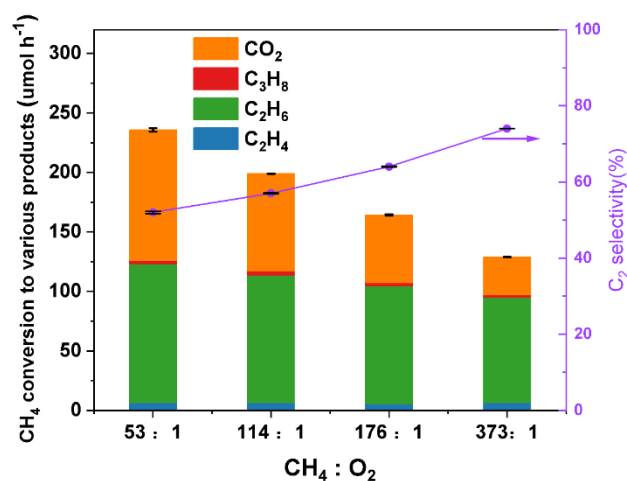


Figure 5-6 CH₄ total conversion rate and C₂ selectivity over PdCu/TiO₂ with different CH₄: O₂ ratios (the ratio was 53: 1, 114: 1, 174: 1, and 373: 1, respectively). Error bars in the figure were the standard error values from three runs.

Table 5-2 Representative works on photocatalytic methane conversion to ethane/ethylene operated at room temperature

Samples	Conditions	Yield rate of C ₂ products (μmol h ⁻¹)	AQE (%)
PdCu/TiO ₂ (this work)	Flow reactor; 303 K; 40 W 365 nm LED; 0.05 g catalyst; O ₂ : CH ₄ = 53 : 1, GHSV = 342000 mL g _{cat} ⁻¹ hour ⁻¹ , 10% of CH ₄ .	62	8.4 at 365 nm
AuPd/ZnO ³⁷	Batch reactor; room temperature; 300 W Xe lamp; Reaction time 4 h; 2 mg catalyst; 0.5 mL CH ₄ .	0.08	-
Au/ZnO ¹⁷	Batch reactor; room temperature; 300 W Xe lamp; Reaction time 4 h; 0.5 mL CH ₄ .	0.01	-

Ga ₂ O ₃ -K ⁶⁹	Batch reactor; 310 K; 300 W Xe lamp; Reaction time 3 h; 0.2 g catalyst; 200 μmol CH ₄	0.054	-
MgO-SiO ₂ ¹⁴²	Batch reactor; 310 K; 300 W Xe lamp; Reaction time 3 h; 0.2 g catalyst; 200 μmol CH ₄	0.009	-
Ce-Al ₂ O ₃ ⁷⁰	Batch reactor; 310 K; 300 W Xe lamp; Reaction time 3 h; 0.2 g catalyst; 200 μmol CH ₄	0.1	-
Pd/Ga ₂ O ₃ ¹⁵⁷	Flow reactor; 300 K; 40W low-pressure mercury lamp; 0.05 g catalyst; 20 mL min ⁻¹ CH ₄ gas with water vapor	47.4	5.1 at 254 nm
Ag-H ₃ PW ₁₂ O ₄₀ /TiO ₂ ³⁶	Batch reactor; room temperature; 400 W Xe lamp; Reaction time 7 h; 0.1 g catalyst; 0.3 MPa CH ₄	2.3	3.5 at 365 nm
Pt-CuO _x /TiO ₂ ¹⁰⁰	Flow reactor; 313 K; 40 W 365 nm LED; 0.1 g catalyst; CH ₄ : O ₂ =400: 1, 10%CH ₄ , GHSV = 2400 h ⁻¹	6.8	0.5 at 365 nm
Pt/Ga-TiO ₂ -SiO ₂ ¹⁸	Batch reactor; room temperature; 300 W Xe lamp; Reaction time 4 h; 0.2 g catalyst; 44.6 μmol CH ₄	0.314	0.0001 at 350 nm
Au/TiO ₂ ³⁰	Flow reactor; room temperature; 300 W Xe lamp; 5 mg catalyst; 10%CH ₄ , 90% Ar, GHSV= 120000 mL g ⁻¹ h ⁻¹	0.41	-
Ga-ETS-10-0.2 ⁶⁶	Batch reactor; room temperature; reaction time 5 h; 150 W Hg lamp; 0.2 g catalyst; 200 μmol CH ₄	2.2	-

(Zn ⁺ , Zn ²⁺)-ZSM-5 ⁷²	Batch reactor; room temperature; reaction time 8 h; 150 W Hg lamp; 1 g catalyst; 200 μmol CH ₄	2.9	0.55 at 300-400 nm
TiO ₂ /SiO ₂ ¹⁷⁹	Batch reactor; 310 K; reaction time 3 h; 300 W Xe lamp; 0.2 g catalyst; 200 μmol CH ₄	0.2	-
SiO ₂ -Al ₂ O ₃ -TiO ₂ ⁶⁴	Batch reactor; 310 K; reaction time 3 h; 250 W Xe lamp; 1 g catalyst; 200 μmol CH ₄	0.69	-
H-MOR ¹⁸⁰	Batch reactor; 310 K; reaction time 3 h; 250 W Xe lamp; 1 g catalyst; 200 μmol CH ₄	0.074	
FSM-16 ²⁹	Batch reactor; 310 K; reaction time 3 h; 300 W Xe lamp; 0.2 g catalyst; 200 μmol CH ₄	0.018	
GaN: ZnO ¹⁸¹	Batch reactor; 293 K; reaction time 2 h; 300 W Xe lamp; 0.05 g catalyst; 300 μmol CH ₄	2.85	
Zn ₅ (OH) ₈ Cl ₂ ·H ₂ O ¹⁸²	Batch reactor; 298 K; reaction time 3 h; 300 W Xe lamp; 0.05 g catalyst; pure CH ₄	39.4	

The apparent quantum efficiency (AQE) was then calculated using equation 5.2. The optimised catalyst represents 8.4% AQE at 365 nm, being a record in this field. An excessive amount of O₂ would generate more superoxide radicals O₂^{·-}, which was considered as an active species to promote the conversion rate but also to increase overoxidation to CO₂.^{12,26} Thus, as the O₂ amount is reduced (with the CH₄: O₂ ratio increased from 53: 1 to 373: 1), a slight decrease of

methane conversion rate to ethane is observed, while overoxidation to CO_2 shows a notable decrease to less than one third, from 110 to $32 \mu\text{mol h}^{-1}$, resulting in a high C_2 selectivity of ca. 75%. Such high selectivity is comparable to the most excellent OCM catalysts (e.g., Li/MgO ; $\text{Mn/Na}_2\text{WO}_4/\text{SiO}_2$) by thermocatalysis operated at $>873 \text{ K}$.^{145,183} Therefore, the optimised experimental condition is the GHSV of $342,000 \text{ mL g}_{\text{cat}}^{-1} \text{ hour}^{-1}$ with the ratio of CH_4 to O_2 at 373: 1 operated at room temperature. The control experiments were also carried out and they show that no products are observed in the absence of methane, without photocatalysts or under dark conditions, proving that this is a photocatalytic process and the only carbon source is methane (Figure 5-7).

Apart from the high conversion rate and high selectivity, stability is another

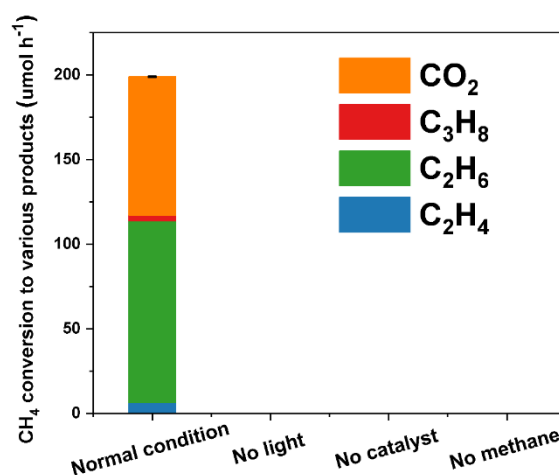


Figure 5-7 Photocatalytic OCM process under various controlling conditions. (Reaction condition: GHSV = $342\,000 \text{ mL g}_{\text{cat}}^{-1} \text{ hour}^{-1}$, CH_4 : O_2 = 114: 1, 10% of CH_4 , Ar as balance gas, 365 nm LED 40 W, 30 °C)

important index, in particular considering the future application. Therefore, a long-term stability test was carried out under the optimised condition as shown in Figure 5-8. Almost no change of the CH_4 conversion rate to C_2 is noticed

during the term of 112-hour test, indicating the extremely high stability of PdCu nanoalloy as the catalytic active sites. This is to the best my knowledge the first such example of over 100 hours stability test in photocatalytic methane conversion, although it is not uncommon in thermocatalysis to evaluate a catalyst with such long reaction time.^{9,184}

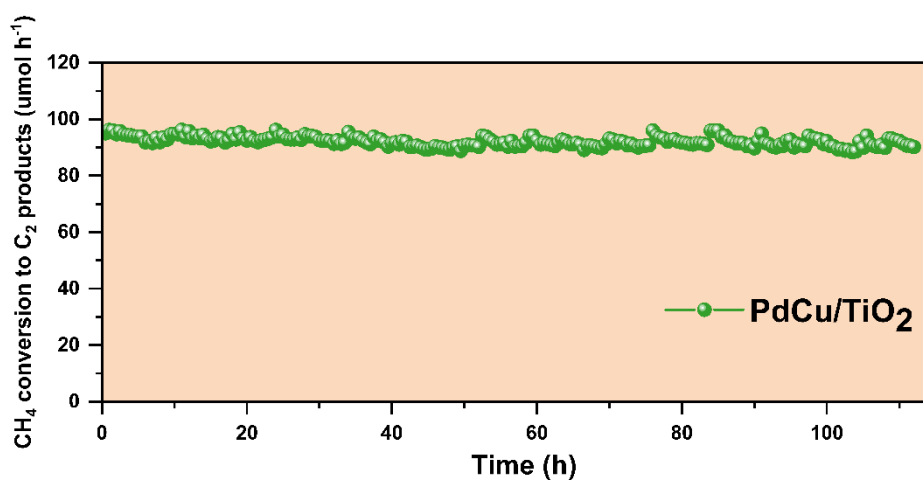


Figure 5-8 C₂ generation over PdCu/TiO₂ during a 112 hours reaction with the CH₄: O₂ ratio at 373: 1, these data were collected every 30 minutes. (Reaction condition: GHSV = 342 000 mL g_{cat}⁻¹ hour⁻¹, CH₄: O₂ = 373: 1, 10% of CH₄, Ar as balance gas, 365 nm LED 40 W, 30 °C)

TOF and TON, reflecting the efficiency and stability of a catalyst, are useful indexes widely used to evaluate the catalyst. Therefore, they were used to evaluate the PdCu nanoalloy co-catalyst for the conversion of methane to ethane/ethylene compared with other photocatalysts, as shown in Figure 5-9 (eq. 5-4 and 5-5 were used for the calculation of TOF and TON). The reported representative photocatalysts in methane conversion to C₂ products generally exhibit a very small TON of <10 and a moderate TOF of <5 h⁻¹, and two very recent benchmark work achieved TON of 442³⁰ and TOF of 25 h⁻¹,¹⁶² respectively. PdCu/TiO₂ shows the turnover frequency (TOF) of C₂ generation

(116 h⁻¹) among all the reported photocatalysts operated at $\lambda > 300$ nm and room temperature, being a new benchmark. Equally importantly, the TON achieved on our catalyst under the optimised condition also set a new record of 12,642. This unprecedented result indicated that PdCu nanoalloy is a stable and effective active site for the selective conversion of methane to C₂ products. In addition, the total conversion amount of CH₄ to C₂ products during this long-term test is 10316 μ mol, which is even more than 15 times higher than the molar amount of the used photocatalyst substrate (~ 625 μ mol). This result further confirms the advance of my photocatalyst.

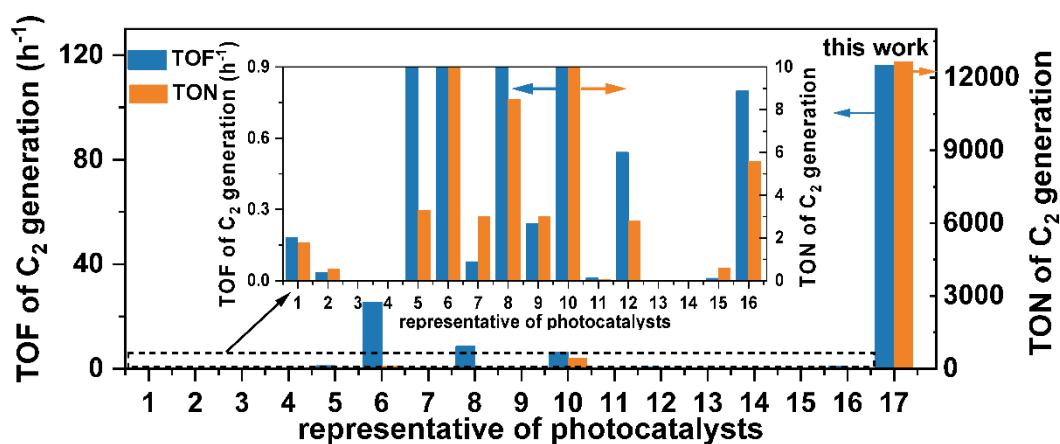


Figure 5-9 Summary of TON and TOF achieved on PdCu/TiO₂ and other reported representative photocatalysts ($\lambda > 300$ nm) under room temperature (1: AuPd/ZnO³⁷; 2: Au/ZnO¹⁷; 3: Ga₂O₃-K⁶⁹; 4: MgO-SiO₂¹⁴²; 5: Ce-Al₂O₃⁷⁰; 6: Au/WO₃¹⁶²; 7: Ag-H₃PW₁₂O₄₀/TiO₂³⁶; 8: Pt-CuO_x/TiO₂¹⁰⁰; 9: Pt/Ga-TiO₂-SiO₂¹⁸; 10: Au/TiO₂³⁰; 11: TiO₂/SiO₂¹⁷⁹; 12: SiO₂-Al₂O₃-TiO₂⁶⁴; 13: H-MOR¹⁸⁰; 14: FSM-16²⁹; 15: GaN: ZnO¹⁸¹; 16: Zn₅(OH)₈Cl₂·H₂O¹⁸², 17: this work.). The insert figure is the zoomed rectangle region indicated with the dash line in the figure showing the range of TON between 0-10 and TOF between 0-0.9. Among them, the values of photocatalyst 3, 4, 13 and 14 are still too small to see in the enlarged insert. The calculation method is shown in section 5.1.6.

5.2.2 Characterisations of the photocatalysts

The structure of the photocatalysts was first investigated by powder X-ray diffraction (PXRD), as shown in Figure 5-10. All samples exhibit the typical peaks assigned to the anatase phase (JCPDS no. 84-1286). Neither Pd nor Cu diffraction peaks are observed in all modified samples, probably owing to the low content (Table 5-1) or high dispersion.³⁶

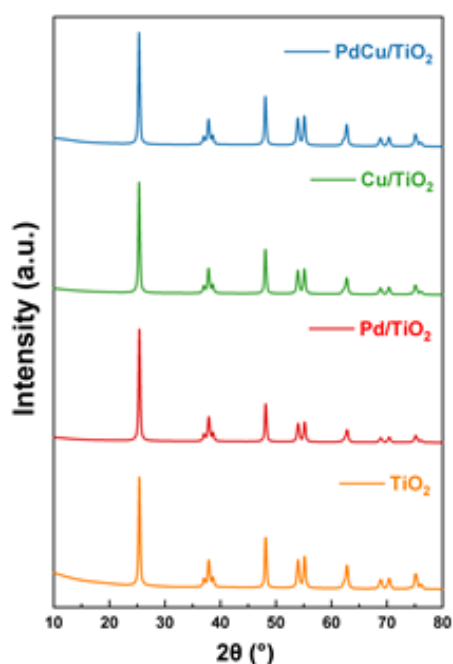


Figure 5-10 XRD spectra of TiO₂, Pd/TiO₂, Cu/TiO₂ and PdCu/TiO₂.

Raman spectra were further used to investigate the structure, as shown in Figure 5-11. Consistent with the results of PXRD, all samples display typical Raman peaks of the anatase phase, at 144 cm⁻¹(E_g), 198 cm⁻¹(E_g), 399 cm⁻¹(B_{1g}), 512 cm⁻¹(A_{1g}), and 639 cm⁻¹(E_g), respectively, suggesting the stable framework of anatase TiO₂ after cocatalyst loading.

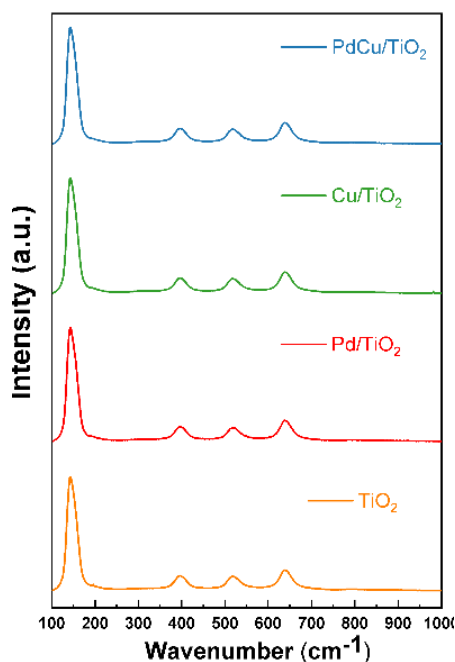


Figure 5-11 Raman spectra of TiO_2 , Pd/TiO_2 , Cu/TiO_2 and PdCu/TiO_2 .

The ultraviolet-visible diffuse reflectance spectroscopy (UV-Vis DRS) was used to study the photo-absorption properties, as shown in Figure 5-12. The absorption (both absorption peak and absorption edge) of all samples remains almost the same, indicating that TiO_2 harvests light for photo-induced carrier generation. A slightly enhanced light absorption at the visible light region after the introduction of co-catalyst nanoparticles is observed, probably due to the interband absorption and/or scattering by these particles.¹⁵²

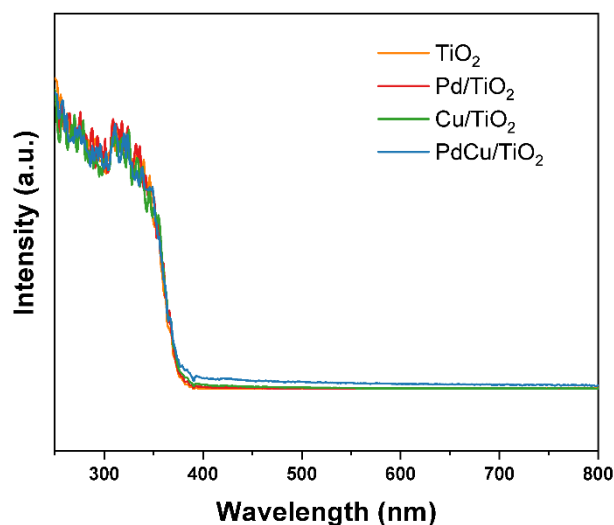


Figure 5-12 UV-Vis absorption spectra of TiO₂, Pd/TiO₂, Cu/TiO₂ and PdCu/TiO₂

All technologies mentioned above could not provide effective information on the small PdCu alloy particles, thus high-angle annular dark-field scanning transmission electron microscopy (HAADF-STEM) was carried out to gain a microscale view of the PdCu/TiO₂ sample (Figure 5-13).

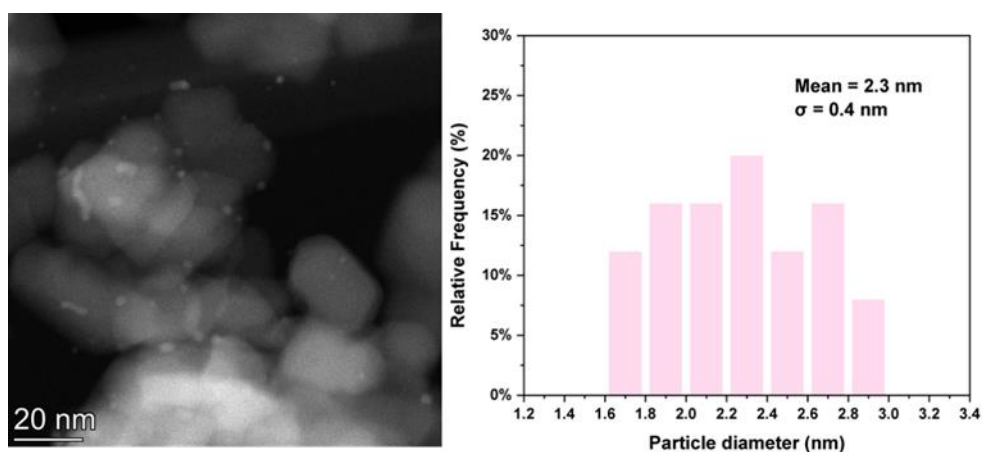


Figure 5-13 Representative STEM image and particle size distributions of PdCu alloy over PdCu/TiO₂

It should be noted that bright nanoparticles are distributed evenly on the supports, with an average size of 2.3 nm. These nanoparticles were further identified by the high-resolution TEM (HR-TEM) image, as shown in Figure 5-14, in which the distinct lattice fringes are seen with a d-spacing of 0.228 nm, corresponding to the (111) plane of PdCu alloy.^{185,186}

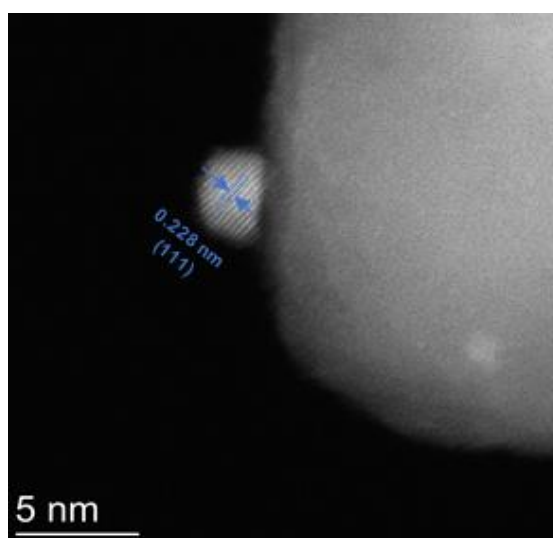


Figure 5-14 HR-TEM image of PdCu/TiO₂

In order to confirm the formation of PdCu alloy, the Energy Dispersive X-Ray Analysis (EDX) was applied to scan the nanoparticles, as shown in Figure 5-15. Both Pd and Cu are distributed homogeneously within the 2 nm nanoparticle, and a distinct boundary can be identified to distinguish the nanoparticle from TiO₂.

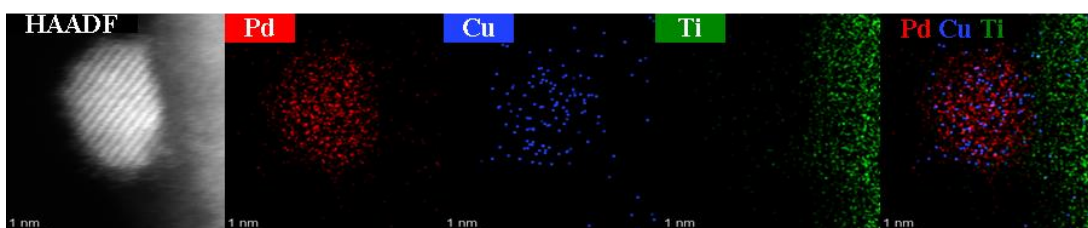


Figure 5-15 HAADF-STEM image and EDX elements mapping of PdCu/TiO₂

Moreover, the element intensity for Pd or Cu can only be visible within the nanoparticle observed and no signal of Pd or Cu can be detected on the TiO₂ support by the STEM image (Figure 5-16), confirming the accuracy of the element mapping for PdCu detection.

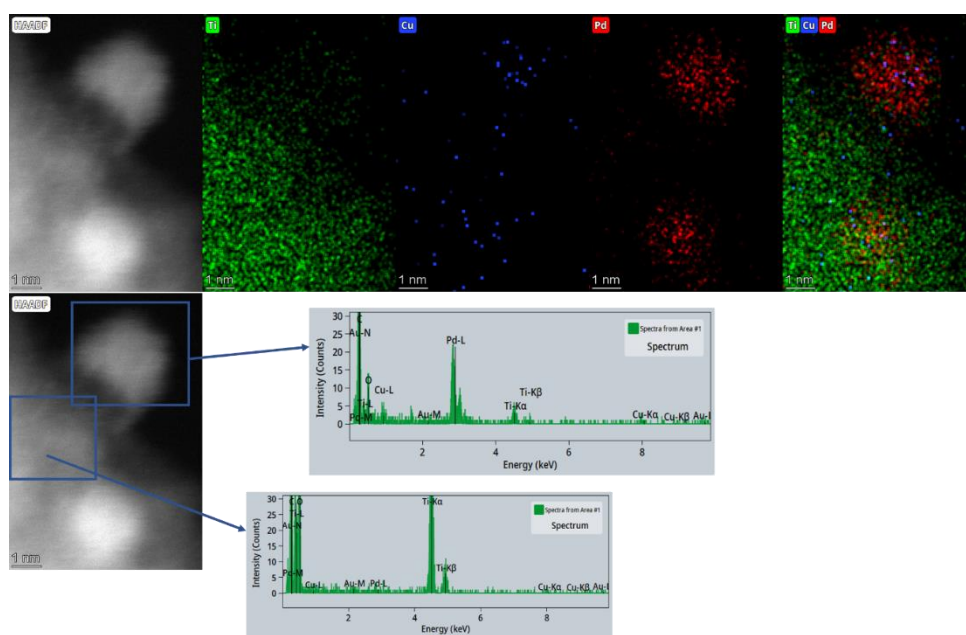


Figure 5-16 HAADF-STEM image and EDX element mapping of the selected area (element mapping of the PdCu nanoparticles and the support).

These results suggest the successful formation of PdCu alloy with the support of TiO₂. Furthermore, the PdCu alloy structure and the average size remain unchanged after 8 hours of reaction, as shown in Figure 5-17 and 5-18, indicating the high stability of these nanoparticles.

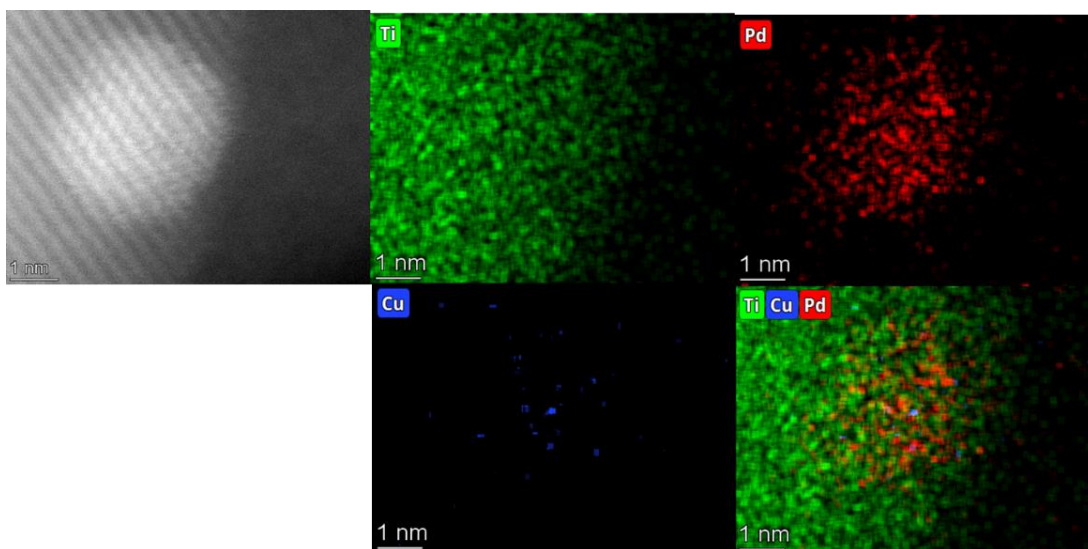


Figure 5-18 Top view of HAADF-STEM image and EDX element mapping of PdCu/TiO₂ after reactions.

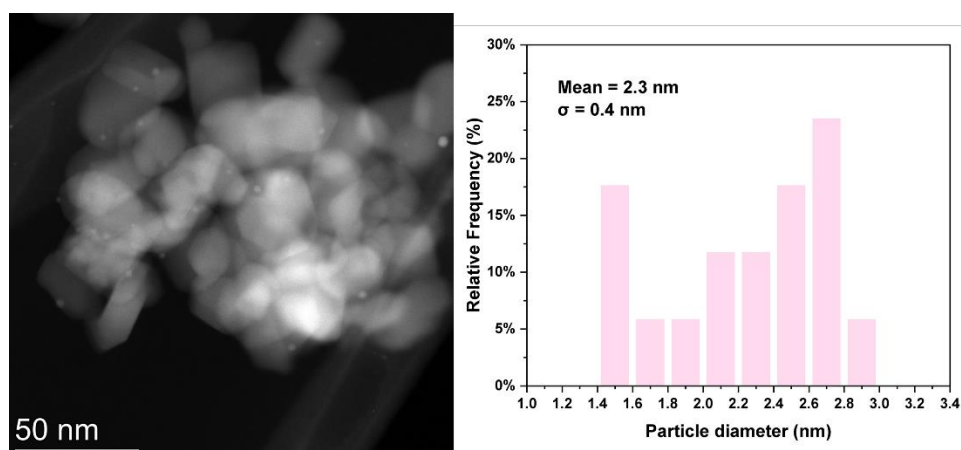
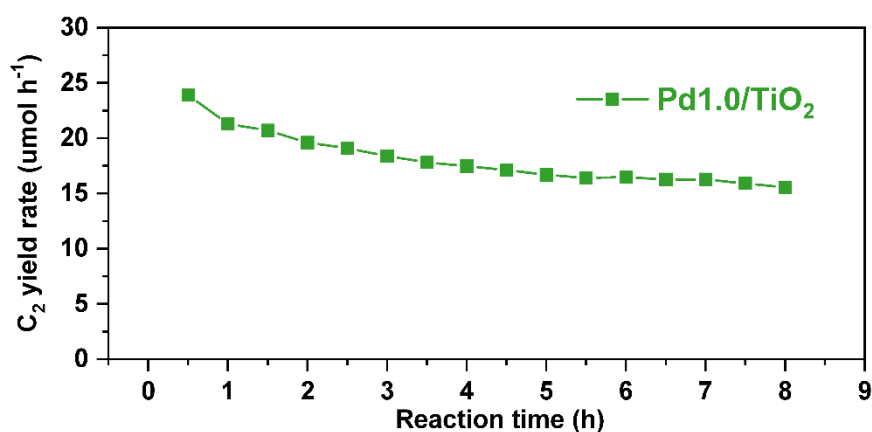


Figure 5-17 Representative STEM image and particle size distributions of PdCu alloy over PdCu/TiO₂ after reactions

X-ray photoelectron spectroscopy (XPS) was then carried out to analyse the chemical states of this effective co-catalyst. In order to have a higher resolution of the spectra to make a clear identification, two samples, Pd₁/TiO₂ and Pd₁Cu₁/TiO₂ with larger loading amount (1 wt%) of co-catalysts were used.

Both samples exhibit a similar C₂ yield trend to their counterparts with low loading amounts with increasing time (Figure 5-19).

a.



b.

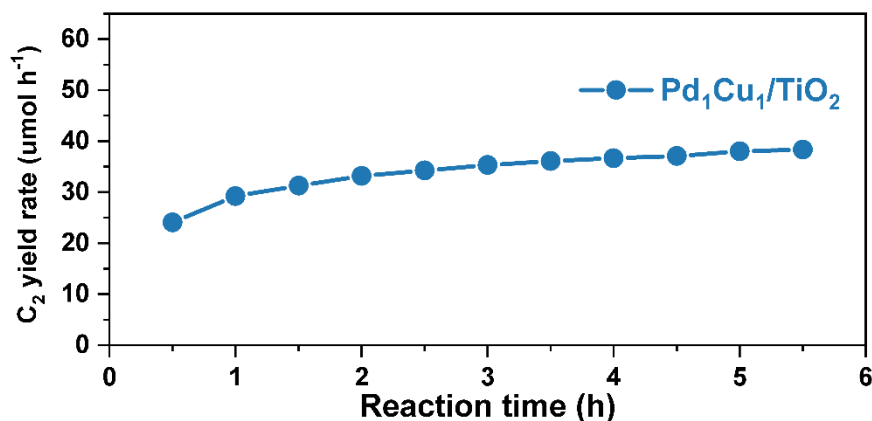


Figure 5-19 The trend of C₂ yield rate of Pd_{1.0}/TiO₂ (a) and Pd₁Cu₁/TiO₂ (b) over time.

The Pd 3d XPS spectra of Pd₁Cu₁/TiO₂ exhibited two peaks at 334.7 eV Pd 3d_{5/2} and 340.0 eV Pd 3d_{3/2}, respectively (Figure 5-20), and Pd₁/TiO₂ showed similar peaks at 334.6 eV Pd 3d_{5/2} and 339.9 eV Pd 3d_{3/2}, respectively. Both of them were identical to the metallic states of Pd, and the small positive shift of 0.1 eV after the introduction of Cu can be attributed to the interaction between Pd and Cu.¹⁸⁷

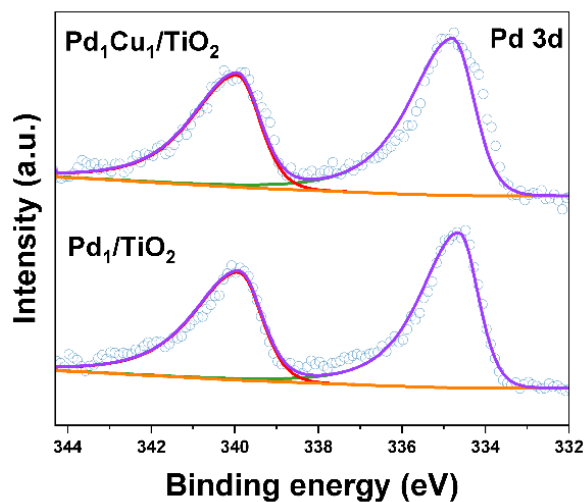


Figure 5-20 XPS spectra of Pd₁/TiO₂ and Pd₁Cu₁/TiO₂ (Pd 3d) before reaction.

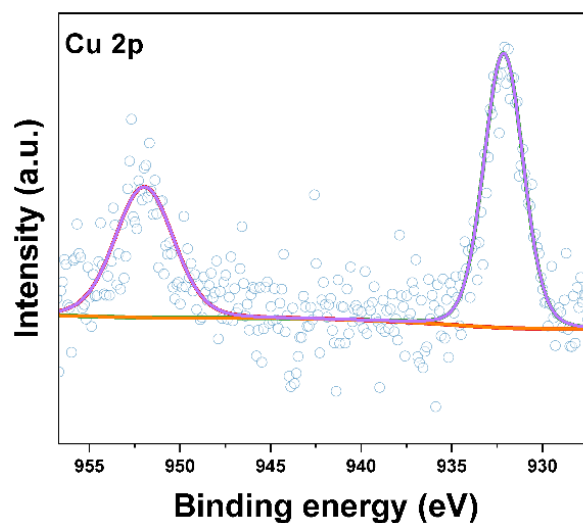


Figure 5-21 XPS spectra of Pd₁Cu₁/TiO₂ (Cu 2p) before reaction.

The peaks assigned to Cu 2p_{3/2} and Cu 2p_{1/2} are at around 932 and 951 eV and no satellite feature of Cu 2p, all these indicate metallic Cu and Cu^I excluding the existence of Cu^{II}, as shown in Figure 5-21. In order to distinguish the metallic Cu from Cu^I, Auger spectroscopy data was collected and analysed (Figure 5-22). The peak at around 919.0 eV confirms the metallic state of Cu¹⁸⁸.

Thus, the metallic PdCu alloy nanoparticles were successfully deposited on TiO₂.

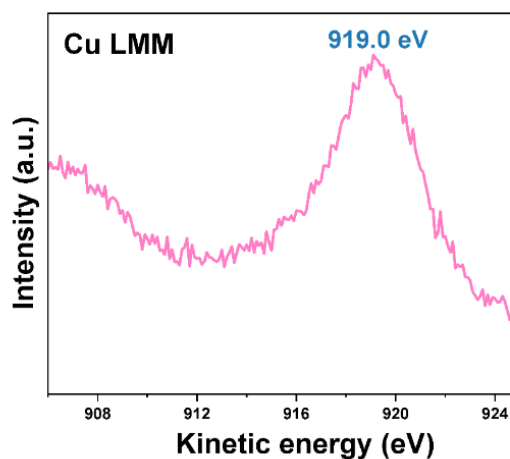


Figure 5-22 Auger Cu LMM spectrum of Pd₁Cu₁/TiO₂ before reaction

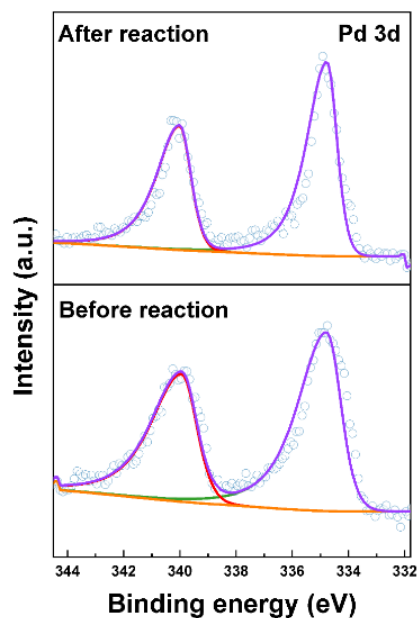


Figure 5-23 XPS spectra of Pd₁Cu₁/TiO₂ (Pd 3d) before and after the reaction

The XPS measurement of Pd₁Cu₁/TiO₂ after 6 hours of photocatalytic OCM reaction was also carried out, as shown in Figure 5-23, 5-24, and Figure 5-25,

and no change of peaks for Pd 3d spectra, Cu 2p spectra and Auger Cu LMM spectra indicated the high stability of the PdCu alloy nanoparticles. Overall, we have successfully synthesized a PdCu alloy nanoparticles decorated TiO₂ photocatalyst with high stability in the photocatalytic OCM reaction.

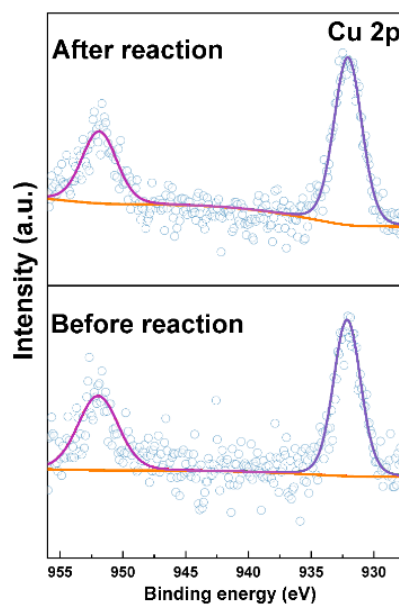


Figure 5-24 XPS spectra of Pd₁Cu₁/TiO₂ (Cu 2p) before and after the reaction.

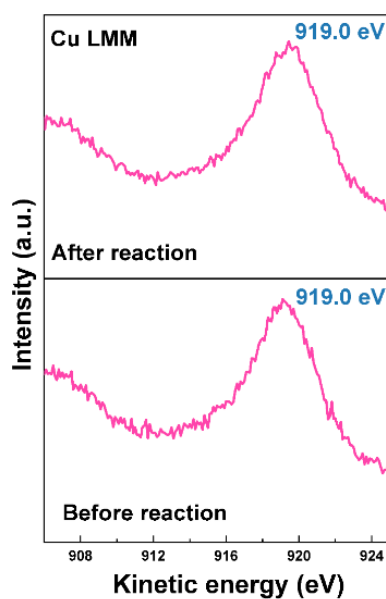


Figure 5-25 Auger Cu LMM spectrum of Pd₁Cu₁/TiO₂ before and after reactions.

5.2.3 Investigation of photo-induced charge transfer

The mechanism of the photocatalytic OCM process over PdCu/TiO₂ was then investigated, starting from charge excitation to the surface reaction. When a n-type semiconductor is in direct contact with a metal, the smaller work function (or higher Fermi level) of the semiconductor allows electrons in the metal to align the Fermi energy level.^{131,189} After the equilibrium of the Fermi levels is achieved, a Schottky barrier formed will prevent the negative charges in the metal from travelling back to the conduction band (CB) of the semiconductor. It can be hypothesized that in my case, after the introduction of Pd or PdCu nanoparticles on TiO₂, photoelectrons after excitation from the valence band (VB) of TiO₂ likely stay on the CB of TiO₂, while photoholes might transfer to Pd or PdCu nanoparticles. In order to confirm this hypothesis, in situ EPR and in situ XPS were carried out. As shown in Figure 5-26, under dark conditions, pristine TiO₂ itself exhibits some signals related to the small amount of surface oxygen species (e.g., adsorbed superoxide).¹⁹⁰

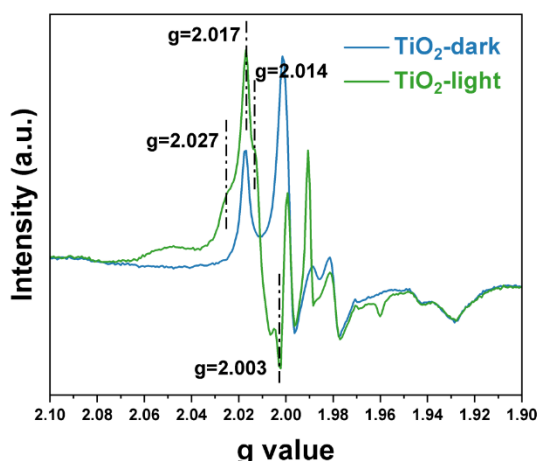


Figure 5-26 In situ EPR spectra of TiO₂ under dark conditions and light irradiation in an argon atmosphere

Compared with this, two sets of new paramagnetic species appear under light irradiation, as shown in Figure 5-26. One set of g values (2.003, 2.014, 2.017) can be attributed to the bridge oxygen radical (e.g., $\text{Ti}^{4+}\text{-O}^{\cdot-}\text{-Ti}^4$) and another set of g values (2.003, 2.017, 2.027) is owing to the terminal oxygen radical (e.g., $\text{Ti}^{4+}\text{-O}^{2-}\text{-Ti}^{4+}\text{-O}^{\cdot-}$), which is equivalent to photoholes located on O^{2-} anions.^{88,191,192} After loading of Pd nanoparticles, the intensity of both sets shows an obvious decrease (Figure 5-27), indicating the transfer of photoholes from TiO_2 to Pd nanoparticles or the photoholes in TiO_2 being consumed by the electrons from the d-band of Pd.

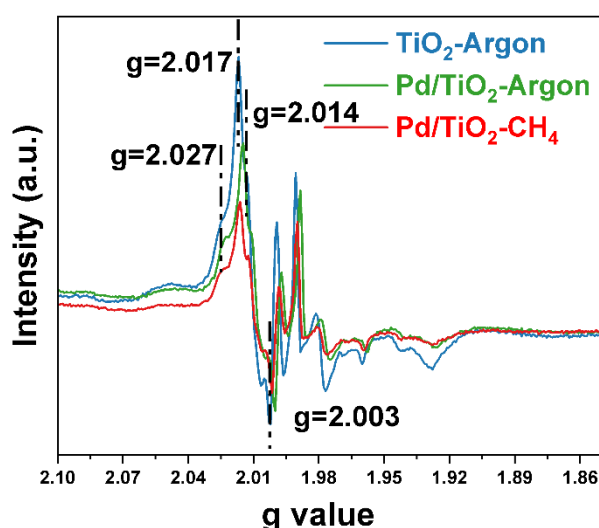


Figure 5-27 In situ EPR spectra of TiO_2 and Pd/TiO_2 in an argon atmosphere and CH_4 atmosphere upon light irradiation.

Furthermore, the valence-band XPS was used to identify the valence band maximum (VBM) of TiO_2 before and after loading the alloy cocatalyst. Figure 5-28 shows that some metal induced states are formed on the TiO_2 in addition to the VBM of TiO_2 after the introduction of Pd or PdCu alloy, which was also reported previously by the first-principles calculations based on density functional theory (DFT)¹⁹³. These states can trap the photoholes from the valence band of TiO_2 , consistent with the in situ EPR results.

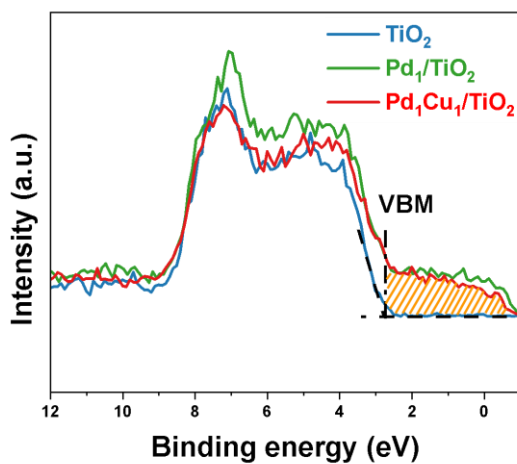


Figure 5-28 Valence-band XPS spectra of TiO_2 , Pd_1/TiO_2 , and $\text{Pd}_1\text{Cu}_1/\text{TiO}_2$.

In situ XPS was then carried out to further confirm the charge transfer from TiO_2 to Pd in PdCu/TiO_2 via the observation of Pd chemical state in the presence and absence of light irradiation, as shown in Figure 5-29.

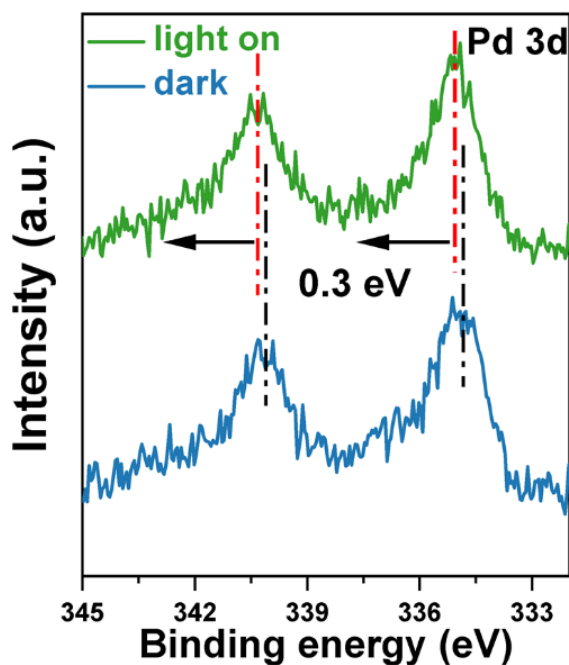


Figure 5-29 In situ Pd 3d XPS spectra of PdCu/TiO_2 under the dark condition and under light irradiation.

A positive shift of ~ 0.3 eV for both Pd $3d_{5/2}$ and $3d_{3/2}$ peaks are clearly observed during light irradiation, showing direct evidence that Pd works as a hole acceptor during the photocatalytic reaction. All these measurements confirm that the alloy functions as the efficient hole acceptor, which would promote the separation of photo-induced charge carriers and lower the oxidative potential, thus improving methane conversion and mitigating the overoxidation of the products by photoholes. Moreover, when the argon atmosphere was replaced by methane atmosphere in the in-situ EPR measurement, the intensity of these two sets of g values is reduced further (Figure 5-27). This result implies that methane has a similar function as Pd, i.e. methane can donate the electrons to the orbitals of Pd. It is unable to compare the spectra of PdCu/TiO₂ here with other samples due to the inference of the very strong Cu EPR signal by shifting the baseline, as shown in Figure 5-30.

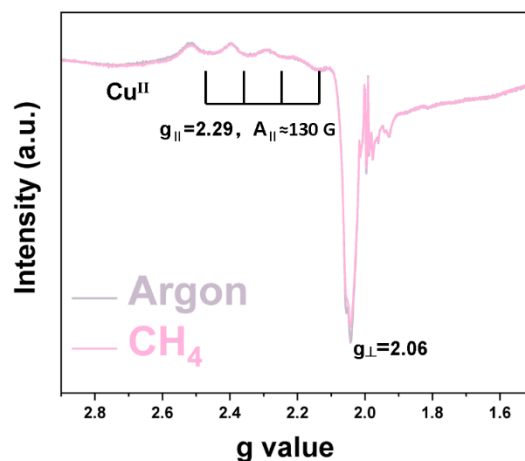


Figure 5-30 In situ EPR spectra of PdCu/TiO₂ under argon atmosphere and CH₄ atmosphere upon light irradiation.

Noted that even a trace amount of Cu^{II} species (far below the detection limit of XPS) would have a strong EPR signal and shift the baseline.^{100,156} However, it was very hard to completely rule out the influence of Cu^{II} as the surface of metallic Cu was very easy to be oxidized more or less under aerobic conditions, although the chemical state of

Cu remained mainly at a metallic state before and after reaction as discussed above. In addition, the overlap of Cu^{II} signal under argon atmosphere and methane atmosphere suggests that methane can not be easily activated on Cu only.

The enhanced charge separation was further proved by photoluminescence (PL) and transient photocurrent response, as shown in Figure 5-31 and Figure 5-32. Although all four samples have similar light absorption based on UV-Vis DRS spectra (Figure 5-12), different intensities of photoluminescence were observed over four samples. Among them, pristine TiO_2 displays the highest PL intensity, suggesting the highest radiative recombination rates of photo-induced electrons and holes. After loading Pd or Cu, the PL intensity is reduced, and loading the alloy dramatically reduces the PL intensity by 50%, likely due to effective enhancement of the charge transfer and separation in TiO_2 .

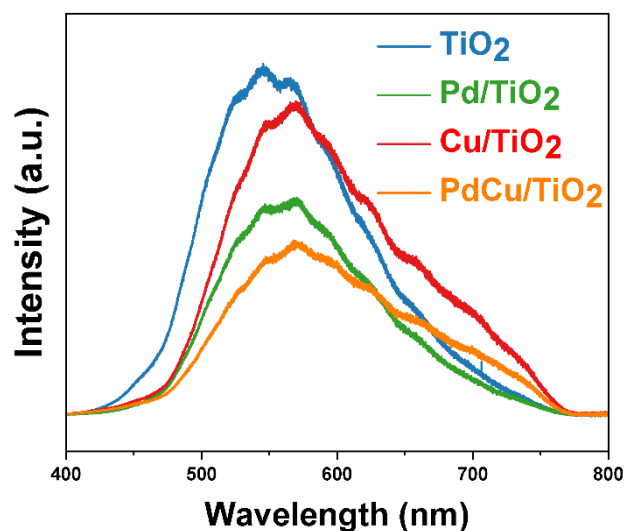


Figure 5-31 Photoluminescence spectra of TiO_2 , Pd/TiO_2 , Cu/TiO_2 and PdCu/TiO_2 .

Furthermore, PdCu/TiO_2 also exhibits the highest photocurrent, more than 4 and 2 times higher than the pristine TiO_2 and single metal decorated TiO_2 , respectively, which consolidates the efficient transfer of photo-induced carriers from TiO_2 to the

alloy nanoparticles. As the photocatalytic OCM involves two redox reactions (methane oxidation by photoholes and oxygen reduction by photoelectrons), we also carried out the electrochemical oxygen reduction experiments, as shown in Figure 5-33.

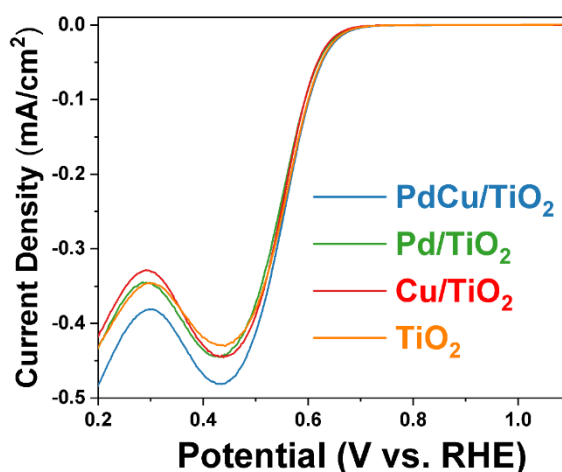


Figure 5-32 Electrochemical oxygen reduction spectra over TiO_2 , Pd/TiO_2 , Cu/TiO_2 and PdCu/TiO_2 in 0.1 M KOH electrolyte.

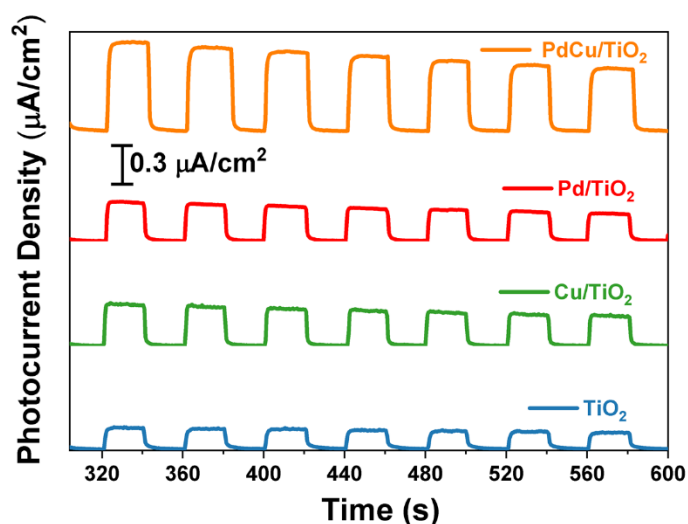


Figure 5-33 Photocurrent densities of TiO_2 , Pd/TiO_2 , Cu/TiO_2 and PdCu/TiO_2 .

All samples present a similar onset potential, because the co-catalysts work as the hole acceptors in all cases and the active sites for oxygen reduction should be located on

TiO₂ itself. The enhanced reduction current density after loading of co-catalysts can be attributed to the efficient charge transfer. All these characterisations suggest that photoholes transfer to the alloy PdCu after the excitation for the subsequent oxidation reaction and photoelectrons are located on TiO₂ for the reduction reaction.

5.2.4 Investigation of the photocatalytic mechanism

After an investigation of the charge separation and transfer, the next step is to observe the interface reactions in a completed photocatalytic cycle. DFT calculations were then carried out in order to reveal the interaction between the surface of the photocatalyst and the reactant methane, as shown in Figure 5-34.

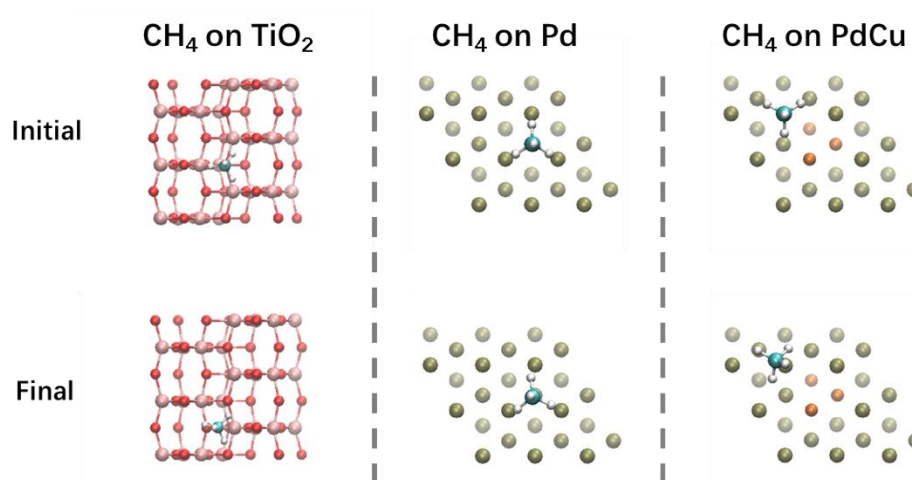


Figure 5-34 DFT calculated structures of methane adsorption on anatase, Pd and PdCu surfaces.

A series of configurations for methane adsorption on the (101) surface of anatase TiO₂, (111) surface of Pd and (111) surface of PdCu were screened, and three representative initial structures and the corresponding final structures with the lowest energies are displayed here. Methane molecules show a final adsorption structure with three C-H

bonds pointing down to the surface and one C-H bond pointing up. The length of the C-H bond in the highly symmetric methane molecule in the gas phase was calculated as 1.099 Å and there is almost no change of all the C-H distance (pointing up and down) after adsorption on TiO₂, as shown in Table 5-3.

Table 5-3 DFT calculations results of methane adsorption on TiO₂, Pd and PdCu.

System	Adsorption energy (kJ/mol)	C-H bond distance (H down) (Å)	C-H bond distance (H down) (Å)	C-H bond distance (H down) (Å)	C-H bond distance (H up) (Å)
CH ₄ on TiO ₂	-22.54	1.101	1.101	1.099	1.099
CH ₄ on Pd	-24.71	1.104	1.103	1.102	1.101
CH ₄ on PdCu	-22.38	1.106	1.104	1.099	1.000

In contrast, the length of C-H (pointing down) could be extended to 1.102-1.104 Å when methane was on the surface of Pd, indicating a stronger interaction between H of methane and Pd than that between H of methane and TiO₂. Such softened C-H bonds in methane through the interaction with the Pd surface have also been observed previously¹⁷⁵, and they were easier to be activated, in particular beneficial for the holes with lower oxidative potential in Pd. It should be noted that the elongation of C-H bonds of the methane molecule is also observed over the PdCu surface, in which the length of C-H bonds (pointing down) could be up to 1.106 Å, indicating that the pre-activation effect is maintained after the formation of alloy nanoparticles. However, the strong interaction between H and the active sites may also result in the stronger

binding of as-formed products (e.g., C₂H₆ in this work), mitigating their desorption and accelerating coking that would block the active sites to cause the catalyst deactivation. This is likely to explain the declining activity trend of Pd/TiO₂ (Figure 5-3). To further prove this assumption, the Raman spectroscopy investigation of the catalyst using a higher energy laser (enhanced by a factor of ten) was carried out after the photocatalytic OCM reaction to detect coke species in the range of 1000 – 3000 cm⁻¹, as shown in Figure 5-35. Before the reaction, the sample exhibits two peaks with low intensity at around 1350 (D mode) and 1600 cm⁻¹ (G mode) and a very small peak at ~2900 cm⁻¹ related to the combination of two modes under very strong laser excitation, respectively, which could be attributed to the tiny residue of amorphous carbon adsorbed on the TiO₂ photocatalyst^{194–197}. After only 5 hours of reaction over Pd/TiO₂, all peak intensities are strongly enhanced. These typical bands confirm the formation of cokes during photocatalytic OCM reaction over Pd/TiO₂, resulting in rapid deactivation.

Raman spectroscopy with high energy laser was also carried out to further examine the cokes species on the optimised catalyst PdCu/ TiO₂ after the 112 hours stability

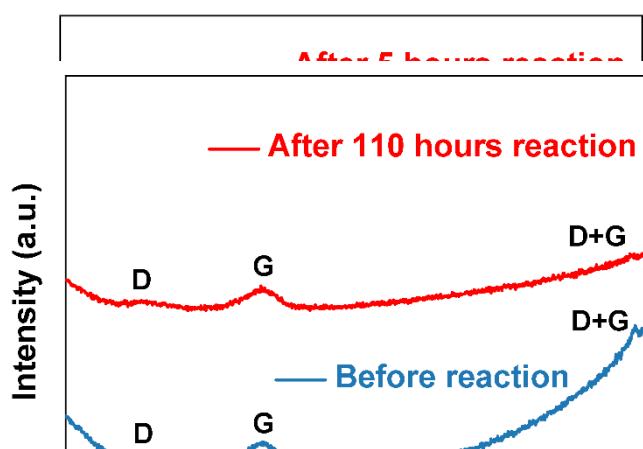


Figure 5-36 Raman spectra of PdCu/TiO₂ before and after 110 hours of reaction in the range of 1000-3000 cm⁻¹.

test. Interestingly, all peak intensities in particular the peak at $\sim 2900\text{ cm}^{-1}$ was dramatically reduced, as shown in Figure 5-36. These results further support the conclusion that the introduction of Cu could promote the release of as-formed products and enhance coke resilience. Thus incorporation of a tiny amount of Cu to form alloy nanoparticles with Pd could weaken binding to adsorbates (e.g., ethane in my cases), resulting in the coke-resistant phenomenon as reported in thermocatalysis.^{127,160,178,198}

DFT calculations were thus conducted to gain an in-depth understanding of ethane adsorption on Pd and PdCu. Several initial positions of ethane on Pd (111) were investigated and final structures always end with two carbon atoms above two Pd atoms. The adsorption energies are also the same, thus one representative final structure with two carbons above two Pd atoms is displayed in Figure 5-37.

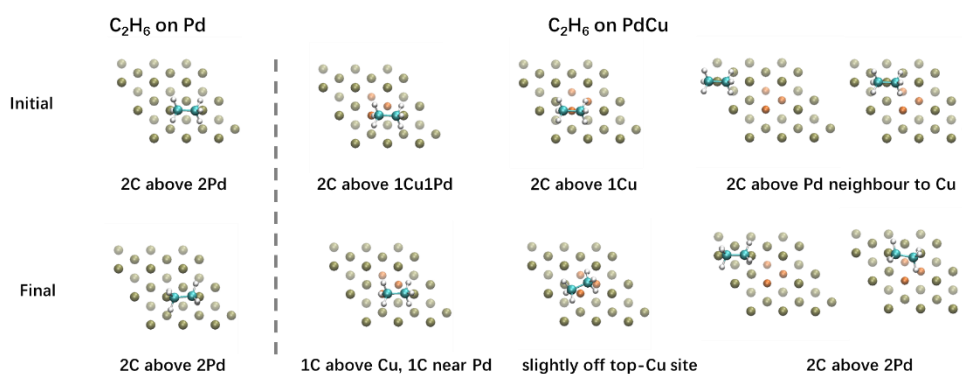


Figure 5-37 DFT calculated structures of ethane adsorption on Pd and PdCu surfaces. (For colours in Fig. 4a and b: red – O, pink – Ti, tan – Pd, orange – Cu, teal – C, white – H. Brighter colours of metal atoms denote atoms in the top (surface) layer)

Table 5-4 DFT calculations results of ethane adsorption on Pd and PdCu.

System	Final structures	Adsorption energy (kJ/mol)
C ₂ H ₆ on Pd	2 carbon above 2 Pd	-40.61
C ₂ H ₆ on PdCu	1 carbon above Pd and 1 carbon above 1 Cu (direct involvement of Cu)	-36.80
C ₂ H ₆ on PdCu	2 carbon above 1 Cu	-36.27
C ₂ H ₆ on PdCu	2 carbon above 2 Pd neighbored one Cu atom (indirect involvement of Cu)	-39.80 or -40.42 (depending on the distance of Pd to Cu)

Then, representative structures of ethane adsorbed on a model alloy where one Pd atom per layer was replaced with one Cu atom were studied: a structure with one carbon atom of ethane above a Pd atom and the other carbon above a Cu atom, a structure with both carbons of ethane above one Cu, and two structures with two carbons above two Pd atoms neighbour to Cu. As expected, the direct involvement of Cu atoms effectively decreased the adsorption energies of the ethane molecule (Table 5-4), by up to ca. 4 kJ/mol, suggesting the as-formed ethane products can be more easily released from PdCu than from pure Pd, avoiding the consecutive reactions to form cokes. A similar strategy was recently used with the isolation of the Pd site by other components to inhibit coke accumulation in a hydrogenation reaction.¹⁸⁷ Thus, it is reasonable to witness an unchanged activity after even 112 hours of reaction over PdCu/TiO₂ using the alloy nanoparticles.

Based on the discussion above, a probable reaction mechanism for photocatalytic OCM reaction over PdCu/TiO₂ was proposed as shown in Figure 5-38. Upon light irradiation, photoelectrons excited from the valence band (VB) of TiO₂ to the conduction band (CB) would reduce oxygen to form superoxide radicals on TiO₂, while photoholes from the valence band of TiO₂ would transfer to PdCu alloy nanoparticles where methane is adsorbed, as indicated by DFT modelling. The generated positively charged states would break the pre-softened C-H bonds in the adsorbed methane molecules to form methyl radicals and protons. The coupling of methyl radicals produces ethane molecules and some of them may be further dehydrogenated to form ethylene. The protons would then be consumed by the superoxide radicals to generate water, thus completing the cycle. Moreover, the efficient charge transfer and activation of methane after the introduction of Pd nanoparticles would generate more methyl radicals, which also enhances C₂ selectivity rather than overoxidation to CO₂ owing to the second-order nature of the coupling reaction to form ethane.¹⁴⁷ The formation of alloy with Cu is important to further increase the charge separation as proved by both PL and photocurrent measurement, to maintain a moderate binding of the absorbates, and more crucially to reduce the adsorption energy of the product of interest, thus maintaining high selectivity to C₂ and avoiding coking. The synergy effect of PdCu alloy nanoparticles demonstrates a stable, efficient, and selective photocatalytic OCM cycle.

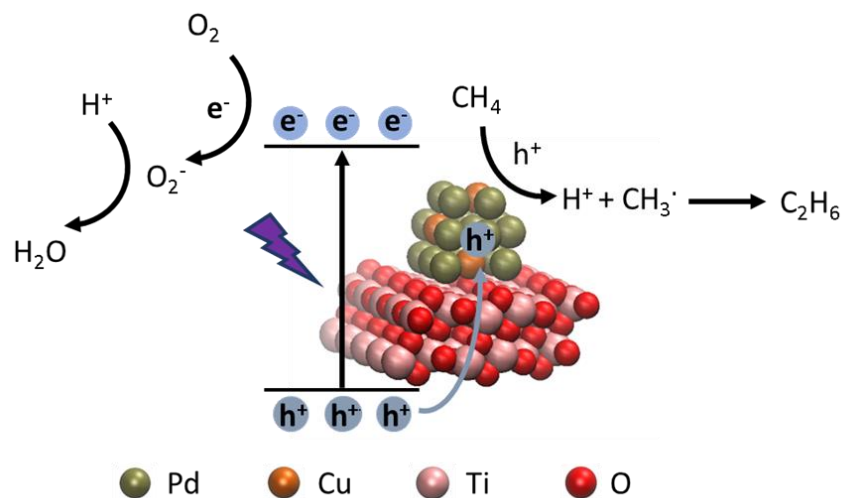


Figure 5-38 Possible reaction scheme for photocatalytic OCM over PdCu/TiO₂.

5.3 Conclusion

In summary, a continuous photocatalytic OCM process has been reported over PdCu/TiO₂ under ambient conditions with the highest efficiency and stability. The C₂ yield rate of 62 μmol h⁻¹ has been achieved with the ratio of CH₄/O₂ = 53:1 and a space velocity of 342000 mL g_{cat}⁻¹ hour⁻¹, generating the highest AQE of 8.4% at 365 nm exceeding all the previously reported AQE in photocatalytic methane conversion to C₂ product under ambient conditions thanks to the synergy of Pd and Cu in the alloy co-catalyst. Through the manipulation of the ratio of CH₄ to O₂, CO₂ production decreased by more than two-thirds and high C₂ selectivity of 75% has been obtained, which is comparable to or even higher than the best OCM catalysts (e.g., Li/MgO; Mn/Na₂WO₄/SiO₂) in thermocatalysis operated at >873 K. An unprecedented high TON of 12,642 has thus been achieved together with this high C₂ selectivity, being a new record in the photocatalytic methane coupling reaction. Furthermore, the remarkable stability has been demonstrated as there is no any decay of the activity up to 112 hours test, which is so far the longest reaction time reported in photocatalytic

methane conversion. The excellent activity should be attributed to the successful formation of PdCu alloy nanoparticles, as confirmed by high-quality HAADF-STEM. The functions of Pd and Cu were thoroughly investigated by a series of technologies (including in-situ EPR and in-situ XPS). It is found that photo-induced holes on TiO₂ can be effectively consumed by the electrons from PdCu, which not only retards the charge recombination but also generates new oxidative orbitals with lower oxidative potential on PdCu, thus driving the selective conversion of methane to ethane instead of CO₂. DFT calculations provided an in-depth understanding of the synergy effect between Pd and Cu. Pd works as the active site to soften the C-H bond in methane and Cu enhances the coke-resilience of the catalysts via decreasing the adsorption energy of as-formed products. Overall, the findings in this work demonstrate that the assembly of different components to form multifunction nanoparticles would be a promising strategy to meet the challenges in photocatalytic methane conversion. Although the results achieved in this chapter are improved compared with chapter 4, a few factors should be further improved, including: 1. the conversion rate up to the level of mmol h⁻¹; 2. higher selectivity to 90%; 3. higher AQY to >10% ensuring a higher light utilisation efficiency; 4. the optimisation of this flow reactor, such as the relationship between activity and catalyst mass, the light utilisation efficiency and the thickness of membrane; 5. the investigation of reaction temperature, in particular the kinetic viewpoint; 6. the investigation of photophysics at the time scale of microseconds; 7. the simplification of photocatalyst fabrication procedure to be time-saving and easy-operation; 8. the understanding of interface interaction between methane and catalyst with experimental evidence. In addition, it is interesting to find that the functional model of the metallic co-catalyst (Pd or PdCu) as hole acceptor is different from that (Pt) as electron acceptor in previous chapter. The work function of

Pt is at around 6.10 eV,¹⁹⁹ while the work function of PdCu can vary from 5.35 eV for pure Pd to 4.70 eV for pure copper.²⁰⁰ All these values are higher than the work function of TiO₂ (~4.5 eV) and the electron is expected to input from the CB of TiO₂ to the Pt or PdCu from the consideration of Fermi level.^{27,201} The conclusion that PdCu as hole acceptor gained in this chapter seems to challenge the assumption that noble metal cocatalyst act as sinks for photoelectrons in many reports at the first glance. However, it should be noted that the values given above are for bulk metals and the real work function for small nanoparticles is hard to be determined so far due to the limited resolution (~ μm) of probe/beam.^{202,203} As the sizes of Pt (3.5-6 nm) and PdCu (~2.3 nm) in both chapters are far away from the range, the direct application of the band-alignment theory using the values of bulk metal is not appropriate. Furthermore, the interfacial band-alignment and electronic properties in metallic nanoparticles/semiconductors is greatly affected by the preparation methods (e.g., photodeposition, wet impregnation, precipitation and colloidal synthesis) and the widely claimed Schottky barrier (depletion region) by band bending does not always exist, especially in small nanoscale.¹⁵¹ This results in the different functions (hole acceptor/electron acceptor) of the same metallic nanoparticle by different preparation techniques. An advanced four-dimensional STEM technique developed recently to visualise the charge distribution in metallic Au nanoparticles on SrTiO₃ indicated that even the post-synthesis treatments of the same nanoparticle could vary the charge transfer behaviour (positive charges accumulation or negative charges accumulation) during reaction.²⁰⁴ Moreover, the accumulation of charges (photoelectrons/photoholes) on the metallic nanoparticle was found to change according to its specific local environment via the direct observation of Kelvin probe force microscopy under illumination.²⁰³ As different preparation methods were used for different metallic

nanoparticles (photodeposition for Pt in Chapter 4 and colloidal synthesis for PdCu/Pd in Chapter 5), it is reasonable to observe the different function models (hole acceptors/electron acceptors) based on the characterisations. The accurate determination of work function for metallic nanoparticle and the absolute understanding of band-alignment are very hard based on current techniques. It should be careful to propose the charge transfer pathway rather than the direct use of the term “electron sink by formation of Schottky barrier” obtained from idealised bulk TiO₂-noble metal junctions to rule all the photocatalytic systems. Independent research with more direct experimental evidence is highly recommended to resolve the specific role of metallic nanoparticles with different preparation methods in different catalyst systems, for example, the in situ techniques in this chapter and TAS measurement in next chapter.

6 Au/TiO₂ catalyst for photocatalytic oxidative coupling of methane with high selectivity and efficiency

As mentioned in previous two chapters, it is highly desired to develop a photocatalyst that can couple two methane molecules to value-added C₂ products under mild condition with high efficiency, selectivity, and stability. Although the previous chapters have achieved certain progress, such as the design of an efficient flow reactor, the precise control and synthesis of nanomaterials with multi-function, two most important criteria, CH₄ conversion rate (at the level of $\mu\text{mol h}^{-1}$) and selectivity to C₂ products are still moderate (<90%). This leads to a lower space time yield, far compared with those reported by conventional thermocatalytic OCM processes. The fabrication procedure of photocatalysts is time-consuming and difficult to scale-up, also impeding its further practical application. Furthermore, the understanding of the reaction mechanism on interface interaction between methane and a catalyst needs to be improved. In addition, the parameters of this flow system have not been optimized, resulting in the low light utilisation efficiency.

Herein, after a screening process of various noble metals on TiO₂ photocatalyst, Au with an excellent C₂ selectivity was selected as the targeted co-catalyst. Then, a facile and rapid (60 seconds) sputtering method was developed to homogeneously load Au on TiO₂ with exceptional activity. The optimised sample Au_{60s}/TiO₂ exhibits the highest methane conversion rate of 862 $\mu\text{mol h}^{-1}$ with a decent C₂ selectivity of 90% among all the reported photocatalytic methane conversion to C₂ processes, and it can be further improved to ca. 1.1 mmol h⁻¹ with the selectivity at around 90% (86% to C₂ and 93% to C₂₊) via manipulation of the ratio between CH₄ and O₂. This unprecedented

activity corresponds to the highest AQE of 10.3 ± 0.6 at 365 nm, suggesting the high utilisation efficiency of light. For the first time, the space time yield is as high as $23.4 \text{ mol kg}_{\text{cat}}^{-1} \text{ h}^{-1}$ for C_2 or $24.5 \text{ mol kg}_{\text{cat}}^{-1} \text{ h}^{-1}$ for C_{2+} , which is also comparable to all the benchmark thermal catalysts in conventional OCM processes operated at the high temperature ($>953 \text{ K}$) and the selectivity to C_2/C_{2+} is also at least 20% higher than that in conventional OCM processes. The photophysics was investigated by TAS, in situ XPS and TRPL, while the surface chemistry was explored by in situ EPR and in situ DRIFTS. The multi-function of Au is revealed, such as hole acceptor to promote charge separation and lower oxidative potential of photoholes, enhanced methane adsorption, active site for selective activation of C-H and coupling of C-C.

6.1 Experimental section

6.1.1 Materials preparation

The Au/TiO₂ on glass fibre membrane was prepared using a facile and rapid sputtering method, as shown in Figure 6-1. Typically, certain amount of TiO₂ (anatase, Millennium PC-50) was dispersed in 500 mL of deionized water and the mixture was sonicated for 20 minutes to achieve a good dispersion. Then, the mixture was filtered using a membrane (glass fiber, diameter 37 mm) to form a uniform TiO₂ nanoparticle layer on top of the membrane. The membrane was then transferred to the oven to dry at 60 °C. The loading process of Au was carried out using a simple and rapid way with a sputter machine (Agar Sputter Coater). The membrane loaded with TiO₂ was put on the middle of the round plate in the chamber. Next, the chamber was sealed, and a vacuum pump was turned on to evacuate the air. Then, certain amount of argon was introduced to the chamber and the sputter process was conducted using a current at ca.

30 mA. Different sputtering time could be set and the optimized sample was obtained with only 1 minute sputtering time. After refilling with air, the window of chamber was opened and the Au/TiO₂ sample on the glass fibre membrane was ready to use for photocatalytic methane conversion. The Au/TiO₂ with different sputtering times were denoted as Au_x/TiO₂, x = 5, 10, 20, 40, 60, 90 seconds. While the Au/TiO₂ with different loading amount of TiO₂ were denoted as Au/TiO₂-y, y = 5, 10, 15, 20, 25, 30 mg.

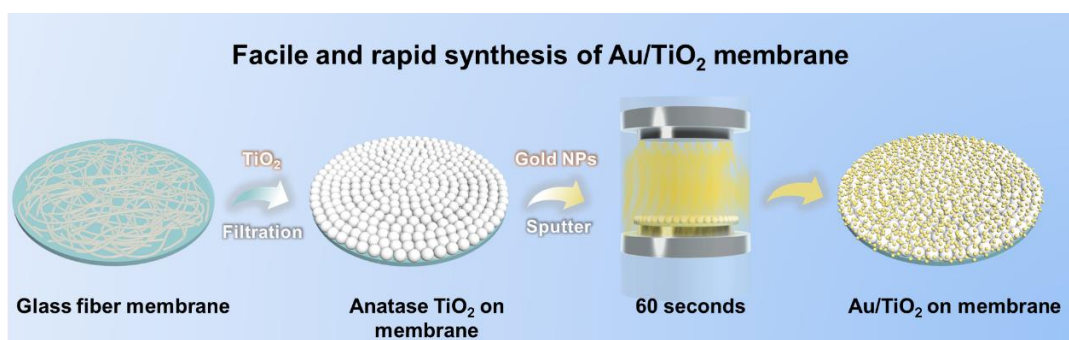


Figure 6-1 Schematic illustration of Au_{60s}/TiO₂ on glass fibre membrane preparation procedure

To synthesise the TiO₂ and Au/TiO₂ glass slides for TAS measurements, a doctor bladed method was used to prepare a homogenous and transparent film. A commercial Titania paste (Aldrich) was selected as the precursor of TiO₂ and a thin layer of TiO₂ was deposited on a 2×2 cm² glass slide. Then, the glass slide was transferred to the Muffle furnace and heated at 490 °C for 2 hours with a heating rate of 20 °C/min. After cooling to room temperature, a TiO₂ coated glass slide for TAS measurement was obtained. The loading of Au on this TiO₂ glass slide was via a simple photodeposition method. Typically, the TiO₂ glass slide was immersed in 10 mL of MeOH/H₂O solution (V_{H₂O}: V_{MeOH} = 4: 1) with a Au concentration of 0.1 mg/mL. After purging with argon for 3 minutes, the mixture was irradiated with a 365 nm LED light source

(95 W) for 15 seconds, during which the argon gas was supplied constantly. Then, the Au/TiO₂ glass slide was rinsed with DI water and dried at room temperature. Finally, the Au/TiO₂ glass slide was calcinated at 400 °C for 2 hours with a heating rate of 20 °C/min. In order to make sure that the Au/TiO₂ on the glass slide is same as Au_{60s}/TiO₂ prepared by the sputtering method, 22 Au/TiO₂ glass slides were fabricated, and the samples were scratched from each slide. The obtained powders were filtered on the glass fiber membrane and tested the photocatalytic OCM activity, which shows a similar activity (both C₂ yield rate and selectivity) to that of Au_{60s}/TiO₂. Thus, the Au/TiO₂ glass slide was used to carry out the TAS to explore the reaction mechanism on Au_{60s}/TiO₂.

6.1.2 Materials characterisations

The powder X-ray (XRD) spectra were recorded with a Stoe STADI-P instrument (2° to 40°, step 0.5 ° at 5.0 s/step) using Mo K α 1 (wavelength 0.70930 Å, 50 kV and 30 mA), in which the Au/TiO₂ membranes were cut into small pieces to fit the disk sample holder. Ultraviolet-visible diffuse reflectance spectroscopy (UV-Vis DRS) measurements were conducted by a SHIMADZU UV-2550 in reflectance mode using standard BaSO₄ powder as a reference. XPS Analysis was measured using a ThermoScientific XPS K-alpha and the data was analysed with CasaXPS software using C 1s peak at 284.8 eV for calibration. In situ XPS experiment was conducted using a Thermo Fisher ESCALAB 250Xi equipped with a 365 LED light source. PL spectroscopy was recorded by Renishaw InVia Raman with an excitation laser of 325 nm. TRPL was carried out by an FLS 920 fluorescence lifetime spectrophotometer (Edinburgh instrument, UK) with a 340 nm excitation laser and 455 nm detection wavelength. SEM imaging was conducted

using a Jeol JSM 7600 FEG-SEM with Energy Dispersive-X-Ray (EDX) module. STEM images were performed using a Cs-Corrected Jeol 2100FC Microscopy operating at 200KV. EPR was measured using a Bruker EMX PLUS spectrometer with a Xenon lamp (300 W). During the experiments, the mixtures of 30 μ L DMPO (200 mM in water) and 30 μ L sample (1 mg/mL in water) were used for the detection of hydroxyl radicals. For the detection of superoxide radicals, 1 mL MeOH was added in the above mixture as the holes scavenger. The signals were recorded under dark condition and 5 minutes light irradiation. TAS measurements were conducted by my collaborator Ms C. Li and Prof A. Cowan from the Department of Chemistry, University of Liverpool. The details of the experiment were described in Section 3.9. In situ DRIFTS was conducted by my collaborator Dr Q. Liu from the Institute of Analysis, Guangdong Academy of Sciences (China National Analytical Center, Guangzhou). The details of the experiment were described in Section 3.10.

6.1.3 Photocatalytic activity for methane conversion

The photocatalytic activity measurement of OCM was carried out using the system described in Section 3.11 with a few modifications. The power of light source can be adjusted from 10 to 100 W. The temperature of the reaction system could be controlled from room temperature to 140 °C. The loading amount of catalyst on the glass fiber membrane was optimised according to the reaction.

6.1.4 The calculation of CH₄ conversion rate and C₂/C₂₊ selectivity

The CH₄ conversion rate (r_{CH_4}) and C₂/C₂₊ selectivity calculation were based on the observable products (C₂H₆, C₂H₄, C₃H₆, C₃H₈, C₄H₈, C₄H₁₀ and CO₂) analysed and the formula was shown below:

$$r_{CH_4} = 2 \times (n_{C_2H_6} + n_{C_2H_4}) + 3 \times (n_{C_3H_8} + n_{C_3H_6}) + 4 \times (n_{C_4H_8} + n_{C_4H_{10}}) + n_{CO_2} \dots \text{eq. 6-1}$$

$$C_2 \text{ selectivity} = \frac{2 \times (n_{C_2H_6} + n_{C_2H_4})}{r_{CH_4}} \times 100\% \dots \text{eq. 6-2}$$

$$C_{2+} \text{ selectivity} = \frac{2 \times (n_{C_2H_6} + n_{C_2H_4}) + 3 \times (n_{C_3H_8} + n_{C_3H_6}) + 4 \times (n_{C_4H_{10}} + n_{C_4H_8})}{r_{CH_4}} \times 100\% \dots \text{eq. 6-3}$$

where n is the yield rate of different products.

6.1.5 Apparent quantum efficiency (AQE)

For the measurement of AQE, the light intensity was set to be 18.5 mw cm⁻². The flow rate of methane and air was set to 320 mL/min and 12 mL/min, respectively. The reaction temperature was maintained at 120 °C. Only C₂H₆, C₂H₄, C₃H₈ and CO₂ as products have been observed under irradiation with low intensity, thus they were taken into consideration in the calculation. To confirm the reproducibility, four membranes prepared at different times were used for this measurement, and the average value was obtained. The calculation formula was shown below:

$$AQE = \frac{(2 \times n_{C_2H_6} + 4 \times n_{C_2H_4} + 3 \times n_{C_3H_8} + 8 \times n_{CO_2}) \times N_A}{\text{Number of incident photons}} \times 100\% \dots \text{eq. 6-4}$$

where n is the yield rate of different products, N_A is the Avogadro constant, and the irradiation area was approximately 7 cm^2 . The light intensity was 18.5 mw cm^{-2} .

6.2 Results and discussion

6.2.1 Preliminary investigation

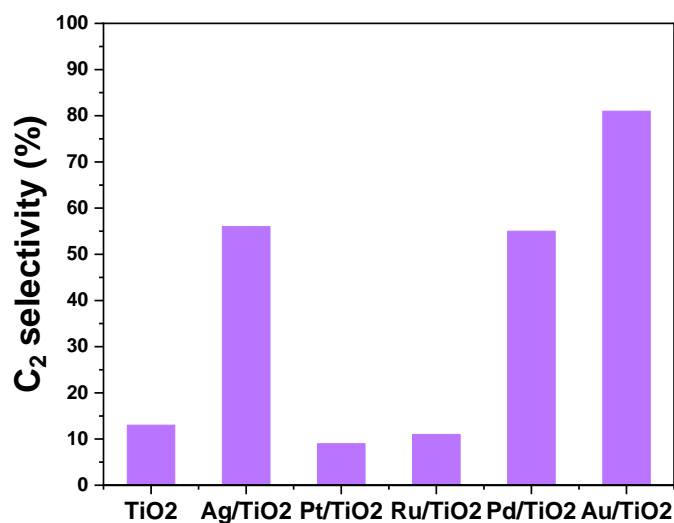


Figure 6-2 C₂ selectivity over different noble metal co-catalysts decorated TiO₂ with equal molar amount at 1.5 hour reaction time. (Reaction condition: gas hourly space velocity (GHSV = $342\ 000 \text{ mL g}_{\text{cat}}^{-1} \text{ hour}^{-1}$), CH₄: O₂ = 114: 1, 10% of CH₄, Ar as balance gas, 365 nm LED 40 W, 30 °C)

During the evaluation of different noble metal co-catalysts for photocatalytic OCM reaction, it is found that the loading of Au can greatly improve the C₂ selectivity (Figure 6-2) despite of the relatively lower C₂ yield rate than Pd (Figure 5-1) presented in Chapter 5. The C₂ selectivity over Au can reach as high as 81%, which is even higher than the optimised sample PdCu/PC-50 (75%) under the optimised reaction condition in Chapter 5. Therefore, Au was selected as the most effective single co-catalyst for further investigation in this Chapter.

6.2.2 Rapid preparation of Au/TiO₂ on glass fibre membranes

The loading methods of co-catalysts are photodeposition, impregnation, and NaBH₄ reduction method in Chapter 4 and 5, which are time-consuming with multi-steps, difficult to scale up. Thus, a facile and rapid sputtering method was developed to load metallic Au nanoparticles on TiO₂ efficiently, as shown in Figure 6-1.

The loading amount of gold can be easily controlled by the sputtering time. Figure 6-3 shows the relationship between loading amount and sputtering time. With the increasing sputtering time, the colour of the membrane gradually changes from pink to brown, probably due to the metallic lustre when increasing Au loading (Figure 6-4).

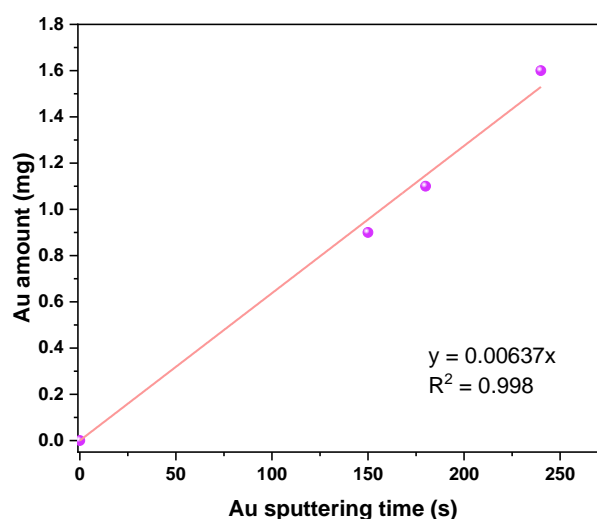


Figure 6-3 The relationship between Au loading amount and the sputtering time.

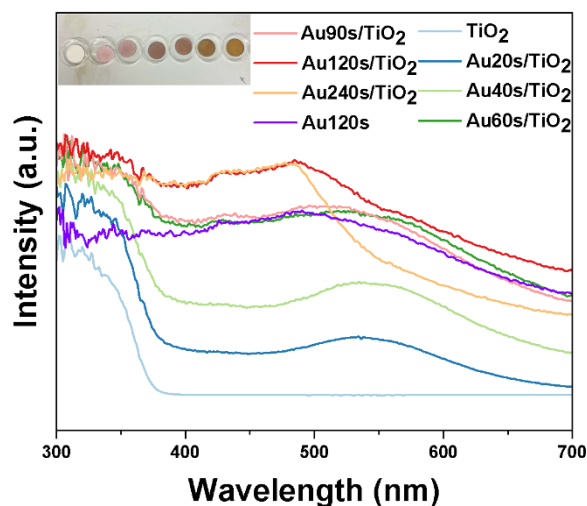


Figure 6-4 UV-Vis absorption spectra of membranes with different Au sputter time on 5 mg TiO₂ and pure Au without TiO₂ with 120s sputtering time. The insert is the photo of Au/TiO₂ on the glass fibre membranes (from left to right is Au0s, Au20s, Au40s, Au60s, Au90s, Au120s, Au240s).

The UV-Vis absorption spectra were further used to investigate the light absorption of the samples, as shown in Figure 6-4. For pure TiO₂ (the sample with 0 s sputter time), the absorption edge is at around 380 nm corresponding to the band gap of ca. 3.2 eV. After sputtering for 20 s and 40 s, a strong absorption peak at 550 nm assigned to the localised surface resonance (LSPR) of Au nanoparticles appears. Furthermore, no shift of the peak position can be observed after increasing the sputtering time from 20 s to 40 s, suggesting that the increasing sputtering time can only increase the loading amount of Au rather than change the size of the nanoparticles.²⁰⁵ The absorption edge belongs to TiO₂ can still be observed at around 400 nm. Further increasing sputtering time leads to a severe scattering of light due to the closely spaced nanoparticles,²⁰⁶ which results in the difficult observation of both LSPR peak and the absorption edge

of TiO₂. As shown by the 120 s Au sputtering on glass fibre membrane without TiO₂, the scattering is from visible region to the UV region. This scattering also explains the brown colour of the membranes with long sputtering time.

6.2.3 Photocatalytic OCM activity over Au/TiO₂/membrane

The photocatalytic OCM activity of these Au/TiO₂ membranes was then evaluated in the flow reactor (described in Section 3.10), as shown in Figure 6-5.

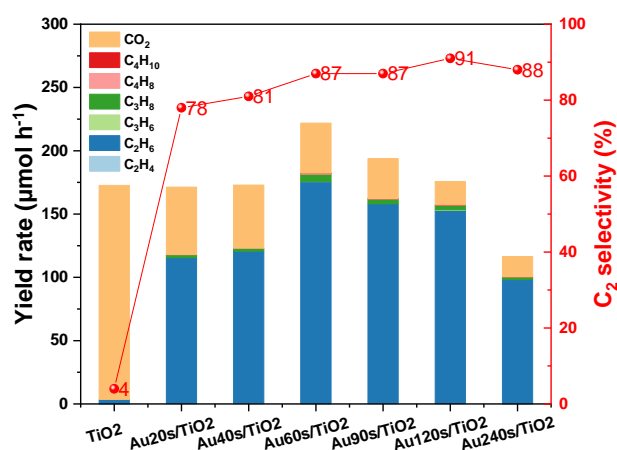


Figure 6-5 Photocatalytic OCM activity over Au/TiO₂ with different Au sputtering times (Au 0 s, Au 20 s, Au 40 s, Au 60 s, Au 90 s, Au 120 s, Au 240 s) on 5 mg TiO₂. (Reaction condition: 320 mL/min CH₄ and 4 mL/min Air, 365 nm LED 100 W, 338 K)

The main product over pure TiO₂ is CO₂, while the major product for Au/TiO₂ is C₂H₆, together with CO₂ and C₃H₈ and trace amount of other hydrocarbon products. The selectivity is significantly shifted to C₂ products once Au is introduced, from 4% over pure TiO₂ to more than 75% over all Au/TiO₂ samples. The C₂ yield rate exhibits a volcano trend with the increasing Au sputtering time, reaching the highest value (176 μmol h⁻¹) with an excellent selectivity of 87% at 60 s sputtering time. This sputtering time also gives a CH₄ conversion rate as high as 404 μmol h⁻¹, which is 2.3 times

higher than that of pristine TiO₂, suggesting a higher utilisation efficiency of photo-induced charges or a more effective methane activation. Further increasing the amount of Au can slightly increase the C₂ selectivity, while the C₂ yield rate decreases with a larger extent. As discussed above, excessive amount of Au nanoparticles can lead to

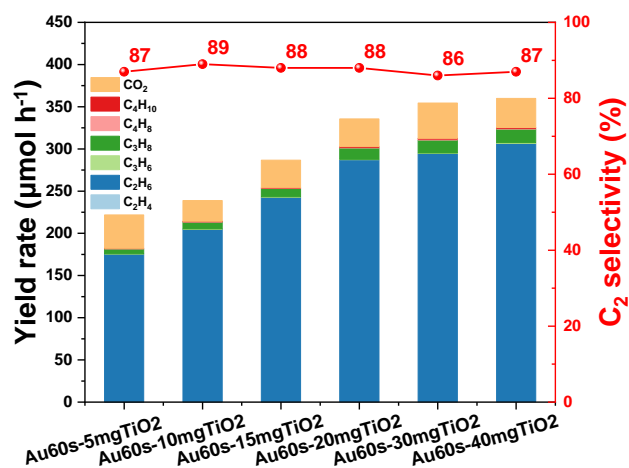


Figure 6-6 Photocatalytic OCM activity over Au60s/TiO₂ with different amounts of TiO₂ (5 mg, 10 mg, 15 mg, 20 mg, 30 mg and 40 mg). (Reaction condition: 320 mL/min CH₄ and 4 mL/min Air, 365 nm LED 100 W, 338 K)

strong scattering effect, which is detrimental to the effective light absorption. Taking into consideration of both C₂ yield rate and C₂ selectivity, as well as the cost of noble metals, 60 s was selected as the optimum sputtering time.

After the optimisation of the sputtering time, the amount of TiO₂ was also investigated as shown in Figure 6-6. The C₂ yield rate increases with the higher amount of TiO₂, reaching 287 μmol h⁻¹ with 20 mg TiO₂, while the C₂ selectivity remains similar at around 88%. However, when the amount of TiO₂ exceeds 20 mg, the yield rate of C₂ products can hardly increase. This is because the light cannot penetrate the whole TiO₂ layer and the excessive amount (>20 mg) of TiO₂ at the relatively bottom position cannot be excited to drive the photocatalytic reaction, which will be discussed in detail

in section 6.2.5. Thus, the optimum amount of TiO₂ is 20 mg, while the ideal Au sputter time is 60 s corresponding to 0.38 mg. This optimum membrane was used for further investigation.

The influence of different reaction temperatures was then studied, as shown in Figure 6-7. The C₂ yield rate can be further increased through raising the reaction temperature, from 287 μmol h⁻¹ at 338 K to 388 μmol h⁻¹ at 393 K. The C₂ selectivity remains almost constant at 90%, indicating the stable performance of Au as a co-catalyst even under relatively high temperature (393 K/120 °C). This is also the highest C₂ yield rate among all the reported photocatalytic methane conversion processes, as shown in Table 6-1.

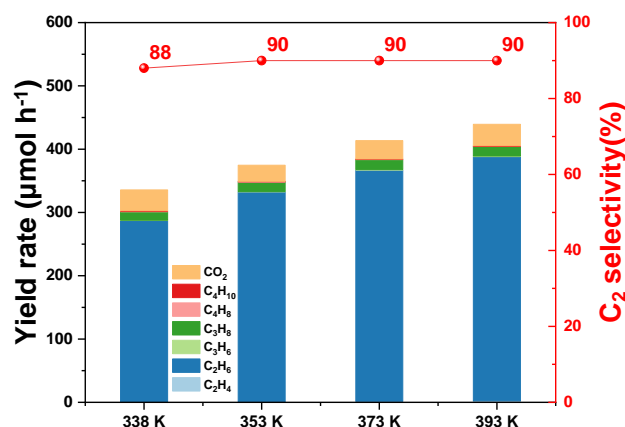


Figure 6-7 Photocatalytic OCM activity over Au60s/TiO₂ operated at different temperatures (338 K, 353 K, 373 K and 393 K). (Reaction condition: 20 mg TiO₂, 320 mL/min CH₄, 4 mL/min Air, 365 nm LED 100 W)

Table 6-1 Comparison of methane conversion to ethane/ethylene over different photocatalysts

Catalysts	Conditions	C ₂ yield rate ($\mu\text{mol h}^{-1}$)	C ₂ selectivity	AQE (%)
Au/TiO ₂ (This work)	Flow reactor; 393 K; 100 W 365 nm LED; 0.02 g catalyst; O ₂ : CH ₄ = 1: 133, GHSV = 996, 000 mL g _{cat} ⁻¹ hour ⁻¹ .	468	86%	10.3±0.6 at 365 nm
Pd ₁ /TiO ₂ ²⁰⁷	Batch reactor; Room temperature; 300 W Xe lamp; 3.0 mg catalyst; 0.1 MPa CH ₄ .	2.73	94.3%	3.05 at 350 nm
AuPd/ZnO ³⁷	Batch reactor; room temperature; 300 W Xe lamp; 2 mg catalyst; 0.5 mL CH ₄ .	0.08	99.9%	-
Au/Ga ₂ O ₃ ²⁰⁸	Flow reactor; 300 K; 40 W Hg lamp; 50 mg catalyst; 20 mL min ⁻¹ CH ₄ , 3.3-3.6 kPa H ₂ O.	57	92.2%	4.3 at 254 nm
Au/ZnO ¹⁷	Batch reactor; room temperature; 300 W Xe lamp; 0.5 mL CH ₄ .	0.01	100%	-
Ga ₂ O ₃ -K ⁶⁹	Batch reactor; 310 K; 300 W Xe lamp; 0.2 g catalyst; 200 $\mu\text{mol CH}_4$	0.054	96%	-
Pd-Bi/Ga ₂ O ₃ ²⁰⁹	Flow reactor; ca. 320 K; 300 W Xe lamp; 0.8 g catalyst; 3 mL min ⁻¹ CH ₄ , 27 mL min ⁻¹ Ar	1.10	97%	0.2 at 220-300 nm

MgO-SiO ₂ ¹⁴²	Batch reactor; 310 K; 300 W Xe lamp; 0.2 g catalyst; 200 μmol CH ₄	0.009	98%	-
Ce-Al ₂ O ₃ ⁷⁰	Batch reactor; 310 K; 300 W Xe lamp; 0.2 g catalyst; 200 μmol CH ₄	0.1	78%	-
Au-ZnO/TiO ₂ ¹⁵⁸	Flow reactor; 413 K; 300 W Xe lamp; 0.02 g catalyst; 69 mL min ⁻¹ CH ₄ , 1 mL min ⁻¹ Air.	100	90%	7.2 at 360 nm
Pd/Ga ₂ O ₃ ¹⁵⁷	Flow reactor; 300 K; 40W low-pressure mercury lamp; 0.05 g catalyst; 20 mL min ⁻¹ CH ₄ gas, 3.6 kPa.	47.4	75.8%	5.1 at 254 nm
Ag-H ₃ PW ₁₂ O ₄₀ /TiO ₂ ³⁶	Batch reactor; room temperature; 400 W Xe lamp; 0.1 g catalyst; 0.3 MPa CH ₄	2.3	90%	3.5 at 365 nm
Pt-CuO _x /TiO ₂ ¹⁰⁰	Flow reactor; 313 K; 40 W 365 nm LED; 0.1 g catalyst; CH ₄ : O ₂ =400: 1, 10%CH ₄ , GHSV = 2400 h ⁻¹	6.8	60%	0.5 at 365 nm
Pt/Ga-TiO ₂ -SiO ₂ ¹⁸	Batch reactor; room temperature; 300 W Xe lamp; 0.2 g catalyst; 44.6 μmol CH ₄	0.314	90%	0.0001 at 350 nm
Au/TiO ₂ ³⁰	Flow reactor; room temperature; 300 W Xe lamp; 5 mg catalyst; 10% CH ₄ , 90% Ar, GHSV= 120000 mL g ⁻¹ h ⁻¹	0.41	96%	-
Ga-ETS-10-0.2 ⁶⁶	Batch reactor; room temperature; 150 W Hg lamp; 0.2 g catalyst; 200 μmol CH ₄	2.2	74%	-

(Zn ⁺ , Zn ²⁺)-ZSM-5 ⁷²	Batch reactor; room temperature; 150 W Hg lamp; 1 g catalyst; 200 μmol CH ₄	2.9	99.6%	0.55 at 300-400 nm
TiO ₂ /SiO ₂ ¹⁷⁹	Batch reactor; 310 K; 300 W Xe lamp; 0.2 g catalyst; 200 μmol CH ₄	0.2	90%	-
SiO ₂ -Al ₂ O ₃ -TiO ₂ ⁶⁴	Batch reactor; 310 K; 250 W Xe lamp; 1 g catalyst; 200 μmol CH ₄	0.69	84%	-
H-MOR ¹⁸⁰	Batch reactor; 310 K; 250 W Xe lamp; 1 g catalyst; 200 μmol CH ₄	0.074	88%	
FSM-16 ²⁹	Batch reactor; 310 K; 300 W Xe lamp; 0.2 g catalyst; 200 μmol CH ₄	0.018	94%	
GaN: ZnO ¹⁸¹	Batch reactor; 293 K; 300 W Xe lamp; 0.05 g catalyst; 300 μmol CH ₄	2.85	98%	-
Zn ₅ (OH) ₈ Cl ₂ ·H ₂ O ¹⁸²	Batch reactor; 298 K; 300 W Xe lamp; 0.05 g catalyst; pure CH ₄	39.4	93%	-

The concentration of O₂ might play an important role in the manipulation of CH₄ conversion and C₂ production, thus different flow rates of O₂ were also investigated, as shown in Figure 6-8. Expectedly, both the conversion rate of CH₄ and the selectivity of C₂ products increases with more available O₂ molecules. When the flow rate of air reaches 12 mL/min, corresponding to the ratio of CH₄: O₂ at 133: 1, the CH₄ conversion rate and the yield rate of C₂ products can reach as high as 1.09 mmol h⁻¹ and 468 μmol h⁻¹, resulting in a C₂ selectivity of 86%. This is consistent with previous

chapter that higher concentration of O_2 can promote the generation of superoxide radicals, benefiting the conversion of methane while also promoting the overoxidation to CO_2 .¹⁰⁰

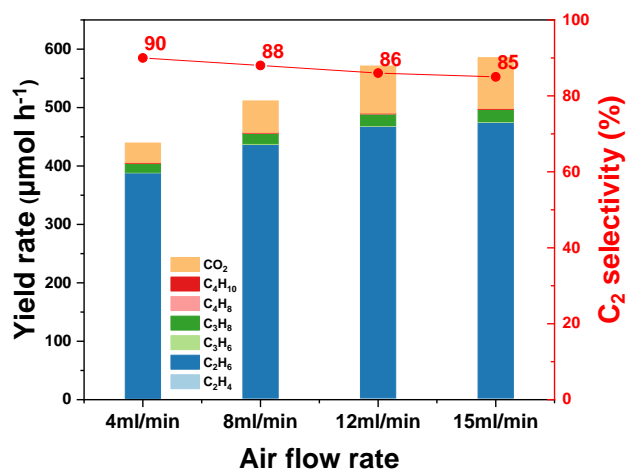


Figure 6-8 Photocatalytic OCM activity over Au60s/TiO₂ at 393 K with different Air flow rates. (Reaction condition: 20 mg TiO₂, 320 mL/min CH₄, 365 nm LED 100 W)

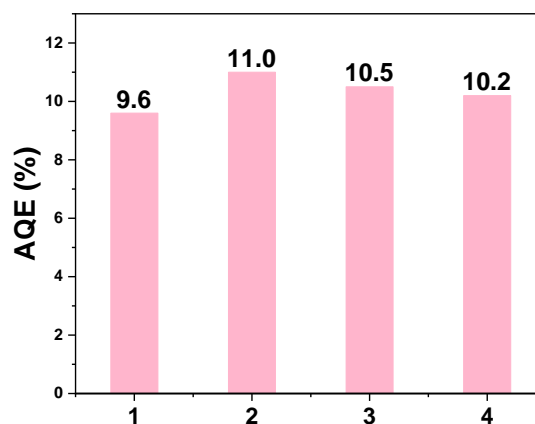


Figure 6-9 AQE of four Au60s/TiO₂ (20 mg TiO₂) membranes prepared at similar procedures but different times.

Therefore, it is reasonable to see an increase of CO₂ production when an air flow rate of 15 mL min⁻¹ was applied, which is nearly 10% increase compared with that at the flow rate of 12 mL min⁻¹. Considering a small increase (only 1.4%) of C₂ yield rate at the flow rate of 15 mL min⁻¹, 12 mL min⁻¹ was selected as the optimum air flow rate for later investigation. The optimised experimental condition is the GHSV of 977,

430 mL $\text{g}_{\text{cat}}^{-1} \text{hour}^{-1}$ with the ratio of CH_4 to O_2 at 133: 1 operated at 393 K. The methane conversion rate sets a new record with the unit of mmol h^{-1} in photocatalytic methane conversion to C_2 products at a high selectivity of around 90%. In particular, most of photocatalytic processes with such high level of selectivity often had a conversion rate of a few ten $\mu\text{mol h}^{-1}$, nearly 1000 times smaller than the current results. The AQE is the most important index for photocatalysis. In order to gain a reliable and reproducible AQE of this efficient photocatalyst, four Au60s/ TiO_2 (20 mg TiO_2) on glass fibre membranes were fabricated at different batches and tested under the optimised condition, as shown in Figure 6-9. The AQE was obtained via the method described at section 6.1.5. The Au60s/ TiO_2 membrane on average exhibits a high AQE of 10.3 ± 0.6 at 365 nm, which is also the highest among all the photocatalytic methane to ethane/ethylene processes (Table 6-1). This result indicates the high performance of Au60s/ TiO_2 is not only attributed to the optimisation of reaction systems but more importantly owing to its intrinsic photocatalytic properties. Such excellent activity of Au60s/ TiO_2 allows the comparison with those representative OCM catalysts by thermocatalysis, as shown in Table 6-2.

Table 6-2 Comparison of this work with representative OCM thermal catalysts (Note that some publications may use C₂₊ rather than C₂ taking higher hydrocarbons into account. Thus, the values for C₂ are in blue while the values for C₂₊ are in orange).

Catalyst	Reaction condition	Selectivity of C ₂ /C ₂₊ (%)	Space time yield (STY) of C ₂ /C ₂₊ products (mol h ⁻¹ kg ⁻¹ cat)
Au60s/TiO ₂ (This work)	393 K, 100 W 365 nm LED, O ₂ : CH ₄ = 1: 133, GHSV = 977, 430 mL g ⁻¹ h ⁻¹	86/93	23.4/24.5
Li-MgO ²¹⁰	1023 K, O ₂ : CH ₄ = 1: 3, GHSV = 10275 mL g ⁻¹ h ⁻¹	55	36.12
Li/MgO ²¹¹	993 K, O ₂ : CH ₄ = 1: 2, GHSV = 747 mL g ⁻¹ h ⁻¹	50.3	0.25
MnOx-Na ₂ WO ₄ /SiO ₂ ²¹²	953 K, O ₂ : CH ₄ = 1: 5, GHSV = 10,000 mL g ⁻¹ h ⁻¹	72	30.9
Ir-Mn _x O _y -Na ₂ WO ₄ ²¹³	1023 K, O ₂ : CH ₄ = 1: 4, GHSV = 60,000 mL g ⁻¹ h ⁻¹	46.7	40.02
TiO ₂ -Na ₂ WO ₄ /SiO ₂ ²¹⁴	973 K, O ₂ : CH ₄ = 1: 5, GHSV = 8,000 mL g ⁻¹ h ⁻¹	73	15
Mn ₂ O ₃ -TiO ₂ -Na ₂ WO ₄ /SiO ₂ ²¹⁵	1073 K, O ₂ : CH ₄ = 1: 5, GHSV = 8,000 mL g ⁻¹ h ⁻¹	76	18.3
La ₂ O ₃ ²¹⁶	1023 K, O ₂ : CH ₄ = 1: 4, GHSV = 600,000 mL g ⁻¹ h ⁻¹	64	83.7
LiCa ₂ Bi ₃ O ₄ Cl ₆ ²¹⁷	993 K, O ₂ : CH ₄ = 1: 2, GHSV = 1,500 mL g ⁻¹ h ⁻¹	46.5	6.5

Mn _x O _y - Na ₂ WO ₄ /SBA- 15 ²¹⁸	1023 K, O ₂ : CH ₄ = 1: 4, GHSV = 72, 000 mL g ⁻¹ h ⁻¹	67	67
Sm ₂ O ₃ ²¹⁹	1073 K, O ₂ : CH ₄ = 1: 4, GHSV = 18, 000 mL g ⁻¹ h ⁻¹	41	36.3

It should be noted that the space time yield (STY) of C₂/C₂₊ products over Au60s/TiO₂ is comparable to those classic thermal catalysts with a significantly higher temperature (at least 560 K higher). Such high temperature will undoubtedly increase the capital and operation cost, but it can completely be avoided in this efficient photocatalytic system using Au60s/TiO₂ as the photocatalyst. More importantly, Au60s/TiO₂ exhibits an unprecedented superiority of C₂/C₂₊ selectivity, which is around 90% and at least 20% higher than those in thermocatalysis. Considering the easy and rapid (60 seconds) fabrication of this unique membrane, this Au60s/TiO₂ shows the greatest potential for future practical application among all the photocatalytic methane conversion processes to the best of my knowledge.

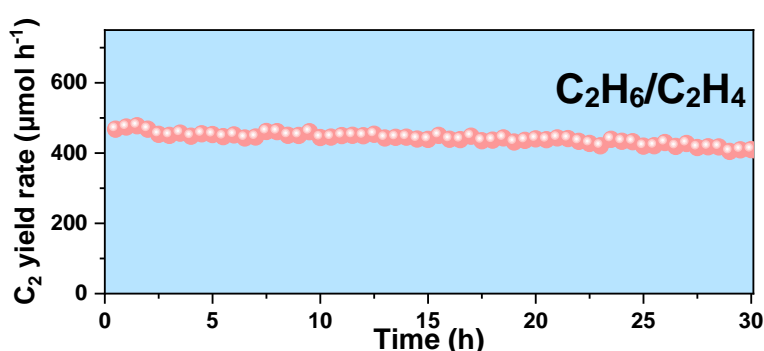


Figure 6-10 Stability test of Au60s/TiO₂ under the optimised reaction condition (Reaction condition: 20 mg TiO₂, 320 mL/min CH₄, 12 mL/min Air, 393 K, 365 nm LED 100 W)

The stability of Au60s/TiO₂ was also evaluated under the optimised reaction condition, as shown in Figure 6-10. Au60s/TiO₂ shows a stable C₂ yield rate in a 30-hour run despite of the fluctuation of the gas flow. Unlike the thermal catalysts that often suffer from deactivation of sintering or coke accumulation at high temperature, the high stability of Au60s/TiO₂ may benefit from the relatively mild photocatalytic reaction condition. Finally, a series of controlling experiments were carried out, as shown in Figure 6-11.

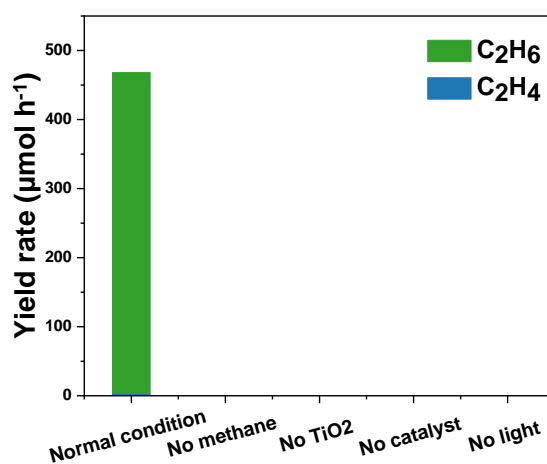


Figure 6-11 Controlling experiments over Au60s/TiO₂ under at optimised reaction condition (The normal reaction condition: 20 mg TiO₂, 320 mL/min CH₄, 12 mL/min Air, 393 K, 365 nm LED 100 W.)

Without light, the heating at 393 K cannot drive the reaction, indicating this reaction is a photon-driven process rather than a thermocatalysis process. This result is expected as OCM in thermocatalysis always requires a very high temperature as a driving force (Table 6-2). Furthermore, no production of C₂ products can be observed without the introduction of methane, which confirms CH₄ as the only carbon source. No products can be detected without a photocatalyst. This result excludes the self-decomposition of inert methane molecule via a photochemical process. Moreover, only loading of Au without TiO₂ also shows no activity, highlighting the important

role of TiO₂ as the main photocatalyst. The role of TiO₂ and Au was further investigated in section 6.2.5.

6.2.4 Characterisation of the optimised sample

The XRD patterns were used to examine the structure of the as prepared Au/TiO₂ membranes, as shown in Figure 6-12. All XRD patterns shows the typical peaks assigned to the anatase TiO₂ (JCPDS no. 84-1286). No peaks for Au species can be observed even after 90s sputter process (ca. 2.9 wt.%), this is probably owing to the high dispersion of Au as small nanoparticles, which is further confirmed by STEM in latter discussion.

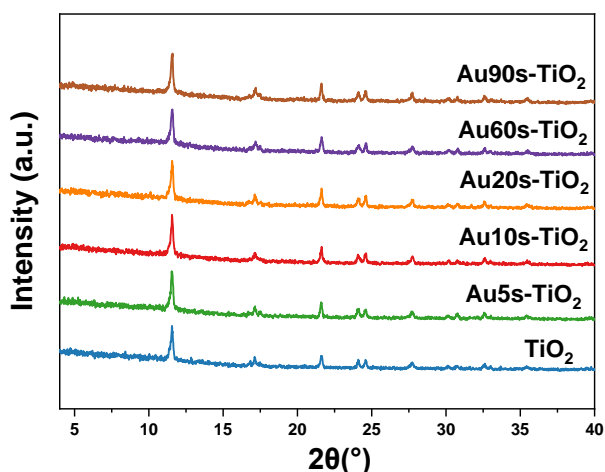


Figure 6-12 XRD patterns of TiO₂ with different Au sputter times (0 s, 5s, 10 s, 20 s, 60 s and 90 s).

The morphology of the Au60s/TiO₂ membrane was then investigated by SEM, as shown in Figure 6-13. From the top view of the SEM image (Figure 6-13 a and b), the TiO₂ nanoparticles generally disperses homogenously on the support of glass fibre membranes. While few long glass fibres can extend to the TiO₂ layer from the side view of the SEM image (Figure 6-13d), and the TiO₂ layer is approximately 238 μm

(Figure 6-13e). Using EDX mapping the distribution of Au on TiO_2 after the sputtering treatment can be observed (Figure 6-13 c and f). The intensity of Au element decreases with the increasing depth of membrane (Figure 6-13 f). This suggests that the Au mainly locates on the top surface of the TiO_2 layer, favouring to drive methane conversion during the photocatalytic reaction.

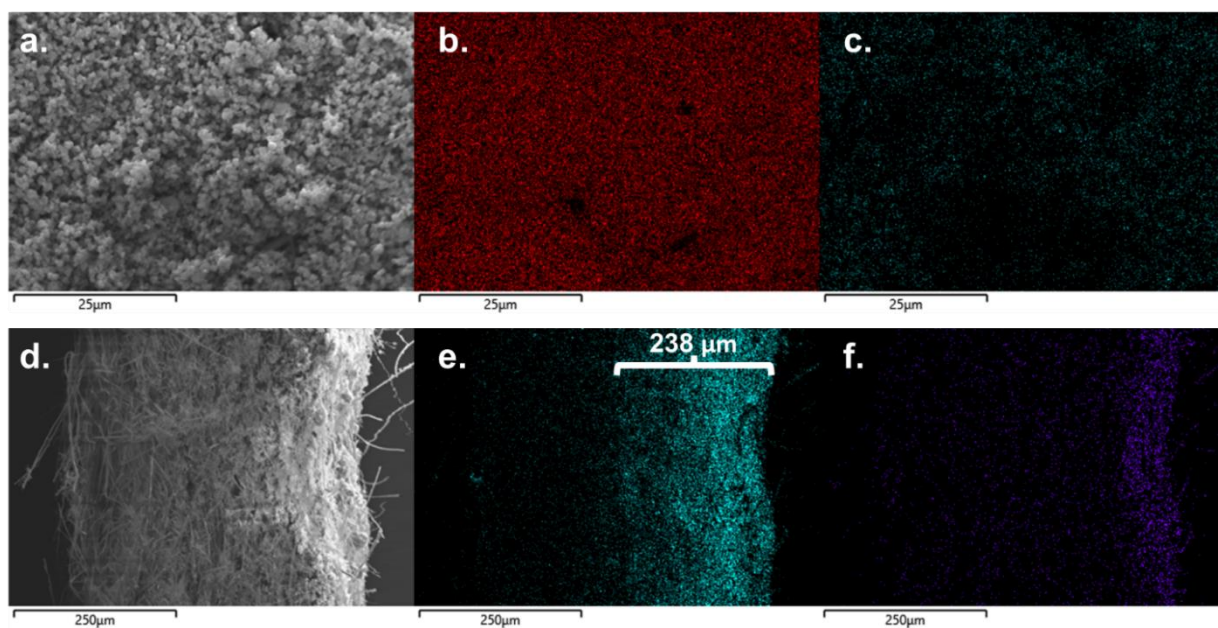


Figure 6-13 Top view SEM image (a) and EDX image of $\text{Au}_{60\text{s}}/\text{TiO}_2$ membrane (b for Ti element, c for Au element); Side view SEM image (d) and EDX image of $\text{Au}_{60\text{s}}/\text{TiO}_2$ membrane (e for Ti element, f for Au element).

To gain more structure information of Au over $\text{Au}_{60\text{s}}/\text{TiO}_2$ membrane, the sample was scratched from the membrane and used for STEM analysis, as shown in Figure 6-14. The STEM images show the distribution of small Au nanoparticles on the support of TiO_2 , in which the Au nanoparticles are the bright spots in the high angle annular dark-field image (STEM-HAADF, Figure 6-14 a) and the dark spots in the bright-field image (STEM-BF, Figure 6-14 b). The average particle size of the Au nanoparticles is determined to be 5.3 nm, as shown in Figure 6-14 c. These nanoparticles were

further identified by high-resolution STEM images (Figure 6-14 d, e), where the d spacing of lattice fringes is 0.230 nm, corresponding to the Au (111) planes.¹⁷

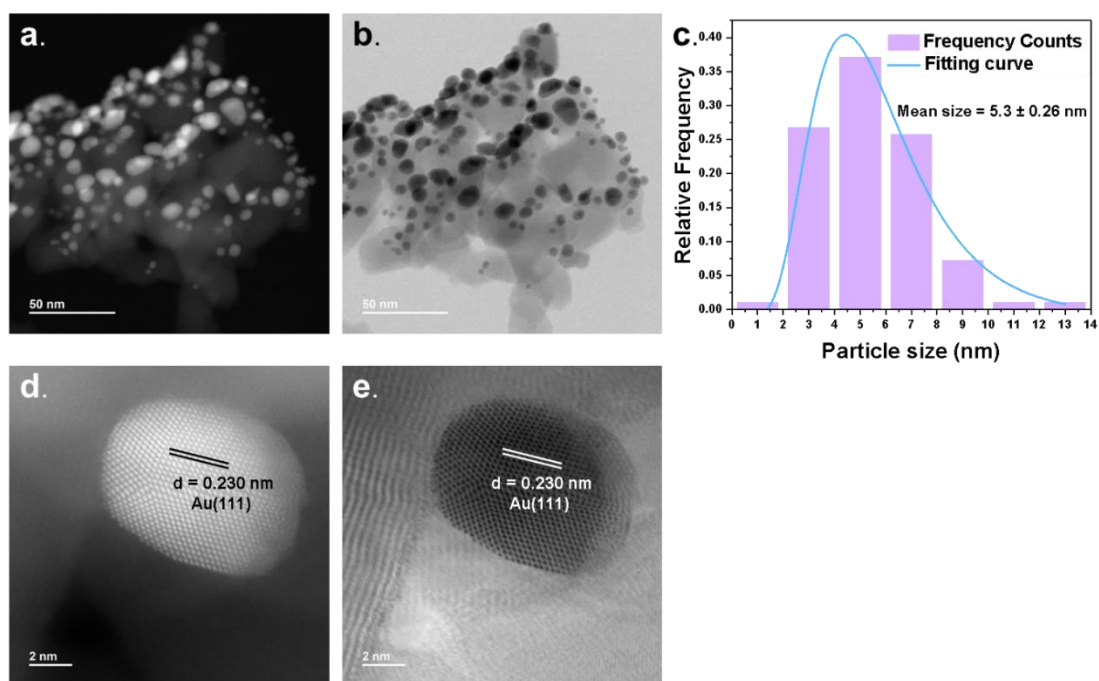


Figure 6-14 STEM-HAADF image of Au₆₀s/TiO₂ (a), STEM-BF image of Au₆₀s/TiO₂ (b), particle sizes distribution of Au on TiO₂ (c), high resolution STEM-HAADF image of Au nanoparticle (d) and high-resolution STEM-BF image of Au nanoparticle (e).

The chemical state of Au in the Au₆₀s/TiO₂ membrane was then investigated by XPS, as shown in Figure 6-15. Two types of Au species can be observed in the Au 4f spectra, in which the Au 4f_{7/2} at ca. 83.6 eV dominates the chemical states with a small amount of species at around 84.6 eV. The difference in binding energy is 1.0 eV, smaller than that between Au(0) and Au(I) (ca. 2 eV).^{220,221} Both species likely belong to partially negatively and positively charged metallic Au as the main Au 4f_{7/2} at ca. 83.6 eV is more negative than the metallic Au state (84.0 eV).²²¹ This is likely due to the injection of electrons from n-type semiconductor TiO₂ to Au during the loading process.¹⁸⁹

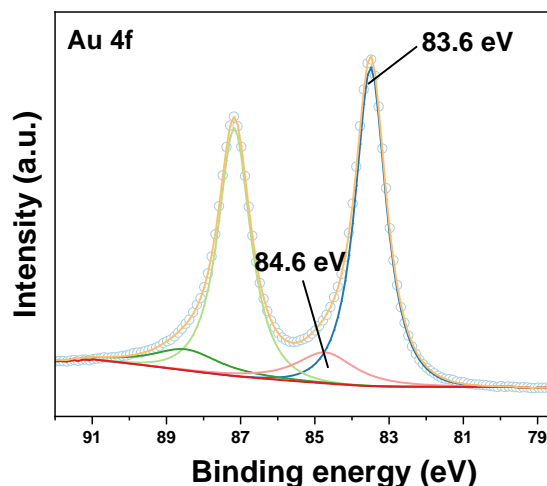


Figure 6-15 The XPS spectra of Au 4f in Au60s/TiO₂.

6.2.5 Investigation of the photocatalytic mechanism

The influence of the catalyst amount on the light response of the membrane was first investigated, as shown in Figure 6-16. BiVO₄ powder with an absorption edge at around 525 nm is used as a reference, which was firstly deposited on the surface of the glass fibre membrane. Then, different amounts of TiO₂ powder were introduced on top of the BiVO₄ layer and UV-Vis reflectance spectra were collected. Notably, after 10 mg of TiO₂ loading the typical light absorption of BiVO₄ exhibits a more than 90% decrease. Further loading of TiO₂ to 20 mg leads to nearly disappearance of the absorption edge of BiVO₄, indicates that light can hardly pass through the 20 mg TiO₂ layer to reach the BiVO₄ layer. This result explains almost no yield rate increases when more TiO₂ (> 20 mg) is loaded as mentioned in Section 6.2.3. The most appropriate loading amount of TiO₂ is thus fixed at 20 mg.

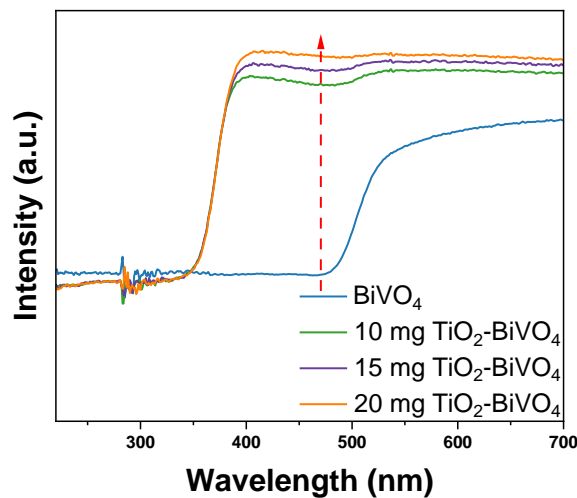


Figure 6-16 The UV-Vis reflectance spectrum of $\text{BiVO}_4/\text{TiO}_2$ mixed membranes (BiVO_4 , 10 mg TiO_2 (top)- BiVO_4 (bottom), 15 mg TiO_2 (top)- BiVO_4 (bottom), 20 mg TiO_2 (top)- BiVO_4 (bottom))

In the previous discussion, TiO_2 was regarded as the main photocatalyst and Au was considered as a co-catalyst. However, the Au itself may act as the main photocatalyst to drive the photocatalytic reaction via interband electronic transitions or surface plasma function reported previously,²⁰⁶ where TiO_2 only provides a suitable conduction band (CB) to accept the electron excited from Au. To clarify this, a series of semiconductors (SnO_2 and Ta_2O_5) with larger bandgap that can be hardly excited by 365 nm light source but with similar CB position to TiO_2 were used to couple with Au and tested in photocatalytic OCM,²²² as shown in Figure 6-17. The Au sputtering time of 2 minutes was used in order to provide as much Au nanoparticles as possible for interband electronic transitions. It should be noted that only the membrane loaded with TiO_2 show the activity of methane conversion, thus TiO_2 rather than Au as the main photocatalyst drives the reaction.

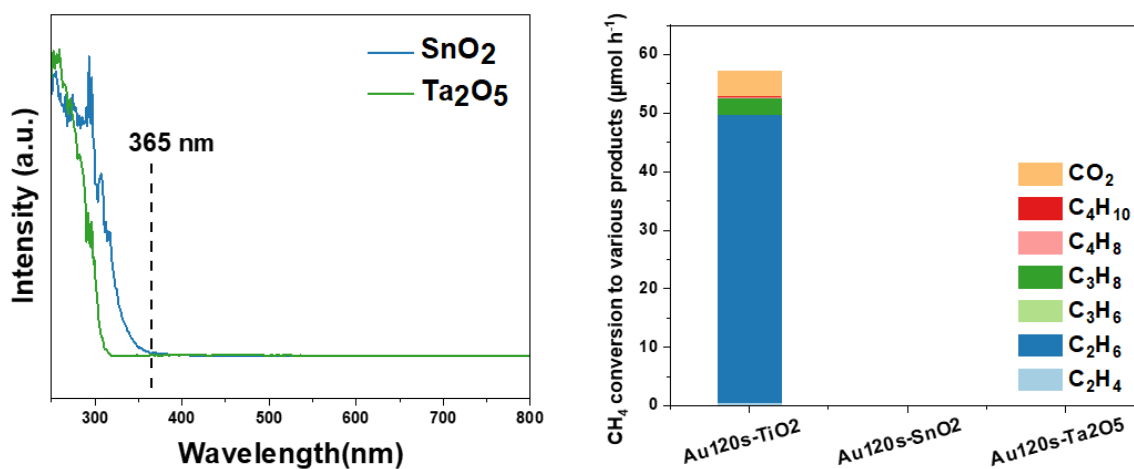


Figure 6-17 a. UV-vis absorption spectra of SnO₂ and Ta₂O₅. b. Photocatalytic OCM activity over Au120s/TiO₂, Au120s/SnO₂, Au120s-Ta₂O₅, and Au120s/GaN. (Reaction condition: CH₄: O₂= 114: 1, 40 W 365 nm LED, 285 mL/min total flow rate, 10% of CH₄, 303 K)

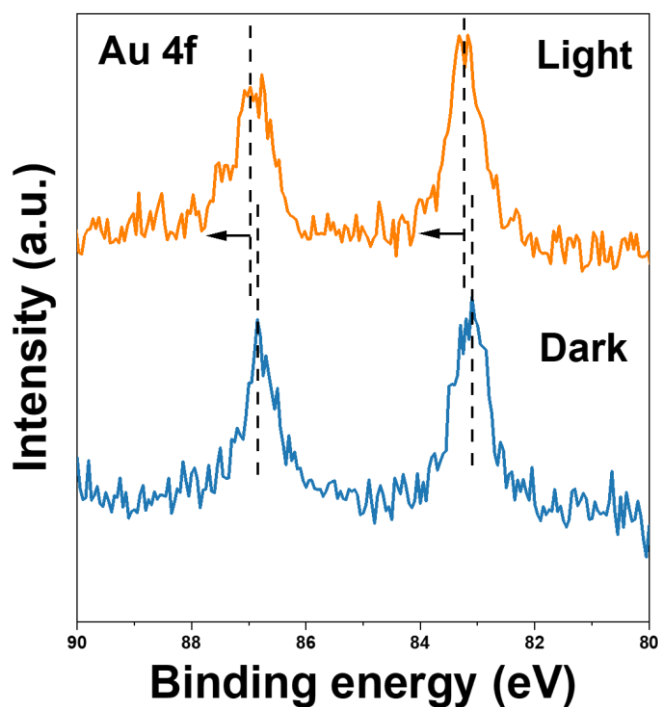


Figure 6-18 In situ XPS spectra of Au60s/TiO₂ (Au 4f) under dark and light irradiation conditions.

So far, the role of Au is most likely to be a co-catalyst to accept the as-formed photo-induced carriers formed on the main photocatalyst TiO_2 after 365 nm light excitation. During the excitation, two types of photo-induced carriers (electrons and holes) are generated. To distinguish which carrier is transferred to Au, the in situ XPS was conducted as shown in Figure 6-18. In the Au 4f spectra, a positive shift is observed when the sample is under light irradiation, suggesting that Au probably works as the hole acceptor in $\text{Au60s}/\text{TiO}_2$ during photocatalytic reaction.

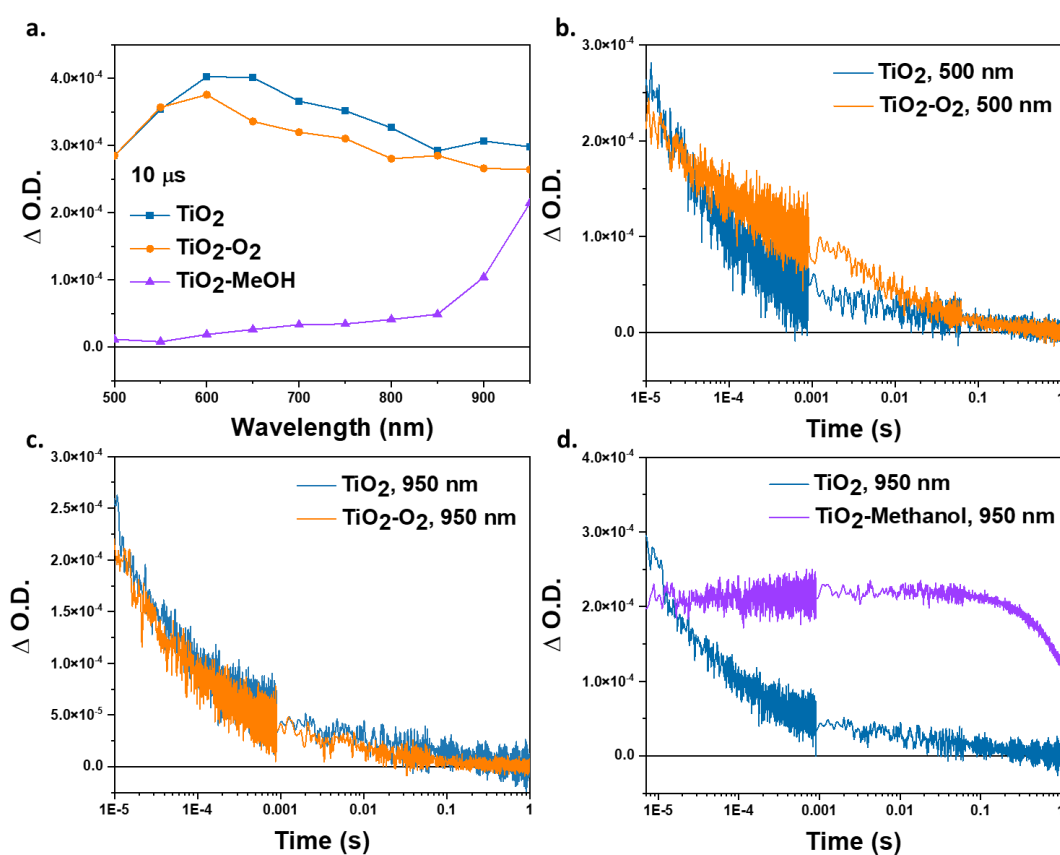


Figure 6-19 a. TAS spectra of TiO_2 excited by pulsed 355 nm excitation (0.40 mJ cm^{-2}) at the time scale of 10 μs under argon atmosphere, oxygen atmosphere and methanol vapor, respectively; b. TAS decay kinetics of TiO_2 probed at 500 nm and excited by pump 355 nm excitation under argon and oxygen atmosphere, respectively; c. TAS decay kinetics of TiO_2 probed at 950 nm and excited by pump 355 nm excitation under argon and oxygen atmosphere, respectively; d. TAS decay kinetics of TiO_2 probed at 950 nm and excited by pump 355 nm excitation under argon atmosphere with or without methanol vapor, respectively.

TAS, a useful technique to investigate the charge carrier dynamics, was further used to experimentally identify the function of Au at μs -s timescale. As shown in Figure 6-19a, a broad absorption appears from 500 to 950 nm after excitation of TiO_2 by a 355 nm laser under argon atmosphere probed at 10 μs timescale. Then, oxygen and methanol as the well-known efficient electron and hole scavengers, respectively, was used to identify the nature of the excited states. After introduction of O_2 (an electron scavenger), the amplitude after 600 nm exhibits a clear decrease. In contrast, the amplitude between 500 nm and 600 nm almost disappears entirely in the presence of MeOH, while the amplitude from 850 nm to 950 nm reduces much less (Figure 6-19 a). Then, kinetic trace probe was used to further reveal the nature of these excited species clearer. Kinetic trace probed at 500 nm (Figure 6-19 b) and 950 nm (Figure 6-19 c) with/without O_2 suggest that the signal probed at 500 nm features a longer-lived species while the signal probed at 950 nm features a slightly shorter-lived species in the presence of oxygen. Furthermore, kinetic trace probe at 950 nm confirms the generation of a long-lived species with the addition of MeOH (Figure 6-19d). Therefore, the signal observed at 500 nm to 550 nm is mainly attributed to photoholes in TiO_2 and the signal observed at 850 nm to 950 nm is assigned to photoelectrons in TiO_2 , similar to previous observations.¹¹⁰

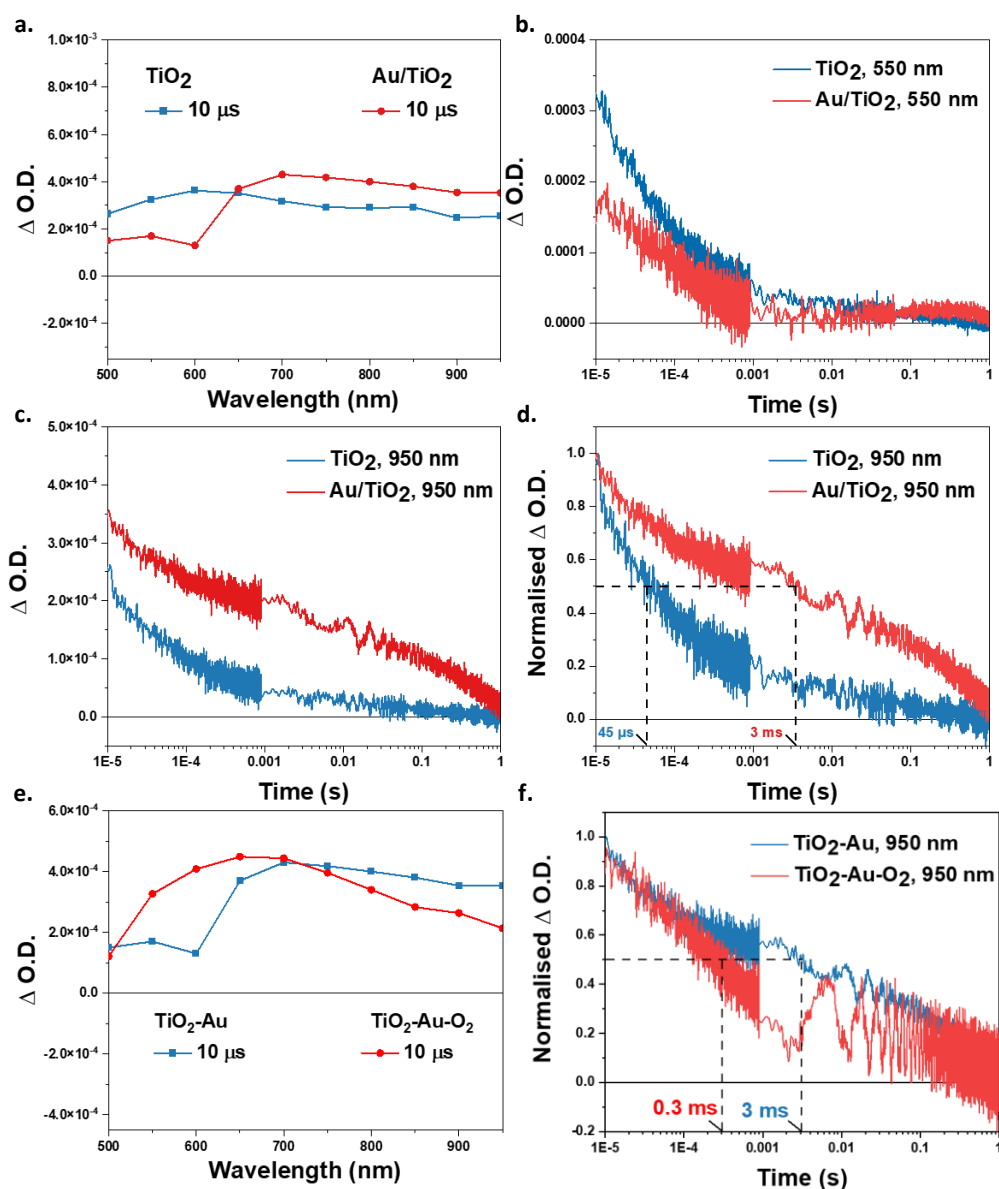


Figure 6-20 a. TAS spectra of TiO_2 and Au/TiO_2 excited by pulsed 355 nm excitation (0.40 mJ cm^{-2}) observed at $10 \mu\text{s}$ under argon atmosphere, respectively; b. TAS decay kinetics of TiO_2 and Au/TiO_2 probed at 550 nm excited by pump 355 nm under argon atmosphere; c. TAS decay kinetics of TiO_2 and Au/TiO_2 probed at 950 nm excited by pump 355 nm under argon atmosphere; d. Normalisation of TAS decay kinetics of TiO_2 and Au/TiO_2 probed at 950 nm and excited by pump 355 nm under argon atmosphere; e. TAS spectra of Au/TiO_2 excited by pulsed 355 nm excitation observed at $10 \mu\text{s}$ under argon and oxygen atmosphere, respectively; f. Normalisation of TAS decay kinetics of Au/TiO_2 probed at 950 nm and excited by pump 355 nm under argon and oxygen atmosphere, respectively.

Then, the TAS spectra of Au/TiO₂ was acquired in a comparison to pristine TiO₂ under argon atmosphere (Figure 6-20). After the introduction of Au, the amplitude at the region of photoholes (500-550 nm) in TiO₂ shows a decrease while that at the region of photoelectrons (850-950 nm) exhibits an increase. This result suggests that Au probably acts as hole acceptor like MeOH in the composite. The kinetic decay probed at 550 nm further indicates a shorter lifetime of photoholes on TiO₂ after introduction of Au (Figure 6-20b). However, as Au has a surface plasmonic resonance effect at the range of 500-700 nm (Figure 6-4), it may have some influence on the TAS observation although the pump wavelength is 355 nm to avoid the excitation of this effect. Thus, the kinetic trace probed at 950 nm was further monitored to avoid the interference, as shown in Figure 6-20c. The lifetime of photoelectrons significantly increases after the loading of Au, again indicating Au a hole acceptor. Then, the normalisation was applied to the kinetic decay curves to determine the half-life time of the signal

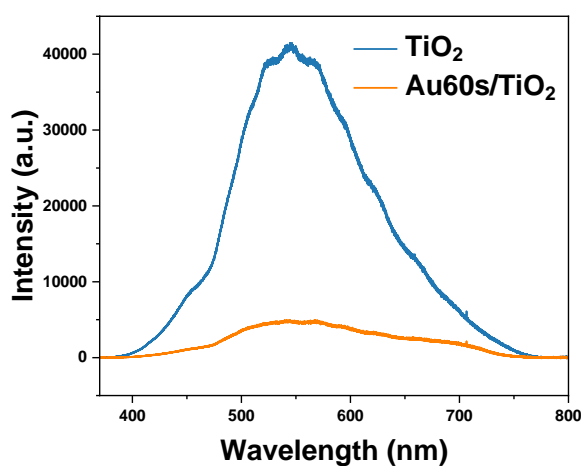


Figure 6-21 Photoluminescence spectra of TiO₂ and Au60s/TiO₂.

observed at 950 nm (Figure 6-20d). The half-life time of photoelectrons on TiO₂ increases over 60-fold from 45 μ s (TiO₂) to 3 ms (Au/TiO₂). In order to further confirm the signal with longer lifetime at 950 nm is photoelectrons, TAS spectra of Au/TiO₂ was collected under oxygen atmosphere for comparison (Figure 6-20e). The amplitude

at the range from 850 nm to 950 nm reduces with the introduction of oxygen, like the observation of photoelectrons in TiO₂. The normalisation was further applied to the kinetic decay curves of the signal detected at 950 nm (Figure 6-20f). The half-life time of the signal on Au/TiO₂ decreases from 3 ms under argon atmosphere to 0.3 ms under oxygen atmosphere, proving that the signal with longer lifetime at 950 nm belongs to photoelectrons. This result consolidates the role of Au as an efficient hole acceptor to extend the lifetime of photoelectrons on TiO₂. This is consistent with the result observed by in situ XPS. The photoholes of TiO₂ can migrate to Au owing to the more positive VB of TiO₂ than the Fermi level of Au. The photoholes are probably trapped by the d-band states in Au, or in other word the electrons from the d-band of Au are donated to TiO₂ to consume photoholes.¹⁹³ Such process can effectively decrease the oxidative potential of the original photoholes in TiO₂, avoiding the non-selective overoxidation to CO₂ during photocatalytic methane conversion.

The charge transfer process was further investigated by PL, as shown in Figure 6-21. Compared with the pristine TiO₂, the PL intensity greatly decreases for nearly 90% after 60 seconds Au sputtering, indicating the efficient separation of photo-induced electrons and holes by the introduction of Au. However, considering the significant decrease of light absorption by the scattering of Au nanoparticles based on the UV-Vis spectra in Figure 6-4, this can also in part contribute to the decrease of PL intensity.

To avoid the influence of light absorption, the time-resolved PL (TRPL) was carried out to investigate the charge transfer dynamic of these photoluminescence species, as shown in Figure 6-22. The decay spectra curves were fitted by biexponential decay kinetics function via eq. 3-2 in section 3.4 while the average lifetime $\langle\tau_{av}\rangle$ was determined by eq. 3-3 in section 3.4. The average lifetime $\langle\tau_{av}\rangle$ is 12.0 and 8.4 ns for the pristine TiO_2 and $\text{Au60s}/\text{TiO}_2$, respectively. The shorter fluorescence lifetime after the introduction of Au compared to the pure TiO_2 suggests a more efficient hole transfer from TiO_2 to Au.²²³ This result further consolidates that Au acts as a hole acceptor is responsible for the shorten fluorescence lifetime and also the quenching of PL intensity.

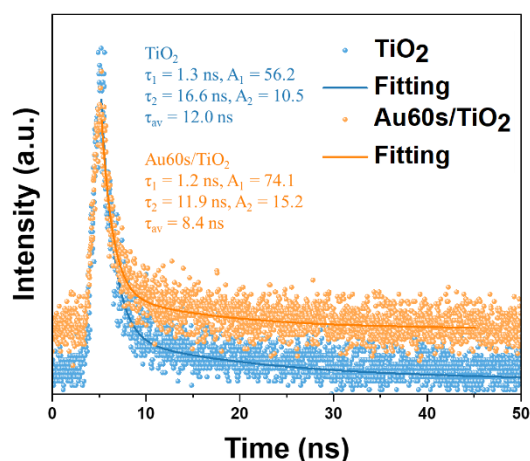


Figure 6-22 TRPL spectra of TiO_2 and $\text{Au60s}/\text{TiO}_2$.

The above characterisations reveal the pathway for the photo-induced charges transfer, in which the photoholes after excitation will transfer from TiO_2 to Au and photoelectrons remain in the CB of TiO_2 . Then, the interface reactions by these photo-induced charges were investigated. In the photocatalytic OCM process, two main half reactions will happen after the migration of photo-induced charges to the surface. One is the reduction of oxygen to form superoxide radicals by photoelectrons and the other one is the oxidation of methane to form methyl radicals by photoholes, respectively.

Therefore, EPR with DMPO as the spin trap reagent was conducted to monitor the generation of superoxide radicals over TiO_2 and Au60s/TiO_2 under light irradiation, as shown in Figure 6-23. Notably, a higher intensity of DMPO adduct is observed over Au60s/TiO_2 under light irradiation, indicating a larger amount of superoxide radicals can be generated. Following previous discussion of promoted charge separation by Au nanoparticles, more photoelectrons can be left in the CB of TiO_2 , which reduce oxygen to form more superoxide radicals to drive the photocatalytic methane conversion cycle.

For the other half oxidation reaction by photoholes, it is necessary evaluate the oxidation ability of photoholes after transferring to the d bands of Au co-catalyst. The

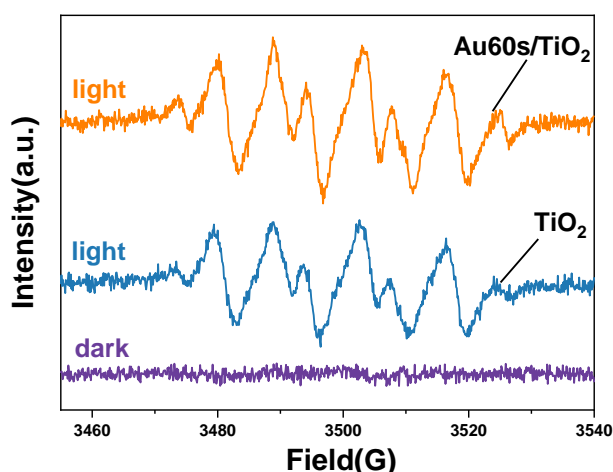


Figure 6-23 In situ EPR spectra of superoxide radicals using DMPO as a spin trap over TiO_2 and Au60s/TiO_2 in CH_3OH aqueous solution under 5 minutes light irradiation.

accurate work function of small Au species on Au60s/TiO_2 cannot be determined, thus there is a question that the photoholes potential on the Au species maybe too small resulting in the loss of oxidation ability for methane oxidation. The direct capture and observation of the methyl radicals are very difficult, thus hydroxyl radical with a more positive redox potential ($E^0(\cdot\text{OH}/\text{H}_2\text{O}) = 2.8 \text{ V, SHE}$) than methane oxidation

($E^0(\cdot\text{CH}_3/\text{CH}_4) = 1.73 \text{ V, SHE}$) was chosen for this study. As shown in Figure 6-24, Au60s/TiO₂ exhibits a higher intensity of DMPO-OH adduct than that of pristine TiO₂ under light irradiation, suggesting that more hydroxyl radicals can be formed over Au60s/TiO₂. This experiment confirms that when the photoholes on TiO₂ are trapped by the more negative states (d-bands on Au), they are still able to activate the first C-H bond in CH₄. Furthermore, the introduction of Au can increase the availability of photoholes to generate more products.

Apart from being a hole acceptor, Au could play other roles to enable the efficient and

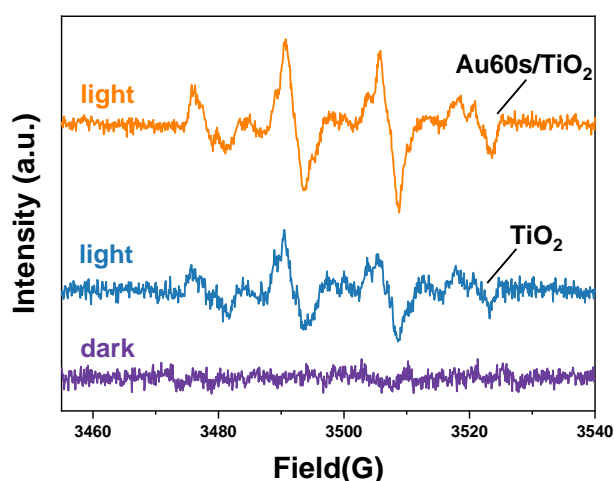


Figure 6-24 In situ EPR spectra of hydroxyl radicals using DMPO as a spin trap over TiO₂ and Au60s/TiO₂ in aqueous solution under 5 minutes light irradiation.

selective conversion of methane in the whole process. Thus, in situ DRIFTS was carried out to investigate the adsorption of methane under dark condition and photocatalytic transformation of methane under light irradiation condition on both catalysts (TiO₂ and Au60s/TiO₂). As shown in Figure 6-25, the typical C-H deformation vibration mode of CH₄ at $\sim 1306 \text{ cm}^{-1}$ are observed after the introduction of CH₄ on both catalysts under dark condition.^{26,224} It should be noted that the intensity of this vibration mode enhances significantly and quickly over Au60s/TiO₂, more than

5 times higher than that of pristine TiO₂ after 30 minutes adsorption. In addition, a new peak at ~1540 cm⁻¹ probably assigned to the C-H symmetric deformation vibrational mode or bending mode of methane gradually emerges on Au60s/TiO₂ with increasing adsorption time,^{37,225} while no similar peak can be observed over pristine TiO₂. The above result suggests that the introduction of Au can effectively enhance the methane adsorption, benefiting the following methane conversion process.

To gain insight into the function of Au during the photocatalytic process, in situ

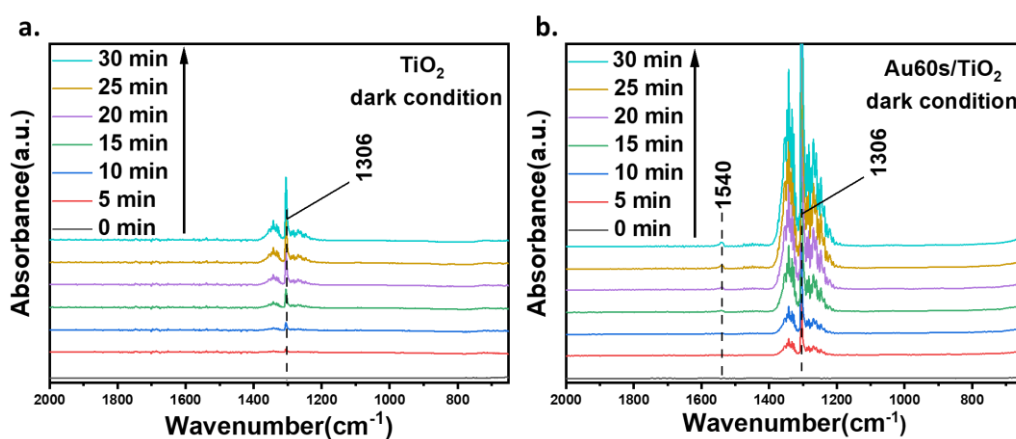


Figure 6-25 In situ CH₄ adsorption DRIFTS spectrum for TiO₂ (a) and Au60s/TiO₂ (b) under dark condition.

DRIFTS was then carried out with light irradiation (Figure 6-26). Upon light irradiation, the bands assigned to the C-H vibration mode of CH₄ at ~1306 cm⁻¹ exhibit a decrease trend with increasing time over both catalysts. Notably, this band on Au60s/TiO₂ shows more than 5 times higher intensity than that on pristine TiO₂ at time 0 min, decreases to the similar intensity on both catalysts after 10 minutes illumination. This result suggests the existence of Au nanoparticles can efficiently drive the methane conversion process. Furthermore, the CH₂/CH₃ deformation vibrational modes at around 1440 and 1420 cm⁻¹ only appears and enhances on Au60s/TiO₂ with light irradiation, indicating the rapid dissociation of CH₄ to CH_x (x=3,

2) on the surface of Au60s/TiO₂.²⁰⁷ In the meantime, the peak at ca. 876 cm⁻¹ corresponding to the C-C stretching emerges and its intensity also enhances gradually with longer light illumination time,²²⁶ further demonstrating the efficient C-H abstraction of methane and C-C coupling formation to ethane. In contrast, another broad IR band at ~1030 cm⁻¹ attributed to the C-O stretching vibration mode keeps rising on pristine TiO₂ apart from the C-C stretching at ~876 cm⁻¹,^{41,226} which is likely due to CO₂ formation.²²⁷ For pure TiO₂, the photoholes are represented as the O⁻ (surface lattice oxygen), e.g., the bridge oxygen radical (e.g., Ti⁴⁺-O⁻-Ti⁴⁺) and the terminal oxygen radical (e.g., Ti⁴⁺-O²⁻-Ti⁴⁺-O⁻),^{88,191,192} which may couple with the methyl radicals to give -CH₃O species during the activation of C-H bond of CH₄. Moreover, the photoholes on the VB of TiO₂ has strong oxidative potential, which may further drive the consecutive dehydrogenation to the intermediates (-CH₂O and CHO) for CO₂ generation. However, similar band cannot be observed in the spectra over Au60s/TiO₂, despite a much more efficient methane conversion rate. More importantly, another IR bands at 690-740 cm⁻¹ assigned to CH₃ rock in Au-CH₃ can only be detected over Au60s/TiO₂,^{30,228} providing further evidence that CH₄ can be activated on Au. As proved by in situ XPS and TAS, photoholes on TiO₂ can be transferred to the Au nanoparticles. Thus, the selective C-H bond cleavage process and the C-C coupling process happen on the Au nanoparticles, effectively avoiding the participation of surface lattice oxygen from TiO₂. Moreover, the more negative oxidative potential of the states in Au can also avoid the overoxidation and deep dehydrogenation. This in situ DRIFTS result also explains the highly selective conversion of methane to ethane after Au modification and the low C₂ selectivity with

CO₂ production on pure TiO₂. Thus, the functions of Au have been demonstrated as an efficient hole acceptor, methane adsorption sites and methane activation sites.

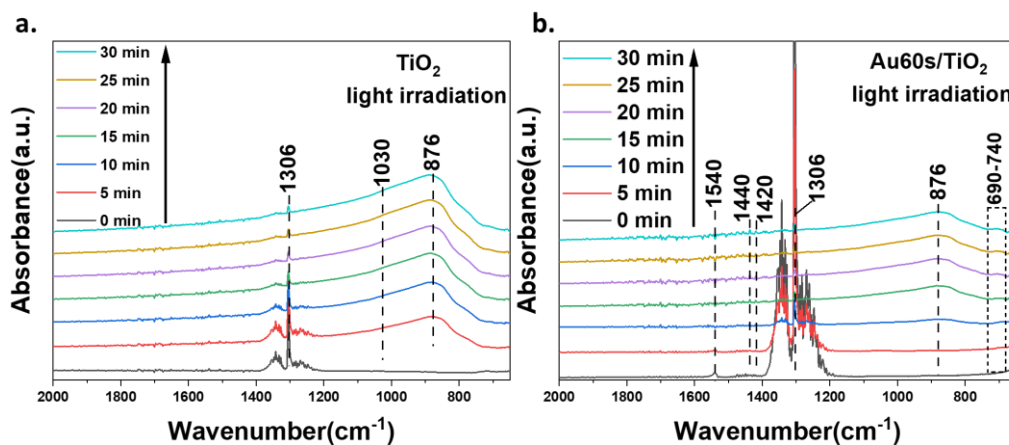


Figure 6-26 In situ DRIFTS spectra of photocatalytic methane conversion over TiO₂ (a) and Au₆₀s/TiO₂ (b).

The influence of Au on the reaction kinetic of the photocatalytic OCM was also investigated and the activation energy of methane can be derived on different catalysts, as shown in Figure 6-27. The main product for TiO₂ in photocatalytic OCM reaction is CO₂ (selectivity >90%) at different temperatures. The methane conversion rate also exhibits a similar increasing trend with increasing temperature as that of Au₆₀s/TiO₂ (Figure 6-7). From the transformation of Arrhenius equation ($k=A\exp(-E_a/RT)$), the apparent activation energy (E_a) could be obtained by fitting the reaction rate (r) and $1/T$ (T is temperature in K) ($\ln r_{\text{CH}_4} = -E_a/RT + \ln C$, C is a constant), as shown in Figure 6-27b. The incorporation of Au remarkably reduces the E_a from 7.7 kJ mol⁻¹ over pure TiO₂ to ca. 5.5 kJ mol⁻¹ over Au₆₀s/TiO₂, highlighting the extra function of Au during the activation of CH₄. This low E_a is more than ten time lower than one of the most classic thermal catalysts Li/MgO (generally ~100 kJ mol⁻¹) in the conventional OCM process.²²⁹ Such low E_a enables the comparable activity of

Au60s/TiO₂ under room temperature to that attained by conventional high-temperature thermal catalysis (Table 6-2).

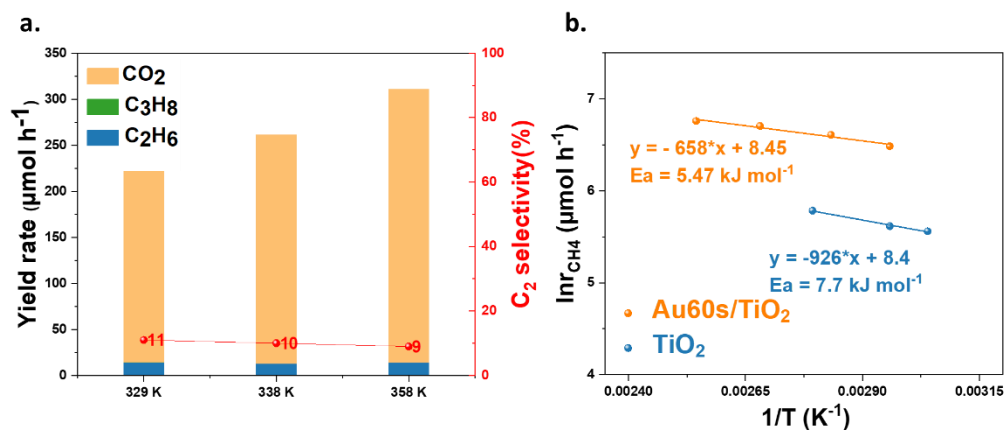


Figure 6-27 (a) Photocatalytic OCM activity over TiO₂ operated at different temperatures (329 K, 338 K and 358 K). (Reaction condition: 20 mg TiO₂, 320 mL/min CH₄, 4 mL/min Air, 365 nm LED 100 W); (b) Kinetics of methane conversion over Au60s/TiO₂ and TiO₂ catalysts.

Overall, the mechanism of photocatalytic OCM reaction over Au/TiO₂ is proposed in Figure 6-28. Under UV light irradiation, electrons are excited from the VB of TiO₂ to its CB, while the photoholes are transferred to the Au nanoparticles, generating long lived photoelectrons for oxygen reduction and photoholes for methane oxidation. The photoholes in Au can effectively and selectively abstract the C-H bond of the pre-adsorbed methane molecule to generate methyl radicals and protons. The combination of methyl radicals gives ethane molecules while the protons can be removed by superoxide radicals to form water. This process can avoid not only the direct overoxidation of intermediates (e.g., methyl radicals) and products (e.g., ethane) by the highly oxidative photoholes in TiO₂ but also the involvement of surface lattice oxygen to form CO₂ related species (e.g., -OCH₃), leading to high selectivity to C₂

products rather than CO₂ by-product. Furthermore, the enhanced adsorption of methane by Au loading is beneficial for the high conversion of methane.

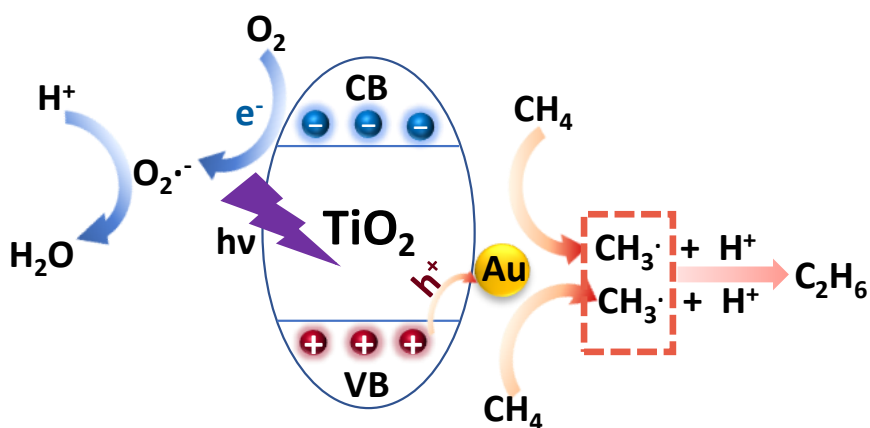


Figure 6-28 Possible photocatalytic OCM process over Au_{60s}/TiO₂

6.3 Conclusion

In summary, a facile and rapid sputtering method (60 seconds) has been developed to synthesise efficient photocatalyst Au/TiO₂ for photocatalytic OCM reaction in the flow reaction system. The optimised sample Au_{60s}/TiO₂ exhibits the highest C₂ yield rate 468 μmol h⁻¹ with the high C₂ selectivity of 86% at the space velocity of 977, 430 mL g_{cat}⁻¹ hour⁻¹ at 393 K, setting the new record in photocatalytic methane conversion to C₂ products. This methane conversion rate also reaches the level of ca. 1.1 mmol h⁻¹ for the first time, corresponding to the highest AQE of 10.3±0.6 at 365 nm. Furthermore, the unprecedented space time yield (23.4 mol kg_{cat}⁻¹ h⁻¹ for C₂ or 24.5 mol kg_{cat}⁻¹ h⁻¹ for C₂₊) is also comparable to all the benchmark catalysts attained by conventional OCM processes operated at the high temperature (>953 K), while the selectivity to C₂/C₂₊ is at least 20% higher than that reported by conventional OCM processes (Table 6-2). The photocatalytic mechanism behind this excellent

performance was thoroughly investigated by a series of in situ techniques (e.g., XPS, EPR, DRIFTS) and spectroscopy (e.g., TAS, TRPL). It has been revealed that Au acts as a hole acceptor for photoholes transfer from TiO₂, which not only reduces charge recombination but also lowers the oxidative potential of the original photoholes and avoids the participation of lattice oxygen of TiO₂ to reduce CO₂ production during the methane activation process. Au nanoparticles also benefit the adsorption of methane, act as the catalytic active centre to drive the C-H selective cleavage and promote the C-C coupling process to form ethane molecules. The unique multi-function of Au nanoparticles enables the photocatalytic methane conversion process with high efficiency and selectivity. This robust operation process with such high performance implies the great potential for the future practical application. Interestingly, Au nanoparticles prepared by sputtering method is proved as a hole acceptor with solid experimental evidence (TAS and in situ XPS) in this chapter, which is similar to the PdCu nanoparticles prepared by colloidal synthesis in previous chapter. However, the selectivity to desired C₂ products and overoxidation CO₂ by-product is different in these two systems (Figure 6-2), suggesting the different oxidative potential of photoholes after transfer from TiO₂ to these two nanoparticles co-catalysts. As discussed in the conclusion section in chapter 5, the accurate determination of work function over small nanoparticles is very difficult. Therefore, the direct comparison of the specific oxidative level on Au and PdCu cannot be achieved at this moment. The information for accurate band position that only allows the selective cleavage of C-H bond in methane to form C₂ without overoxidation is uncertain. The specific position needs to be estimated and investigated in future work to provide understanding of interfacial band-alignments and guidance for effective photocatalyst design.

7 Overall conclusions

The current progress of photocatalytic methane conversion to high-value chemicals, including the development of photocatalysts and co-catalysts, design of reaction systems, and mechanistic understanding, was reviewed in Chapter 2. Overall, photocatalytic methane conversion has achieved great success over the past few decades. Table 2-2 in Section 2.2 clearly shows that photocatalytic methane conversion exhibit superiority in the selectivity toward various products. Almost all the products of interest can find a photocatalytic system with a selectivity >90% and even 100%. For those reactions often carried out at very high temperatures (e.g., NOCM or MDA, at >673 K, sometimes even >1273 K), the product yield operated at room temperature could be estimated to be ca. 0.0002% and 0.000007% respectively due to the thermodynamic equilibrium.^{10,11} While the special function of photons could break the limitation of thermodynamic equilibrium, leading to a 100 to 10000 times improvement in conversion when operation at room temperature. Despite of the substantial progress, the photocatalytic methane conversion is still at infant stage. The efficiency of photocatalytic methane conversion was very moderate, in which the yield rate of target products was often at the level of several $\mu\text{mol h}^{-1}$ and the AQE was usually much lower than 10%. Majority of photocatalytic methane conversion processes used a batch reactor to evaluate the catalytic activity, which could only be regarded as a trail test, far away to meet the requirement of industrial applications.

In my thesis, photocatalytic OCM reaction was selected as the target reaction, because coupling of two methane molecules to produce C_2 products ($\text{C}_2\text{H}_6/\text{C}_2\text{H}_4$) via OCM is

one of the most general and highly profitable but challenge processes for long chain chemical synthesis by either thermocatalysis or photocatalysis.

The first example of a flow fix-bed reactor for photocatalytic OCM was designed. This reactor allows the control of flow rates to manipulate the residence time of the reactants and products to avoid overoxidation. Such system can also control the reaction temperature, the ratio of different gases, the light intensity, and the mass of catalysts (or thickness of the membrane), which can evaluate the photocatalyst in a more scientific (e.g., single pass conversion, yield and selectivity) manner, closer to real application. Then, a series of typical semiconductors were scanned using this flow system and the most active TiO_2 is selected as the base for further investigation. The commonly used electron acceptor Pt was introduced to enhance the charge separation on TiO_2 , while CuO_x clusters was decorated as well to accept the photoholes. The optimised sample $\text{Cu}_{0.1}\text{Pt}_{0.5}/\text{TiO}_2$ exhibits the highest C_2 yield of $68 \mu\text{mol g}^{-1} \text{h}^{-1}$ at a space velocity of $24000 \text{ ml g}^{-1} \text{h}^{-1}$, more than twice the sum of the yield rate of Pt/TiO_2 ($10.7 \mu\text{mol g}^{-1} \text{h}^{-1}$) and Cu/TiO_2 ($19 \mu\text{mol g}^{-1} \text{h}^{-1}$), and is approximately 3.5 times higher than that of TiO_2 . A high C_2 selectivity of 60% is also comparable to that attained by conventional thermocatalysis ($> 953 \text{ K}$). Characterisation suggests that Pt and CuO_x function as electron acceptor and hole acceptor, respectively, to promote charge separation and the holes transferred to the CuO_x can avoid deep dehydrogenation and the overoxidation of C_2 products.

Despite of the interesting results achieved in Chapter 4, the C_2 yield rate and apparent quantum efficiency (AQE) are very moderate and the short stability test period is another concern. Moreover, the investigation of reaction mechanism mainly focuses on the charge transfer with ex situ characterisation. Therefore, various noble metals

with unique catalytic potential for C-H bond activation in methane molecule reported in the conventional catalysis were introduced on TiO₂ to form a new co-catalyst/photocatalyst system. After screening, Pd is found to be the most efficient co-catalyst and then it is used to form nanoalloy with a series of non-noble transition metals to further improve the conversion/yield rate and stability. The optimised sample PdCu/TiO₂ exhibits the highest methane conversion rate of 2480 $\mu\text{mol g}^{-1} \text{h}^{-1}$ to C₂ products at a high space velocity of 342000 mL g_{cat}⁻¹ h⁻¹, 20 times higher than the benchmark photocatalytic result obtained at room temperature reported previously. Such high activity also gives the highest AQE of 8.4% among all ambient photocatalytic methane conversion to C₂ processes, suggesting a high light utilisation efficiency. A >110 hours stability with the high C₂ selectivity (75%) has been achieved at room temperature, resulting in the unprecedented TOF of 116 h⁻¹ and TON of 12642. The reason behind such activity and stability are correlated by in situ EPR, XPS and simulation DFT calculations. Benefiting from the junction between Pd and TiO₂, the excited photoholes in the VB of TiO₂ can migrate to Pd, shifting its oxidative potential of photoholes to a more negative position. These photoholes can selectively abstract the pre-soften C-H bond of methane molecule on Pd nanoparticles to form desired C₂ products. While the adsorption of C₂ products can be weakened via the alloy formation with metallic Cu, allowing the timely release of as-formed C₂ products and avoiding the further consecutive reaction for coke formation.

However, the space time yield is still very moderate, only several mol kg_{cat}⁻¹ h⁻¹, hard to compare with those benchmark catalysts in thermocatalysis. Moreover, the C₂ selectivity is only 75%, comparable to the best reported traditional OCM processes, which can not show the superiority of selectivity control in photocatalysis. In addition,

the fabrication process of the catalyst is time-consuming with multi-steps, hard to scale up. The reaction system has not been carefully optimised, for instance, the relationship between mass of catalyst (the thickness of membrane) and the light utilisation efficiency. Thus, a facile and rapid (only 60 seconds) sputter method is developed to fabricate a highly efficient Au/TiO₂ on glass fibre membrane. After optimisation of a series of parameters, the Au60s/20mgTiO₂ exhibits the highest C₂ yield rate of 468 μmol h⁻¹ at the space velocity of 977, 430 mL g_{cat}⁻¹ hour⁻¹ at 393 K. This corresponds to a space time yield of 23.4 mol kg_{cat}⁻¹ h⁻¹ (C₂) or 24.5 mol kg_{cat}⁻¹ h⁻¹ (C₂₊) and in particular, the selectivity is as high as 86% (C₂) or 93% (C₂₊). Such high space time yield is comparable to all the benchmark catalysts in conventional OCM processes operated at the high temperature (>953 K), while the selectivity to C₂/C₂₊ is at least 20% higher than that in conventional OCM processes (Table 6-2 in section 6.2.3). Furthermore, the high light utilisation efficiency is reflected by the highest AQE (10.3±0.6 at 365 nm). Such excellent performance with the rapid fabrication procedure shows the great potential for the future application of this photocatalyst. The charge transfer is identified with in situ XPS and TAS, in which photoholes generated on TiO₂ can be transferred to Au. This transfer process can lower the oxidative potential of photoholes to avoid overoxidation and deep dehydrogenation to achieve high selectivity to desired C₂ products. The multi-function of Au during the photocatalytic OCM process is further revealed by in situ DRIFTS, including enhanced methane adsorption, selective activation of C-H bond and promotion of C-C coupling reaction. From the kinetic viewpoint, the activation energy (E_a) of methane over Au/TiO₂ is only 5.47 kJ mol⁻¹, which is lower than that of TiO₂ (7.70 kJ mol⁻¹), more than ten time lower than one of the most classic thermal catalysts Li/MgO (generally ~100 kJ

mol⁻¹) in conventional OCM process,²²⁹ reasoning the high performance even operated at 393 K.

8 Future works

The thesis has realised the main objectives, such as the build-up of photocatalytic OCM flow reaction system, the modification of TiO₂ with various co-catalysts (e.g., nanoparticles, nanoalloy, clusters) for the efficient conversion of CH₄ to C₂ products with high yield rate, selectivity, stability and AQE. The understanding of photophysics and surface chemistry was also improved by advanced characterisations (e.g., TAS, in situ XPS, in situ EPR and in situ DRIFTS) and DFT calculation. This original work has provided a new photocatalytic methane conversion avenue and also developed a reaction system for the evaluation of a photocatalyst, which already stimulates follow-up investigations^{158,208} since firstly published (Chapter 4).

Although the high methane conversion rate (>1.0 mmol h⁻¹ or >50 mmol g⁻¹ h⁻¹) is achieved, the single-pass conversion (<1.0%) is very low. This is far away from the techno-economic target (conversion over 35% with C₂₊ selectivity over 88%) for commercialization reported.²³⁰ However, it is important to keep in mind that this target was set out for thermocatalysis operated at very high temperature (>953 K) considering the high capital cost. On the other hand, the low single-pass methane conversion also results in the lack of more valuable products (e.g., ethylene, propane). Even though previous report already showed that ethane could be dehydrogenated to form ethylene over Pd/TiO₂²³¹ and it is easier to activate ethane to proceed the consecutive reaction to form more value-added products (e.g., ethylene, propane), primary product (ethane) is always observed rather than ethylene and other C₂₊ products in this thesis. The low conversion leads to the relatively low concentration of primary product (ethane) compared to reactant (methane). From the kinetic point of

view, the reaction rate related to both reaction rate constant and reactant concentration. Therefore, there is a real need to improve the single-pass methane conversion, which can be realised from two aspects (photocatalyst and reaction system).

Considering the inert nature of methane, such as low polarizability and hydrophobicity, its adsorption capacity on TiO₂ should be very limited. Substrate adsorption is the prerequisite for the later catalytic conversion process, the limited adsorption amount of methane is likely to be the reason for low conversion. Based on this specific need, the catalyst structure can be modified through the construction of hierarchical structures and the interface engineering chemistry. The formation of porous structure can enhance the mass transfer, methane adsorption and residence time, while the hydrophobic treatment of the surface can attract and enrich the methane molecules. Furthermore, other types of photocatalysts other than inorganic materials can also be explored. Emerging polymeric photocatalysts, including graphitic carbon nitride, covalent triazine frameworks and covalent organic frameworks, that may have stronger interaction with methane molecules show enormous potential. Considering all these photocatalysts used so far, an attractive material that has many potential merits is recommended, metal-organic frameworks (MOFs), a hybrid porous material connected by organic linkers and metal/metal cluster nodes. This could be one excellent candidate for methane conversion in future.²³²⁻²³⁴ If considering co-catalysts, MOFs with porous structure is also an excellent platform to adapt a large quantity of cocatalysts. Besides one single-photocatalyst, the coordination of different photocatalysts or assembly of multi-component with different functions is another available strategy. For example, TiO₂ can be highly dispersed in a porous support (e.g., zeolite and molecule sieve) to promote the interaction with methane molecules.

The design of an appropriate reaction system is also equally important. The reactor used in this thesis is the fix-bed reactor, in which the catalyst powder is dispersed on a glass fibre membrane support. Therefore, the conversion can not be simply improved via the increase of the catalyst mass, because the light can not pass through the thick catalyst layer as discussed in section 6.2.5. A pertinent design of the reactor is needed. For example, a hollow tube reactor can be used to fill a catalyst and a tube light source can be inserted in the centre to provide a continued irradiation for the whole bed, which allows the extension of the effective bed to enhance conversion. During the photocatalytic OCM process, some methyl radicals may release from the surface of catalyst and couple in the gas phase to form ethane. Thus, how to modify the reactor to decrease of the void volume (gas phase) and increase the residence time of this radical on a catalyst bed may be another strategy to obtain more valuable products.

Apart from considering the photocatalyst and reaction system as two separated aspects, they can be taken together to design. The catalysts need to be dispersed on the glass fibre membrane support in this thesis and the catalyst powder itself is accumulated together. Actually, this commercial membrane can be fabricated in one lab, thus catalyst powder can be introduced into the membrane support during the casting process. More polymeric transparent membranes can be developed to encapsulate the nanoparticle photocatalysts. The separation of this nanoparticles via the cross-link fibre can increase its utilisation efficiency and the enormous micro channels in the membrane can increase the interaction time between methane molecules and photocatalysts. This is a development from simple fixed-bed reactor to more sophisticated membrane reactor.

Finally, the in-depth understanding of the mechanism behind photocatalytic OCM process is indispensable, including both photophysics and surface chemistry reaction. In Chapter 6, the charge transfer has been identified by TAS under argon atmosphere, but a measurement under the real reaction condition (e.g., methane and oxygen atmosphere) is highly sought-after to gain comprehensive insight. Although TAS can identify the role of the co-catalyst (hole/electron acceptor), sometimes it can not tell the chemical nature of the species. For instance, copper species often has several valences ($\text{Cu}^0/\text{Cu}^{\text{I}}/\text{Cu}^{\text{II}}$) together and it is hard to determine which valence is the key reaction sites. Thus, the combination of TAS with other in situ/operando techniques (e.g., XAS) is highly recommended to monitor the generation and transportation of photo-induced carriers. After the elucidation of the charge transfer pathway, a thorough understanding of the active sites and intermediates (especially gas phase) under reaction condition is equally useful. Advanced techniques such as vacuum ultraviolet soft photoionization molecular-beam mass spectrometry can monitor the intermediates and resolve the elementary step in the gas phase, which can then help design more efficient photocatalysts and control the selectivity to higher-value chemicals.

Overall, apart from the improving the photocatalytic performance and the understanding of fundamental mechanism, scientific models should be set up to evaluate the economics of photocatalytic OCM process, facilitating the translation of these studies from laboratories to demo systems, contributing to zero carbon industrial processes. A systematic economic model that considers a series of parameters, such as the efficiency of light source, selection of catalysts, and capital expenditure, etc. is needed to achieve this goal.

9 References

1. Li, X., Wang, C. & Tang, J. Methane transformation by photocatalysis. *Nat. Rev. Mater.* **7**, 617–632 (2022).
2. Schwach, P., Pan, X. & Bao, X. Direct Conversion of Methane to Value-Added Chemicals over Heterogeneous Catalysts: Challenges and Prospects. *Chem. Rev.* **117**, 8497–8520 (2017).
3. Chen, L., Hong, J., Butt, H.-J. & wooh, sanghyuk. Liquid Repellent Metal-Oxide Photocatalysts. *Chem. - A Eur. J.* (2018) doi:10.1002/chem.201804411.
4. Xu, Y., Bao, X. & Lin, L. Direct conversion of methane under nonoxidative conditions. *J. Catal.* **216**, 386–395 (2003).
5. Guo, X. *et al.* Direct, nonoxidative conversion of methane to ethylene, aromatics, and hydrogen. *Science.* **344**, 616–619 (2014).
6. Xie, P. *et al.* Oxo dicopper anchored on carbon nitride for selective oxidation of methane. *Nat. Commun.* **13**, 1375 (2022).
7. Amos, R. D. An accurate ab initio study of the multipole moments and polarizabilities of methane. *Mol. Phys.* **38**, 33–45 (1979).
8. Gunsalus, N. J. *et al.* Homogeneous Functionalization of Methane. *Chem. Rev.* **117**, 8521–8573 (2017).
9. Song, Y. *et al.* Dry reforming of methane by stable Ni–Mo nanocatalysts on

- single-crystalline MgO. *Science*. **367**, 777–781 (2020).
10. Li, L., Fan, S., Mu, X., Mi, Z. & Li, C.-J. J. Photoinduced conversion of methane into benzene over GaN nanowires. *J. Am. Chem. Soc.* **136**, 7793–7796 (2014).
 11. Yuliati, L. & Yoshida, H. Photocatalytic conversion of methane. *Chem. Soc. Rev.* **37**, 1592–1602 (2008).
 12. Xie, J. *et al.* Highly selective oxidation of methane to methanol at ambient conditions by titanium dioxide-supported iron species. *Nat. Catal.* **1**, 889–896 (2018).
 13. Hu, Y., Higashimoto, S., Takahashi, S., Nagai, Y. & Anpo, M. Selective photooxidation of methane into methanol by nitric oxide over V-MCM-41 mesoporous molecular sieves. *Catal. Letters* **100**, 35–37 (2005).
 14. Ward, M. D., Brazdil, J. F., Mehandru, S. P. & Anderson, A. B. Methane photoactivation on copper molybdate. An experimental and theoretical study. *J. Phys. Chem.* **91**, 6515–6521 (1987).
 15. Suzuki, T., Wada, K., Shima, M. & Watanabe, Y. Photoinduced partial oxidation of methane into formaldehyde on silica-supported molybdena. *J. Chem. Soc. Chem. Commun.* **0**, 1059–1060 (1990).
 16. Zhou, Y., Zhang, L. & Wang, W. Direct functionalization of methane into ethanol over copper modified polymeric carbon nitride via photocatalysis. *Nat.*

- Commun.* **10**, 506 (2019).
17. Meng, L. *et al.* Gold plasmon-induced photocatalytic dehydrogenative coupling of methane to ethane on polar oxide surfaces. *Energy Environ. Sci.* **11**, 294–298 (2018).
 18. Wu, S. *et al.* Ga-Doped and Pt-Loaded Porous TiO₂–SiO₂ for Photocatalytic Nonoxidative Coupling of Methane. *J. Am. Chem. Soc.* **141**, 6592–6600 (2019).
 19. Yoshida, H., Matsushita, N., Kato, Y. & Hattori, T. Active sites in sol-gel prepared silica-alumina for photoinduced non-oxidative methane coupling. in *Physical Chemistry Chemical Physics* vol. 4 2459–2465 (Royal Society of Chemistry, 2002).
 20. Shi, D., Feng, Y. & Zhong, S. Photocatalytic conversion of CH₄ and CO₂ to oxygenated compounds over Cu/CdS–TiO₂/SiO₂ catalyst. *Catal. Today* **98**, 505–509 (2004).
 21. Zhou, L. *et al.* Light-driven methane dry reforming with single atomic site antenna-reactor plasmonic photocatalysts. *Nat. Energy* **5**, 61–70 (2020).
 22. Han, B., Wei, W., Li, M., Sun, K. & Hu, Y. H. A thermo-photo hybrid process for steam reforming of methane: Highly efficient visible light photocatalysis. *Chem. Commun.* **55**, 7816–7819 (2019).
 23. Takata, T. *et al.* Photocatalytic water splitting with a quantum efficiency of almost unity. *Nature* **581**, 411–414 (2020).

24. Bard, A. J. Photoelectrochemistry. *Science*. **207**, 139–144 (1980).
25. Linsebigler, A. L., Lu, G. & Yates Jr, J. T. Photocatalysis on TiO₂ surfaces: principles, mechanisms, and selected results. *Chem. Rev.* **95**, 735–758 (1995).
26. Chen, X. *et al.* Photocatalytic oxidation of methane over silver decorated zinc oxide nanocatalysts. *Nat. Commun.* **7**, 12273 (2016).
27. Kudo, A. & Miseki, Y. Heterogeneous photocatalyst materials for water splitting. *Chem. Soc. Rev.* **38**, 253–278 (2009).
28. Scaife, D. E. Oxide semiconductors in photoelectrochemical conversion of solar energy. *Sol. Energy* **25**, 41–54 (1980).
29. Yuliati, L., Tsubota, M., Satsuma, A., Itoh, H. & Yoshida, H. Photoactive sites on pure silica materials for nonoxidative direct methane coupling. *J. Catal.* **238**, 214–220 (2006).
30. Lang, J., Ma, Y., Wu, X., Jiang, Y. & Hu, Y. H. Highly efficient light-driven methane coupling under ambient conditions based on an integrated design of a photocatalytic system. *Green Chem.* **22**, 4669–4675 (2020).
31. Song, H. *et al.* Visible-Light-Mediated Methane Activation for Steam Methane Reforming under Mild Conditions: A Case Study of Rh/TiO₂ Catalysts. *ACS Catal.* **8**, 7556–7565 (2018).
32. Meng, X. *et al.* Photothermal conversion of CO₂ into CH₄ with H₂ over Group VIII nanocatalysts: An alternative approach for solar fuel production. *Angew.*

- Chemie - Int. Ed.* **53**, 11478–11482 (2014).
33. Ogura, K. & Kataoka, M. Photochemical conversion of methane. *J. Mol. Catal.* **43**, 371–379 (1988).
 34. Pignatello, J. J., Oliveros, E. & MacKay, A. Advanced Oxidation Processes for Organic Contaminant Destruction Based on the Fenton Reaction and Related Chemistry. *Crit. Rev. Environ. Sci. Technol.* **36**, 1–84 (2006).
 35. Hu, A., Guo, J.-J., Pan, H. & Zuo, Z. Selective functionalization of methane, ethane, and higher alkanes by cerium photocatalysis. *Science*. **361**, 668–672 (2018).
 36. Yu, X. *et al.* Stoichiometric methane conversion to ethane using photochemical looping at ambient temperature. *Nat. Energy* **5**, 511–519 (2020).
 37. Jiang, W. *et al.* Pd-Modified ZnO–Au Enabling Alkoxy Intermediates Formation and Dehydrogenation for Photocatalytic Conversion of Methane to Ethylene. *J. Am. Chem. Soc.* **143**, 269–278 (2021).
 38. Gondal, M. A., Hameed, A., Yamani, Z. H. & Arfaj, A. Photocatalytic transformation of methane into methanol under UV laser irradiation over WO₃, TiO₂ and NiO catalysts. *Chem. Phys. Lett.* **392**, 372–377 (2004).
 39. Yoshida, H. *et al.* Hydrogen production from methane and water on platinum loaded titanium oxide photocatalysts. *J. Phys. Chem. C* **112**, 5542–5551 (2008).
 40. Zhang, W., Yu, Y. & Yi, Z. Controllable synthesis of SrCO₃ with different

- morphologies and their co-catalytic activities for photocatalytic oxidation of hydrocarbon gases over TiO₂. *J. Mater. Sci.* **52**, 5106–5116 (2017).
41. Yu, X., De Waele, V., Löfberg, A., Ordonsky, V. & Khodakov, A. Y. Selective photocatalytic conversion of methane into carbon monoxide over zinc-heteropolyacid-titania nanocomposites. *Nat. Commun.* **10**, 700 (2019).
 42. Kaliaguine, S. L., Shelimov, B. N. & Kazansky, V. B. Reactions of methane and ethane with hole centers O⁻. *J. Catal.* **55**, 384–393 (1978).
 43. Yu, L. & Li, D. Photocatalytic methane conversion coupled with hydrogen evolution from water over Pd/TiO₂. *Catal. Sci. Technol.* **7**, 635–640 (2017).
 44. Yu, L., Shao, Y. & Li, D. Direct combination of hydrogen evolution from water and methane conversion in a photocatalytic system over Pt/TiO₂. *Appl. Catal. B Environ.* **204**, 216–223 (2017).
 45. Reiche, H. & Bard, A. J. Heterogeneous Photosynthetic Production of Amino Acids from Methane-Ammonia-Water at Pt/TiO₂ Implications in Chemical Evolution. *Journal of the American Chemical Society* vol. 101 3127–3128 (1979).
 46. Yazdanpour, N. & Sharifnia, S. Photocatalytic conversion of greenhouse gases (CO₂ and CH₄) using copper phthalocyanine modified TiO₂. *Sol. Energy Mater. Sol. Cells* **118**, 1–8 (2013).
 47. Li, Z., Pan, X. & Yi, Z. Photocatalytic oxidation of methane over CuO-

- decorated ZnO nanocatalysts. *J. Mater. Chem. A* **7**, 469–475 (2019).
48. Song, H. *et al.* Direct and Selective Photocatalytic Oxidation of CH₄ to Oxygenates with O₂ on Cocatalysts/ZnO at Room Temperature in Water. *J. Am. Chem. Soc.* **141**, 20507–20515 (2019).
49. Zhang, B. *et al.* Anisotropic photoelectrochemical (PEC) performances of ZnO single-crystalline photoanode: Effect of internal electrostatic fields on the separation of photogenerated charge carriers during PEC water splitting. *Chem. Mater.* **28**, 6613–6620 (2016).
50. Noel, Y., Zicovich-Wilson, C. M., Civalleri, B., D’Arco, P. & Dovesi, R. Polarization properties of ZnO and BeO: An ab initio study through the Berry phase and Wannier functions approaches. *Phys. Rev. B - Condens. Matter Mater. Phys.* **65**, 1–9 (2002).
51. Li, Z., Boda, M. A., Pan, X. & Yi, Z. Photocatalytic Oxidation of Small Molecular Hydrocarbons over ZnO Nanostructures: The Difference between Methane and Ethylene and the Impact of Polar and Nonpolar Facets. *ACS Sustain. Chem. Eng.* **7**, 19042–19049 (2019).
52. Yang, J. *et al.* Solar-driven efficient methane catalytic oxidation over epitaxial ZnO/La_{0.8}Sr_{0.2}CoO₃ heterojunctions. *Appl. Catal. B Environ.* **265**, 118469 (2020).
53. Noceti, R. P., Taylor, C. E. & D’Este, J. R. Photocatalytic conversion of methane. *Catal. Today* **33**, 199–204 (1997).

54. Taylor, C. E. & Noceti, R. P. New developments in the photocatalytic conversion of methane to methanol. *Catal. Today* **55**, 259–267 (2000).
55. Gondal, M. A., Hameed, A. & Suwaiyan, A. Photo-catalytic conversion of methane into methanol using visible laser. *Appl. Catal. A Gen.* **243**, 165–174 (2003).
56. Hameed, A., Ismail, I. M. I., Aslam, M. & Gondal, M. A. Photocatalytic conversion of methane into methanol: Performance of silver impregnated WO₃. *Appl. Catal. A Gen.* **470**, 327–335 (2014).
57. Villa, K., Murcia-López, S., Andreu, T. & Morante, J. R. Mesoporous WO₃ photocatalyst for the partial oxidation of methane to methanol using electron scavengers. *Appl. Catal. B Environ.* **163**, 150–155 (2015).
58. Villa, K., Murcia-López, S., Andreu, T. & Morante, J. R. On the role of WO₃ surface hydroxyl groups for the photocatalytic partial oxidation of methane to methanol. *Catal. Commun.* **58**, 200–203 (2015).
59. Villa, K., Murcia-López, S., Morante, J. R. & Andreu, T. An insight on the role of La in mesoporous WO₃ for the photocatalytic conversion of methane into methanol. *Appl. Catal. B Environ.* **187**, 30–36 (2016).
60. Yang, J., Hao, J., Wei, J., Dai, J. & Li, Y. Visible-light-driven selective oxidation of methane to methanol on amorphous FeOOH coupled m-WO₃. *Fuel* **266**, 117104 (2020).

61. Ozin, G. A. & Hugues, F. Selective photoactivation of carbon-hydrogen bonds in paraffinic hydrocarbons. Dimerization of alkanes. *J. Phys. Chem.* **86**, 5174–5179 (1982).
62. Hill, W., Shelimov, B. N. & Kazansky, V. B. Photoinduced reactions of methane with molybdena supported on silica. *J. Chem. Soc. Faraday Trans. 1 Phys. Chem. Condens. Phases* **83**, 2381–2389 (1987).
63. Kato, Y., Yoshida, H. & Hattori, T. Photoinduced non-oxidative coupling of methane over silica-alumina and alumina around room temperature. *Chem. Commun.* **0**, 2389–2390 (1998).
64. Kato, Y., Matsushita, N., Yoshida, H. & Hattori, T. Highly active silica-alumina-titania catalyst for photoinduced non-oxidative methane coupling. *Catal. Commun.* **3**, 99–103 (2002).
65. Yuliati, L., Itoh, H. & Yoshida, H. Modification of Highly Dispersed Cerium Oxides on Silica with Highly Dispersed Titanium Oxides as a New Photocatalyst Design for Nonoxidative Direct Methane Coupling. *Chem. Lett.* **35**, 932–933 (2006).
66. Li, L. *et al.* Synergistic Effect on the Photoactivation of the Methane C-H Bond over Ga³⁺-Modified ETS-10. *Angew. Chemie Int. Ed.* **51**, 4702–4706 (2012).
67. Yuliati, L., Hamajima, T., Hattori, T. & Yoshida, H. Highly dispersed Ce(III) species on silica and alumina as new photocatalysts for non-oxidative direct methane coupling. *Chem. Commun.* 4824–4826 (2005) doi:10.1039/b507698f.

68. Yoshida, H. *et al.* Active Ag species in MFI zeolite for direct methane conversion in the light and dark. *Res. Chem. Intermed.* **29**, 897–910 (2003).
69. Yuliati, L., Hattori, T., Itoh, H. & Yoshida, H. Photocatalytic nonoxidative coupling of methane on gallium oxide and silica-supported gallium oxide. *J. Catal.* **257**, 396–402 (2008).
70. Yuliati, L., Hamajima, T., Hattori, T. & Yoshida, H. Nonoxidative coupling of methane over supported ceria photocatalysts. *J. Phys. Chem. C* **112**, 7223–7232 (2008).
71. Yoshida, H., Chaskar, M. G., Kato, Y. & Hattori, T. Fine structural photoluminescence spectra of silica-supported zirconium oxide and its photoactivity in direct methane conversion. *Chem. Commun.* **2**, 2014–2015 (2002).
72. Li, L. *et al.* Efficient Sunlight-Driven Dehydrogenative Coupling of Methane to Ethane over a Zn⁺-Modified Zeolite. *Angew. Chemie Int. Ed.* **50**, 8299–8303 (2011).
73. Murcia-López, S. *et al.* Controlled Photocatalytic Oxidation of Methane to Methanol through Surface Modification of Beta Zeolites. *ACS Catal.* **7**, 2878–2885 (2017).
74. Sastre, F., Fornés, V., Corma, A. & García, H. Selective, room-temperature transformation of methane to C1 oxygenates by deep UV photolysis over zeolites. *J. Am. Chem. Soc.* **133**, 17257–17261 (2011).

75. Huang, H. *et al.* Solar-Light-Driven CO₂ Reduction by CH₄ on Silica-Cluster-Modified Ni Nanocrystals with a High Solar-to-Fuel Efficiency and Excellent Durability. *Adv. Energy Mater.* **8**, 1702472 (2018).
76. Sushkevich, V. L., Palagin, D., Ranocchiari, M. & van Bokhoven, J. A. Selective anaerobic oxidation of methane enables direct synthesis of methanol. *Science*. **356**, 523–527 (2017).
77. Jin, Z. *et al.* Hydrophobic zeolite modification for in situ peroxide formation in methane oxidation to methanol. *Science*. **367**, 193–197 (2020).
78. Singh, S. P., Anzai, A., Kawaharasaki, S., Yamamoto, A. & Yoshida, H. Non-oxidative coupling of methane over Pd-loaded gallium oxide photocatalysts in a flow reactor. *Catal. Today* 0–1 (2020) doi:10.1016/j.cattod.2020.04.023.
79. Kohno, Y., Tanaka, T., Funabiki, T. & Yoshida, S. Reaction mechanism in the photoreduction of CO₂ with CH₄ over ZrO₂. *Phys. Chem. Chem. Phys.* **2**, 5302–5307 (2000).
80. Shimura, K., Yoshida, T. & Yoshida, H. Photocatalytic Activation of Water and Methane over Modified Gallium Oxide for Hydrogen Production. *J. Phys. Chem. C* **114**, 11466–11474 (2010).
81. Yuliati, L., Itoh, H. & Yoshida, H. Photocatalytic conversion of methane and carbon dioxide over gallium oxide. *Chem. Phys. Lett.* **452**, 178–182 (2008).
82. Teramura, K., Tanaka, T., Ishikawa, H., Kohno, Y. & Funabiki, T.

- Photocatalytic Reduction of CO₂ to CO in the Presence of H₂ or CH₄ as a Reductant over MgO. *J. Phys. Chem. B* **108**, 346–354 (2004).
83. Yoshida, H., Chaskar, M. G., Kato, Y. & Hattori, T. Active sites on silica-supported zirconium oxide for photoinduced direct methane conversion and photoluminescence. *J. Photochem. Photobiol. A Chem.* **160**, 47–53 (2003).
84. Murcia-López, S., Villa, K., Andreu, T. & Morante, J. R. R. Partial oxidation of methane to methanol using bismuth-based photocatalysts. *ACS Catal.* **4**, 3013–3019 (2014).
85. Murcia-López, S., Villa, K., Andreu, T. & Morante, J. R. R. Improved selectivity for partial oxidation of methane to methanol in the presence of nitrite ions and BiVO₄ photocatalyst. *Chem. Commun.* **51**, 7249–7252 (2015).
86. Zhu, W. *et al.* Facet-Dependent Enhancement in the Activity of Bismuth Vanadate Microcrystals for the Photocatalytic Conversion of Methane to Methanol. *ACS Appl. Nano Mater.* **1**, 6683–6691 (2018).
87. Pan, X., Chen, X. & Yi, Z. Photocatalytic oxidation of methane over SrCO₃ decorated SrTiO₃ nanocatalysts via a synergistic effect. *Phys. Chem. Chem. Phys.* **18**, 31400–31409 (2016).
88. Shoji, S. *et al.* Photocatalytic uphill conversion of natural gas beyond the limitation of thermal reaction systems. *Nat. Catal.* **3**, 148–153 (2020).
89. Shimura, K., Kawai, H., Yoshida, T. & Yoshida, H. Bifunctional rhodium

cocatalysts for photocatalytic steam reforming of methane over alkaline titanate. *ACS Catal.* **2**, 2126–2134 (2012).

90. Li, N., Li, Y., Jiang, R., Zhou, J. & Liu, M. Photocatalytic coupling of methane and CO₂ into C₂-hydrocarbons over Zn doped g-C₃N₄ catalysts. *Appl. Surf. Sci.* **498**, 143861 (2019).
91. Tahir, B., Tahir, M. & Amin, N. A. S. Photo-induced CO₂ reduction by CH₄/H₂O to fuels over Cu-modified g-C₃N₄ nanorods under simulated solar energy. *Appl. Surf. Sci.* **419**, 875–885 (2017).
92. Muhammad, A., Tahir, M., Al-Shahrani, S. S., Mahmood Ali, A. & Rather, S. U. Template free synthesis of graphitic carbon nitride nanotubes mediated by lanthanum (La/g-CNT) for selective photocatalytic CO₂ reduction via dry reforming of methane (DRM) to fuels. *Appl. Surf. Sci.* **504**, 144177 (2020).
93. Shi, S., Sun, Z., Bao, C., Gao, T. & Hu, Y. H. The special route toward conversion of methane to methanol on a fluffy metal-free carbon nitride photocatalyst in the presence of H₂O₂. *Int. J. Energy Res.* **44**, 2740–2753 (2020).
94. Liu, H. *et al.* Light assisted CO₂ reduction with methane over SiO₂ encapsulated Ni nanocatalysts for boosted activity and stability. *J. Mater. Chem. A* **5**, 10567–10573 (2017).
95. Liu, H., Song, H., Meng, X., Yang, L. & Ye, J. Light irradiation enhanced CO₂ reduction with methane: A case study in size-dependent optical property of Ni

- nanoparticles. *Catal. Today* **335**, 187–192 (2019).
96. Liu, H. *et al.* Light assisted CO₂ reduction with methane over group VIII metals: Universality of metal localized surface plasmon resonance in reactant activation. *Appl. Catal. B Environ.* **209**, 183–189 (2017).
97. Liu, H. *et al.* Conversion of Carbon Dioxide by Methane Reforming under Visible-Light Irradiation: Surface-Plasmon-Mediated Nonpolar Molecule Activation. *Angew. Chemie - Int. Ed.* **54**, 11545–11549 (2015).
98. Shields, B. J. & Doyle, A. G. Direct C(sp³)-H Cross Coupling Enabled by Catalytic Generation of Chlorine Radicals. *J. Am. Chem. Soc.* **138**, 12719–12722 (2016).
99. Hwang, S. J. *et al.* Trap-Free Halogen Photoelimination from Mononuclear Ni(III) Complexes. *J. Am. Chem. Soc.* **137**, 6472–6475 (2015).
100. Li, X., Xie, J., Rao, H., Wang, C. & Tang, J. Platinum- and CuO_x -Decorated TiO₂ Photocatalyst for Oxidative Coupling of Methane to C₂ Hydrocarbons in a Flow Reactor. *Angew. Chemie Int. Ed.* **59**, 19702–19707 (2020).
101. Li, N. *et al.* Plasma-Assisted Photocatalysis of CH₄ and CO₂ into Ethylene. *ACS Sustain. Chem. Eng.* **7**, 11455–11463 (2019).
102. Copéret, C. C-H bond activation and organometallic intermediates on isolated metal centers on oxide surfaces. *Chem. Rev.* **110**, 656–680 (2010).
103. Ohkubo, K. & Hirose, K. Light-Driven C–H Oxygenation of Methane into

- Methanol and Formic Acid by Molecular Oxygen Using a Perfluorinated Solvent. *Angew. Chemie* **130**, 2148–2151 (2018).
104. Isaka, Y., Kawase, Y., Kuwahara, Y., Mori, K. & Yamashita, H. Two-Phase System Utilizing Hydrophobic Metal–Organic Frameworks (MOFs) for Photocatalytic Synthesis of Hydrogen Peroxide. *Angew. Chemie Int. Ed.* **58**, 5402–5406 (2019).
105. Miao, T. J. & Tang, J. Characterization of charge carrier behavior in photocatalysis using transient absorption spectroscopy. *J. Chem. Phys.* **152**, 194201 (2020).
106. Vlček, A., Kvapilová, H., Towrie, M. & Zálíš, S. Electron-Transfer Acceleration Investigated by Time Resolved Infrared Spectroscopy. *Acc. Chem. Res.* **48**, 868–876 (2015).
107. Buhrke, D. & Hildebrandt, P. Probing Structure and Reaction Dynamics of Proteins Using Time-Resolved Resonance Raman Spectroscopy. *Chem. Rev.* **120**, 3577–3630 (2020).
108. Sahoo, S. K., Umapathy, S. & Parker, A. W. Time-Resolved Resonance Raman Spectroscopy: Exploring Reactive Intermediates. *Appl. Spectrosc.* **65**, 1087–1115 (2011).
109. Hao, L. *et al.* Surface-Halogenation-Induced Atomic-Site Activation and Local Charge Separation for Superb CO₂ Photoreduction. *Adv. Mater.* **31**, 1900546 (2019).

110. Tang, J., Durrant, J. R. & Klug, D. R. Mechanism of Photocatalytic Water Splitting in TiO₂. Reaction of Water with Photoholes, Importance of Charge Carrier Dynamics, and Evidence for Four-Hole Chemistry. *J. Am. Chem. Soc.* **130**, 13885–13891 (2008).
111. Grigioni, I. *et al.* In Operando Photoelectrochemical Femtosecond Transient Absorption Spectroscopy of WO₃/BiVO₄ Heterojunctions. *ACS Energy Lett.* **4**, 2213–2219 (2019).
112. Murthy, D. H. K. *et al.* Origin of the overall water splitting activity of Ta₃N₅ revealed by ultrafast transient absorption spectroscopy. *Chem. Sci.* **10**, 5353–5362 (2019).
113. Sprick, R. S. *et al.* Water Oxidation with Cobalt-Loaded Linear Conjugated Polymer Photocatalysts. *Angew. Chemie Int. Ed.* **59**, 18695–18700 (2020).
114. Shen, S., Wang, X., Chen, T., Feng, Z. & Li, C. Transfer of photoinduced electrons in anatase-rutile TiO₂ determined by time-resolved mid-infrared spectroscopy. *J. Phys. Chem. C* **118**, 12661–12668 (2014).
115. Dai, X. *et al.* Capturing the Long-Lived Photogenerated Electrons in Au/TiO₂ upon UV or Visible Irradiation by Time-Resolved Infrared Spectroscopy. *J. Phys. Chem. C* **123**, 20325–20332 (2019).
116. Yamakata, A., Ishibashi, T. A. & Onishi, H. Water- and oxygen-induced decay kinetics of photogenerated electrons in TiO₂ and Pt/TiO₂: A time-resolved infrared absorption study. *J. Phys. Chem. B* **105**, 7258–7262 (2001).

117. Wang, Y., Hu, P., Yang, J., Zhu, Y. & Chen, D. C–H bond activation in light alkanes: a theoretical perspective. *Chem. Soc. Rev.* **50**, 4299–4358 (2021).
118. Ma, J. *et al.* Exploring the Size Effect of Pt Nanoparticles on the Photocatalytic Nonoxidative Coupling of Methane. *ACS Catal.* **11**, 3352–3360 (2021).
119. Luo, L. *et al.* Water enables mild oxidation of methane to methanol on gold single-atom catalysts. *Nat. Commun.* **12**, 1218 (2021).
120. Fan, Y. *et al.* Selective photocatalytic oxidation of methane by quantum-sized bismuth vanadate. *Nat. Sustain.* (2021) doi:10.1038/s41893-021-00682-x.
121. Song, H. *et al.* Selective Photo-oxidation of Methane to Methanol with Oxygen over Dual-Cocatalyst-Modified Titanium Dioxide. *ACS Catal.* 14318–14326 (2020) doi:10.1021/acscatal.0c04329.
122. Brückner, A. In situ electron paramagnetic resonance: A unique tool for analyzing structure-reactivity relationships in heterogeneous catalysis. *Chem. Soc. Rev.* **39**, 4673–4684 (2010).
123. Cui, X. *et al.* Room-Temperature Methane Conversion by Graphene-Confined Single Iron Atoms. *Chem* **4**, 1902–1910 (2018).
124. Meunier, F. C. Pitfalls and benefits of: In situ and operando diffuse reflectance FT-IR spectroscopy (DRIFTS) applied to catalytic reactions. *React. Chem. Eng.* **1**, 134–141 (2016).
125. M., A. Á., Bobadilla, L. F., Garcilaso, V., Centeno, M. A. & Odriozola, J. A.

- CO₂ reforming of methane over Ni-Ru supported catalysts: On the nature of active sites by operando DRIFTS study. *J. CO₂ Util.* **24**, 509–515 (2018).
126. Matam, S. K., Aguirre, M. H., Weidenkaff, A. & Ferri, D. Revisiting the problem of active sites for methane combustion on Pd/Al₂O₃ by operando XANES in a lab-scale fixed-bed reactor. *J. Phys. Chem. C* **114**, 9439–9443 (2010).
127. Wolfbeisser, A. *et al.* Surface composition changes of CuNi-ZrO₂ during methane decomposition: An operando NAP-XPS and density functional study. *Catal. Today* **283**, 134–143 (2017).
128. Li, X., Yang, X., Zhang, J., Huang, Y. & Liu, B. In Situ/Operando Techniques for Characterization of Single-Atom Catalysts. *ACS Catal.* **9**, 2521–2531 (2019).
129. Tauc, J., Grigorovici, R. & Vancu, A. Optical Properties and Electronic Structure of Amorphous Germanium. *Phys. status solidi* **15**, 627–637 (1966).
130. Farrell, B. L., Igenegbai, V. O. & Linic, S. A Viewpoint on Direct Methane Conversion to Ethane and Ethylene Using Oxidative Coupling on Solid Catalysts. *ACS Catal.* **6**, 4340–4346 (2016).
131. Wang, Z., Li, C. & Domen, K. Recent developments in heterogeneous photocatalysts for solar-driven overall water splitting. *Chem. Soc. Rev.* (2018) doi:10.1039/C8CS00542G.

132. Brezicki, G., Kammert, J. D., Gunnoe, T. B., Paolucci, C. & Davis, R. J. Insights into the Speciation of Cu in the Cu-H-Mordenite Catalyst for the Oxidation of Methane to Methanol. *ACS Catal.* 5308–5319 (2019) doi:10.1021/acscatal.9b00852.
133. Wu, J.-F. *et al.* Mechanistic Insights on the Direct Conversion of Methane into Methanol over Cu/Na–ZSM-5 Zeolite: Evidence from EPR and Solid-State NMR. *ACS Catal.* 8677–8681 (2019) doi:10.1021/acscatal.9b02898.
134. Xu, Y. & Schoonen, M. A. A. A. The absolute energy positions of conduction and valence bands of selected semiconducting minerals. *Am. Mineral.* **85**, 543–556 (2000).
135. Li, F. B. & Li, X. Z. The enhancement of photodegradation efficiency using Pt-TiO₂ catalyst. *Chemosphere* **48**, 1103–1111 (2002).
136. Samsudin, M. F. R., Mahmood, A. & Sufian, S. Enhanced photocatalytic degradation of wastewater over RGO-TiO₂/BiVO₄ photocatalyst under solar light irradiation. *J. Mol. Liq.* **268**, 26–36 (2018).
137. Zhou, B. X. *et al.* Theory-Driven Heterojunction Photocatalyst Design with Continuously Adjustable Band Gap Materials. *J. Phys. Chem. C* **122**, 28065–28074 (2018).
138. Grundner, S., Luo, W., Sanchez-Sanchez, M. & Lercher, J. A. Synthesis of single-site copper catalysts for methane partial oxidation. *Chem. Commun.* **52**, 2553–2556 (2016).

139. Zhang, Y. *et al.* Covalent organic framework-supported Fe–TiO₂ nanoparticles as ambient-light-active photocatalysts. *J. Mater. Chem. A* **7**, 16364–16371 (2019).
140. Song, H., Meng, X., Wang, Z., Liu, H. & Ye, J. Solar-Energy-Mediated Methane Conversion. *Joule* **3**, 1606–1636 (2019).
141. Yun, C., Anpo, M., Mizokoshi, Y. & Kubokawa, Y. OXIDATION OF ALKANES AND ALKENES BY N₂O OVER UV IRRADIATED MgO. *Chem. Lett.* **9**, 799–802 (1980).
142. Yuliati, L., Hattori, T. & Yoshida, H. Highly dispersed magnesium oxide species on silica as photoactive sites for photoinduced direct methane coupling and photoluminescence. *Phys. Chem. Chem. Phys.* **7**, 195 (2005).
143. Yoshida, H., Matsushita, N., Kato, Y. & Hattori, T. Synergistic active sites on SiO₂-Al₂O₃-TiO₂ photocatalysts for direct methane coupling. *J. Phys. Chem. B* **107**, 8355–8362 (2003).
144. Li, L. *et al.* Synergistic Effect on the Photoactivation of the Methane C–H Bond over Ga³⁺-Modified ETS-10. *Angew. Chemie Int. Ed.* **51**, 4702–4706 (2012).
145. Arndt, S. *et al.* A critical assessment of Li/MgO-Based catalysts for the oxidative coupling of methane. *Catal. Rev. - Sci. Eng.* **53**, 424–514 (2011).
146. Kumar, S. G. & Devi, L. G. Review on modified TiO₂ photocatalysis under

- UV/visible light: Selected results and related mechanisms on interfacial charge carrier transfer dynamics. *Journal of Physical Chemistry A* vol. 115 13211–13241 (2011).
147. Su, Y. S., Ying, J. Y. & Green, W. H. Upper bound on the yield for oxidative coupling of methane. *J. Catal.* **218**, 321–333 (2003).
148. Li, X., Pi, Y., Xia, Q., Li, Z. & Xiao, J. TiO₂ encapsulated in Salicylaldehyde-NH₂-MIL-101(Cr) for enhanced visible light-driven photodegradation of MB. *Appl. Catal. B Environ.* **191**, 192–201 (2016).
149. Ohsaka, T., Izumi, F. & Fujiki, Y. Raman spectrum of anatase, TiO₂. *J. Raman Spectrosc.* **7**, 321–324 (1978).
150. Li, W. S., Shen, Z. X., Li, H. Y., Shen, D. Z. & Fan, X. W. Blue shift of Raman peak from coated TiO₂ nanoparticles. *J. Raman Spectrosc.* **32**, 862–865 (2001).
151. Farsinezhad, S., Sharma, H. & Shankar, K. Interfacial band alignment for photocatalytic charge separation in TiO₂ nanotube arrays coated with CuPt nanoparticles. *Phys. Chem. Chem. Phys.* **17**, 29723–29733 (2015).
152. Sorcar, S. *et al.* CO₂, water, and sunlight to hydrocarbon fuels: a sustained sunlight to fuel (Joule-to-Joule) photoconversion efficiency of 1%. *Energy Environ. Sci.* **12**, 2685–2696 (2019).
153. Xia, J., Masaki, N., Jiang, K. & Yanagida, S. Deposition of a thin film of TiO_x from a titanium metal target as novel blocking layers at conducting glass/TiO₂

- interfaces in ionic liquid mesoscopic TiO₂ dye-sensitized solar cells. *J. Phys. Chem. B* **110**, 25222–25228 (2006).
154. Li, J., Zeng, J., Jia, L. & Fang, W. Investigations on the effect of Cu²⁺/Cu¹⁺ redox couples and oxygen vacancies on photocatalytic activity of treated LaNi_{1-x}Cu_xO₃ (x=0.1, 0.4, 0.5). *Int. J. Hydrogen Energy* **35**, 12733–12740 (2010).
155. Shimokawabe, M., Asakawa, H. & Takezawa, N. Characterization of copper/zirconia catalysts prepared by an impregnation method. *Appl. Catal.* **59**, 45–58 (1990).
156. Li, G., Dimitrijevic, N. M., Chen, L., Rajh, T. & Gray, K. A. Role of Surface/Interfacial Cu²⁺ Sites in the Photocatalytic Activity of Coupled CuO–TiO₂ Nanocomposites. *J. Phys. Chem. C* **112**, 19040–19044 (2008).
157. Ishimaru, M., Amano, F., Akamoto, C. & Yamazoe, S. Methane coupling and hydrogen evolution induced by palladium-loaded gallium oxide photocatalysts in the presence of water vapor. *J. Catal.* **397**, 192–200 (2021).
158. Song, S. *et al.* A selective Au-ZnO/TiO₂ hybrid photocatalyst for oxidative coupling of methane to ethane with dioxygen. *Nat. Catal.* **4**, 1032–1042 (2021).
159. Besenbacher, F. *et al.* Design of a surface alloy catalyst for steam reforming. *Science*. **279**, 1913–1915 (1998).
160. Song, K. *et al.* Effect of alloy composition on catalytic performance and coke-resistance property of Ni-Cu/Mg(Al)O catalysts for dry reforming of methane.

- Appl. Catal. B Environ.* **239**, 324–333 (2018).
161. Kang, X., Li, Y., Zhu, M. & Jin, R. Atomically precise alloy nanoclusters: syntheses, structures, and properties. *Chem. Soc. Rev.* **49**, 6443–6514 (2020).
 162. Wu, X. Y. *et al.* Visible-light driven room-temperature coupling of methane to ethane by atomically dispersed Au on WO₃. *J. Energy Chem.* **61**, 195–202 (2021).
 163. Abis, L., Dimitritatos, N., Sankar, M., Freakley, S. J. & Hutchings, G. J. Plasmonic oxidation of glycerol using AuPd/TiO₂ catalysts. *Catal. Sci. Technol.* **9**, 5686–5691 (2019).
 164. Shu, Y. *et al.* Hollow echinus-like pdcuco alloy for superior efficient catalysis of ethanol. *ACS Appl. Mater. Interfaces* **10**, 4743–4749 (2018).
 165. Dovesi, R. *et al.* Quantum-mechanical condensed matter simulations with CRYSTAL. *Wiley Interdiscip. Rev. Comput. Mol. Sci.* **8**, 1–36 (2018).
 166. Perdew, J. P., Burke, K. & Ernzerhof, M. Generalized gradient approximation made simple. *Phys. Rev. Lett.* **77**, 3865–3868 (1996).
 167. Grimme, S., Antony, J., Ehrlich, S. & Krieg, H. A consistent and accurate ab initio parametrization of density functional dispersion correction (DFT-D) for the 94 elements H-Pu. *J. Chem. Phys.* **132**, (2010).
 168. Hou, Q., Li, X., Pi, Y. & Xiao, J. Construction of In₂S₃@NH₂-MIL-68(In)@In₂S₃Sandwich Homologous Heterojunction for Efficient

- CO₂Photoreduction. *Ind. Eng. Chem. Res.* **68**, (2020).
169. Doll, K. & Harrison, N. M. Chlorine adsorption on the Cu(111) surface. *Chem. Phys. Lett.* **317**, 282–289 (2000).
170. Wang, H. *et al.* Covalent organic framework photocatalysts: structures and applications. *Chem. Soc. Rev.* **49**, 4135–4165 (2020).
171. Gatti, C., Saunders, V. R. & Roetti, C. Crystal field effects on the topological properties of the electron density in molecular crystals: The case of urea. *J. Chem. Phys.* **101**, 10686–10696 (1994).
172. Li, X. *et al.* Facilitation of the visible light-induced Fenton-like excitation of H₂O₂ via heterojunction of g-C₃N₄/NH₂-Iron terephthalate metal-organic framework for MB degradation. *Appl. Catal. B Environ.* **202**, 653–663 (2017).
173. Wang, H., Li, X., Ruan, Q. & Tang, J. Ru and RuO: X decorated carbon nitride for efficient ammonia photosynthesis. *Nanoscale* **12**, 12329–12335 (2020).
174. Lang, S. M., Frank, A. & Bernhardt, T. M. Activation and catalytic dehydrogenation of methane on small Pd_x⁺ and Pd_xO⁺ clusters. *J. Phys. Chem. C* **117**, 9791–9800 (2013).
175. Koitaya, T., Ishikawa, A., Yoshimoto, S. & Yoshinobu, J. C-H Bond Activation of Methane through Electronic Interaction with Pd(110). *J. Phys. Chem. C* **125**, 1368–1377 (2021).
176. He, J. *et al.* CdS Nanowires Decorated with Ultrathin MoS₂ Nanosheets as an

- Efficient Photocatalyst for Hydrogen Evolution. *ChemSusChem* **9**, 624–630 (2016).
177. Meng, Y. *et al.* Theoretical research on a coke-resistant catalyst for the partial oxidation of methane: Pt/Cu single-atom alloys. *New J. Chem.* **44**, 3922–3929 (2020).
178. Marcinkowski, M. D. *et al.* Pt/Cu single-atom alloys as coke-resistant catalysts for efficient C-H activation. *Nat. Chem.* **10**, 325–332 (2018).
179. Yuliati, L., Itoh, H. & Yoshida, H. Preparation of isolated highly dispersed titanium oxides on silica by sol-gel method for photocatalytic non-oxidative direct methane coupling. *Stud. Surf. Sci. Catal.* **162**, 961–968 (2006).
180. Kato, Y., Yoshida, H., Satsuma, A. & Hattori, T. Photoinduced non-oxidative coupling of methane over H-zeolites around room temperature. *Microporous Mesoporous Mater.* **51**, 223–231 (2002).
181. Wang, G. *et al.* Light-Induced Nonoxidative Coupling of Methane Using Stable Solid Solutions. *Angew. Chemie - Int. Ed.* **60**, 20760–20764 (2021).
182. Souza, J. D., Souza, V. S. & Scholten, J. D. Synthesis of Hybrid Zinc-Based Materials from Ionic Liquids: A Novel Route to Prepare Active Zn Catalysts for the Photoactivation of Water and Methane. *ACS Sustain. Chem. Eng.* **7**, 8090–8098 (2019).
183. Si, J. *et al.* Oxidative Coupling of Methane: Examining the Inactivity of the

- MnO_x-Na₂WO₄/SiO₂ Catalyst at Low Temperature. *Angew. Chemie Int. Ed.* **61**, (2022).
184. Tian, J. *et al.* Direct conversion of methane to formaldehyde and CO on B₂O₃ catalysts. *Nat. Commun.* **11**, 5693 (2020).
185. Guo, Z., Kang, X., Zheng, X., Huang, J. & Chen, S. PdCu alloy nanoparticles supported on CeO₂ nanorods: Enhanced electrocatalytic activity by synergy of compressive strain, PdO and oxygen vacancy. *J. Catal.* **374**, 101–109 (2019).
186. Wang, F. *et al.* Monodisperse CuPd alloy nanoparticles supported on reduced graphene oxide as efficient catalyst for directed C–H activation. *Catal. Commun.* **153**, 106296 (2021).
187. Liu, F. *et al.* Integration of Bimetallic Electronic Synergy with Oxide Site Isolation Improves the Selective Hydrogenation of Acetylene. *Angew. Chemie Int. Ed.* **60**, 19324–19330 (2021).
188. Li, N., Yan, W., Zhang, W., Wang, Z. & Chen, J. Photoinduced formation of Cu@Cu₂O@C plasmonic nanostructures with efficient interfacial charge transfer for hydrogen evolution. *J. Mater. Chem. A* (2019) doi:10.1039/C9TA05846J.
189. McFarland, E. W. & Tang, J. A photovoltaic device structure based on internal electron emission. *Nature* **421**, 616–618 (2003).
190. Feng, N. *et al.* Efficient and selective photocatalytic CH₄ conversion to

- CH₃OH with O₂ by controlling overoxidation on TiO₂. *Nat. Commun.* **12**, (2021).
191. Hirakawa, T., Nakaoka, Y., Nishino, J. & Nosaka, Y. Primary passages for various TiO₂ photocatalysts studied by means of luminol chemiluminescent probe. *J. Phys. Chem. B* **103**, 4399–4403 (1999).
192. Zhu, S. *et al.* Efficient Photooxidation of Methane to Liquid Oxygenates over ZnO Nanosheets at Atmospheric Pressure and Near Room Temperature. *Nano Lett.* **21**, 4122–4128 (2021).
193. Jin, C. *et al.* Effects of single metal atom (Pt, Pd, Rh and Ru) adsorption on the photocatalytic properties of anatase TiO₂. *Appl. Surf. Sci.* **426**, 639–646 (2017).
194. Hardcastle, F. D., Ishihara, H., Sharma, R. & Biris, A. S. Photoelectroactivity and Raman spectroscopy of anodized titania (TiO₂) photoactive water-splitting catalysts as a function of oxygen-annealing temperature. *J. Mater. Chem.* **21**, 6337–6345 (2011).
195. Ouyang, Y. & Chen, L. Surface-enhanced Raman scattering studies of few-layer graphene on silver substrate with 514 nm excitation. *J. Mol. Struct.* **992**, 48–51 (2011).
196. Dresselhaus, M. S., Jorio, A., Hofmann, M., Dresselhaus, G. & Saito, R. Perspectives on carbon nanotubes and graphene Raman spectroscopy. *Nano Lett.* **10**, 751–758 (2010).

197. Saito, R., Hofmann, M., Dresselhaus, G., Jorio, A. & Dresselhaus, M. S. Raman spectroscopy of graphene and carbon nanotubes. *Adv. Phys.* **60**, 413–550 (2011).
198. Han, Z. *et al.* Propane dehydrogenation over Pt-Cu bimetallic catalysts: The nature of coke deposition and the role of copper. *Nanoscale* **6**, 10000–10008 (2014).
199. Derry, G. N. & Ji-zhong, Z. Work function of Pt (111). *Phys. Rev. B* **39**, 1940–1941 (1989).
200. van Langeveld, A. D., Hendrickx, H. A. C. M. & Nieuwenhuys, B. E. The surface composition of Pd-Cu alloys: A comparative investigation of photoelectric work function measurements, Auger electron spectroscopy and calculations based on a broken bond approximation. *Thin Solid Films* **109**, 179–192 (1983).
201. Kashiwaya, S. *et al.* The Work Function of TiO₂. *Surfaces* **1**, 73–89 (2018).
202. Schultz, T. *et al.* Reliable Work Function Determination of Multicomponent Surfaces and Interfaces: The Role of Electrostatic Potentials in Ultraviolet Photoelectron Spectroscopy. *Adv. Mater. Interfaces* **4**, 1–8 (2017).
203. Liu, Y. *et al.* Bipolar charge collecting structure enables overall water splitting on ferroelectric photocatalysts. *Nat. Commun.* **13**, 4245 (2022).
204. Zachman, M. J. *et al.* Measuring and directing charge transfer in heterogenous

- catalysts. *Nat. Commun.* **13**, 3253 (2022).
205. Funston, A. M., Novo, C., Davis, T. J. & Mulvaney, P. Plasmon coupling of gold nanorods at short distances and in different geometries. *Nano Lett.* **9**, 1651–1658 (2009).
206. Sarina, S. *et al.* Viable Photocatalysts under Solar-Spectrum Irradiation: Nonplasmonic Metal Nanoparticles. *Angew. Chemie Int. Ed.* **53**, 2935–2940 (2014).
207. Zhang, W. *et al.* High-performance photocatalytic nonoxidative conversion of methane to ethane and hydrogen by heteroatoms-engineered TiO₂. *Nat. Commun.* **13**, 2806 (2022).
208. Amano, F. & Ishimaru, M. Hydroxyl Radical Formation on Metal-Loaded Ga₂O₃ Photocatalysts for Dehydrogenative Coupling of Methane to Ethane with Water. *Energy & Fuels* **36**, 5393–5402 (2022).
209. Singh, S. P. *et al.* A Pd-Bi Dual-Cocatalyst-Loaded Gallium Oxide Photocatalyst for Selective and Stable Nonoxidative Coupling of Methane. *ACS Catal.* **11**, 13768–13781 (2021).
210. Liao, W. T., Lee, W. J., Chen, C. Y., Hsieh, L. Te & Lai, C. C. Influence of precursors of Li₂O and MgO on surface and catalytic properties of Li-promoted MgO in oxidative coupling of methane. *J. Chem. Technol. Biotechnol.* **75**, 828–834 (2000).

211. Ito, T., Wang, J. X., Lin, C. H. & Lunsford, J. H. Oxidative dimerization of methane over a lithium-promoted magnesium oxide catalyst. *J. Am. Chem. Soc.* **107**, 5062–5068 (1985).
212. Si, J. *et al.* Oxidative Coupling of Methane: Examining the Inactivity of the MnO_x-Na₂WO₄/SiO₂ Catalyst at Low Temperature. *Angew. Chemie Int. Ed.* **61**, (2022).
213. Liu, W. C., Ralston, W. T., Melaet, G. & Somorjai, G. A. Oxidative coupling of methane (OCM): Effect of noble metal (M = Pt, Ir, Rh) doping on the performance of mesoporous silica MCF-17 supported Mn_xO_y-Na₂WO₄ catalysts. *Appl. Catal. A Gen.* **545**, 17–23 (2017).
214. Wang, P., Zhang, X., Zhao, G., Liu, Y. & Lu, Y. Oxidative coupling of methane: MO_x-modified (M = Ti, Mg, Ga, Zr) Mn₂O₃-Na₂WO₄/SiO₂ catalysts and effect of MO_x modification. *Cuihua Xuebao/Chinese J. Catal.* **39**, 1395–1402 (2018).
215. Wang, P., Zhao, G., Wang, Y. & Lu, Y. MnTiO₃-driven low-temperature oxidative coupling of methane over TiO₂-doped Mn₂O₃-Na₂WO₄/SiO₂ catalyst. *Sci. Adv.* **3**, 2003–2003 (2017).
216. Le Van, T., Che, M., Kermarec, M., Louis, C. & Tatibouët, J. M. Structure sensitivity of the catalytic oxidative coupling of methane on lanthanum oxide. *Catal. Letters* **6**, 395–400 (1990).
217. Thomas, J. M., Ueda, W., Williams, J. & Harris, K. D. M. New families of

- catalysts for the selective oxidation of methane. *Faraday Discuss. Chem. Soc.* **87**, 33 (1989).
218. Yildiz, M. *et al.* Enhanced catalytic performance of $\text{Mn}_x\text{O}_y\text{-Na}_2\text{WO}_4/\text{SiO}_2$ for the oxidative coupling of methane using an ordered mesoporous silica support. *Chem. Commun.* **50**, 14440–14442 (2014).
219. Elkins, T. W. & Hagelin-Weaver, H. E. Oxidative coupling of methane over unsupported and alumina-supported samaria catalysts. *Appl. Catal. A Gen.* **454**, 100–114 (2013).
220. Young, A. J. *et al.* One-step synthesis and XPS investigations of chiral NHC-Au(0)/Au(i) nanoparticles. *Nanoscale* **11**, 8327–8333 (2019).
221. Casaletto, M. P., Longo, A., Martorana, A., Prestianni, A. & Venezia, A. M. XPS study of supported gold catalysts: the role of Au⁰ and Au^{+ δ} species as active sites. *Surf. Interface Anal.* **38**, 215–218 (2006).
222. Li, X., Yu, J. & Jaroniec, M. Hierarchical photocatalysts. *Chem. Soc. Rev.* **45**, 2603–2636 (2016).
223. Hao, X. *et al.* Architecture of high efficient zinc vacancy mediated Z-scheme photocatalyst from metal-organic frameworks. *Nano Energy* **52**, 105–116 (2018).
224. Li, C. & Xin, Q. FT-IR spectroscopic investigation of methane adsorption on cerium oxide. *J. Phys. Chem.* **96**, 7714–7718 (1992).

225. Beckerle, J. D., Johnson, A. D., Yang, Q. Y. & Ceyer, S. T. Collision induced dissociative chemisorption of CH₄ on Ni(111) by inert gas atoms: The mechanism for chemistry with a hammer. *J. Chem. Phys.* **91**, 5756–5777 (1989).
226. Finnie, K. S., Luca, V., Moran, P. D., Bartlett, J. R. & Woolfrey, J. L. Vibrational spectroscopy and EXAFS study of Ti(OC₂H₅)₄ and alcohol exchange in Ti(iso-OC₃H₇)₄. *J. Mater. Chem.* **10**, 409–418 (2000).
227. Tao, F. F. *et al.* Understanding complete oxidation of methane on spinel oxides at a molecular level. *Nat. Commun.* **6**, 7798 (2015).
228. Poater, A., Ragone, F., Correa, A. & Cavallo, L. Comparison of different ruthenium-alkylidene bonds in the activation step with N-heterocyclic carbene Ru-catalysts for olefins metathesis. *Dalt. Trans.* **40**, 11066–11069 (2011).
229. Arndt, S. *et al.* A Critical Assessment of Li/MgO-Based Catalysts for the Oxidative Coupling of Methane. *Catal. Rev.* **53**, 424–514 (2011).
230. Kuo, J. C. W., Kresge, C. T. & Palermo, R. E. Evaluation of direct methane conversion to higher hydrocarbons and oxygenates. *Catal. Today* **4**, 463–470 (1989).
231. Zhang, R. *et al.* Photocatalytic Oxidative Dehydrogenation of Ethane Using CO₂ as a Soft Oxidant over Pd/TiO₂ Catalysts to C₂H₄ and Syngas. *ACS Catal.* **8**, 9280–9286 (2018).
232. Zeng, L., Guo, X., He, C. & Duan, C. Metal-Organic Frameworks: Versatile

- Materials for Heterogeneous Photocatalysis. *ACS Catal.* **6**, 7935–7947 (2016).
233. Connolly, B. M. *et al.* Tuning porosity in macroscopic monolithic metal-organic frameworks for exceptional natural gas storage. *Nat. Commun.* **10**, 1–11 (2019).
234. Xue, D. X., Wang, Q. & Bai, J. Amide-functionalized metal-organic frameworks: Syntheses, structures and improved gas storage and separation properties. *Coord. Chem. Rev.* **378**, 2–16 (2019).
235. Okabe, K., Sayama, K., Kusama, H. & Arakawa, H. Photo-Oxidative Coupling of Methane over TiO₂-based Catalysts. *Chem. Lett.* **26**, 457–458 (1997).
236. Tahir, B., Tahir, M. & Amin, N. A. S. Tailoring performance of La-modified TiO₂ nanocatalyst for continuous photocatalytic CO₂ reforming of CH₄ to fuels in the presence of H₂O. *Energy Convers. Manag.* **159**, 284–298 (2018).
237. Thampi, K. R., Kiwi, J. & Grätzel, M. Room temperature photo-activation of methane on TiO₂ supported molybdena. *Catal. Letters* **1**, 109–116 (1988).
238. László, B. *et al.* Photo-induced reactions in the CO₂-methane system on titanate nanotubes modified with Au and Rh nanoparticles. *Appl. Catal. B Environ.* **199**, 473–484 (2016).
239. Wada, K., Yamada, H., Watanabe, Y. & Mitsudo, T. A. Selective photo-assisted catalytic oxidation of methane and ethane to oxygenates using supported vanadium oxide catalysts. *J. Chem. Soc. - Faraday Trans.* **94**, 1771–

1778 (1998).

240. López, H. H. & Martínez, A. Selective photo-assisted oxidation of methane into formaldehyde on mesoporous VO_x/SBA-15 catalysts. *Catal. Letters* **83**, 37–41 (2002).
241. Hu, Y., Nagai, Y., Rahmawaty, D., Wei, C. & Anpo, M. Characteristics of the photocatalytic oxidation of methane into methanol on V-containing MCM-41 catalysts. *Catal. Letters* **124**, 80–84 (2008).
242. Anpo, M., Shioya, Y. & Che, M. Photoinduced methanol formation from methane and no at 275 k on highly dispersed vanadium oxide supported on vycor glass and its reaction intermediate species. *Res. Chem. Intermed.* **17**, 15–26 (1992).
243. Jiang, H. *et al.* Synergistic photothermal and photochemical partial oxidation of methane over noble metals incorporated in mesoporous silica. *Chem. Commun.* **55**, 13765–13768 (2019).
244. Krishna, V., Kamble, V. S., Selvam, P. & Gupta, N. M. Sunlight-assisted photocatalytic oxidation of methane over uranyl-anchored MCM-41. *Catal. Letters* **98**, 113–116 (2004).
245. Kohno, Y., Tanaka, T., Funabiki, T. & Yoshida, S. Photoreduction of carbon dioxide with methane over ZrO₂. *Chem. Lett.* **26**, 993–994 (1997).
246. Wada, K., Yoshida, K., Takatani, T. & Watanabe, Y. Selective photo-oxidation

- of light alkanes using solid metal oxide semiconductors. *Appl. Catal. A, Gen.* **99**, 21–36 (1993).
247. Shimura, K. *et al.* Photocatalytic Steam Reforming of Methane over Sodium Tantalate. *J. Phys. Chem. C* **114**, 3493–3503 (2010).
248. Du, J. *et al.* Evoked methane photocatalytic conversion to C₂ oxygenates over ceria with oxygen vacancy. *Catalysts* **10**, 1–11 (2020).
249. Pan, F. *et al.* Integrating photocatalysis and thermocatalysis to enable efficient CO₂ reforming of methane on Pt supported CeO₂ with Zn doping and atomic layer deposited MgO overcoating. *Appl. Catal. B Environ.* **260**, 118189 (2020).
250. Jiang, L., Zhang, Y., Qiu, Y. & Yi, Z. Improved photocatalytic activity by utilizing the internal electric field of polar semiconductors: A case study of self-assembled NaNbO₃ oriented nanostructures. *RSC Adv.* **4**, 3165–3170 (2014).

10 Appendix

Table 10-1 Representative photocatalysts used for methane conversion to various products

Co-catalyst/photocatalyst	Experimental Conditions	Methane Conversion	Main Products	Product Rates	Product Selectivity	AQY
TiO ₂ ³⁸	Batch reaction, 355 nm high power UV laser, 300 mg catalyst, CH ₄ saturated in 60 mL water, room temperature	21%	CH ₃ OH H ₂	128 μmol h ⁻¹ 5 mmol h ⁻¹	-	-
TiO ₂ ²³⁵	Batch reaction, 100 W Hg lamp, 5 g catalyst, CH ₄ : O ₂ = 4: 1, 40 kPa reaction gas, 473 K	13.0%	C ₂ H ₆ CO ₂	- -	3.9% 93.0%	-
TiO ₂ ⁴²	Batch reaction, Hg lamp (λ>320 nm), 100 mg catalyst, 0.097 Torr CH ₄ , 0.152 Torr O ₂ , room temperature to 623 K, reaction time 1.5 h	-	C ₂ H ₆	1.61 mol h ⁻¹	ca. 27.6%	-
Pt/TiO ₂ ³⁹	Flow reaction, 300 W Xe lamp, 500 mg catalyst, CH ₄ 50%, H ₂ O 1.4%, Ar 48.6%, GHSV = 3600 mL g ⁻¹ h ⁻¹ , 323 K	-	CO ₂ H ₂	10.8 μmol h ⁻¹ 45.6 μmol h ⁻¹	85%	0.6% (345-385 nm)
Pt/TiO ₂ ⁴⁴	Batch reaction, 4 W 254 nm UV lamp, 75 mg catalyst, 80 mL CH ₄ (circulation rate of 10 mL/min), 75 mL	1.1%	C ₂ H ₆ CO ₂	2 μmol h ⁻¹ 2 μmol h ⁻¹	61.7% 32%	3.3% based on H ₂

	water, room temperature, reaction time 6 h		H ₂	16 μmol h ⁻¹	-	generation; 4.7% based on CH ₄ conversion (254 nm)
Pt/TiO ₂ ⁴⁵	Batch reaction, 1.6 kW Xe lamp, 100 mg catalyst, 20 mL 2 M NH ₄ Cl solutions, reaction time 64 h	-	Amino acids	~0.0078 μmol h ⁻¹	-	-
Pt/black TiO ₂ ²²	Flow reaction, 150 W Xenon lamp (λ>420 nm), 15 mg catalyst, H ₂ O: CH ₄ = 1: 1, GHSV = 80000 mL g ⁻¹ h ⁻¹ , 773 K	-	H ₂	2.775 mmol h ⁻¹	-	60% (λ>420 nm, 773 K)
Pd/TiO ₂ ⁴³	Batch reaction, 4 W 254 nm UV lamp, 75 mg catalyst, 80 mL CH ₄ (circulation rate of 10 mL/min), 75 mL water, room temperature, reaction time 6 h.	1%	C ₂ H ₆ CO ₂ H ₂	2.1 μmol h ⁻¹ 1.5 μmol h ⁻¹ 9 μmol h ⁻¹	72% 29% -	2.83% based on H ₂ generation; 2.76% based on CH ₄ conversion (254 nm)
Rh/TiO ₂ ³¹	Flow reaction, Xe lamp (λ>420 nm), 20 mg catalyst, CH ₄ 10%, H ₂ O 3%, Ar 87%, GHSV = 3000 mL g ⁻¹ h ⁻¹ , 533 K	-	CO ₂ H ₂	28.8 μmol h ⁻¹ 139 μmol h ⁻¹	- -	7.5% (450 nm)
FeO _x /TiO ₂ ¹²	Batch reaction, 300 W Xe lamp (λ<710 nm), 10 mg catalyst, 20%	15%	CH ₃ OH	3.5 μmol h ⁻¹	90%	-

	CH ₄ , 80% Ar, 6mL H ₂ O, 4 mL 2 mM H ₂ O ₂ , 298 K, reaction time 3 h					
Ag/TiO ₂ ¹⁰¹	Batch reaction, Xe lamp, 100 mg catalyst, CO ₂ : CH ₄ : Ar = 7.5: 7.5: 85, 2 MPa, ca. 308 K, reaction time 2 h	-	CO C ₂ H ₄	114.9 μmol h ⁻¹ 68.6 μmol h ⁻¹	-	-
Au/TiO ₂ ³⁰	Flow reaction, 300 W Xe lamp, 5 mg catalyst, 10% CH ₄ , 90% Ar, GHSV = 120000 mL g ⁻¹ h ⁻¹ , room temperature	-	C ₂ H ₆	0.41 μmol h ⁻¹	95.9%	-
Au-CoO _x /TiO ₂ ¹²¹	Batch reaction, 300 W Xe lamp, 10 mg catalyst, 2 MPa CH ₄ , 0.1 MPa O ₂ , 100 mL H ₂ O, 298 ± 2 K, reaction time 2 h	0.07%	CH ₃ OH CH ₃ OOH	15 μmol h ⁻¹ 10.4 μmol h ⁻¹	56.1% 38.9%	1.2% (368 nm) based on CH ₃ OH and CH ₃ OH
Pt/Ga-TiO ₂ -SiO ₂ ¹⁸	Batch reaction, 300 W Xe lamp, 200 mg catalyst, 44.6 μmol CH ₄ , room temperature, reaction time 4 h	6.24%	C ₂ H ₆ H ₂	0.314 μmol h ⁻¹ 0.42 μmol h ⁻¹	90.1%	0.0001% (350 nm)
La/TiO ₂ ²³⁶	Flow reaction, 200 W Hg lamp, 250 mg catalyst, CH ₄ : CO ₂ = 1: 1, GHSV = 4800 mL g ⁻¹ h ⁻¹ , 373 K, reaction time 6 h	-	C ₂ H ₆ H ₂ CO	118 μmol h ⁻¹ 45 μmol h ⁻¹ 188 μmol h ⁻¹	-	-
Pt-CuO _x /TiO ₂ ¹⁰⁰	Flow reaction, 40 W 365 nm LED, 100 mg catalyst, CH ₄ :O ₂ = 400:1, 10% CH ₄ ,	-	C ₂ H ₄ /C ₂ H ₆ CO ₂	6.8 μmol h ⁻¹	60%	0.5% (365 nm)

	GHSV = 2400 h ⁻¹ , 313 K					
Zn-H ₃ PW ₁₂ O ₄₀ /TiO ₂ ⁴¹	Batch reaction, 400 W Xe lamp, 100 mg catalyst, 0.3 MPa CH ₄ , 0.1 MPa air, room temperature, reaction time 6 h	-	CO	42.9 μmol h ⁻¹	84%	7.1% (362 nm)
Ag-H ₃ PW ₁₂ O ₄₀ /TiO ₂ ³⁶	Batch reaction, 400 W Xe lamp, 100 mg catalyst, 0.3 MPa CH ₄ , room temperature, reaction time 7 h	-	C ₂ H ₆	2.3 μmol h ⁻¹	90%	3.5% (362 nm)
SrCO ₃ /TiO ₂ ⁴⁰	Batch reaction, 300 W Xe lamp, 250 mg catalyst, 100 μL CH ₄ , room temperature, reaction time 10 h	45%	CO ₂	-	-	-
TiO ₂ /MoO ₃ ²³⁷	Batch reaction, solar simulator, 200 mg catalyst, 2 mL CH ₄ , 1 mL O ₂ , 315 K, reaction time ca. 10 to 20 h	-	CO CO ₂	ca. 4.3 μmol h ⁻¹ (for both)	-	>0.81% (300-400 nm)
CuPc/TiO ₂ ⁴⁶	Batch reaction, 125 W Hg lamp, 1.0 g catalyst, CO ₂ : CH ₄ : He = 9: 9: 2, 40 psig, reaction time 3 h	19%	Oxalic acid Acetaldehyde Acetic acid CO	-	-	-
Au/titanate nanotubes ²³⁸	Flow reaction, Hg lamp, 500 mg catalyst, CH ₄ : CO ₂ = 1: 1, CH ₄ 0.9 mL min ⁻¹ , Argon 28.2 mL min ⁻¹ , GHSV	ca. 3%	H ₂ , C ₂ H ₆	52 μmol h ⁻¹ 5.7 μmol h ⁻¹	-	-

	= 3600 mL h ⁻¹ g ⁻¹ , 403 K					
FSM-16 ²⁹	Batch reaction, 300 W Xe lamp, 200 mg catalyst, 200 μmol CH ₄ , ca. 310 K, reaction time 3 h	0.0568%	C ₂ H ₆	0.018 μmol h ⁻¹	94%	-
Beta Zeolite ⁸¹¹⁷⁴	Batch reaction, 185 nm UV lamp, 2 g catalyst, 3.7 mmol CH ₄ , 0.925 mmol O ₂ , room temperature, reaction time 5 min	6.2%	CH ₃ OH HCHO HCOOH	130 μmol h ⁻¹ 59 μmol h ⁻¹ 41 μmol h ⁻¹	56.5% 25.8% 17.7%	-
H-MOR ¹⁸⁰	Batch reaction, 250 W Xe lamp, 1 g catalyst, 200 μmol CH ₄ , ca. 310 K, reaction time 3 h	0.122%	C ₂ H ₆	0.074 μmol h ⁻¹	88%	
SiO ₂ -Al ₂ O ₃ ⁶³	Batch reaction, 250 W Xe lamp, 1 g catalyst, 100 μmol CH ₄ , ca. 310 K, reaction time 18 h	5.9%	C ₂ H ₆	0.0986 μmol h ⁻¹	60%	-
SiO ₂ -Al ₂ O ₃ (20 mol% Al) ¹⁹	Batch reaction, 250 W Xe lamp, 1 g catalyst, 200 μmol CH ₄ , ca. 310 K, reaction time 6 h	-	C ₂ H ₆	0.0167 μmol h ⁻¹	100%	-
SiO ₂ -Al ₂ O ₃ -TiO ₂ ⁶⁴	Batch reaction, 250 W Xe lamp, 1 g catalyst, 200 μmol CH ₄ , ca. 310 K, reaction time 3 h	2.47%	C ₂ H ₆ H ₂	0.69 μmol h ⁻¹ 1.18 μmol h ⁻¹	83.8%	-
MoO ₃ (5wt%)/SiO ₂ ¹⁵	Flow reaction, 200 W Hg lamp, 25 mg catalyst, CH ₄ : O ₂ : He = 6: 2: 25, GHSV = 10000 h ⁻¹ , 493 K	-	HCHO CH ₃ OH	5.8 μmol h ⁻¹ 0.2 μmol h ⁻¹	96.7% 3.3%	-

Ce(0.1)Ti(0.1)/SiO ₂ ⁶⁵	Batch reaction, 300 W Xe lamp, 200 mg catalyst, 200 μmol CH ₄ , ca. 310 K, reaction time 3 h	-	C ₂ H ₆	0.04 μmol h ⁻¹	-	-
ZrO ₂ /SiO ₂ (0.1) ⁸³	Batch reaction, 250 W Xe lamp, 0.5 g catalyst, 200 μmol CH ₄ , ca. 305 K, reaction time 3 h	0.112%	C ₂ H ₆	0.036 μmol h ⁻¹	ca. 96.0%	-
TiO ₂ /SiO ₂ ¹⁷⁹	Batch reaction, 300 W Xe lamp, 200 mg catalyst, 200 mol CH ₄ , ca. 310 K, reaction time 3 h	0.3%	C ₂ H ₆	ca. 0.20 μmol h ⁻¹	>90%	-
Cu/CdS-TiO ₂ /SiO ₂ ²⁰	Flow reaction, 125 W Hg lamp, 10 g catalyst, CH ₄ : CO ₂ = 1: 1, GHSV = 200 h ⁻¹ , 373 K	1.47%	CH ₃ COC H ₃	-	92.3%	-
Ga ₂ O ₃ -K ⁶⁹	Batch reaction, 300 W Xe lamp, 200 mg catalyst, 200 μmol CH ₄ , ca. 310 K, reaction time 3 h	0.17%	C ₂ H ₆ H ₂	0.054 μmol h ⁻¹ 0.036 μmol h ⁻¹	96%	-
Ga-ETS-10-0.2 ⁶⁶	Batch reaction, 150 W Hg lamp, 200 mg catalyst, 200 μmol CH ₄ , room temperature, reaction time 5 h	14.9%	C ₂ H ₆	2.178 μmol h ⁻¹	73.9%	-
(Zn ⁺ , Zn ²⁺)-ZSM-5 ⁷²	Batch reaction, 150 W Hg lamp, 1 g catalyst, 200 μmol CH ₄ , room temperature, reaction time 8 h	23.8%	C ₂ H ₆ H ₂	2.9 μmol h ⁻¹ 2.8 μmol h ⁻¹	99.6%	0.55% (300-400 nm)

Ce ³⁺ -Al ₂ O ₃ ⁶⁷	Batch reaction, 300 W Xe lamp, 200 mg catalyst, 200 μmol CH ₄ , ca. 310 K, reaction time 3 h	0.21%	C ₂ H ₆	0.05 μmol h ⁻¹	72%	-
Ce-Al ₂ O ₃ ⁷⁰	Batch reaction, 300 W Xe lamp, 200 mg catalyst, 200 μmol CH ₄ , ca. 310 K, reaction time 3 h	0.366%	C ₂ H ₆	0.095 μmol h ⁻¹	78%	-
Ni/Al ₂ O ₃ ⁹⁶	Flow reaction, Xe lamp (300 nm < λ < 800 nm), 50 mg catalyst, CH ₄ : CO ₂ = 1: 1, GHSV = 24000 mL g ⁻¹ h ⁻¹ , 823 K	-	H ₂ CO	390 μmol h ⁻¹ 390 μmol h ⁻¹	Ratio(H ₂ /CO) = ~ 1	19.0% (450 nm)
Ni/SiO ₂ -yolk ⁹⁴	Flow reaction, Xe lamp (300 nm < λ < 800 nm), catalyst containing 0.030 g Ni, CH ₄ : CO ₂ = 1: 1, GHSV = ~14360 mL g ⁻¹ h ⁻¹ , 823 K	-	H ₂ CO	~1260 μmol h ⁻¹ ~1260 μmol h ⁻¹	Ratio(H ₂ /CO) = ~ 1	-
Silica cluster-Ni/SiO ₂ ⁷⁵	Flow reaction, 500 W Xe lamp, 0.0243 g portion of catalyst, 11.7% CH ₄ , 11.5% CO ₂ , Ar balance, total flow rate 118.7 mL min ⁻¹ , 919 K under irradiation	-	H ₂ CO	250.3 mmol h ⁻¹ 291.2 mmol h ⁻¹	-	-
MgO ¹⁴¹	Batch reaction, Hg lamp, 4.2 μmol CH ₄ , 3.0 Torr N ₂ O, 293 K, reaction time 3 h	-	C ₂ H ₆ C ₂ H ₄	0.6 nmol h ⁻¹ , 0.04 nmol h ⁻¹	-	-
MgO-SiO ₂ ¹⁴²	Batch reaction, 300 W Xe lamp, 200 mg catalyst, 200 μmol	0.028%	C ₂ H ₆	0.009 μmol h ⁻¹	97.9%	-

	CH ₄ , ca. 310 K, reaction time 3 h					
V ₂ O ₅ /SiO ₂ ²³⁹	Flow reaction, 200 W Hg lamp, 25 mg catalyst, He: CH ₄ : O ₂ = 10: 3: 1, GHSV = 33600 mL g ⁻¹ h ⁻¹ , 493 K, reaction time 2 h	0.48%	HCHO	34 μmol h ⁻¹	76%	-
VO _x /SBA-15 ²⁴⁰	Flow reaction, 250 W Hg lamp, 50 mg – 150 mg catalyst, N ₂ : CH ₄ : O ₂ = 10: 3: 1, GHSV = 31500 mL g ⁻¹ h ⁻¹ , 493 K, reaction time 2~5 h	0.3%	HCHO	70.5 μmol h ⁻¹	95.4%	-
Rh-Au/SBA-15 ⁹⁷	Flow reaction, Xe lamp (visible light), 5 mg catalyst, CH ₄ : CO ₂ = 1:1, GHSV = 240000 ml g ⁻¹ h ⁻¹ , 773 K	-	H ₂ CO	129 mmol h ⁻¹ 126 mmol h ⁻¹	Ratio(H ₂ /CO) = ~ 1	-
Bi-V-beta zeolite ⁷³	Batch reaction, 450 W Hg lamp, 150 mg catalyst in 300 mL H ₂ O, CH ₄ /He=20%, ca. 343 K, reaction time 2 h	-	CH ₃ OH CO ₂	1.6 μmol h ⁻¹ 23 μmol h ⁻¹	6.3% 91%	-
AgNa-Y zeolite ⁶¹	Batch reaction, 450 W Hg lamp (220<λ<700 nm), 0.75 g catalyst, 1 atm CH ₄ , <308 K, reaction time 3 h	-	C ₂ H ₆	1000 mol mol _{Ag} ⁻¹ h ⁻¹	>90%	-
V-MCM-41 ¹³	Batch reaction, 100 W leg lamp (λ>270 nm), 150 μmol CH ₄ /g catalyst, CH ₄ /NO=1, 295 K, reaction time 5 h	7%	CH ₃ OH CO ₂	1.6 μmol h ⁻¹ g ⁻¹ 0.4 μmol h ⁻¹ g ⁻¹	80% 20%	-
V-MCM-41 ²⁴¹	Batch reaction, 100 W Hg lamp (λ>270 nm), 16 μmol CH ₄ , 16 μmol	7.1%	CH ₃ OH	0.335 μmol h ⁻¹	88.4%	-

	NO, 295 K, reaction time 3 h		CO ₂	0.034 $\mu\text{mol h}^{-1}$	9.1%	
V/Vycor oxide ²⁴²	Batch reaction, Hg lamp ($\lambda > 270$ nm), NO: CH ₄ = 10: 1, 2.0 Torr CH ₄ , 275 K	-	CH ₃ OH	ca. 0.6 nmol	-	-
Rh/MCM-41 ²⁴³	Flow reaction, 200 W Hg-Xe lamp, 8 mg catalyst, 1% CH ₄ , 0.5% O ₂ , 98.5% Ar, GHSV = 75000 ml g ⁻¹ h ⁻¹ , 423 K	49%	CO H ₂	72.3 $\mu\text{mol h}^{-1}$ 235.7 $\mu\text{mol h}^{-1}$	ca. 50 -	1.8% (≥ 250 nm) based on CH ₄ conversion
UO ₂ ²⁺ /MCM-41 ²⁴⁴	Batch reaction, sunlight, 100 mg catalyst, 0.15 % CH ₄ in air, 1.2 bar, room temperature, reaction time 2.5 h	100%	CO ₂	-	-	-
MgO ⁸²	Batch reaction, 500 W Hg lamp, 300 mg catalyst, 50 μmol CH ₄ , 150 μmol CO ₂ , room temperature, reaction time 30 h	36%	CO H ₂	0.45 $\mu\text{mol h}^{-1}$ 0.02 $\mu\text{mol h}^{-1}$	-	-
ZrO ₂ ²⁴⁵	Batch reaction, 500 W Hg lamp, 300 mg catalyst, 50 μmol CH ₄ , 150 μmol CO ₂ , reaction time 5 h	-	CO	0.14 $\mu\text{mol h}^{-1}$	-	-
Ga ₂ O ₃ ⁸¹	Batch reaction, 300 W Xe lamp, 200 mg catalyst, 200 μmol CH ₄ , 200 μmol CO ₂ , 473 K, reaction time 3 h	-	C ₂ H ₆ CO H ₂	0.35 $\mu\text{mol h}^{-1}$ 0.36 $\mu\text{mol h}^{-1}$ 0.83 $\mu\text{mol h}^{-1}$	52.9% 27.5% -	-

Pd/Ga ₂ O ₃ ⁷⁸	Flow reaction, 300 W Xe lamp, 800 mg catalyst, 10% CH ₄ in Ar, GHSV = 2250 mL g ⁻¹ h ⁻¹ , ca. 320 K	0.006%	C ₂ H ₆ H ₂	0.22 μmol h ⁻¹ 0.23 μmol h ⁻¹	Ratio(C ₂ H ₆ /H ₂) = 0.96	-
Pt/Ga ₂ O ₃ ⁸⁰	Flow reaction, 300 W Xe lamp, 800 mg catalyst, CH ₄ 50%, H ₂ O 1.5%, Ar 48.5%, GHSV = 3750 mL g ⁻¹ h ⁻¹ , ca. 308 K	-	CO ₂ H ₂	7.65 μmol h ⁻¹ 30.6 μmol h ⁻¹	Ratio(H ₂ /CO ₂) = 4	7.9% (254 ± 20 nm)
ZnO ²⁴⁶	Flow reaction, 200 W Hg lamp, 0.25 g catalyst, CH ₄ : O ₂ : He = 3: 1: 10, CH ₄ 7.5 mmol h ⁻¹ , Space velocity = 141 mmol g ⁻¹ h ⁻¹ , 493 K	-	HCHO	4.7 μmol h ⁻¹ 33 μmol h ⁻¹	ca. 10.6% ca. 74.3%	-
Ag/ZnO ²⁶	Batch reaction, 300 W Xe lamp, 500 mg catalyst, CH ₄ 100 ppm, N ₂ 78.9%, O ₂ 21.1%, room temperature, reaction time 2.5 h. Flow reaction, 300 W Xe lamp, 500 mg catalyst, CH ₄ 100 ppm, N ₂ 78.9%, O ₂ 21.1%, GHSV = 3000 mL g ⁻¹ h ⁻¹ , room temperature	100% (batch reaction); 98.5% (flow reaction)	CO ₂	-	100%	8% (<400 nm) 0.1% (~470 ± 12 nm)
Au/ZnO ¹⁷	Batch reaction, 300 W Xe lamp, 1 mg catalyst, 1.0 bar Ar, 0.5 mL CH ₄ , room temperature, reaction time 4 h	0.4%	C ₂ H ₆ H ₂	0.0113 μmol h ⁻¹ 0.01 μmol h ⁻¹	Ratio(C ₂ H ₆ /H ₂) = 1	-

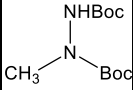
Au/ZnO ⁴⁸	Batch reaction, 300 W Xe lamp, 10 mg catalyst, 2 MPa CH ₄ , 0.1 MPa O ₂ , 100 mL H ₂ O, 298 ± 2 K, reaction time 2 h	-	CH ₃ OOH CH ₃ OH HCHO	61.7 μmol h ⁻¹ 20.6 μmol h ⁻¹ 43.2 μmol h ⁻¹	46.9% 15.7% 32.8%	11.7% (368 nm)
AuPd/ZnO ³⁷	Batch reaction, 300 W Xe lamp, 2 mg catalyst, 0.5 mL CH ₄ in argon, room temperature, 1 atm, reaction time 4 h	-	C ₂ H ₄ C ₂ H ₆	~0.026 μmol h ⁻¹ ~0.053 μmol h ⁻¹	33.0% ~66.9%	-
CuO/ZnO ⁴⁷	Batch reaction, 300 W Xe lamp, 500 mg catalyst, CH ₄ 200 ppm, N ₂ 78.9%, O ₂ 21.1%, room temperature, reaction time 2 h. Flow reaction, 300 W Xe lamp, 500 mg catalyst, CH ₄ 100 ppm, N ₂ 78.9%, O ₂ 21.1%, GHSV = 1800 mL g ⁻¹ h ⁻¹ , room temperature	100% (batch reaction); 92.5% (flow reaction)	CO ₂	-	100%	-
ZnO nanosheets ⁵¹	Batch reaction, Xe lamp, 500 mg catalyst, CH ₄ 100 ppm, N ₂ 78.9%, O ₂ 21.1%, room temperature, reaction time 2 h	80%	CO ₂	-	-	-
ZnO/La _{0.8} Sr _{0.2} CoO ₃ ⁵²	Flow reaction, 300 W Xe lamp, 300 mg catalyst, 500 ppm CH ₄ , 20% O ₂ , N ₂ (balance), GHSV = 40000 mL g ⁻¹ h ⁻¹ , 643 K	14.7%	CO ₂	-	-	-

WO ₃ ⁵⁷	Flow reaction, Hg lamp, 300 mg catalyst, 20% CH ₄ /He, 300 mL H ₂ O, 1 mM Fe ³⁺ , GHSV = 4480 mL g ⁻¹ h ⁻¹ , 308 K	-	CH ₃ OH CO ₂	20.25 μmol h ⁻¹ 12.99 μmol h ⁻¹	58.5% 37.5%	-
WO ₃ ³⁸	Batch reaction, 355 nm high power UV laser, 300 mg catalyst, CH ₄ saturated in 60 mL water, room temperature	29%	CH ₃ OH H ₂	160 μmol h ⁻¹ 2.4 mmol h ⁻¹	-	-
WO ₃ /F ⁵⁸	Batch reaction, Hg lamp, 300 mg catalyst, 300 mL H ₂ O, 4.5 mL min ⁻¹ CH ₄ , 17.9 mL min ⁻¹ He, 328 K, reaction time 2 h	-	CH ₃ OH C ₂ H ₆ CO ₂	2.1 μmol h ⁻¹ 1.0 μmol h ⁻¹ 8.2 μmol h ⁻¹	-	-
Ag ₂ O@WO ₃ ⁵⁶	Batch reaction, laser beam, 300 mg catalyst, 70 mL H ₂ O, 100 mL min ⁻¹ CH ₄ for 15 mins, reaction time 1.5 h	-	H ₂ CH ₃ OH	~2.7 mmol h ⁻¹ from 780 to 108 μmol h ⁻¹	-	-
La-WO ₃ ⁵⁹	Flow reaction, Hg lamp, 300 mg catalyst, 20% CH ₄ /He, 300 mL H ₂ O, GHSV = 4480 mL g ⁻¹ h ⁻¹ , 308 K	-	CH ₃ OH CO ₂	9.5 μmol h ⁻¹ 9.8 μmol h ⁻¹	47% -	-
La/WO ₃ ⁵⁴	Flow reaction, Hg lamp, 1 g catalyst, 750 mL H ₂ O, 0.045 g methyl viologen dichloride, 200 μL 30% H ₂ O ₂ , CH ₄ : He = 5: 16, GHSV = 1260 mL g ⁻¹ h ⁻¹ , ~367 K	10%	CH ₃ OH	1.34 mol h ⁻¹	-	-

FeOOH/m-WO ₃ ⁶⁰	Batch reactor, 300 W Xe lamp (420 nm λ <math><780\text{ nm}</math>), 20 mg catalyst, 18 mL H ₂ O, CH ₄ : N ₂ = 1: 9, 1 atm, 1.5 mM H ₂ O ₂ , 298 ± 1 K, reaction time 4 h	4.65%	CH ₃ OH	4.22 μmol h ⁻¹	91.0%	-
CuMoO ₄ ¹⁴	Flow reaction, 1000 W Xe lamp, 400 mg catalyst, CH ₄ :O ₂ =9:1, 373 K	-	CH ₃ OH	6 μmol h ⁻¹	~100%	-
Pt/NaTaO ₃ :La ²⁴⁷	Flow reaction, 300 W Xe Lamp, 1 g catalyst, H ₂ O 1.5%, CH ₄ 50%, Ar 48.5%, GHSV = 3000 mL g ⁻¹ h ⁻¹ , 413 K	0.6%	H ₂	270 μmol h ⁻¹	-	30% based on H ₂ evolution (240-270 nm)
Rh/K ₂ Ti ₆ O ₁₃ ⁸⁹	Flow reaction, 300 W Xe lamp, 800 mg catalyst, H ₂ O 1.5%, CH ₄ 50%, Ar 48.5%, GHSV = 3000 mL g ⁻¹ h ⁻¹ , 323 K	-	H ₂ CO ₂	90 μmol h ⁻¹ 22.5 μmol h ⁻¹	Ratio(H ₂ /CO ₂) = 4	-
BiVO ₄ ⁸⁴	Batch reaction, 450 W Hg lamp, 300 mg catalyst, 300 mL H ₂ O, CH ₄ 20%, He 80%, 328 K, reaction time 2 h	1.0%	CH ₃ OH CO ₂	6.3 μmol h ⁻¹ 5.7 μmol h ⁻¹	48% 43%	-
BiVO ₄ ⁸⁵	Batch reaction, 450 W Hg lamp, 300 mg catalyst, 300 mL H ₂ O, 1 mM NaNO ₂ , CH ₄ 20%, He 80%, 328 K, reaction time 1.5 h	-	CH ₃ OH	3 μmol h ⁻¹	100%	-
BiVO ₄ bipyramids ⁸⁶	Batch reaction, 350 W Xe lamp, 200 mg catalyst, 20 mL H ₂ O, CH ₄ 10%, Ar 90%,	0.96%	CH ₃ OH	22.38 μmol h ⁻¹	85.0%	-

	338 K, reaction time 1 h					
SrCO ₃ /SrTiO ₃ ⁸⁷	Batch reaction, 300 W Xe lamp, 200 mg catalyst, CH ₄ 200 ppm, N ₂ 78.9%, O ₂ 21.1%, room temperature, reaction time 5 h	100%	CO ₂	-	-	-
Rh/SrTiO ₃ ⁸⁸	Flow reaction, 150 W Hg-Xe lamp, 5 mg catalyst, CH ₄ 1%, CO ₂ 1%, Ar 98%, GHSV = 120000 mL g ⁻¹ h ⁻¹	52%	CO H ₂	270 μmol h ⁻¹ 264 μmol h ⁻¹	Ratio(H ₂ /CO) ≈ 1	5.9%
Cu _{19.8} Ru _{0.2} ²¹	Flow reaction, supercontinuum laser 19 W cm ⁻² , 1.5 mg catalyst, CH ₄ 50%, CO 50%, GHSV = 640000 mL g ⁻¹ h ⁻¹ , room temperature	-	CO H ₂	2970 μmol h ⁻¹ 2970 μmol h ⁻¹	Ratio(H ₂ /CO) ≈ 1	-
NiO ³⁸	Batch reaction, 355 nm high power UV laser, 300 mg catalyst, CH ₄ saturated in 60 mL water, room temperature	20%	CH ₃ OH H ₂	80 μmol h ⁻¹ 2.7 mmol h ⁻¹	-	-
CeO ₂ ²⁴⁸	Batch reaction, 300 W Xe lamp, 2 mg catalyst, 15 mL H ₂ O, 4 mL min ⁻¹ , 0.2 bar, 298 K, reaction time 2 h	-	C ₂ H ₅ OH	0.0228 μmol h ⁻¹	91.5%	-
MgO/Pt/Zn-CeO ₂ ²⁴⁹	Flow reaction, 200-1 K lamp, 5 mg catalyst, CO ₂ : CH ₄ : Ar = 1: 1: 8, GHSV = 168000 mL g ⁻¹ h ⁻¹ , 873 K	38.8%	CO H ₂	2.58 mmol h ⁻¹ 1.78 mmol h ⁻¹	-	-

NaNbO ₃ ²⁵⁰	Batch reaction, 300 W Xe lamp, 150 mg catalyst, 0.5 mL CH ₄ , 5 mL O ₂ , reaction time 7 h	10%	CO ₂	ca. 0.64 $\mu\text{mol h}^{-1}$	-	-
GaN ¹⁰	Batch reaction, 300 W Xe lamp, 0.35 mg catalyst, 150 μmol CH ₄ , 278 K, reaction time 12 h	0.98%	Benzene	0.019 $\mu\text{mol h}^{-1}$	96.5%	ca. 0.72% (290-380 nm) based on production of benzene
g-C ₃ N ₄ ⁹³	Batch reaction, 300 W Xe lamp, 15 mg catalyst, 50 mM H ₂ O ₂ , 25 mL H ₂ O, 30 bar CH ₄ , 308 K, reaction time 2 h	-	CH ₃ OH	2.1 $\mu\text{mol h}^{-1}$	-	Pseudo AQE 15% (420 nm) based on production of methanol
Cu-0.5/polymeric carbon nitride (PCN) ¹⁶	Batch reaction, 500 W Xe lamp, 20 mg catalyst, 25 mL H ₂ O, CH ₄ : N ₂ = 1: 9, total flow rate 100 mL min ⁻¹ , reaction time 1h	-	C ₂ H ₅ OH	2.12 $\mu\text{mol h}^{-1}$	-	-
Cu/g-C ₃ N ₄ nanorods ⁹¹	Batch reaction, solar simulator, 15 mg catalyst, CO ₂ : CH ₄ = 1: 1, 0.20 bar, 373 K, reaction time 2 h	-	CO H ₂	2.13 $\mu\text{mol h}^{-1}$ 1.14 $\mu\text{mol h}^{-1}$	66.6% 32.5%	-

0.5% Ru/Zn-g-C ₃ N ₄ ⁹⁰	Batch reaction, 150 W Xe lamp, 0.1 g catalyst, CO ₂ : CH ₄ : Ar = 7.5: 7.5: 85, 0.50 bar, 353 K, reaction time 3 h	-	CO CH ₃ CHO C ₂ H ₅ OH	47.9 μmol h ⁻¹ 13.04 μmol h ⁻¹ 50.05 μmol h ⁻¹	27.5% 15% 57.5%	-
La/g-C ₃ N ₄ nanotubes ⁹²	Flow reaction, 35 W Xe lamp, 150 mg catalyst, CO ₂ : CH ₄ = 1: 1, 323 K	-	CO H ₂	90.3 μmol h ⁻¹ 5.85 μmol h ⁻¹	-	1.98% (420 nm) based on CO production; 0.13% (420 nm) based on H ₂ production
Au ₁ /black phosphorus nanosheets ¹¹⁹	Batch reaction, 1.2 W Xe lamp, 200 mg catalyst, 20 mL H ₂ O, 30 bar CH ₄ , 3 bar O ₂ , 363 K, reaction time 2 h	-	CH ₃ OH	11.35 μmol h ⁻¹	>99%	17.4% (350 nm)
(<i>n</i> -Bu ₄ N) ₂ CeCl ₆ ³⁵	Batch reaction, 400 nm LEDs, 0.05 mmol di- <i>tert</i> -butylazodicarboxylate (DBAD), 5000 kPa CH ₄ , 0.5 mol% (<i>n</i> -Bu ₄ N) ₂ CeCl ₆ , 20 mol% 2,2,2-trichloroethanol, 2.5 mol% tetrabutylammonium Chloride, 2.6 mL CH ₃ CN, room temperature, reaction time 2 h.	-		15.75 μmol h ⁻¹ 25 μmol h ⁻¹	-	

	Flow reaction, 400 nm LEDs, 5 mmol DBAD, 1800 kPa CH ₄ , 1 mol% (<i>n</i> - Bu ₄ N) ₂ CeCl ₆ , 20 mol% 2,2,2- trichloroethanol, 40 mol% TFA, 100 mL CH ₃ CN					
--	---	--	--	--	--	--